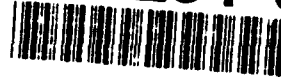


AFIT/DS/AA/94-4

AD-A284 887



NUMERICAL SIMULATION OF DYNAMIC-STALL
SUPPRESSION BY TANGENTIAL BLOWING

DISSERTATION
Matthew C. Towne
Major, USAF

AFIT/DS/AA/94-4

DTIC QUALITY INSPECTED 3

Approved for public release; distribution unlimited

164100
94-30532



The views expressed in this dissertation are those of the author and do not reflect the official policy or position of the Department of Defense or the U. S. Government.

Accession For	
NTIS CRA&I	✓
DTIC TAB	
Unannounced	
Justification	
By _____	
Distribution/	
Availability Codes	
Dist	Avail and/or Special
A-1	

AFIT/DS/AA/94-4

**NUMERICAL SIMULATION OF DYNAMIC-STALL SUPPRESSION
BY TANGENTIAL BLOWING**

DISSERTATION

**Presented to the Faculty of the School of Engineering
of the Air Force Institute of Technology**

Air University

**In Partial Fulfillment of the
Requirements for the Degree of
Doctor of Philosophy**

Matthew C. Towne, M.S., B.S.

Major, USAF

July 1994

Approved for public release; distribution unlimited

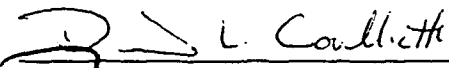
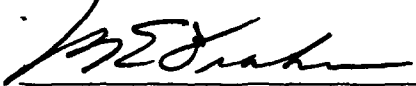
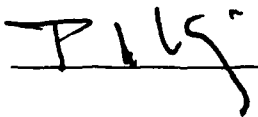
AFIT/DS/AA/94-4

NUMERICAL SIMULATION OF DYNAMIC-STALL SUPPRESSION
BY TANGENTIAL BLOWING

Matthew C. Towne, M.S., B.S.

Major, USAF

Approved:

<u></u>	<u>20 Jul '94</u>
<u>Gerald A Haren</u>	<u>20 Jul 94</u>
<u></u>	<u>20 Jul 94</u>
<u></u>	<u>21 July 94</u>
<u></u>	<u>21 July 94</u>

J. S. Przemieniecki 12 Aug. 94

J. S. Przemieniecki
Senior Dean

Acknowledgements

Many have given me assistance and support throughout this academic endeavor. First and foremost, I thank God, my creator and re-creator, for placing His mighty yet kind providential hand upon me throughout this program. May He receive all the glory and honor for any positive results from this research.

My warmest thanks goes to my most wonderful wife, Donna, for her prayers, support, and encouragement throughout this work.

I want to thank Maj Tom Buter who has been a first-class advisor to me. His tireless assistance and prodding throughout this research has been a true godsend to me.

To my friend and fellow student Capt Dennis Lileikis, I owe a debt of gratitude. I was always left richer after the many technical discussions we had.

Thanks also goes to Dr. Miguel Visbal who provided me with his Navier-Stokes code to use for this research, and for patiently sharing his priceless dynamic-stall and fluid-dynamics expertise with me.

I wish to also thank Dr. Joe Shang who was instrumental in identifying the research area. Along with my advisor, I wish to thank committee member Col Gerry Hasen and Lt Col Richard Newsome of Seiler Labs for problem definition and refinement. Thanks also to Maj Dave Coulliette for serving on my committee and for the technical exchanges we had over the pseudocompressible technique. I also appreciate Dr. Milton Franke serving as a committee member and for Dr. Paul King serving as the Dean's representative.

I wish to acknowledge Ohio Supercomputer Center for providing CRAY Y-MP computer.

Last, but not least, I want to thank the people at the Department of Aeronautics at the Air Force Academy for sponsoring me in this tremendous educational opportunity.

Matthew C. Towne

Table of Contents

	Page
Acknowledgements	iii
List of Figures	vii
List of Tables	xvi
List of Symbols	xvii
Abstract	xx
I. Introduction	1-1
II. Background	2-1
2.1 Experimental and Computational Observations of Dynamic Stall	2-1
2.2 A Closer Look at the Dynamic Stall Phenomenon	2-5
2.3 A Closer Look at the Onset of Dynamic Stall	2-8
2.4 Statement of the Problem	2-16
III. Formulation of the Numerical Model	3-1
3.1 Navier-Stokes Equations	3-1
3.2 Boundary and Initial Conditions	3-3
3.3 Boundary Conditions at the Jet Slot	3-4
3.4 Numerical Scheme	3-6
IV. Results and Discussion	4-1
4.1 Natural Case	4-2
4.1.1 Initial Acceleration Effect	4-3
4.1.2 Initial Condition Effect	4-5
4.1.3 Compressibility Assessment	4-8

	Page
4.1.4 Comparison with Experiment	4-15
4.2 Control via Tangential Blowing	4-16
4.2.1 Slot-Location and Width Effects	4-17
4.2.2 Jet Velocity Effects	4-27
4.2.3 Effect of Delaying α_b	4-33
4.2.4 Jet Orientation Angle Effect	4-35
4.2.5 Jet Profile Effect	4-40
4.2.6 Effect of Pulsed Blowing	4-42
4.2.7 Compressibility Assessment	4-45
4.3 Control via Suction	4-50
4.3.1 Effect of Delaying α_b	4-50
4.3.2 Suction Velocity Effects	4-51
4.3.3 Slot Width Effects	4-52
4.3.4 Suction versus Tangential Blowing	4-55
V. Conclusions	5-1
Appendix A. Grid Constants and Flux Jacobians	A-1
A.1 Grid Constants	A-1
A.2 Flux Jacobians	A-1
Appendix B. Natural Numerical Artifacts Effects	B-1
B.1 Grid Study	B-1
B.2 Temporal Discretization Study	B-6
B.3 Dissipation Coefficient Study	B-8
Appendix C. Tangential Blowing Numerical Artifacts Effects	C-1
C.1 Global and Slot Grid Study	C-1
C.2 Temporal Discretization Study	C-7
C.3 Dissipation Coefficient Study	C-8

	Page
Appendix D. $M_\infty < 0.2$ Grid and Time-Step Study	D-1
Appendix E. Suction Slot Grid Study	E-1
Appendix F. Incompressible Flow Code	F-1
F.1 Incompressible Flow Governing Equations	F-1
F.2 Beam-Warming Scheme for Incompressible Flow	F-2
F.2.1 Pseudocompressible Modification to Governing Equations	F-2
F.2.2 Steady-State Incompressible Flow	F-3
F.2.3 Local Time Step	F-7
F.2.4 Artificial Viscosity	F-7
F.2.5 Outflow Boundary Conditions	F-8
F.2.6 Time-Accurate Incompressible Flow	F-9
F.3 Incompressible Flow in Driven Cavity	F-11
F.3.1 Boundary and Initial Conditions	F-12
F.3.2 Steady-State Results	F-12
F.3.3 Time-Accurate Results	F-12
F.4 Incompressible Flow About a Cylinder	F-14
F.5 Difficulties with Pseudocompressibility Technique for Dynamic-Stall Problem	F-17
Bibliography	BIB-1
Vita	VITA-1

List of Figures

Figure	Page
1.1. Increase in fighter operating envelope using potential dynamic stall technology implementation (Lang and Francis, 1985)	1-2
2.1. Vorticity contours for pitching NACA 0015 airfoil; 361x201 grid, $Re_c = 2.4 \times 10^4$, $M_\infty = 0.2$, $\Omega_0^+ = 0.2$	2-6
2.2. Close-up of reverse-flow region for pitching NACA 0015 airfoil; 361x201 grid, $Re_c = 2.4 \times 10^4$, $M_\infty = 0.2$, $\Omega_0^+ = 0.2$	2-10
2.2. Close-up of reverse-flow region for pitching NACA 0015 airfoil; 361x201 grid, $Re_c = 2.4 \times 10^4$, $M_\infty = 0.2$, $\Omega_0^+ = 0.2$ (concluded)	2-11
2.3. Pressure gradient, pressure contours (levels 1-5: 16.46, 16.54, 16.64, 16.88, 17.13), velocities and isovorticity contours for $0.10c \leq X \leq 0.25c$ region; 361x201 grid, $Re_c = 2.4 \times 10^4$, $M_\infty = 0.2$, $\Omega_0^+ = 0.2$	2-13
2.4. Sketch of velocity profile and simplified model of fluid particles at the critical chord-wise station based on case having $Re_c = 2.4 \times 10^4$, $M_\infty = 0.2$, $\Omega_0^+ = 0.2$, $X \approx 0.17c$	2-14
3.1. Conventions for pitching airfoil (Visbal and Shang, 1989)	3-3
3.2. Slot-blowing conventions.	3-5
4.1. Six of the grids used as part of the grid refinement analysis	4-2
4.2. Acceleration profile for three t_0^+ values	4-3
4.3. Effect of t_0^+ variation on C_l and C_p ; 361x201, $Re_c = 2.4 \times 10^4$, $M_\infty = 0.2$, $\Omega_0^+ = 0.2$	4-4
4.4. Effect of t_0^+ variation on isovorticity contours; 361x201, $Re_c = 2.4 \times 10^4$, $M_\infty = 0.2$, $\Omega_0^+ = 0.2$	4-5
4.5. Effect of t_0^+ variation on C_l and C_p ; 361x201, $Re_c = 2.4 \times 10^4$, $M_\infty = 0.2$, $\Omega_0^+ = 0.6$	4-6
4.6. Effect of t_0^+ variation on isovorticity contours; 361x201, $Re_c = 2.4 \times 10^4$, $M_\infty = 0.2$, $\Omega_0^+ = 0.6$	4-6

Figure	Page
4.7. Starting solution C_i limit cycle and its effect for two pitch rates; 385x201, $Re_c = 2.4 \times 10^4$, $M_\infty = 0.2$	4-7
4.8. Effect of initial condition on C_p and isovorticity contours ($\alpha = 22^\circ$); 385x201, $Re_c = 2.4 \times 10^4$, $M_\infty = 0.2$, $\Omega_0^+ = 0.2$	4-8
4.9. Effect of M_∞ on C_i and effect of t_0^+ on C_i (at $M_\infty = 0.05$); 385x201, $Re_c = 1.0 \times 10^4$, $\Omega_0^+ = 0.2$	4-10
4.10. Effect of t_0^+ on C_p and isovorticity contours ($\alpha = 25^\circ$); 385x201, $Re_c = 1.0 \times 10^4$, $M_\infty = 0.05$, $\Omega_0^+ = 0.2$	4-11
4.11. Effect of M_∞ on C_p ; 385x201, $Re_c = 1.0 \times 10^4$, $\Omega_0^+ = 0.2$	4-11
4.12. Effect of M_∞ on isovorticity contours ($\alpha = 25^\circ$); 385x201, $Re_c = 1.0 \times 10^4$, $\Omega_0^+ = 0.2$	4-12
4.13. Effect of M_∞ on C_p ; 385x201, $Re_c = 1.0 \times 10^4$, $\Omega_0^+ = 0.2$	4-13
4.14. Isovorticity contours and contours of vorticity-transport equation terms; 361x201, $\alpha = 20^\circ$, $Re_c = 2.4 \times 10^4$, $M_\infty = 0.2$, $\Omega_0^+ = 0.2$	4-14
4.15. Isovorticity contours and contours of vorticity-transport equation terms; 361x201, $\alpha = 22^\circ$, $Re_c = 2.4 \times 10^4$, $M_\infty = 0.2$, $\Omega_0^+ = 0.2$	4-15
4.16. Profiles of $\nabla \cdot \mathbf{V}$ and vorticity-transport equation terms for natural case at $X = 0.1c$; 361x201, $\alpha = 15^\circ, 20^\circ, 22^\circ, 25^\circ, 27^\circ$, $Re_c = 2.4 \times 10^4$, $M_\infty = 0.2$, $\Omega_0^+ = 0.2$	4-16
4.17. Comparison of computed velocity profile ($M_\infty = 0.2$) with experiment ($M_\infty < 0.05$) at $X = 0.1c$ (Lovato, 1992) and isovorticity contours for the computed solution (385x201); $Re_c = 2.4 \times 10^4$, $\Omega_0^+ = 0.05$ (Note: s_n is the coordinate direction normal to the wall).	4-17
4.18. Effect of tangential blowing at $X = 0.0c$, $X = 0.2c$, $X = 0.4c$ slots on C_i ; 343x201, $v_j = 2.83U_\infty$, $\phi = 10^\circ$, $Re_c = 2.4 \times 10^4$, $M_\infty = 0.2$, $\Omega_0^+ = 0.2$	4-18
4.19. Effect of tangential blowing at $X = 0.0c$ and $0.4c$ slots on vorticity contours; 385x201, $v_j = 2.83U_\infty$, $\phi = 10^\circ$, $Re_c = 2.4 \times 10^4$, $M_\infty = 0.2$, $\Omega_0^+ = 0.2$	4-19
4.20. Effect of tangential blowing at $X = 0.0c$, $X = 0.4c$ slots (individually and simultaneously) on C_i ; 385x201, $v_j = 2.83U_\infty$, $\phi = 10^\circ$, $Re_c = 2.4 \times 10^4$, $M_\infty = 0.2$, $\Omega_0^+ = 0.2$	4-20

Figure	Page
4.21. Effect of $X = 0.0c$ and $0.4c$ simultaneous tangential blowing on vorticity contours; 385×201 , $v_j = 2.83U_\infty$, $\phi = 10^\circ$, $Re_c = 2.4 \times 10^4$, $M_\infty = 0.2$, $\Omega_0^+ = 0.2$	4-21
4.22. Effect of tangential blowing at $X = 0.0c$, $X = 0.4c$ slots (individually and simultaneously) on C_l for a low pitch rate ($\Omega_0^+ = 0.05$); 385×201 , $v_j = 2.83U_\infty$, $\phi = 10^\circ$, $C_\mu = 0.0292$, $Re_c = 2.4 \times 10^4$, $M_\infty = 0.2$	4-21
4.23. Effect of tangential blowing at $X = 0.0c$ and $0.05c$ slots on vorticity contours; 351×201 , $v_j = 2.8U_\infty$, $\phi = 10^\circ$, $Re_c = 2.4 \times 10^4$, $M_\infty = 0.2$, $\Omega_0^+ = 0.2$	4-23
4.24. Effect of tangential blowing at $X = 0.0c$ and $0.05c$ slots on C_p for constant \dot{m} ; 351×201 , $\alpha = 22^\circ$, $\phi = 10^\circ$, $Re_c = 2.4 \times 10^4$, $M_\infty = 0.2$, $\Omega_0^+ = 0.2$	4-24
4.25. Effect of tangential blowing on C_p , vorticity contours, and velocity vectors at $\alpha = 27^\circ$; 351×201 , $v_j = 2.83U_\infty$, $\phi = 10^\circ$, $Re_c = 2.4 \times 10^4$, $M_\infty = 0.2$, $\Omega_0^+ = 0.2$	4-25
4.26. Effect of tangential blowing at $X = 0.05c$ slot on C_l for constant C_μ and constant \dot{m} ; $\phi = 10^\circ$, $Re_c = 2.4 \times 10^4$, $M_\infty = 0.2$, $\Omega_0^+ = 0.2$	4-25
4.27. Effect of slot width on isovorticity contours; $\phi = 10^\circ$, $Re_c = 2.4 \times 10^4$, $M_\infty = 0.2$, $\Omega_0^+ = 0.2$	4-26
4.28. Breakdown of incompressible-flow jet assumption for blowing at $X = 0.05c$ slot; $Re_c = 2.4 \times 10^4$, $M_\infty = 0.2$, $\Omega_0^+ = 0.2$	4-27
4.29. Effect of variation in tangential-blowing jet velocity at $0.05c$ slot on C_l ; 351×201 , $\phi = 10^\circ$, $Re_c = 2.4 \times 10^4$, $M_\infty = 0.2$, $\Omega_0^+ = 0.2$	4-28
4.30. Effect of variation in tangential-blowing jet velocity at $0.05c$ slot on isovorticity contours; 351×201 , $\phi = 10^\circ$, $Re_c = 2.4 \times 10^4$, $M_\infty = 0.2$, $\Omega_0^+ = 0.2$	4-29
4.31. Velocity profile for natural case ($\alpha = 15^\circ, 20^\circ, 22^\circ$); 351×201 , $Re_c = 2.4 \times 10^4$, $M_\infty = 0.2$, $\Omega_0^+ = 0.2$	4-30
4.32. Effect of variation in tangential-blowing jet velocity at $0.0c$ slot on isovorticity contours; 385×201 , $\phi = 10^\circ$, $Re_c = 2.4 \times 10^4$, $M_\infty = 0.2$, $\Omega_0^+ = 0.2$	4-31
4.33. Velocity and vorticity profile for natural and $0.05c$ -blowing cases ($v_j = 2.78U_\infty$, $\phi = 10^\circ$) at $X = 0.1c$ ($\alpha = 15^\circ, 20^\circ, 22^\circ$); 351×201 , $Re_c = 2.4 \times 10^4$, $M_\infty = 0.2$, $\Omega_0^+ = 0.2$	4-32

Figure	Page
4.34. Effect of tangential-blowing α_b on vorticity contours ($\alpha = 27.0^\circ$); 361x201, $v_j = 4.14U_\infty$ at $0.05c$, $\phi = 10^\circ$, $Re_c = 2.4 \times 10^4$, $M_\infty = 0.2$, $\Omega_0^+ = 0.2$.	4-34
4.35. Isovorticity contours for natural case; 361x201, $Re_c = 2.4 \times 10^4$, $M_\infty = 0.2$, $\Omega_0^+ = 0.2$	4-34
4.36. Effect of blowing-angle variation (using constant $C_\mu = 0.0292$) on isovorticity contours at $\alpha = 25^\circ$; 385x201, $X = 0.0c$ slot, $Re_c = 2.4 \times 10^4$, $M_\infty = 0.2$, $\Omega_0^+ = 0.2$	4-37
4.37. Effect of blowing-angle variation on C_l ; 385x201, $X = 0.0c$ slot, $Re_c = 2.4 \times 10^4$, $M_\infty = 0.2$, $\Omega_0^+ = 0.2$	4-37
4.38. Effect of blowing-angle variation on C_m about the quarter chord; 385x201, $X = 0.0c$ slot, $Re_c = 2.4 \times 10^4$, $M_\infty = 0.2$, $\Omega_0^+ = 0.2$	4-37
4.39. Dynamic-stall-vortex formation comparison for natural and two blowing angle cases (using constant $C_\mu = 0.0292$); 385x201, blowing at $X = 0.0c$ slot, $Re_c = 2.4 \times 10^4$, $M_\infty = 0.2$, $\Omega_0^+ = 0.2$	4-38
4.40. Effect of a variation in slot velocity profile on C_l ; 385x201, average $v_j = 2.83U_\infty$ at $X = 0.0c$, $\phi = 10^\circ$, $Re_c = 2.4 \times 10^4$, $M_\infty = 0.2$, $\Omega_0^+ = 0.2$. .	4-40
4.41. Effect of variation in slot velocity profile on isovorticity contours at $\alpha = 25^\circ$; 385x201, average $v_j = 2.83U_\infty$ at $X = 0.0c$, $\phi = 10^\circ$, $Re_c = 2.4 \times 10^4$, $M_\infty = 0.2$, $\Omega_0^+ = 0.2$	4-41
4.42. Effect of variation in slot velocity profile on isovorticity contours at $\alpha = 33^\circ$; 385x201, average $v_j = 2.83U_\infty$ at $X = 0.0c$, $\phi = 10^\circ$, $Re_c = 2.4 \times 10^4$, $M_\infty = 0.2$, $\Omega_0^+ = 0.2$	4-41
4.43. Pulse history for the $f^+ = 1.00$ case; $\Omega_0^+ = 0.2$	4-43
4.44. C_l Comparison of frequency variation for of pulsed tangential blowing at $X = 0.0c$; 385x201, $v_j = 2.83U_\infty$ or $v_j = 0$, $\phi = 10^\circ$, $Re_c = 2.4 \times 10^4$, $M_\infty = 0.2$, $\Omega_0^+ = 0.2$	4-43
4.45. Effect of pulsed tangential blowing on isovorticity contours; 385x201, $v_j = 2.83U_\infty$ or $v_j = 0$, $\phi = 10^\circ$, $Re_c = 2.4 \times 10^4$, $M_\infty = 0.2$, $\Omega_0^+ = 0.2$	4-44
4.46. Effect of constant and pulsed tangential blowing at $X = 0.0c$ on C_l ; 385x201, $v_j = 2.83U_\infty$ or $v_j = 0$, $\phi = 10^\circ$, $Re_c = 2.4 \times 10^4$, $M_\infty = 0.2$, $\Omega_0^+ = 0.2$	4-45

Figure	Page
4.47. Effect of M_∞ on C_l and C_p for 0.0c-blowing case; 385x201, $v_j = 2.83U_\infty$, $\phi = 10^\circ$, $Re_c = 1.0 \times 10^4$, $\Omega_0^+ = 0.2$	4-46
4.48. Effect of M_∞ on C_p and isovorticity contours for 0.0c-blowing case at $\alpha = 27^\circ$; 385x201, $v_j = 2.83U_\infty$, $\phi = 10^\circ$, $Re_c = 1.0 \times 10^4$, $\Omega_0^+ = 0.2$	4-47
4.49. Isovorticity contours and contours of vorticity-transport equation terms for 0.05c-blowing case; 361x201, $v_j = 4.14U_\infty$, $\alpha = 27^\circ$, $\phi = 10^\circ$, $Re_c = 2.4 \times 10^4$, $M_\infty = 0.2$, $\Omega_0^+ = 0.2$	4-47
4.50. Isovorticity contours and contours of vorticity-transport equation terms for 0.05c-blowing case; 361x201, $v_j = 4.14U_\infty$, $\alpha = 30^\circ$, $\phi = 10^\circ$, $Re_c = 2.4 \times 10^4$, $M_\infty = 0.2$, $\Omega_0^+ = 0.2$	4-48
4.51. Profiles of $\nabla \cdot \mathbf{V}$ and vorticity-transport equation terms for blowing case; 361x201, $v_j = 4.14U_\infty$, $\alpha = 15^\circ, 20^\circ, 22^\circ, 25^\circ, 27^\circ$, $Re_c = 2.4 \times 10^4$, $M_\infty = 0.2$, $\Omega_0^+ = 0.2$	4-49
4.52. Effect of suction α_b on vorticity contours ($\alpha = 33.0^\circ$); 361x201, $v_s = 0.697U_\infty$, $Re_c = 2.4 \times 10^4$, $M_\infty = 0.2$, $\Omega_0^+ = 0.2$	4-51
4.53. Effect of suction at 0.05c slot on C_l ; 361x201, $v_s = 0.697U_\infty$, $Re_c = 2.4 \times 10^4$, $M_\infty = 0.2$, $\Omega_0^+ = 0.2$	4-52
4.54. Effect of variation in suction velocity at 0.05c slot on isovorticity contours; 361x201, $\alpha_b = 5^\circ$, $Re_c = 2.4 \times 10^4$, $M_\infty = 0.2$, $\Omega_0^+ = 0.2$	4-53
4.55. Effect of variation in suction velocity at 0.05c slot on C_l ; 361x201, $\alpha_b = 5^\circ$, $Re_c = 2.4 \times 10^4$, $M_\infty = 0.2$, $\Omega_0^+ = 0.2$	4-54
4.56. Effect of slot-width variation at 0.05c slot on C_l ; $Re_c = 2.4 \times 10^4$, $M_\infty = 0.2$, $\Omega_0^+ = 0.2$	4-54
4.57. Effect of slot-width variation on isovorticity contours ($\alpha = 36.0^\circ$); 361x201 (a, b) and 351x201 (c), $Re_c = 2.4 \times 10^4$, $M_\infty = 0.2$, $\Omega_0^+ = 0.2$	4-55
4.58. Isovorticity contour comparison for natural case, tangential-blowing control, and suction control at 0.05c slot; 361x201, $\dot{m} = 0.0052\rho_\infty U_\infty c$ for blowing and suction, $Re_c = 2.4 \times 10^4$, $M_\infty = 0.2$, $\Omega_0^+ = 0.2$	4-56
4.59. Isovorticity contour comparison for natural case, tangential-blowing control, and suction control at 0.05c slot over three α 's; 361x201, $\dot{m} = 0.0052\rho_\infty U_\infty c$ for blowing and suction, $Re_c = 2.4 \times 10^4$, $M_\infty = 0.2$, $\Omega_0^+ = 0.2$	4-57

Figure	Page
4.60. C_l , C_d , and C_m (about $X = 0.25c$) comparisons for natural case, tangential-blowing control, and suction control at $0.05c$ slot; 361×201 , $\dot{m} = 0.0052\rho_\infty U_\infty c$ for blowing and suction, $Re_c = 2.4 \times 10^4$, $M_\infty = 0.2$, $\Omega_0^+ = 0.2$	4-57
B.1. Effect of mesh refinement on C_l and C_d ; $Re_c = 2.4 \times 10^4$, $M_\infty = 0.2$, $\Omega_0^+ = 0.2$	B-2
B.2. Effect of mesh refinement on vorticity contours; $Re_c = 2.4 \times 10^4$, $M_\infty = 0.2$, $\Omega_0^+ = 0.2$	B-3
B.3. Effect of mesh refinement on C_p ; $Re_c = 2.4 \times 10^4$, $M_\infty = 0.2$, $\Omega_0^+ = 0.2$	B-3
B.4. Comparison of C_l and C_d for 361×201 , 385×201 , and 505×201 grids; $Re_c = 2.4 \times 10^4$, $M_\infty = 0.2$, $\Omega_0^+ = 0.2$	B-4
B.5. Comparison of C_p for 361×201 , 385×201 , and 505×201 grids; $Re_c = 2.4 \times 10^4$, $M_\infty = 0.2$, $\Omega_0^+ = 0.2$	B-4
B.6. Effect of slot width variation on C_l and vorticity contours ($\alpha = 36^\circ$); $Re_c = 2.4 \times 10^4$, $M_\infty = 0.2$, $\Omega_0^+ = 0.2$	B-5
B.7. Grid refinement in the normal direction and its effect on C_l ; $Re_c = 2.4 \times 10^4$, $M_\infty = 0.2$, $\Omega_0^+ = 0.2$	B-5
B.8. Effect of time step on C_l and C_d ; 385×201 , $Re_c = 2.4 \times 10^4$, $M_\infty = 0.2$, $\Omega_0^+ = 0.2$	B-6
B.9. Effect of time step on vorticity contours; 385×201 , $Re_c = 2.4 \times 10^4$, $M_\infty = 0.2$, $\Omega_0^+ = 0.2$	B-7
B.10. Effect of time step on C_p ; 385×201 , $Re_c = 2.4 \times 10^4$, $M_\infty = 0.2$, $\Omega_0^+ = 0.2$	B-7
B.11. Effect of time step on C_l and C_d ; 505×201 , $Re_c = 2.4 \times 10^4$, $M_\infty = 0.2$, $\Omega_0^+ = 0.2$	B-8
B.12. Effect of time step on C_p and vorticity contours; 505×201 , $Re_c = 2.4 \times 10^4$, $M_\infty = 0.2$, $\Omega_0^+ = 0.2$	B-9
B.13. Effect of halving dissipation coefficient on C_l and isovorticity contours; 385×201 , $\alpha = 25^\circ$, $Re_c = 2.4 \times 10^4$, $M_\infty = 0.2$, $\Omega_0^+ = 0.2$	B-9
B.14. Effect of doubling dissipation coefficient on C_l and isovorticity contours; 361×201 , $\alpha = 25^\circ$, $Re_c = 2.4 \times 10^4$, $M_\infty = 0.2$, $\Omega_0^+ = 0.2$	B-10

Figure	Page
C.1. Effect of tangential blowing at 0.0c slot on C_l and C_p ; $v_j = 2.83U_\infty$, $\phi = 10^\circ$, $Re_c = 2.4 \times 10^4$, $M_\infty = 0.2$, $\Omega_0^+ = 0.2$	C-2
C.2. Effect of tangential blowing at 0.0c on isovorticity contours; $v_j = 2.83U_\infty$, $\phi = 10^\circ$, $\alpha = 27^\circ$, $Re_c = 2.4 \times 10^4$, $M_\infty = 0.2$, $\Omega_0^+ = 0.2$	C-2
C.3. Effect of tangential blowing at 0.0c on C_l and isovorticity contours ($\alpha = 36^\circ$); $v_j = 2.83U_\infty$, $\phi = 10^\circ$, $Re_c = 2.4 \times 10^4$, $M_\infty = 0.2$, $\Omega_0^+ = 0.2$	C-2
C.4. Effect of tangential blowing at 0.4c slot on C_l and C_p ; $v_j = 2.83U_\infty$, $\phi = 10^\circ$, $Re_c = 2.4 \times 10^4$, $M_\infty = 0.2$, $\Omega_0^+ = 0.2$	C-3
C.5. Effect of tangential blowing at 0.4c on isovorticity contours; $v_j = 2.83U_\infty$, $\phi = 10^\circ$, $\alpha = 27^\circ$, $Re_c = 2.4 \times 10^4$, $M_\infty = 0.2$, $\Omega_0^+ = 0.2$	C-3
C.6. Effect of 0.0c-slot grid resolution on C_l for natural and blowing cases; $v_j = 2.83U_\infty$, $\phi = 10^\circ$, $Re_c = 2.4 \times 10^4$, $M_\infty = 0.2$, $\Omega_0^+ = 0.2$	C-5
C.7. Effect of 0.0c-slot grid resolution on C_p and isovorticity contours for blowing case; $v_j = 2.83U_\infty$, $\phi = 10^\circ$, $\alpha = 33^\circ$, $Re_c = 2.4 \times 10^4$, $M_\infty = 0.2$, $\Omega_0^+ = 0.2$	C-5
C.8. Effect of 0.4c-slot grid resolution on C_l for natural and blowing cases; $v_j = 2.83U_\infty$, $\phi = 10^\circ$, $Re_c = 2.4 \times 10^4$, $M_\infty = 0.2$, $\Omega_0^+ = 0.2$	C-5
C.9. Effect of 0.4c-slot grid resolution on C_p and isovorticity contours for blowing case; $v_j = 2.83U_\infty$, $\phi = 10^\circ$, $\alpha = 33^\circ$, $Re_c = 2.4 \times 10^4$, $M_\infty = 0.2$, $\Omega_0^+ = 0.2$	C-6
C.10. Effect of 0.05c-slot grid resolution on C_l for natural and blowing cases ($v_j = 4.14U_\infty$); $\phi = 10^\circ$, $Re_c = 2.4 \times 10^4$, $M_\infty = 0.2$, $\Omega_0^+ = 0.2$	C-6
C.11. Effect of 0.05c-slot grid resolution on C_p and isovorticity contours for blowing case ($v_j = 4.14U_\infty$); $\phi = 10^\circ$, $\alpha = 30^\circ$, $Re_c = 2.4 \times 10^4$, $M_\infty = 0.2$, $\Omega_0^+ = 0.2$	C-7
C.12. Effect of time step on C_l and isovorticity contours ($\alpha = 25^\circ$) for 0.0c-slot blowing case; 385x201, $v_j = 2.83U_\infty$, $\phi = 10^\circ$, $Re_c = 2.4 \times 10^4$, $M_\infty = 0.2$, $\Omega_0^+ = 0.2$	C-8
C.13. Effect of dissipation coefficient on C_l and isovorticity contours ($\alpha = 27^\circ$) for 0.0c-slot blowing case; 385x201, $v_j = 2.83U_\infty$, $\phi = 10^\circ$, $Re_c = 2.4 \times 10^4$, $M_\infty = 0.2$, $\Omega_0^+ = 0.2$	C-8

Figure	Page
C.14. Effect of dissipation coefficient on C_l and isovorticity contours ($\alpha = 27^\circ$) for 0.4c-slot blowing case; 385x201, $v_j = 2.83U_\infty$, $\phi = 10^\circ$, $Re_c = 2.4 \times 10^4$, $M_\infty = 0.2$, $\Omega_0^+ = 0.2$	C-9
C.15. Effect of dissipation coefficient on C_l and isovorticity contours ($\alpha = 30^\circ$) for 0.05c-slot blowing case; 361x201, $v_j = 4.14U_\infty$, $\phi = 10^\circ$, $Re_c = 2.4 \times 10^4$, $M_\infty = 0.2$, $\Omega_0^+ = 0.2$	C-9
D.1. Effect of time step on C_l (385x201) and effect of grid resolution on C_l (385x201 and 505x201— $\Delta t^+ = 0.0005$); $Re_c = 1.0 \times 10^4$, $M_\infty = 0.1$, $\Omega_0^+ = 0.2$	D-1
D.2. Effect of spatial resolution on C_p and isovorticity contours; $Re_c = 1.0 \times 10^4$, $M_\infty = 0.1$, $\Omega_0^+ = 0.2$, $\Delta t^+ = 0.0005$	D-2
D.3. Effect of spatial resolution on C_l and isovorticity contours ($\alpha = 36^\circ$); $Re_c = 1.0 \times 10^4$, $M_\infty = 0.05$, $\Omega_0^+ = 0.2$, $\Delta t^+ = 0.00025$	D-2
D.4. Effect of time step on C_l and C_p ($\alpha = 25^\circ$); 385x201, $Re_c = 1.0 \times 10^4$, $M_\infty = 0.05$, $\Omega_0^+ = 0.2$	D-3
D.5. Effect of time step on isovorticity contours ($\alpha = 25^\circ$); 385x201, $Re_c = 1.0 \times 10^4$, $M_\infty = 0.05$, $\Omega_0^+ = 0.2$	D-3
E.1. Effect of 0.05c-slot grid resolution on C_p and isovorticity contours ($\alpha = 42^\circ$) for suction case; $v_s = 0.697U_\infty$, $Re_c = 2.4 \times 10^4$, $M_\infty = 0.2$, $\Omega_0^+ = 0.2$	E-1
F.1. Steady-state solution for driven cavity; 129x129 grid ($Re_L = 100$, $\Delta\tau^+ = 0.005$, $\beta = 10^3$)	F-13
F.2. u and v velocities along $y/L = 0.5$ and $x/L = 0.5$ stations, respectively (middle of cavity, $Re_L = 100$)	F-13
F.3. Velocity vectors and streamlines for time-dependent driven cavity; $Re_L = 200$, $\Delta\hat{t}^+ = 0.01$, $\Delta\tau^+ = 0.01$, $\beta = 400$)	F-15
F.4. Drag on lid at various times ($Re_L = 200$, $\Delta\hat{t}^+ = 0.01$, $\Delta\tau^+ = 0.01$, $\beta = 400$)	F-16
F.5. Pseudotime sub-iterations needed at various time steps ($Re_L = 200$, $\Delta\hat{t}^+ = 0.01$, $\Delta\tau^+ = 0.01$, $\beta = 400$)	F-16

Figure	Page
F.6. Grid (155x151), streamlines and C_p for cylinder in incompressible flow; $Re_D = 20$, $t_0 = 0.1$, $\beta = 400$, $\epsilon_4 = 1.0$, $\epsilon_2 = 2.0$)	F-17

List of Tables

Table	Page
2.1. Effect of parameter variation on dynamic stall (Lovato, 1992)	2-2
4.1. Summary of Selected Computations	4-1
4.2. Six Cases of Jet-Velocity-Variation Study	4-28
4.3. Solution Sensitivity to Blowing-angle (ϕ) Variation	4-39
C.1. 0.0c- and 0.4c-Slot Grid Study	C-4
C.2. 0.05c-Slot Grid Study	C-4

List of Symbols

Symbol	
c	= chord
C_l, C_d, C_p	= lift, drag, and pressure coefficients
C_p	= momentum blowing coefficient, $\dot{m}v_j/(q_\infty c)$
c_p	= specific heat coefficient
e	= specific internal energy
f	= blowing frequency (blows/sec)
f^+	= non-dimensional blowing frequency, fc/U_∞
L	= square cavity side length
M	= Mach number
\dot{m}	= mass flow rate per unit span (Equation 3.5)
n	= direction normal to surface
p	= ratio of pressure to density, P/ρ
P	= pressure
Pr	= Prandtl number
q_∞	= dynamic pressure, $\frac{1}{2}\rho_\infty U_\infty^2$
Re_c	= chord Reynolds number, $U_\infty c/\nu_\infty$
Re_L	= Reynolds number based on cavity side length, $U_\infty L/\nu_\infty$
s	= stream-wise direction
s_j, s_s	= slot width for jet (blowing) or suction
s_n, s_η	= distance from airfoil surface (normal or η direction)
\bar{s}	= normalized slot length (used for jet profile study)
t	= time
t^+	= non-dimensional time, tU_∞/c (airfoil) and tU_∞/L (cavity)
T	= temperature
u, v	= velocity components in Cartesian frame
U_∞	= free-stream velocity
V_{max}	= maximum velocity in nonuniform jet velocity profile
\mathbf{V}	= velocity vector

Symbol

V	= magnitude of velocity vector
v_j, v_s	= magnitude of jet velocity (blowing) and suction velocity
x, y	= Cartesian coordinates in inertial reference frame
X, Y	= coordinates of moving reference frame attached to airfoil (Figure 3.1)
α	= angle of attack
α_b	= beginning angle of attack for blowing or suction control
β	= profile-altering power used in jet profile study, also used in pseudocompressible modification to continuity equation (Equation F.5)
δ	= central-difference operator
ϵ_2, ϵ_4	= 2 nd -order-implicit and 4 th -order-explicit damping coefficients
μ	= viscosity
ν	= kinematic viscosity, μ/ρ
Ω	= airfoil pitch rate
Ω^+	= non-dimensional pitch rate, $\Omega c/U_\infty$
ω	= vorticity, $u_x - v_y$ in 2-D
ϕ	= blowing angle
ρ	= density
τ	= pseudotime
τ^+	= non-dimensional pseudotime
ξ, η, \hat{t}	= transformed coordinates

Superscripts

k	= pseudotime level
n	= computational time level

Subscripts

j	= at jet slot
max	= maximum
n	= normal direction

Symbol

<i>ref</i>	= reference
<i>s</i>	= at suction slot
<i>x, y</i>	= partial derivative in <i>x, y</i> direction
∞	= free stream
ξ, η	= partial derivatives in ξ, η directions
0	= initial value

Abstract

The use of tangential blowing to suppress the dynamic stall of a pitching airfoil is investigated numerically. The laminar two-dimensional, compressible Navier-Stokes equations are solved time-accurately using a Beam-Warming algorithm. A slot is located at four different positions along the surface of a NACA 0015 airfoil and air is injected in a nearly tangential sense along the upper surface. Suction control is also employed at one of these slot locations to directly compare with tangential-blowing control.

Solution sensitivity to grid refinement, time-step size, numerical smoothing, and initial conditions is investigated at a Reynolds number of 2.4×10^4 . Initial-condition and initial-airfoil-acceleration effects are analyzed for various pitch rates. Compressibility of $M_\infty = 0.2$ solutions is investigated two ways: 1) by comparing the expansion term in the vorticity-transport equation with other terms in the equation to determine its relative significance, and 2) by computing solutions at $M_\infty = 0.1$ and 0.05 at a Reynolds number of 1.0×10^4 . Numerical simulation uncertainties of jet-orientation angle and jet velocity profile are investigated. The numerical simulations are compared with available experimental data. Studies are conducted to establish the effects of slot position, slot width, blowing-initiation angle, blowing velocity, pulsed blowing, and blowing at different pitch rates.

Of the four slot locations investigated, results for the conditions considered indicate that constant tangential blowing applied at 0%-5% chord region (5%-chord location is more effective than 0% location) is the most effective location for tangential-blowing control of dynamic-stall onset. The greatest angle of blowing initiation for successful dynamic-stall-vortex-formation control coincides with the pressure plateau near the leading edge which precedes by a degree or two the formation of the dynamic-stall vortex. This result suggests a possible control strategy based upon detection of this pressure plateau. Tangential-blowing-control effectiveness is found to depend on momentum blowing coefficient (assuming a constant blowing angle during the pitch-up maneuver) such that, for the same mass flow rate, smaller slot widths give longer dynamic-stall-vortex-formation delay. In the direct comparison made between suction control and tangential control, suc-

tion control was found to delay dynamic-stall-vortex formation to a greater angle of attack than tangential-blowing control; however the stronger shear layer produced from blowing control produced a smoother chord-wise loading distribution at the low- Re_c conditions considered.

NUMERICAL SIMULATION OF DYNAMIC-STALL SUPPRESSION BY TANGENTIAL BLOWING

I. Introduction

Extremely high aerodynamic forces are temporarily generated by a streamlined body rapidly pitched beyond its steady stall angle of attack. The term used to describe the aerodynamic events that an airfoil or wing experiences undergoing this unsteady motion is *dynamic stall*. The dynamic stall phenomenon arises in several applications: wind turbine blades, helicopter rotor blades, jet engine compressor blades, and rapidly pitched aircraft wings.

Recognition of the fact that lifting surfaces being pitched up produce $C_{l_{max}}$ values higher than static values has been reported in the literature as early as the 1930's (Kramer, 1932). Silverstein et al. (1938) observed a significant increase in $C_{l_{max}}$ when an aircraft was pitched up at a non-dimensional pitch rate of 0.01. Harper and Flanigan (1950) also demonstrated the lift benefit of an aircraft moving at a high pitch rate. In terms of analysis and prediction of dynamic stall, Carr (1985) credits Harris and Pruyn (1968) and Ham and Garelick (1968) with making early significant progress analyzing the phenomenon. All four of these researchers were studying the phenomenon from the perspective of rotary aircraft aerodynamics. Harris and Pruyn sought to isolate the cause of an under-prediction of rotor lift on high performance helicopters. They found that when the rotor blades were in the retreating portion of their cycle (i.e., blade moving in a direction opposite to the helicopter travel direction—in this region of the helicopter rotor disk, the maximum blade pitch angle is attained), the blades were producing more lift than expected. Ham (Ham and Young, 1966) studied the problem of high blade torsional loads and vibration levels associated with high performance helicopters. Using potential flow theory, he was able to provide theoretical support to experimental evidence that a leading edge vortex is shed during the dynamic stall process (Ham, 1968).

While much of the early work in analyzing dynamic stall considered oscillating airfoils, recently, motivated by an emphasis on fighter supermaneuverability, research has also been conducted on airfoils pitched up at large amplitudes in a non-oscillatory manner (Oshima and Ramaprian, 1992; Walker, et al., 1985a). Dynamically pitched airfoils exhibit maximum lift coefficients two or three times the static maximum lift (Albertson, et al., 1987; Jumper, et al., 1987). This significant increase in maximum lift, albeit transient, is considered to be an exploitable aerodynamic resource for high performance fighters. Hence, greater understanding of the physics associated with dynamic stall is desired by the Air Force with a view toward aircraft maneuverability enhancement (Fant, 1992). For example, a fighter's operating envelope can be increased through relaxation of the stall limit (Figure 1.1) provided the dynamic stall phenomenon is harnessed (Lang

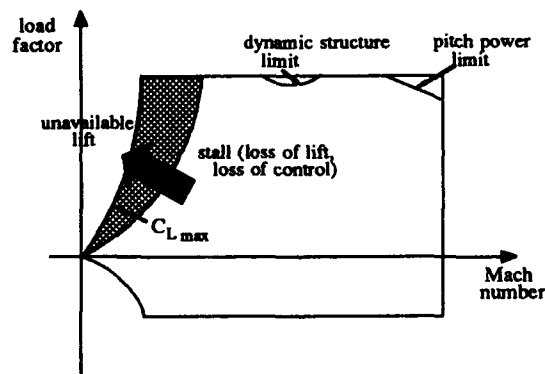


Figure 1.1 Increase in fighter operating envelope using potential dynamic stall technology implementation (Lang and Francis, 1985)

and Francis, 1985). At low speeds, high angle-of-attack performance is crucial for close-in aerial combat since it is associated with tighter, faster turns. An improved ability to quickly point an aircraft and shoot could also result from such an expansion of the operating envelope—a combat capability of perhaps greater importance than enhanced turn performance, according to Lang and Francis.

Aside from an interest in a deeper understanding of the basic physics involved in dynamic stall, a larger area of interest is control of unsteady flows during the initial stages

of separation. Lang and Francis (1985) write, "The ability to manage and control the time dependent, separated flows which earmark the aerodynamic environment is of paramount importance if true supermaneuverable flight is to be achieved." Though 3-D effects are often important in dynamic stall, there is evidence that control techniques developed in 2-D are extendible to 3-D (Carr and McCroskey, 1992). With the extendibility of 2-D results in mind, the research presented in this dissertation is motivated by the Air Force requirement of controlling the time-dependent flow present in the dynamic stall phenomenon.

Some experiments have been conducted to investigate control of dynamic stall. Active-leading-edge suction (Karim and Acharya, 1993), passive suction (Addington, et al., 1992), and leading-edge slats (Carr and McAlister, 1983) have all been shown to suppress dynamic stall to varying degrees. In addition, air blown tangentially (Lovato, 1992) and perpendicularly (Luttges, et al., 1985) over the suction surface have also demonstrated beneficial control effects.

To a lesser extent, control of dynamic stall has been investigated computationally (Visbal, 1991; Ghia, et al., 1992). Tangentially-blown air at the rounded trailing edge (referred to as a *Coanda surface*) of an oscillating circulation control airfoil has been investigated (Shrewsbury and Sankar, 1990). Control applied at the trailing edge did not significantly change the formation of the leading-edge vortex.

There has yet to be a numerical study presented in the literature in which tangential blowing is applied near the leading edge of a pitching airfoil in order to control dynamic stall. It is this gap in the literature toward which this research is directed. Specifically, the research focus presented in this dissertation is the numerical simulation of the effect of tangential blowing over an airfoil undergoing dynamic stall. This is done in an attempt to suppress formation of (i.e., control) the dynamic stall vortex. The flow regime of interest is one of low speed and low Reynolds number. A compressible Navier-Stokes code (Visbal, 1986a) written, well validated, and used by Visbal for several numerical studies on dynamic stall (Visbal, 1991; 1990a; 1990b; 1986b; Visbal and Shang, 1989; 1987) is used at low Mach numbers. In addition to investigation of tangential blowing effects on dynamic stall, results are presented from a brief study of leading-edge (0.05c) suction

(after experimental work of Karim and Acharya (1993). Based on these studies, a control strategy is recommended.

II. Background

To date studies have categorized the impact of parameter variation (e.g., M_∞ , Re_c , Ω_0^+ , geometry) on dynamic stall, but the underlying flow physics causing the dynamic stall behavior is still not fully understood (Carr and McCroskey, 1992). This section will present results from studies undertaken to better understand dynamic stall. Both experimental and computational observations will be presented with emphasis on control of dynamic stall. In addition to these observations, a brief examination is made of the sequence of events that comprise the dynamic stall phenomenon for one specific representative case.

2.1 Experimental and Computational Observations of Dynamic Stall

Carr (1989) classifies stall into two categories: *light* and *deep* stall. Light stall is characterized by trailing edge separation, laminar flow near the leading edge, a separation bubble in the laminar region followed by turbulent flow over the airfoil, and a viscous layer with thickness on the order of the airfoil thickness. In contrast, deep stall is characterized by vortex-dominated flow on the top of the airfoil with the viscous layer thickness on the order of the airfoil chord. Carr shows that airfoil profile has a significant effect on dynamic stall for light stall instances (such as found for helicopters) while deep stall (such as for an airfoil dynamically pitching to high- α —which is the type stall investigated in this research) is fairly insensitive to airfoil profile.

Lovato (1992) gives an overview of experimental observations made in the area of dynamic stall. Based on these observations, several flow variables pertinent to the dynamic stall process have been identified. The effect of a variation in these (α , Ω_0^+ , Re_c , $(X/c)_{pivot}$) on the aerodynamic loads and the flow structure about an airfoil or wing is presented in tabular form (Table 2.1). In this table, u_{max} is the maximum reverse-flow velocity near the surface (3% chord above top surface) for airfoil pitch axis at 40% chord and was obtained from hot-wire measurements (Walker, et al., 1985b). These data were taken to help quantify vortex strength. Vortex dwell time is the length of time the stall vortex stays close to the top surface before convecting downstream. Note that for the range of α and Ω_0^+

Parameter	$\uparrow \alpha$	$\uparrow \Omega_0^+$	$\uparrow Re_c$	$\uparrow (X/c)_{pivot}$
C_p	\uparrow	\uparrow	\downarrow	independent
C_l	\uparrow	\uparrow	\downarrow	independent
C_d	\uparrow	\uparrow	\downarrow	independent
$\alpha_{C_{l,max}}$	\uparrow	\uparrow	\downarrow	\uparrow asymptotically (secondary to Ω_0^+ effects)
$\alpha_{C_{d,max}}$	\uparrow	\uparrow	\downarrow	\uparrow asymptotically (secondary to Ω_0^+ effects)
u_{max} (for $(X/c)_{pivot} = 0.4$)	independent	\uparrow		
vortex dwell time	\uparrow	\uparrow	\downarrow	independent
vortex nature	tighter	tighter, multiple vortices at $\Omega_0^+ > 0.4$		independent

Table 2.1 Effect of parameter variation on dynamic stall (Lovato, 1992)

considered in the collection of experiments summarized, an increase in α and Ω_0^+ results in an increase in aerodynamic loading and correspondingly, a strengthening of the vortical structures above the body surface. An increase in Reynolds number induces a decrease in aerodynamic loads and results in the dynamic stall vortex being convected downstream sooner. Moving the pitch axis aft delays dynamic stall in a similar way as increasing the pitch rate, however there are considerably different vortex dynamics involved once the dynamic-stall vortex has formed (Helin and Walker, 1985).

There have been several experimental studies aimed at control of dynamic stall. Many of the dynamic-stall-control investigations have used static-stall control techniques as a starting point, thus it is appropriate to briefly address boundary-layer control for the static case. When low-momentum fluid particles in a boundary layer face an adverse pressure gradient, then eventually the particles near the wall slow down until their velocity relative to the surface is zero. At this point, the flow outside the boundary layer separates from the surface. Schlichting (1960) classifies some of the more common laminar-flow boundary-layer control techniques into four categories: 1) solid-wall motion, 2) boundary-layer acceleration, 3) suction, 4) geometric (such as laminar-flow airfoils).

Since a boundary layer owes its existence to a difference between velocity of the fluid particles and the velocity of the surface, the solid-wall motion technique seeks to diminish

that velocity-difference by moving the wall in the streamwise direction. With the reduction or elimination of the velocity difference comes a suppression or elimination of separation.

Boundary-layer acceleration employs some device (such as a leading-edge slat or a slot on the surface through which high-velocity fluid passes) to increase the momentum of the fluid particles in the boundary layer. These high-momentum fluid particles are better able to battle the adverse pressure gradient than the low-momentum fluid particles which are present without control, and thus separated flow is suppressed.

The suction technique removes the low-momentum fluid particles present in the boundary layer. Higher-momentum particles from the flow outside the boundary layer then take the place of these low-momentum particles being sucked away, and thus suppress separation.

The goal in using a geometric method of boundary layer control is to sufficiently alter the surface such that the adverse pressure gradient is diminished. For example, laminar airfoils move the maximum thickness point aft resulting a less adverse pressure gradient which in turn, promotes attached flow.

Motivated by successful static-stall blowing-control results, dynamic-stall control was accomplished by McCloud et al. (1960) who used blowing to increase helicopter-rotor performance. They experimented with blowing at the leading edge and mid-chord of a helicopter rotor blade. Successful control was demonstrated for leading-edge blowing yet mid-chord blowing was ineffective.

Carr and McAlister (1983) reported on three different ideas of control. First, they reported that a backward-facing step on the top of the airfoil is ineffective in controlling the flow reversal that leads to dynamic stall. Second, they found that while vortex generators installed at $X/c = 0.2$ were effective in delaying static stall, they had no appreciable effect on dynamic stall. They did however find successful delay of dynamic stall (specifically studied for helicopter applications) by using a leading edge slat attached to an airfoil experiencing dynamic stall.

Beneficial effects have been observed for pulsed, perpendicularly-blown air timed to the onset of dynamic stall for an oscillating airfoil (Luttges, et al., 1985). The slot

through which air was pulsed was located at $X/c = 0.2$. The blowing in this case was being used as a nonmechanical replacement of longitudinal vortex generators at the same chord-station. The flow visualization data taken reveals significant control of dynamic stall at lower angles of attack present in helicopter applications. The most beneficial control occurred for blowing during the pitch-up part of the oscillatory cycle. Freymuth et al. (1989) demonstrated that formation of the dynamic stall vortex can be arrested by use of a rotating circular cylinder in the leading edge of the airfoil. Their motivation for using a rotating nose is that this device eliminates or reduces the amount of clockwise vorticity that is generated at the airfoil nose. Without this source of vorticity the dynamic-stall vortex, which consists of clockwise vorticity, will not form thus controlling dynamic stall.

Ahmed (1992) has proposed the use of a rapidly deforming material on the leading edge (to 25% chord) of rotor blades to actively control dynamic stall. The goal here is to modify the pressure distribution in such a way so as to suppress dynamic stall.

Lovato and Troutt (1992) have experimented with pulsed, tangential blowing through three slots of an airfoil undergoing dynamic stall at blowing frequencies which successfully control the free shear layers present in static airfoil separation. The idea here is to generate free-shear-layer vortices which force vortex pairing to occur in a way that reduces the size of the separation region above the airfoil. The limited results presented show a benefit of this approach.

Addington et al. (1992) were able to suppress dynamic stall at low pitch rates ($\Omega_0^+ < 0.05$) using passive suction. Suction at a volume flow rate greater than or equal to the rate of fluid accumulation under the leading-edge shear layer was found to be extremely successful for suppressing dynamic stall vortex formation (Karim and Acharya, 1993). The researchers note that as long as the reverse flow region under the leading-edge shear layer remains thin (e.g., for higher pitch rates and lower Reynolds numbers) then this suction method of control is quite effective.

Numerical studies have been performed on the basic dynamic stall problem using Navier-Stokes solvers. Mehta (1977) produced low- Re_c results in good agreement with experiment for an oscillating airfoil undergoing dynamic stall. Visbal has studied the

dynamic-stall problem for laminar and turbulent flow over an airfoil experiencing constant pitch (Visbal, 1990a and 1990b; Visbal and Shang, 1989; Visbal, 1986b). In these studies he has numerically investigated the effect of various important variables (e.g., M_∞ , Re_c , Ω_0^+ , $(X/c)_{pivot}$) on dynamic stall. Dindar and Kaynak (1992) investigated the effect of turbulence modeling on dynamic stall computations. They compared a non-equilibrium turbulence model (Johnson-King) with two equilibrium turbulence models (Baldwin-Lomax and Cebeci-Smith). The Johnson-King model proved significantly better for simulating both light and deep dynamic stall.

Computational studies investigating control of dynamic stall have also been conducted. Visbal (1991) presented a preliminary investigation for controlling dynamic stall using two techniques: 1) via a moving wall condition (motivated by Freymuth's experimental study (Freymuth, et al., 1989) using a rotating cylinder in the airfoil leading edge) and 2) by use of uniform suction (suction velocity 4% of free-stream velocity) on the airfoil upper surface. Both techniques were effective. Visbal concluded from his brief study that distributed suction performed better than suction which was concentrated at a slot. Ghia et al. (1992) demonstrated a benefit to modulated suction (maximum suction velocity 5% of free stream). It is worth noting that their vorticity-stream function formulation required that they expel the same amount of mass out of the airfoil into the flow field as that removed from the flow field by suction, thereby insuring mass conservation in the flow domain.

Based upon the body of numerical and experimental work reviewed, some detailed statements regarding the onset of dynamic stall can be made. This is accomplished in the next section through the consideration of a representative case.

2.2 A Closer Look at the Dynamic Stall Phenomenon

This section will examine in more detail the fluid mechanics associated with dynamic stall. Based upon a series of numerical simulations (for flow over a NACA 0015 airfoil pitching about the quarter-chord at a constant non-dimensional pitch rate of 0.2 in low-speed ($M_\infty = 0.2$), low Reynolds number ($Re_c = 1.0 \times 10^4$)), Visbal (1991, 1990a) has provided a very detailed description of the events which comprise the dynamic-stall

phenomenon. In this section a similar discussion is presented, based upon the same pitch-rate and Mach-number conditions applied at $Re_c = 2.4 \times 10^4$. Figure 2.1 shows a sequence

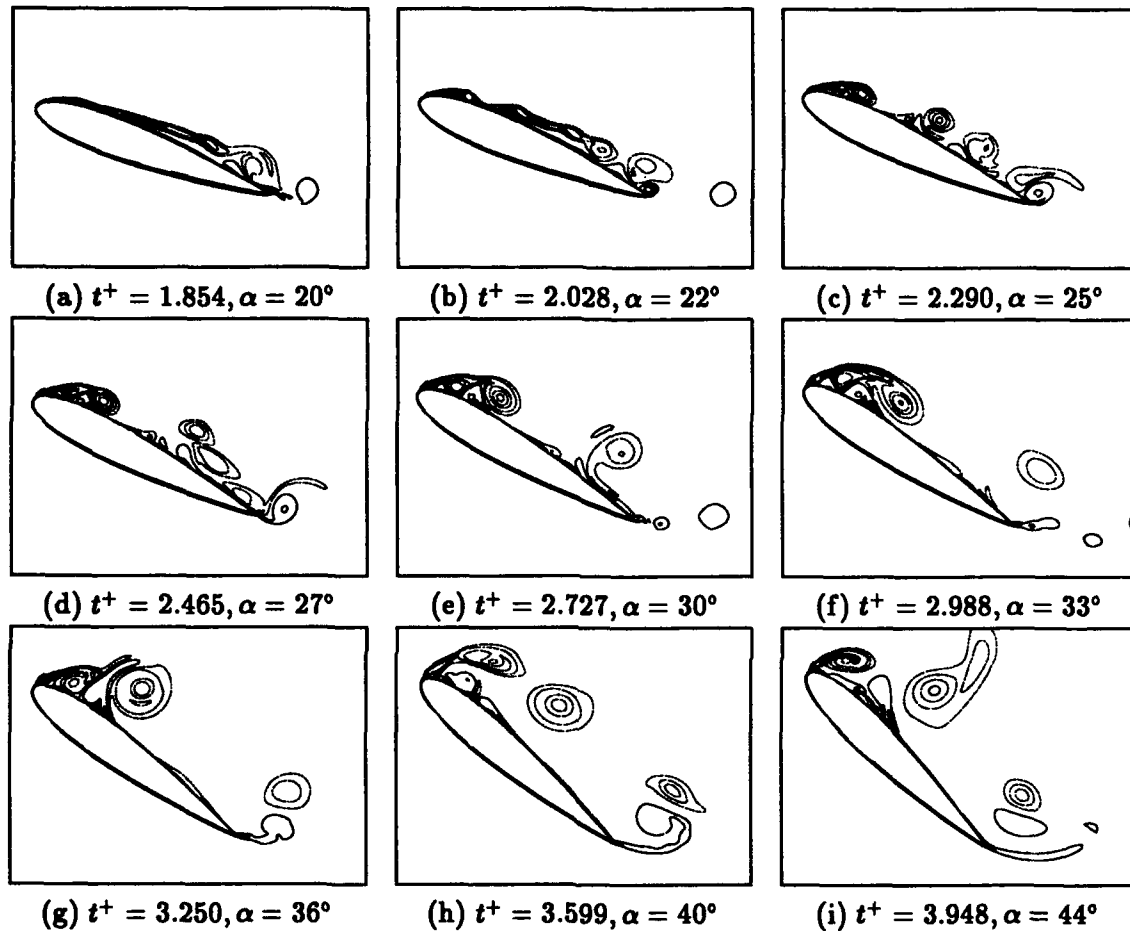


Figure 2.1 Vorticity contours for pitching NACA 0015 airfoil; 361x201 grid, $Re_c = 2.4 \times 10^4$, $M_\infty = 0.2$, $\Omega_0^+ = 0.2$

of instantaneous vorticity contours (not equally spaced) about the pitching airfoil. These results were obtained numerically using a Navier-Stokes code developed by Visbal (1986a). Though details of the dynamic stall process are very sensitive to several flow parameters, this one case serves well for discussion of the typical events that characterize this complex phenomenon.

Flow field vorticity as the airfoil pitches to $\alpha = 20^\circ$ is shown in Figure 2.1(a). Positive vorticity (counterclockwise direction denoted by solid curves in the figure) exists along

the bottom surface of the airfoil. This positive vorticity rolls up at the sharp trailing edge of the airfoil, which is consistent with a vorticity-based description of airfoil lift (e.g., Bertin and Smith, 1979:106–109). Predominantly negative vorticity (clockwise direction denoted by dashed curves) is present above the airfoil upper surface. As α is increased (Figure 2.1 (b) – (i)), both positive and negative vorticity are shed into the wake and advected downstream, though more positive vorticity is shed than negative—a behavior consistent with increasing airfoil lift. In addition, positive vorticity is generated at the surface due to the presence of negative vorticity above the surface. A vortex near a surface inducing vorticity of opposite sign at the surface is typical (Lighthill, 1963:93) and is observed throughout the remaining stages of the pitch up maneuver.

The unstable negative-vorticity shear layer which originates at the airfoil leading edge breaks down into five distinct vortical structures with increasing α (Figure 2.1(b) – (c)). The distinct vortex forming near the leading edge is called the *dynamic stall vortex*. It is fed by the leading-edge shear layer throughout much of the pitch-up maneuver while the other aft vortices are detached from the feeding sheet. Of all the five clockwise vortices forming, the dynamic stall vortex has the greatest amount of vorticity associated with it. It continues to grow, eventually advecting downstream as the airfoil pitches up to high α (Figures 2.1(c) – (i)).

In Figures 2.1(c) and (d) the dynamic-stall vortex and the other four aft-shear-layer vortices are distinct and still detectable. The four aft-shear-layer vortices are drastically changing shape and strength, however. The vorticity in the aft-most shear layer vortex is kept over the top of the airfoil by the presence of the strong trailing-edge counterclockwise vortex. Even so, some of the negative vorticity advects past the strong trailing-edge vortex (Figure 2.1(d)), and is shed into the wake.

The three aft-most clockwise vortices (Figure 2.1(d)) combine into one vortical structure by $\alpha = 30^\circ$ (Figure 2.1(e)). This one structure remains over the aft portion of the airfoil as it pairs up with the strong counterclockwise trailing-edge vortex as shown in Figures 2.1(f) – (i).

By $\alpha = 36^\circ$ (Figure 2.1(g)), the dynamic stall vortex has finally detached from its feeding shear layer. There is a strong eruption of positive vorticity between the dynamic-stall vortex and a secondary leading-edge vortex that is forming. This region of positive vorticity is generated at the surface by the clockwise dynamic-stall vortex as it migrates away from the surface. The secondary leading-edge vortex also breaks away from the leading-edge shear layer and combines with the dynamic stall vortex (Figures 2.1(h) and (i)) while yet a third leading-edge vortex is seen forming from the leading-edge shear layer at $\alpha = 44^\circ$ (Figure 2.1(i)).

As previously stated, the specific details (such as precise location and strength of the dynamic-stall vortex, number of distinct vortical structures the unstable shear layer breaks into) are dependent on several flow parameters (e.g., Re_c , Ω_0^+ , geometry). However, the general events seen for this case shown in Figure 2.1 such as the unstable shear layer, the formation of a dynamic-stall vortex, the severe vortex-vortex and vortex-surface interactions, are the events of which the dynamic-stall phenomenon is comprised.

2.3 A Closer Look at the Onset of Dynamic Stall

To make practical use of the dynamic stall phenomenon described in the previous section, there are basically two approaches to its control: 1) to delay the formation of dynamic-stall vortex or 2) maintain the position of the energetic dynamic-stall vortex over the top of the airfoil after it has formed. The first approach has been demonstrated numerically and experimentally. At the time of this publication, it is still questionable whether or not the second approach can be accomplished. The current investigation takes the first approach, i.e., to delay dynamic stall by delaying the onset of dynamic-stall vortex formation. It follows then that the first step is to isolate the root causes of dynamic-stall vortex formation. The same case as presented in section 2.2 will again be used for this analysis.

Visbal (1991) presented computations which indicate that at low Reynolds number ($Re_c = 1.0 \times 10^4$), the thin reversed-flow region is a major instigator of the shear-layer roll up which progresses to dynamic-stall vortex formation. Other investigators (Karim and Acharya, 1993) have experimentally demonstrated that, under certain conditions, when

the reverse-flow fluid under the strong clockwise shear layer is removed at the accumulation rate via suction near the airfoil leading edge, dynamic stall is delayed significantly.

Around 10% chord at $\alpha = 20^\circ$ (Figure 2.1(a)), the shear layer emanating from the leading edge has lifted noticeably from the upper surface. The flow near the surface at this location is moving upstream toward the airfoil leading edge. A close-up of this region is provided in Figure 2.2. This figure shows velocity vectors (relative to the airfoil surface) overlaid by vorticity contours for the 10% – 25% chord region of the airfoil prior to and after $\alpha = 20^\circ$ along with accompanying C_p plots. In the leading-edge region, negative X/c values represent lower-surface (i.e., pressure side) locations. The vorticity contours in this figure are the same for all plots, however, they are not the same contour levels shown in Figure 2.1.

The pre-separation reverse flow which is possible for unsteady flow (Sears and Telionis, 1975) extends past the 10%-chord region toward the leading edge for $\alpha = 17^\circ$ (Figure 2.2(a)). For the lower angles of attack (up to $\alpha \approx 18^\circ$), this thin layer of reversed flow present along the top surface has little effect on the inviscid flow outside the shear layer, and thus, little effect on the instantaneous surface pressure (Visbal, 1991). However, around $\alpha = 19^\circ$, the reverse-flow region has thickened resulting in the formation of a plateau in the pressure distribution (Figure 2.2(c)) in the 5%- to 15%-chord region. The reverse flow continues to creep toward the airfoil leading edge in the presence of a large adverse pressure gradient. This forward propagation of reversed flow is retarded by the strong feeding shear layer which obtains its strength from the highly favorable pressure gradient at the airfoil leading edge.

At $\alpha = 20^\circ$ (Figure 2.2(d)), dynamic-stall vortex formation is imminent as indicated by the pressure peak at $X \approx 0.18c$. By this time, at the $X \approx 0.16c$ chord station, the shear layer is thicker than at the previous snapshot ($t^+ = 1.767$) and is beginning to bend.

At $\alpha = 21^\circ$ (Figure 2.2(e)), the dynamic-stall vortex has just formed. This is evident in both the C_p plot and the vorticity contours for the 15%- to 20%-chord region. Associated with this infant dynamic stall vortex are two important features — 1) a kink (Visbal, 1990a) in the shear layer at the 16%–18% chord location and 2) a clockwise rotation for a

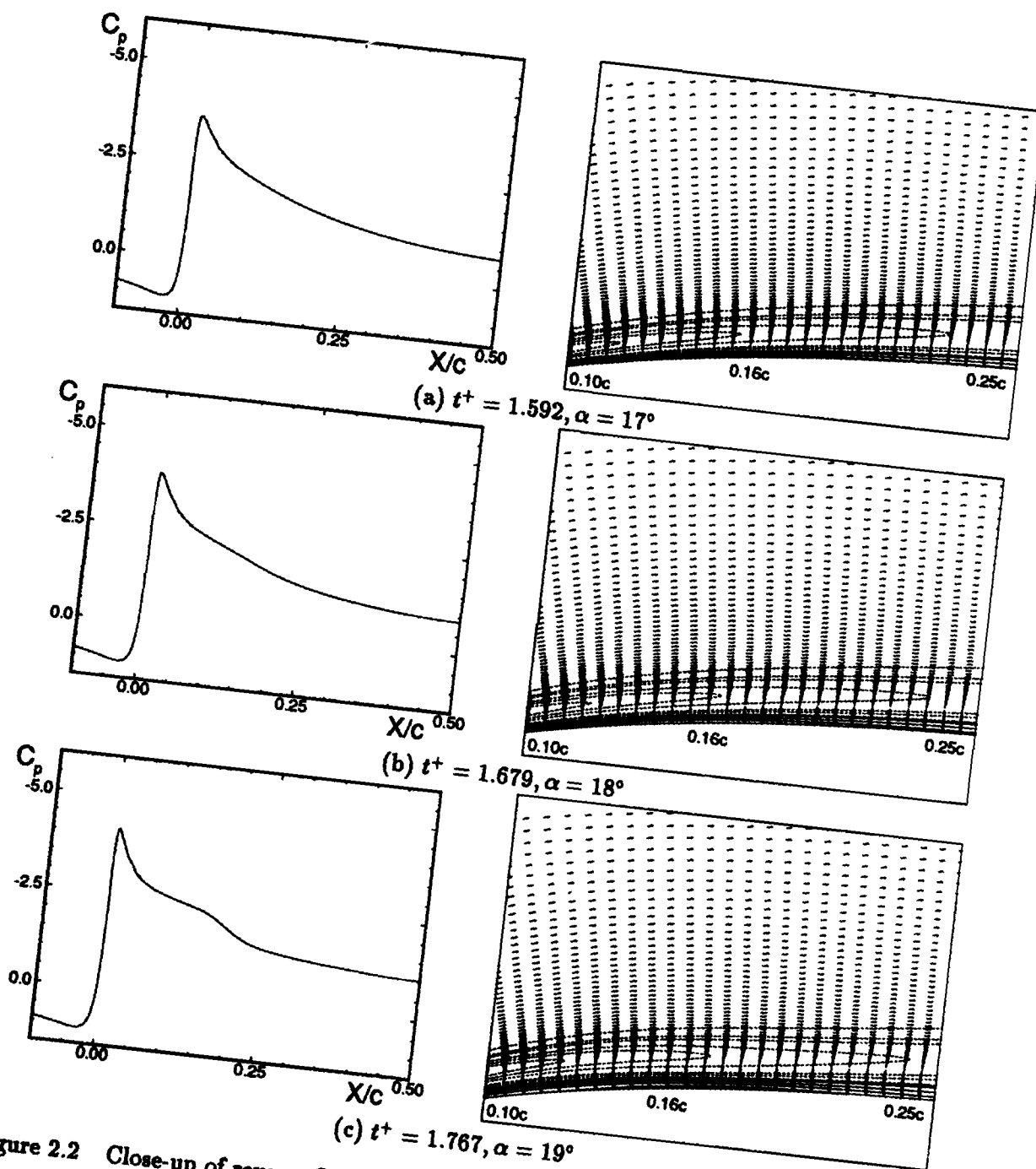


Figure 2.2 Close-up of reverse-flow region for pitching NACA 0015 airfoil; 361x201 grid,
 $Re_c = 2.4 \times 10^4, M_\infty = 0.2, \Omega_0^+ = 0.2$

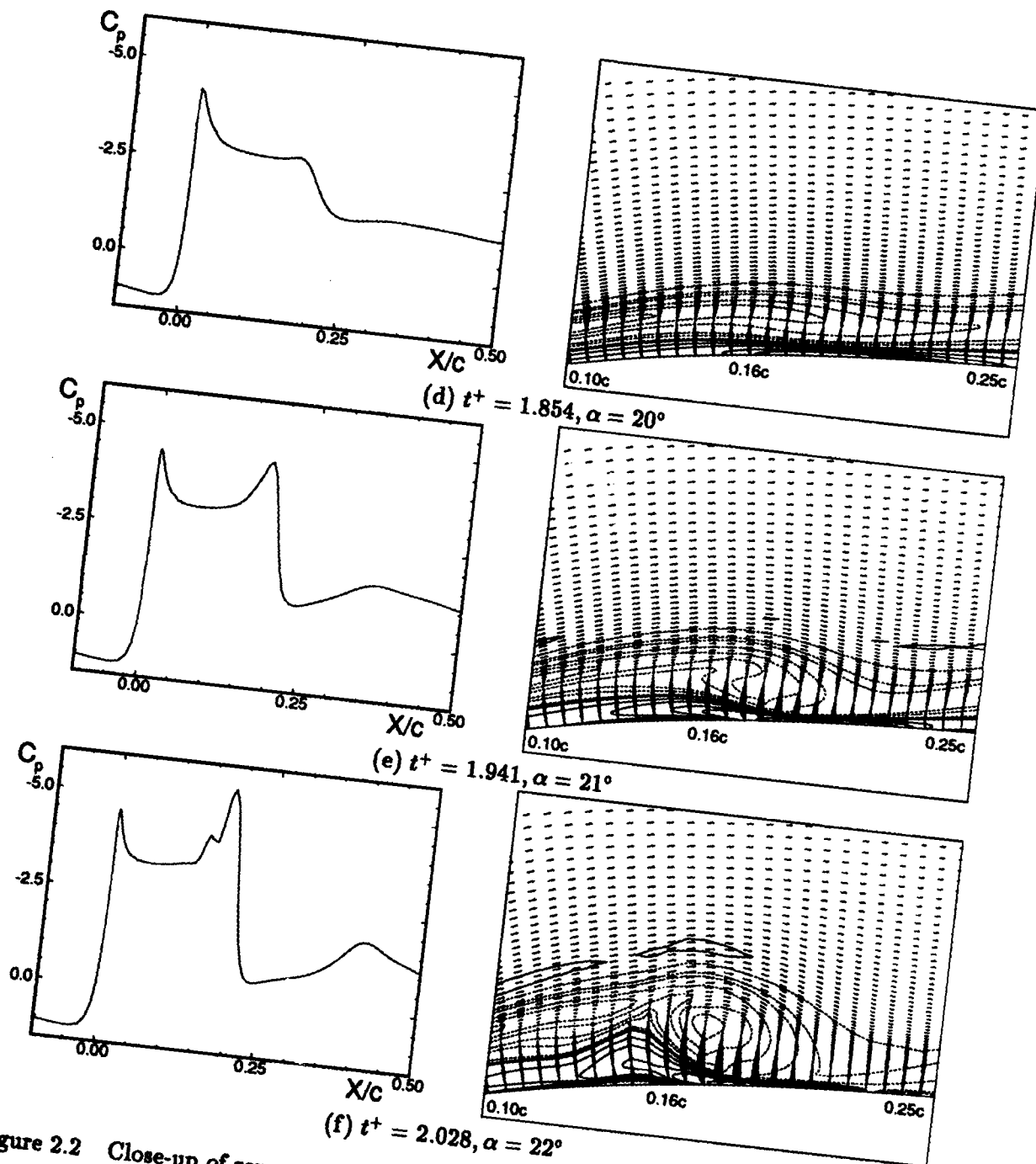


Figure 2.2 Close-up of reverse-flow region for pitching NACA 0015 airfoil; 361x201 grid, $Re_c = 2.4 \times 10^4$, $M_\infty = 0.2$, $\Omega_0^+ = 0.2$ (concluded)

segment of the positive-vorticity shear layer about a center of rotation for the dynamic-stall vortex just aft-chord of this kink. The kink becomes the dividing point between the feeding shear layer and the dynamic-stall vortex. The clockwise rotation of the shear layer in the $X \approx 0.16c$ to $0.21c$ region is an important feature, since its motion produces another kink which develops aft of the first kink as seen in Figure 2.2(f) at $X \approx 0.21c$. This second kink is the dividing point between the dynamic stall vortex and the aft-chord shear layer (which breaks into distinct vortices once cut off from the feeding shear layer (Figure 2.1(c))). Thus, these two important flow features observed at $t^+ = 1.941$ (Figure 2.2(e)) are key to the formation of the dynamic-stall vortex, which is a region of vortical flow that is distinct from both the feeding shear layer and the shear layer aft of the dynamic stall vortex (Figure 2.1(b)). Figure 2.2(f) shows the more fully developed dynamic stall vortex at $\alpha = 22^\circ$.

Figure 2.3 shows the pressure, velocity and vorticity which exists in the $X = 0.10c$ to $0.25c$ region at $\alpha = 19.6^\circ$, 19.8° , and 20.0° — angles prior to the angle of shear-layer kinking which occurs near the leading edge at $\alpha \approx 21^\circ$ (Figure 2.2(e)). For each α in Figure 2.3, the first frame shows pressure-gradient vectors overlaid by pressure contours (not equally spaced — see figure caption for levels). The pressure-gradient-vector arrows point in the direction of increasing pressure and are perpendicular to the pressure contour levels. These pressure-gradient vectors give a sense for relative strengths of the pressure gradient throughout the region of interest. The vectors observed at the bottom of each region are anomalies (i.e., near the surface, pressure gradient-vectors should be parallel with the surface) which appear because of the high-aspect-ratio cells (~ 130) of the mesh at the airfoil surface (the first six cells in this region show this behavior). In regions where the mesh aspect ratio was more reasonable (e.g., ~ 8 in the $0.05c$ region of this grid), this anomalous behavior does not exist. The second frame, for a given α , shows velocity vectors (relative to the airfoil) overlaid with the same pressure-contour levels presented in the first frame. The third frame is a plot of velocity vectors (same scale as in the second frame) overlaid with vorticity contours (as in Figure 2.2, except not identical vorticity-contour levels or velocity-vector scales).

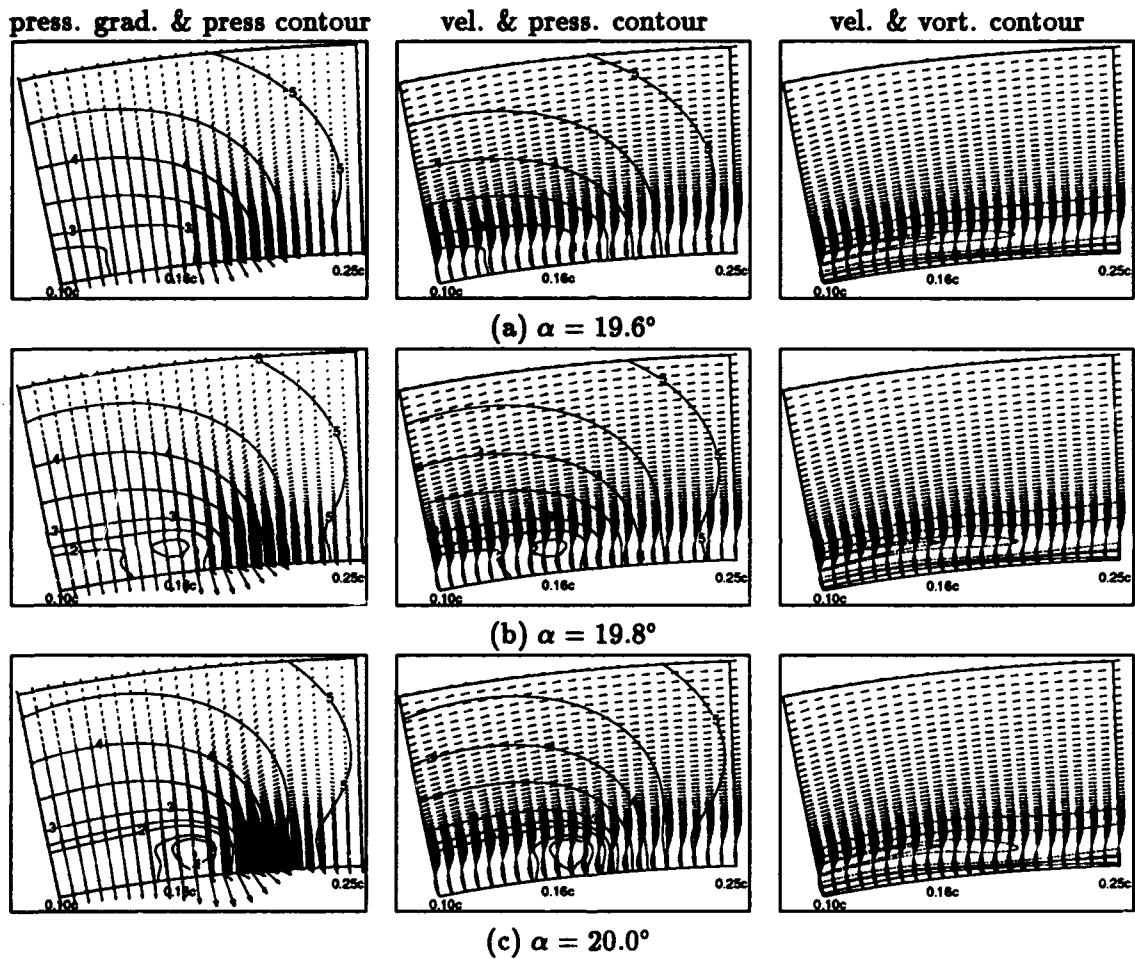


Figure 2.3 Pressure gradient, pressure contours (levels 1-5: 16.46, 16.54, 16.64, 16.88, 17.13), velocities and isovorticity contours for $0.10c \leq X \leq 0.25c$ region; 361x201 grid, $Re_c = 2.4 \times 10^4$, $M_\infty = 0.2$, $\Omega_0^+ = 0.2$

At $\alpha = 19.8^\circ$ (Figure 2.3(b)), a low-pressure pocket appears in the solution at $X \approx 0.16c$, $0.012c$ above the surface. From $\alpha = 19.6^\circ$ to 20.0° , the adverse pressure gradient in the $0.18c < X < 0.23c$ region grows very rapidly (Figure 2.3(a)-(c)). The same strong adverse pressure gradient in this region is depicted in the surface C_p plot at $\alpha = 20^\circ$ (Figure 2.2(d)).

The two sketches shown in Figure 2.4 serve as an aid in explaining why the first shear-

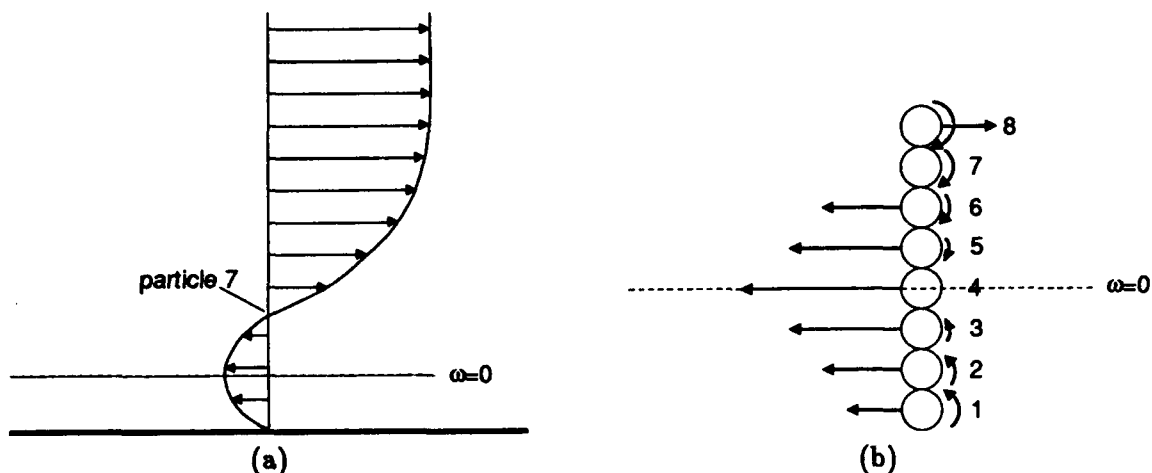


Figure 2.4 Sketch of velocity profile and simplified model of fluid particles at the critical chord-wise station based on case having $Re_c = 2.4 \times 10^4$, $M_\infty = 0.2$, $\Omega_0^+ = 0.2$, $X \approx 0.17c$

layer kink (Figure 2.2(e)) develops. These sketches are meant to conceptually represent the flow at $\alpha = 20^\circ$ (Figure 2.1(d) and Figure 2.3(c)) where the kink first develops ($X \approx 0.17c$). Figure 2.4 (a) is a sketch of the velocity profile, overlaid with the zero-valued vorticity contour ($\omega = 0$). A conceptual model of the individual fluid particles about the $\omega = 0$ contour at this station is depicted in Figure 2.4 (b).

For this two-dimensional case, vorticity near the wall (where $v_x \approx 0$) is given by the following

$$\omega = v_x - u_y \approx -u_y$$

The fluid particles are illustrated (Figure 2.4 (b)) as circular cylinders possessing translational (up-chord or aft-chord) and rotational (clockwise or counterclockwise spin) motion. Particle 4 has the greatest up-chord velocity of the eight particles shown, so $u_y = 0$ at this

point. Hence, this particle resides on the $\omega = 0$ contour. The three particles below particle 4 have up-chord velocities and positive vorticity. Particles 5 through 8 lie above the $\omega = 0$ contour, and thus have negative vorticity. Particles 5 and 6 are depicted with up-chord velocities, particle 7 has zero velocity relative to the airfoil, and particle 8 is shown with an aft-chord velocity.

Figures 2.2(d) and 2.3(c) show that a strong adverse pressure gradient begins at $X \approx 0.17c$ and extends aft-chord to $X \approx 0.25c$. Based upon this simplified model, it is obvious that particles 4 through 8 will tend to rotate together about particle 7 instantaneously. This coordinated rotation of particles 4 – 7 will tend to accelerate particle 4 up-chord. Particles 3 and 5 are spinning in opposite directions and will also tend accelerate non-spinning particle 4 up-chord. To “fill in” for accelerating particle 4, fluid particles aft-chord of this station will be entrained and accelerated up-chord as well, especially along the $\omega = 0$ contour. It must be noted that these translational and rotational motions occur in the presence of a strong adverse pressure gradient which is also forcing these particles up-chord. Observe that this rapid evacuation of near-wall fluid just aft-chord from this station will cause the shear layer to collapse toward the surface (Figure 2.1(e)). This leads to a rapid pooling of fluid just up-chord of this region. Since the flow under consideration is approximately incompressible ($M_\infty = 0.2$), conservation of mass dictates that particle 4 (and any trailing fluid particles along the $\omega = 0$ contour) must move away from the surface. Also, the low-pressure pocket that is centered approximately $0.01c$ above the surface (Figure 2.3(b), (c)) induces the fluid particles to lift away from the surface and thus an abrupt upsurge of fluid and eruption of positive vorticity occurs (Figure 2.1(f)). All of these combined events (rotation of particles 4 through 8 about particle 7, abrupt upsurge of fluid just up-chord of this critical station, and the rapid thinning of the reverse-flow layer under the negative-vorticity shear layer just aft-chord of this critical station) constitute a self-feeding, unstable situation which induces the two main features of dynamic stall vortex formation — 1) the kinking of the strong negative-vorticity shear layer and 2) the clockwise rotation of a segment of the negative-vorticity shear layer about a center of rotation just aft-chord of this kink.

2.4 Statement of the Problem

From the previous discussion, it is apparent that control techniques which eliminate the pooled fluid (Karim and Acharya, 1993) or retard the accumulation of fluid near the critical station (say by retarding the reverse flow as recommended by Visbal (1991)) have promise of being effective at delaying the kinking of the shear layer and thereby delaying dynamic stall. Based upon this description of dynamic stall vortex formation, tangential blowing through a small slot at or near the leading edge, investigated experimentally by Lovato (1992) for dynamic stall and studied by Williams (1961) to control static stall, offers an alternative approach to control of dynamic stall. To date no numerical experimentation using tangential blowing near the leading edge to control dynamic stall has been conducted and thus is the principal focus of investigation in this dissertation. Also, control via suction is examined numerically in order to assess the relative merits of tangential-blowing versus suction control.

III. Formulation of the Numerical Model

In this chapter, both the compressible, laminar-flow governing equations in two dimensions and the associated boundary conditions will be presented. Following that, the numerical scheme used to solve the governing equations will be presented. The dynamic stall phenomenon contains strong viscous and inviscid flow interaction thereby dictating the need to solve the Navier-Stokes equations. It is assumed that the fluid is Newtonian and that Stokes' Law applies.

3.1 Navier-Stokes Equations

The strong conservative form of the two-dimensional, compressible Navier-Stokes equations can be written in general curvilinear coordinates as follows (Visbal, 1986a).

$$\frac{\partial U}{\partial t} + \frac{\partial E}{\partial \xi} + \frac{\partial F}{\partial \eta} = \frac{\partial (V_1 + V_2)}{\partial \xi} + \frac{\partial (W_1 + W_2)}{\partial \eta} \quad (3.1)$$

The flux vectors are given by

$$U = \bar{J} \begin{pmatrix} \rho \\ \rho u \\ \rho v \\ \rho e \end{pmatrix} \quad E = \bar{J} \begin{pmatrix} \rho \tilde{U} \\ \rho u \tilde{U} + \xi_x P \\ \rho v \tilde{U} + \xi_y P \\ (\rho e + P) \tilde{U} - \xi_t P \end{pmatrix} \quad F = \bar{J} \begin{pmatrix} \rho \tilde{V} \\ \rho u \tilde{V} + \eta_x P \\ \rho v \tilde{V} + \eta_y P \\ (\rho e + P) \tilde{V} - \eta_t P \end{pmatrix}$$

$$V_1 = \bar{J} \mu \begin{pmatrix} 0 \\ b_1 u_\xi + b_2 v_\xi \\ b_2 u_\xi + b_3 v_\xi \\ b_1 u u_\xi + b_2 (v u_\xi + u v_\xi) + \\ b_3 v v_\xi + b_4 T_\xi \end{pmatrix} \quad V_2 = \bar{J} \mu \begin{pmatrix} 0 \\ c_1 u_\eta + c_2 v_\eta \\ c_3 u_\eta + c_4 v_\eta \\ c_1 u u_\eta + c_2 u v_\eta + c_3 v u_\eta + \\ c_4 v v_\eta + c_5 T_\eta \end{pmatrix}$$

$$W_1 = \tilde{J}^\mu \begin{pmatrix} 0 \\ c_1 u_\xi + c_3 v_\xi \\ c_2 u_\xi + c_4 v_\xi \\ c_1 u u_\xi + c_2 v u_\xi + c_3 u v_\xi + \\ c_4 v v_\xi + c_5 T_\xi \end{pmatrix} \quad W_2 = \tilde{J}^\mu \begin{pmatrix} 0 \\ d_1 u_\eta + d_2 v_\eta \\ d_2 u_\eta + d_3 v_\eta \\ d_1 u u_\eta + d_2 (v u_\eta + u v_\eta) + \\ d_3 v v_\eta + d_4 T_\eta \end{pmatrix}.$$

\tilde{U} and \tilde{V} are contravariant velocity components given by

$$\tilde{U} = \xi_t + \xi_x u + \xi_y v \quad \tilde{V} = \eta_t + \eta_x u + \eta_y v.$$

The grid and reference-condition-dependent constants b , c , and d are listed in Appendix Section A.1.

The coordinate transformations from the physical Cartesian system to a computational system are defined as

$$\xi = \xi(x, y, t) \quad \eta = \eta(x, y, t) \quad \hat{t} = t.$$

Applying the chain rule gives the following metric relationships.

$$\xi_x = J y_\eta \quad \xi_y = -J x_\eta \quad \xi_t = J(-x_\xi y_\eta + y_\xi x_\eta)$$

$$\eta_x = -J y_\xi \quad \eta_y = J x_\xi \quad \eta_t = J(x_\xi y_\xi - y_\xi x_\xi)$$

$$J = (x_\xi y_\eta - x_\eta y_\xi)^{-1} = \tilde{J}^{-1}$$

3.2 Boundary and Initial Conditions

The boundary conditions used for flow about a pitching airfoil are given in this section. At the surface, no-slip adiabatic conditions are used (Visbal, 1990b).

$$\mathbf{U} = \mathbf{U}_b \quad \frac{\partial T}{\partial n} = 0 \quad \frac{\partial P}{\partial n} = -\rho \mathbf{a}_b \cdot \hat{n} \quad (3.2)$$

\mathbf{U}_b is the airfoil surface velocity and \mathbf{a}_b is the acceleration of the surface given by the following.

$$\mathbf{U}_b = \boldsymbol{\Omega} \times (\mathbf{r}_b - \mathbf{r}_0)$$

$$\mathbf{a}_b = \frac{d\boldsymbol{\Omega}}{dt} \times (\mathbf{r}_b - \mathbf{r}_0) - \boldsymbol{\Omega}^2 (\mathbf{r}_b - \mathbf{r}_0)$$

where \mathbf{r}_0 and \mathbf{r}_b are the position vectors from the inertial reference frame to the center of rotation and to a point on the airfoil, respectively (Figure 3.1). To avoid an infinite

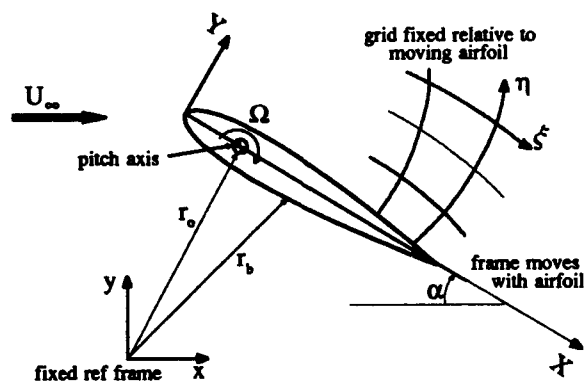


Figure 3.1 Conventions for pitching airfoil (Visbal and Shang, 1989)

acceleration, the airfoil accelerates to its final constant pitch rate (Ω_0) according to the following equation (Visbal and Shang, 1989).

$$\Omega(t) = \Omega_0(1 - e^{-4.6t/t_0}), \quad t \geq 0$$

where t_0 is the time required for the airfoil to reach 99 percent of its final pitch rate Ω_0 .

For the inflow far-field boundary, free stream conditions are imposed.

$$\rho = \rho_\infty \quad u = U_\infty \cos \alpha \quad v = U_\infty \sin \alpha \quad P = P_\infty$$

At the outflow far-field boundary, the pressure is set to the free-stream value and the rest of the flow variables are extrapolated.

$$\frac{\partial}{\partial x} \begin{pmatrix} \rho \\ u \\ v \end{pmatrix} = 0 \quad P = P_\infty$$

For the current simulation, an O-grid structure is proposed. As such, periodic boundary conditions are imposed at the O-grid cut by overlapping five grid points in the ξ -direction.

The flow field for time-periodic flow at zero angle of attack is used as the initial condition.

3.3 Boundary Conditions at the Jet Slot

Implementation of tangential blowing has experimentally been accomplished by using flush slots on a wing through which air is blown from a high-pressure plenum under the surface (Lovato and Troutt, 1992; Lachmann, 1961). Since the slots are flush with the surface, this type of blowing may be more precisely referred to as *nearly* tangential blowing since there must be some nonzero blowing angle (ϕ) specified from the surface tangent at the slot in order for mass flow through a flush slot (of width s_j) to exist (Figure 3.2). (For brevity, whenever “tangential blowing” is used in this document, *nearly* tangential blowing is implied.)

To numerically simulate the effect of a tangential jet, the wall velocity boundary condition for the non-control case (Equation 3.2) is locally altered in the following manner.

$$\mathbf{U} = \mathbf{U}_b + \mathbf{U}_{\text{slot}}$$

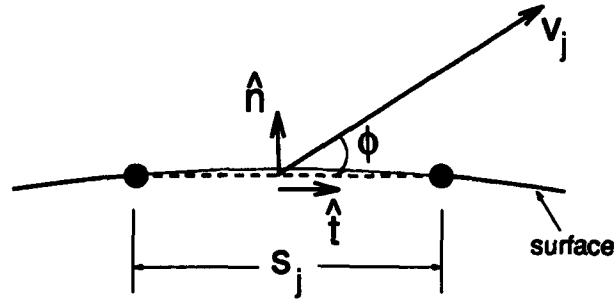


Figure 3.2 Slot-blowing conventions.

where U_{slot} is the velocity relative to the wall (Visbal, 1991) given by the following.

$$U_{slot} = v_j(\cos \phi \hat{t} + \sin \phi \hat{n}) \quad (3.3)$$

The pressure boundary condition (Equation 3.2) was not modified at the slot.

For the suction cases, the tangential-blowing angle is 90° and the magnitude of the jet velocity (v_j) is set to the negative of the suction velocity magnitude (v_s).

Mass flow rate (\dot{m}) and momentum blowing coefficient (C_μ) are dependent upon the blowing angle due to the conventions used in Figure 3.2. Mass flow rate across a surface is given by

$$\dot{m} = \int \rho \mathbf{V} \cdot \mathbf{n} dA \quad (3.4)$$

Thus, assuming a constant v_j profile (Equation 3.3) and a constant jet density, Equation 3.4 becomes the following for mass flow per unit span of the jet at the slot.

$$\dot{m}_j = \rho_j v_j s_j \sin \phi \quad (3.5)$$

A typical definition for momentum blowing coefficient is the following (Lachmann, 1961).

$$C_\mu \equiv \frac{\dot{m} v_j}{q_\infty c} \quad (3.6)$$

Substituting m of Equation 3.5 into Equation 3.6 gives

$$C_\mu = 2 \frac{\rho_j s_j}{\rho_\infty c} \left(\frac{v_j}{U_\infty} \right)^2 \sin \phi. \quad (3.7)$$

For the computations it is assumed that the blowing angle and the blowing- or suction-control velocity remains fixed throughout the pitch-up maneuver. (The one exception to this is for the pulsed-blowing study (Section 4.2.6) in which the blowing velocity is specified to be either $2.83U_\infty$ or zero.) Thus, when experimental results which use a plenum-pressure boundary condition at the slot are compared to the computational results (using slot velocity boundary conditions) presented in this publication, the difference between these slot boundary conditions needs to be accounted for.

3.4 Numerical Scheme

The Beam-Warming scheme (Beam and Warming, 1978) is a popular technique for solving the unsteady Navier-Stokes equations and has been previously used to conduct dynamic-stall research. Since it is an implicit algorithm, the time step constraint is for the sake of accuracy and not for stability (as is the case with explicit methods). In this section, the Beam-Warming scheme is applied to the governing equations for compressible flow.

The Beam-Warming algorithm is an alternating direction implicit (ADI) scheme which employs approximate factorization after flux terms have been linearized in time. This approach, when applied to Equation 3.1, leads to the need for the following flux Jacobians.

$$A = \frac{\partial E}{\partial U} \quad B = \frac{\partial F}{\partial U} \quad R = \frac{\partial V_1}{\partial U_\xi} \quad S = \frac{\partial W_2}{\partial U_\eta}$$

Elements which make up the flux Jacobians are given in Appendix Section A.2.

The Beam-Warming algorithm in factored form for first-order Euler implicit time differencing is given below (Visbal, 1986a).

$$\left[I + \Delta t (\partial_\xi A^n - \partial_{\xi\xi} R^n) \right] D^n = \mathfrak{R}^n \quad (3.8)$$

$$\left[I + \Delta t (\partial_\eta B^n - \partial_{\eta\eta} S^n) \right] \Delta^n U = D^n \quad (3.9)$$

$$\mathfrak{R}^n = \Delta t \left(-\frac{\partial E^n}{\partial \xi} - \frac{\partial F^n}{\partial \eta} + \frac{\partial V^n}{\partial \xi} + \frac{\partial W^n}{\partial \eta} \right) \quad (3.10)$$

$$U^{n+1} = U^n + \Delta^n U \quad (3.11)$$

Second-order accurate central differences are used for spatial derivatives. Therefore, fourth-order explicit and second-order implicit spectral damping are used to damp high frequency numerical oscillations (a numerical phenomenon which occurs when central differences are used in moderate to high- Re_c flow) and enhance stability behavior (Visbal, 1986b). In the ξ -direction, the fourth-order explicit damping term is as follows.

$$-\Delta t \psi \bar{J} \epsilon_4 \delta_{\xi\xi\xi\xi} (JU)$$

where

$$\psi = |\bar{U}| + |\bar{V}| + c \left[(\xi_x^2 + \xi_y^2)^{\frac{1}{2}} + (\eta_x^2 + \eta_y^2)^{\frac{1}{2}} \right]$$

The explicit damping coefficient (ϵ_4) is of order 0.01. The second-order implicit damping term is as follows.

$$-\Delta t \psi \bar{J} \epsilon_2 \delta_{\xi\xi} (JU)$$

The implicit damping coefficient (ϵ_2) is chosen to be $\epsilon_2 \geq 2\epsilon_4$. (For all calculations in this research, $\epsilon_2 = 2\epsilon_4$.) The η -direction damping terms are similar.

This code has been validated for a variety of steady and unsteady problems (Towne and Buter, 1994; Rizzetta and Visbal, 1992; Visbal, 1991; Visbal, 1990a and 1990b; Visbal and Shang, 1989; Visbal, 1986b).

To avoid the expense of regridding at every time level, a grid which is fixed relative to the airfoil was used. As described by Steger (1978), once the initial grid is generated, subsequent physical-coordinate locations and grid speeds can be computed from the prescribed airfoil motion. Nearly orthogonal body-fitted O-grids were generated about the airfoil surface using the hyperbolic grid generator Hypgen (Chan and Steger, 1991). An extensive grid study was conducted on mesh sizes ranging from 203 to 505 points in the

ξ -direction and 101 to 301 points in the η -direction. Each grid was applied to a physical domain which extends nominally 30-chord lengths away from the airfoil. The 385x201 grid used in much of this research has minimum ξ - and η -spacings of $0.000082c$ and $0.00005c$, respectively.

The Visbal code (1986a) requires 7.8 Mwords of memory for the 385x201 grid and takes 1.6 CPU sec/iteration on the CRAY Y-MP8/864 computer. This translates to a data processing rate of 2.1×10^{-5} CPU sec/iteration/grid point. For the nominal time step of $\Delta t^+ = 0.001$ for the 385x201 grid, the time-periodic initial condition (Section 3.2) requires 15,000 - 20,000 iterations ($\sim 7 - 9$ CRAY Y-MP hours) to settle down to a C_l oscillation of $\sim \pm 0.02$. One pitch-up maneuver (at $\Omega_0^+ = 0.2$) to $\alpha = 36^\circ$ takes 3,300 iterations (~ 1.5 CRAY Y-MP hours).

IV. Results and Discussion

Calculations were conducted over the physical domain depicted in Figure 3.1 for a variety of test conditions as shown in Table 4.1. Note that the natural case (i.e., no control) was computed at all listed conditions. Six of the O-grids listed in Table 4.1 that were used

Table 4.1 Summary of Selected Computations

Grid	$Re_c (\times 10^4)$	M_∞	Ω_0^+	Slot X/c	Control ^a
343x201	2.4	0.2	0.2	0.0, 0.2, 0.4	c
351x201	2.4	0.2	0.2	0.0, 0.05	c
	2.4	0.2	0.2	0.05	s
361x201	2.4	0.2	0.2	0.0, 0.05	c
	2.4	0.2	0.2	0.05	s
385x151	2.4	0.2	0.2	N/A	N/A
385x201	1.0	0.05	0.2	N/A	N/A
	1.0	0.1	0.2	0.0	c
	2.4	0.2	0.05	0.0, 0.4	c
	2.4	0.2	0.2	0.0, 0.4	c
	2.4	0.2	0.2	0.0	p
385x301	2.4	0.2	0.2	N/A	N/A
505x201	1.0	0.1	0.2	N/A	N/A
	2.4	0.2	0.2	0.0, 0.4	c

^ac = constant blow, p = pulsed blow, s = suction

for this research are shown in Figure 4.1. As the delay/suppression of dynamic stall onset is of principal interest, the NACA 0015 airfoil studied was usually pitched only to an angle of attack sufficiently past the onset point so as to assess the relative merits of the respective control strategies. For the series of cases considered herein, this angle is typically 36°.

The discussion of results is divided into three major sections: 1) natural (i.e., the baseline against which the control computations are compared), 2) control via tangential blowing, and 3) control via suction. Solution accuracy issues for each major section are addressed in the Appendices B, C, D, E. For the blowing and suction control sections, effects of various free parameters are investigated (e.g., slot location, slot velocity, slot-velocity angle). The different control strategies are compared with one another and to the natural case

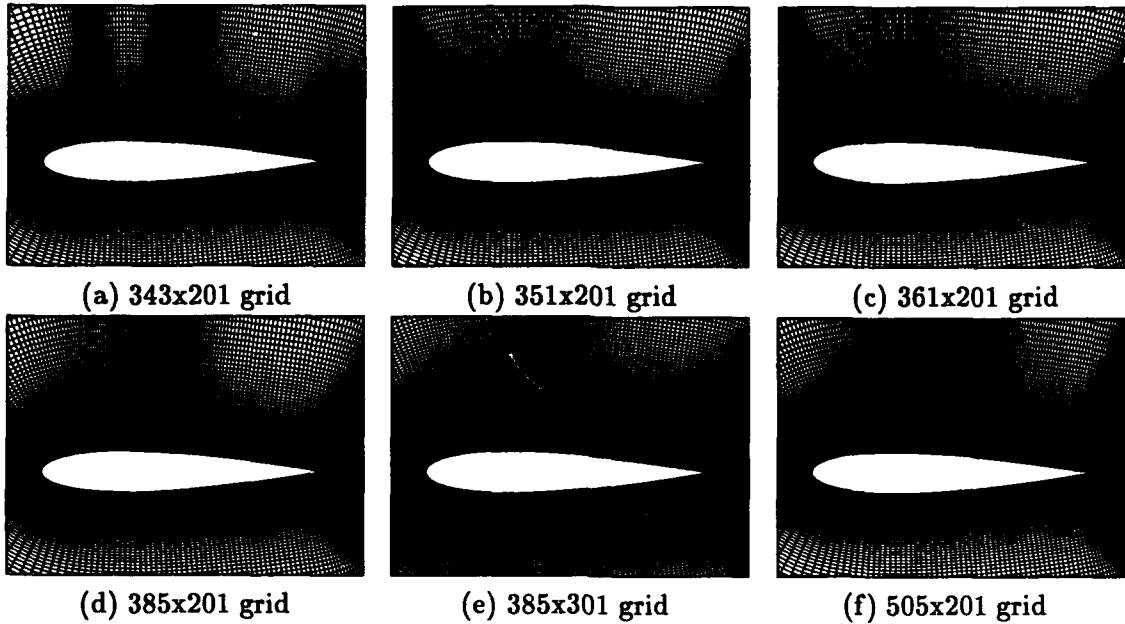


Figure 4.1 Six of the grids used as part of the grid refinement analysis

4.1 Natural Case

This section presents results for the natural case (i.e., no control) which will be used as a reference state (Sections 4.2 and 4.3). In this section, the effects on the solution of the initial acceleration profile and the initial condition prior to pitch up are presented. Compressibility effects present in the computations for low- M_∞ flow are then presented. Finally, the results for the computations are compared with experimental data.

For $M_\infty = 0.2$ cases, solution accuracy considerations with respect to numerical artifacts present in the computations is addressed in Appendix B. The 385x201 and 361x201 grids were found spatially adequate (Appendix B.1) for the natural-case analysis. A time step of $\Delta t^+ = 0.001$ was determined adequate to preserve time-accurate solutions (Appendix B.2) and an explicit dissipation coefficient of $\epsilon_4 = 0.01$ was found satisfactory for all natural cases (Appendix B.3).

For the M_∞ study, $\Delta t^+ = 0.0005$ and 0.00025 were determined necessary for $M_\infty = 0.1$ and 0.05 cases, respectively (Section 4.1.3.1). The 385x201 grid possessed adequate spatial resolution for $\Omega_0^+ = 0.2$ at $Re_c = 1.0 \times 10^4$.

4.1.1 Initial Acceleration Effect. In order to avoid a nearly infinite acceleration to get to the constant pitch rate of Ω_0^+ , the exponential acceleration introduced in Section 3.2 is used. In terms of the computational time t^+ , the equation governing the acceleration to the constant pitch rate is given by

$$\frac{\Omega(t^+)}{\Omega_0^+} = 1 - e^{-4.6 \frac{t^+}{t_0^+}} \quad (4.1)$$

where t_0^+ is the nondimensional time required for the airfoil to reach 99% of its final constant pitch rate (Ω_0^+). Visbal (1986b) presented t_0^+ effects on a 113x51 grid at $M_\infty = 0.2$, $Re_c = 1.0 \times 10^4$, $\Omega_0^+ = 0.6$. He concluded the t_0^+ effect is limited to the early stages of dynamic stall (well before dynamic-stall onset). For the nominal flow conditions of this research ($M_\infty = 0.2$, $Re_c = 2.4 \times 10^4$), a brief study was conducted using t_0^+ values half and double the nominal value of $t_0^+ = 0.5$ for the 385x201 and 361x201 grids. Equation 4.1 is plotted in Figure 4.2(a) for the three values of t_0^+ . In Figure 4.2(b) – (c), the pitch-rate

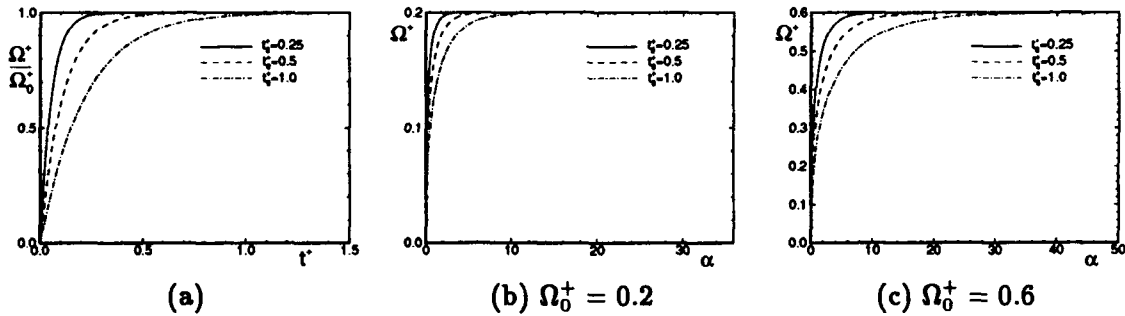


Figure 4.2 Acceleration profile for three t_0^+ values

profiles are also shown (Ω^+ versus α) for two pitch rates using the same three values of t_0^+ . By $\alpha = 10^\circ$ and 27° for $\Omega_0^+ = 0.2$ and 0.6 pitch rates respectively, all acceleration profiles are completed to at least to 99% of the final constant pitch rate.

Researchers (Koochesfahani and Smiljanovski, 1993; Gendrich, et al., 1993) have experimentally and computationally shown that for high enough pitch rates in conjunction with acceleration periods that end well ahead of the leading-edge separation point (i.e, for separation $t^+ > 1.25$ times period of acceleration), the dynamic-stall phenomenon is essentially insensitive to the acceleration profile. The lack of sensitivity is attributed

to the domination of motion-history effects over initial-acceleration effects (Koochesfahani and Smiljanovski, 1993). Gendrich et al. (1993) published results for a NACA 0012 airfoil being pitched at $\Omega_0^+ = 0.2$ about the quarter chord in a $Re_c = 1.6 \times 10^4$, $M_\infty = 0.1$ flow (acceleration period ending at $\alpha = 1.2^\circ, 4.5^\circ, 18.0^\circ$ — leading-edge separation occurring in the range $16^\circ < \alpha < 20^\circ$). Based on integrated-loads, surface-pressure, and surface-pressure-gradient data, they conclude that the initial-acceleration history has little influence on the subsequent dynamic-stall flow field.

Figure 4.3(a) shows the lift coefficient for the three t_0^+ values at the nominal pitch-

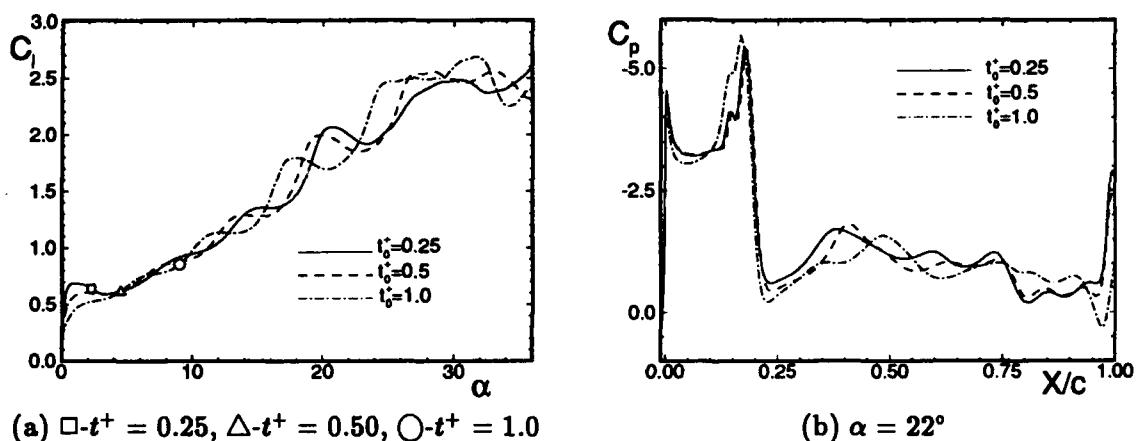


Figure 4.3 Effect of t_0^+ variation on C_l and C_p ; 361x201, $Re_c = 2.4 \times 10^4$, $M_\infty = 0.2$, $\Omega_0^+ = 0.2$

rate and flow conditions computed about the 361x201 grid ($\Delta t^+ = 0.001$, $\epsilon_4 = 0.01$). The symbols in the figure indicate the point on each C_l curve where $\Omega^+ = 0.99\Omega_0^+$. Around $\alpha = 20^\circ$, the difference in these three t_0^+ values appears as an apparent 2° – 3° angle-of-attack shift for C_l . This α -shift leads to a 26% difference in C_l . C_p for the suction-side surface is shown in Figure 4.3(b) at $\alpha = 22^\circ$. Note that the dynamic-stall-vortex suction peak is essentially at the same location and possesses virtually the same strength for the two lower t_0^+ values, however the curves show that there is a small lag in the largest-valued t_0^+ solution. The isovorticity contours at $\alpha = 22^\circ$ and 25° (Figure 4.4) clearly show that there is no α -shift of 2° – 3° in the formation of the dynamic-stall vortex (even though at $\alpha = 25^\circ$, C_l for $t_0^+ = 1.0$ is 22% greater than C_l for the other t_0^+ values), though a minor shift in α can be detected (estimated to be less than a half of a degree). Since the flow

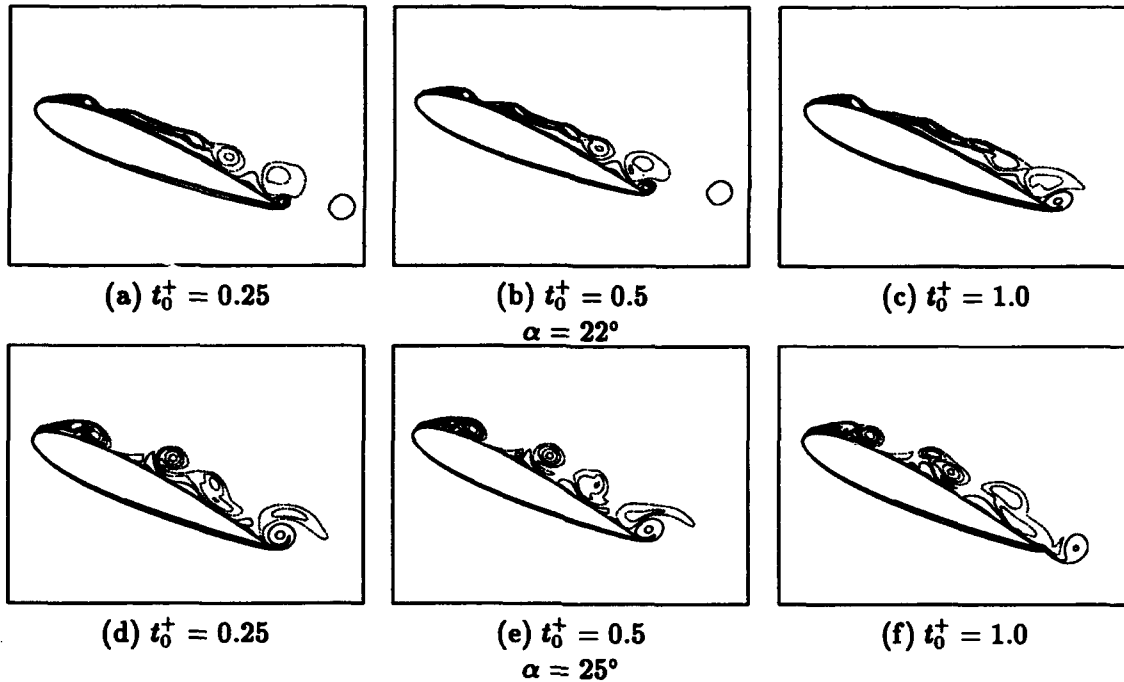


Figure 4.4 Effect of t_0^+ variation on isovorticity contours; 361×201 , $Re_c = 2.4 \times 10^4$, $M_\infty = 0.2$, $\Omega_0^+ = 0.2$

near the forward part of the airfoil does not change much with t_0^+ (Figures 4.3(b) and 4.4), the C_l variation that is observed results mostly from the varied flow that exists aft of the dynamic-stall vortex region. This difference is not of primary importance for this research since emphasis is placed upon control techniques which suppress formation of the dynamic-stall vortex.

As the non-dimensional pitch rate is increased from $\Omega_0^+ = 0.2$ to 0.6 , the t_0^+ effect becomes insignificant (after the acceleration period) as evidenced by C_l and C_p plots (Figure 4.5), as well as the isovorticity contours at angles of attack substantially beyond dynamic-stall vortex formation (Figure 4.6). This behavior is consistent with the observations of Koochesfahani and Smiljanovski (1993) that at high enough pitch rates, initial accelerations effects are dwarfed by motion-history effects.

4.1.2 Initial Condition Effect. For the moderate pitch rate being investigated here ($\Omega_0^+ = 0.2$), an initial-condition effect appears in the integrated loads, much as the

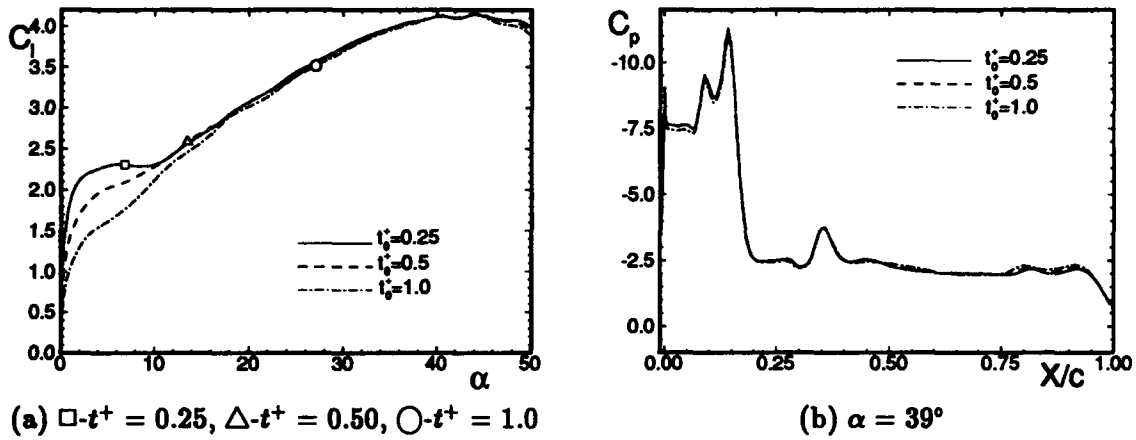


Figure 4.5 Effect of t_0^+ variation on C_l and C_p ; 361x201, $Re_c = 2.4 \times 10^4$, $M_\infty = 0.2$, $\Omega_0^+ = 0.6$

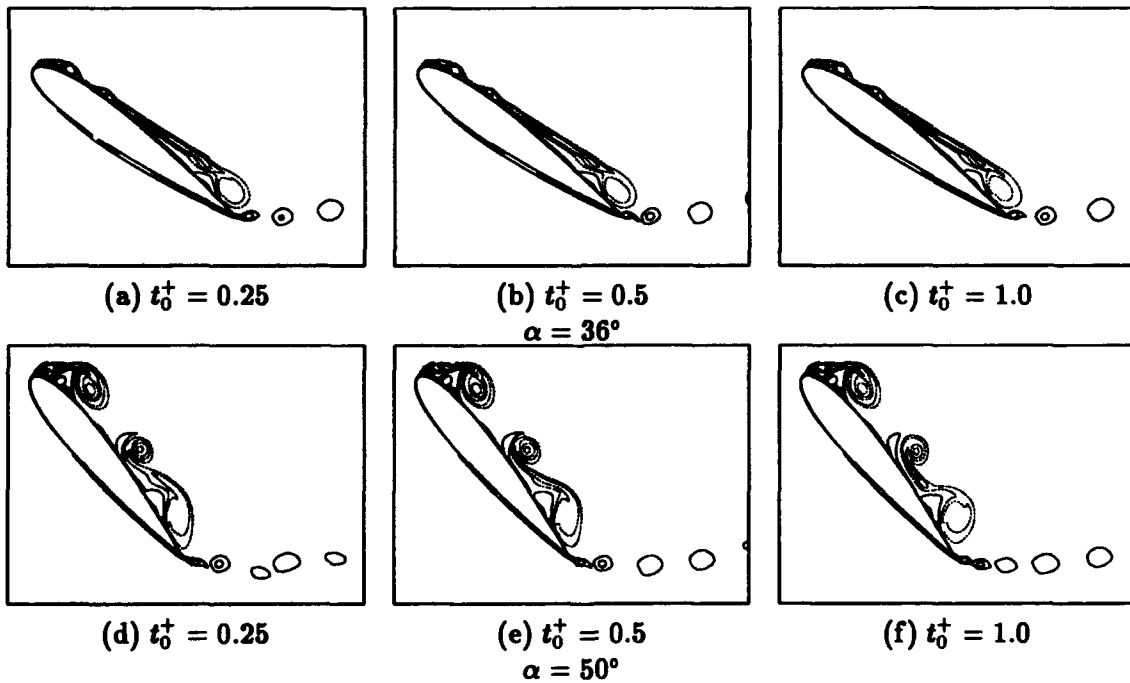


Figure 4.6 Effect of t_0^+ variation on isovorticity contours; 361x201, $Re_c = 2.4 \times 10^4$, $M_\infty = 0.2$, $\Omega_0^+ = 0.6$

initial-acceleration effect makes its appearance (Section 4.1.1). For low- Re_c , low- M_∞ flow, the solution about a NACA 0015 airfoil at $\alpha = 0^\circ$ is periodic as depicted in Figure 4.7(a). Though the sequence of events that characterize dynamic stall are invariant with respect to

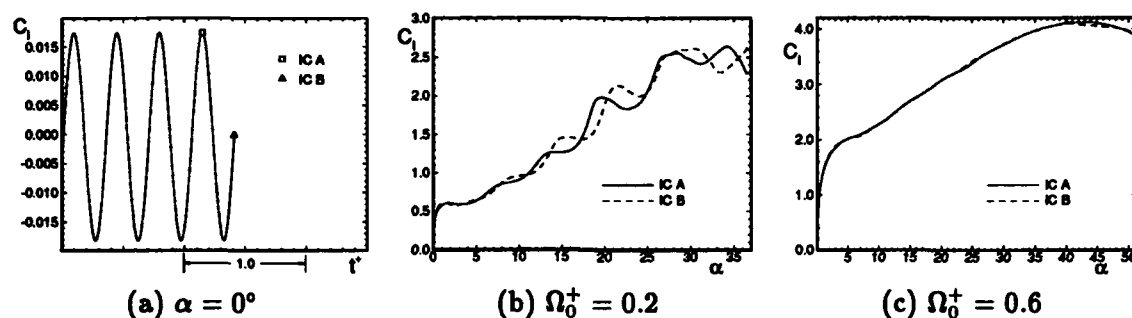


Figure 4.7 Starting solution C_l limit cycle and its effect for two pitch rates; 385x201, $Re_c = 2.4 \times 10^4$, $M_\infty = 0.2$.

the choice of starting position on this cycle (Ghia, et al., 1992), the timing of dynamic-stall development varies according to the initial position of the trailing-edge wake and thus has an impact on the aerodynamic-loading variation with α (Figure 4.7(b)). An effect of the trailing-edge vortex at higher angles of attack was predicted by Shih et al. (1992), however they did not specifically tie a trailing-edge-vortex effect to the initial condition. This initial-condition effect makes sense since the development of the trailing-edge vortex is dependent upon the initial-wake position. Recall that the trailing-edge vortex was previously identified as being critical to the vortex dynamics associated with the development and movement of the vortices born out of the shear layer aft of the dynamic-stall vortex—which is severed from the leading-edge vorticity source upon formation of the dynamic-stall vortex (Section 2.2). This oscillatory initial condition manifests itself in the form of a periodic oscillation superposed on a “smooth” C_l - α curve (Figure 4.7(b)). Surface C_p data and isovorticity contours (Figure 4.8) show that dynamic-stall-vortex formation is, for practical purposes, unaffected by variation in initial condition. Though this effect is less significant at turbulent Reynolds numbers, simulations of this type at laminar Reynolds numbers and moderate to low pitch rates must clearly document the choice of initial condition in order that they be accurately interpreted by other researchers

and so that any timed control strategy be optimally configured. For the purposes of the current research, point A in Figure 4.7(a) was used for all computations.

For the same Re_c , the degree of sensitivity to initial conditions decreases with increasing pitch rate (less than 1% initial condition dependence was observed at $\Omega_0^+ = 0.6$ — Figure 4.7(c)), thus some previous researchers (Ghia, et al., 1992) did not observe dramatic initial-condition dependence. At this high pitch rate, as is the case for the effect of the airfoil initial acceleration (Section 4.1.1), motion-history effects dominate the initial-condition effect.

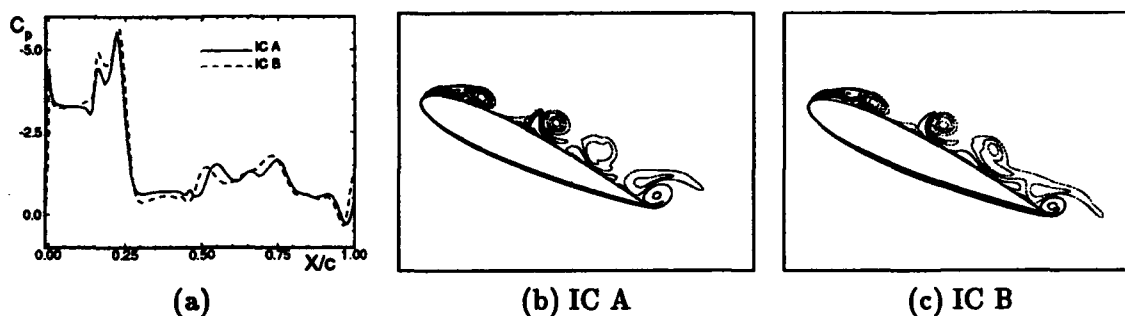


Figure 4.8 Effect of initial condition on C_p and isovorticity contours ($\alpha = 22^\circ$); 385×201 , $Re_c = 2.4 \times 10^4$, $M_\infty = 0.2$, $\Omega_0^+ = 0.2$.

4.1.3 Compressibility Assessment. Oftentimes experimental investigation into the dynamic-stall phenomenon is conducted in very low-speed wind tunnels or in water tunnels, motivated by a desire to obtain flow-visualization data. The experimental data to which comparisons are made in Section 4.1.4 is one such situation where the data were obtained in a low-speed tunnel ($M_\infty < 0.05$), though the computation is conducted at a higher Mach number ($M_\infty = 0.2$). Compressibility effects on dynamic stall have been observed as low as $M_\infty = 0.2$ (Carr and McCroskey, 1992; Fung and Carr, 1991). Thus, there is a question about whether or not it is appropriate to compare $M_\infty = 0.2$ computations with $M_\infty < 0.05$ experimental data. To address this question, two approaches are taken: 1) generate solutions at lower Mach numbers to compare to the $M_\infty = 0.2$ solution, and 2) through analysis of the vorticity-transport equation, compare the relative magnitude of the compressible term that appears in the equation to the other

terms (such as the convective and viscous-diffusion terms). The issue of compressibility will first be addressed by obtaining code results that are “incompressible.”

4.1.3.1 Computations at $M_\infty < 0.2$. One way to address the question of the appropriateness of using a compressible code at $M_\infty = 0.2$ to compare with $M_\infty < 0.05$ wind-tunnel data is to use an incompressible code to generate a dynamic stall solution and then compare the compressible and incompressible code results. This was attempted by using the method of *pseudocompressibility* (also referred to as *artificial compressibility*) (Chorin, 1967); however, this method was abandoned for two reasons. First, pilot calculations determined that the method would take a factor of ten times the computer time that it takes to perform the compressible calculation for the pitch-rate and flow conditions used in this research (Section F.5). Second, the experimental data to be compared against were taken in a *wind* tunnel (a compressible fluid) and not in a *water* tunnel (an incompressible fluid), thus solving the incompressible Navier-Stokes equations introduces the question of whether important compressible physics are being left out of the problem, especially at high- α near the leading-edge region where the local Mach number may be too high to be considered incompressible.

Another way to address the compressibility question is to use the compressible solver at a lower M_∞ thereby retaining all the compressible physics. This approach is hampered by difficulties associated with the application of compressible codes at low M_∞ . As M_∞ is reduced to values near zero (i.e., speed of sound = $a \rightarrow \infty$), explicit schemes are limited in time step by the CFL condition as follows (Anderson, et al., 1984:502).

$$\Delta t^+ \leq \frac{1}{(|u|/\Delta x) + (|v|/\Delta y) + a\sqrt{[1/(\Delta x)^2] + [1/(\Delta y)^2]}}$$

Thus, for explicit schemes the time-step gets prohibitively small for practical calculations as $a \rightarrow \infty$. The Beam-Warming scheme used in this research, being an implicit scheme, is not subject to a formal CFL constraint. However as a practical matter, time steps are usually limited to 5 - 10 times those for explicit schemes due to excessive truncation error (Anderson, et al., 1984:503). Volpe (1993) demonstrated that compressible codes may successfully be used for low- M_∞ flow; however, there is a need to decrease mesh-

cell size to offset the relatively large truncation error terms. Volpe showed that for an impulsively started cylinder, essentially incompressible results may be obtained by running a compressible code at $M_\infty = 0.1$. Based on these encouraging results, this approach of using the same compressible solver at lower M_∞ was employed in the current study to assess the validity of comparing $M_\infty = 0.2$ computations with $M_\infty < 0.05$ experimental data.

To keep the same Re_c and Ω_0^+ necessarily dictates another time-step and grid study at a lower M_∞ (Appendix D). Since, in general, lowering Re_c or raising Ω_0^+ relaxes grid requirements, the approach used was to keep Ω_0^+ the same, but to lower Re_c from 2.4×10^4 to 1.0×10^4 for the lower- M_∞ runs. This avoided the need to generate new, finer grids which likely would have made the low- M_∞ study resource-prohibitive.

Adequate spatial and temporal resolution is demonstrated for the 385x201 grid at $\Delta t^+ = 0.0005$ and 0.00025 for the $M_\infty = 0.1$ and $M_\infty = 0.05$ cases, respectively (Appendix D), at $Re_c = 1.0 \times 10^4$ and $\Omega_0^+ = 0.2$. These cases are compared with the $M_\infty = 0.2$ result for the same Re_c and Ω_0^+ (Figure 4.9(a)). The agreement in C_l is good between these

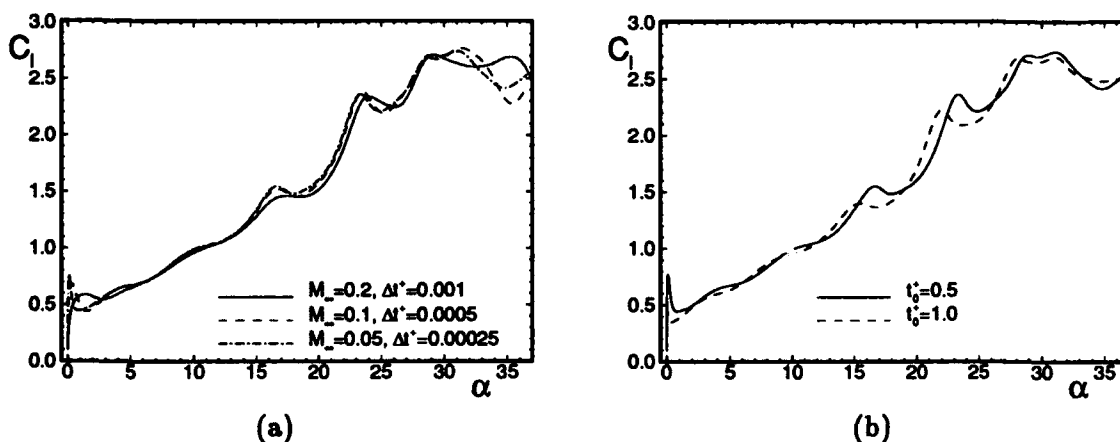


Figure 4.9 Effect of M_∞ on C_l and effect of t_0^+ on C_l (at $M_\infty = 0.05$); 385x201, $Re_c = 1.0 \times 10^4$, $\Omega_0^+ = 0.2$

solutions out to $\alpha = 29^\circ$. The largest discrepancy in C_l in this α range occurs at $\alpha = 16.5^\circ$ where the $M_\infty = 0.2$ solution is 6.4% below the incompressible solution. From that angle on, the $M_\infty = 0.2$ solution tends to lag the incompressible solution by about 0.5° . Note

that as M_∞ decreases, the same initial acceleration of the airfoil ($t_0^+ = 0.5$) generates a more pronounced spike in C_l at the early angles of attack (Figure 4.9(a)). As explained in Section 4.1.1, if this initial acceleration is reduced by increasing t_0^+ from 0.5 to 1.0 (Figure 4.9(b)), the spike is seen to be reduced. As previously demonstrated (Section 4.1.1), this acceleration effect has essentially no effect on the timing of events once beyond the initial acceleration period (Figure 4.10).

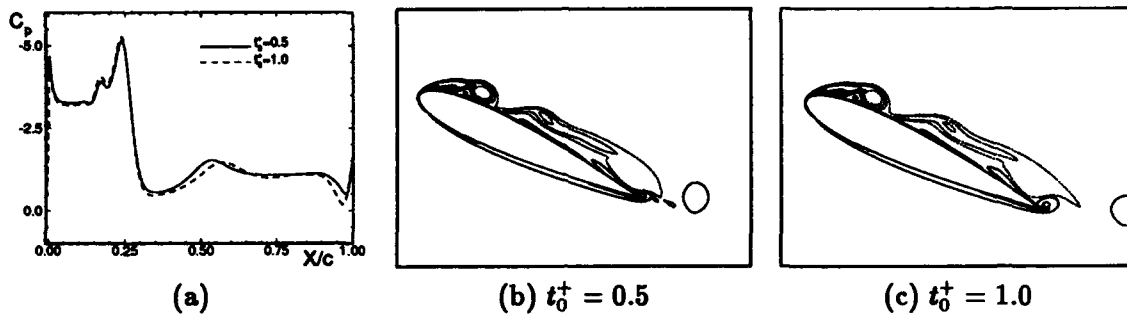


Figure 4.10 Effect of t_0^+ on C_p and isovorticity contours ($\alpha = 25^\circ$); 385x201, $Re_c = 1.0 \times 10^4$, $M_\infty = 0.05$, $\Omega_0^+ = 0.2$

The C_p curves for these three M_∞ solutions are nearly identical to $\alpha = 20^\circ$ (Figure 4.11(a)), at which point only a small discrepancy is evident in the region of the leading edge suction peak. At $\alpha = 22^\circ$, the effect of compressibility in the $M_\infty = 0.2$ solution is

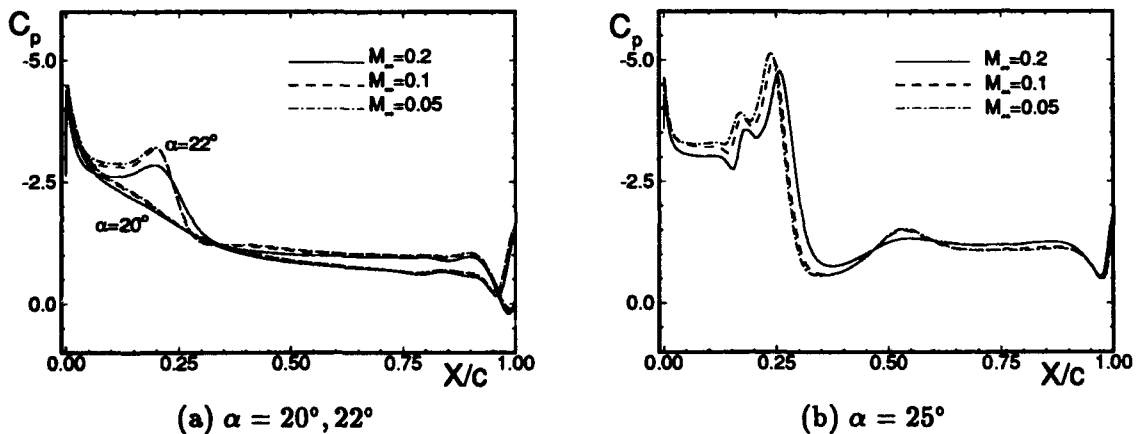
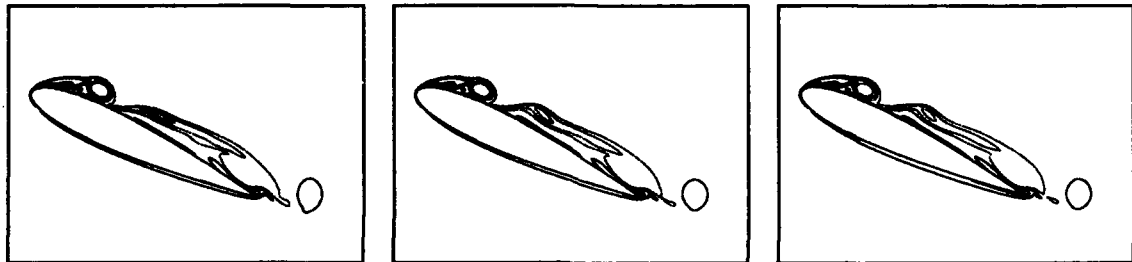


Figure 4.11 Effect of M_∞ on C_p ; 385x201, $Re_c = 1.0 \times 10^4$, $\Omega_0^+ = 0.2$

evident in the form of a reduction in the suction levels near the leading edge and in the

region of the dynamic-stall vortex ($X \approx 0.2c$). The relatively minor difference in solutions continues to be evident at $\alpha = 25^\circ$ (Figure 4.11(b)) as the lower- M_∞ computations again have a greater suction peak associated with the dynamic-stall vortex, although the pressure gradient just aft of the suction peak is the same for all Mach numbers. The location of the dynamic-stall-vortex suction peak is only about 3% more aft in terms of chord length for the $M_\infty = 0.2$ case than the other two lower- M_∞ cases. The isovorticity contours for $\alpha = 25^\circ$ (Figure 4.12) highlight the similarity in the solutions for all three Mach numbers well past the stall-onset region. At this α , the compressibility effect manifests itself as a slight shift in dynamic-stall vortex location ($M_\infty = 0.2$ dynamic-stall-vortex center is slightly more aft-chord than the $M_\infty = 0.05$ vortex center).



(a) $M_\infty = 0.2, \Delta t^+ = 0.001$ (b) $M_\infty = 0.1, \Delta t^+ = 0.0005$ (c) $M_\infty = 0.05, \Delta t^+ = 0.00025$

Figure 4.12 Effect of M_∞ on isovorticity contours ($\alpha = 25^\circ$); 385×201 , $Re_c = 1.0 \times 10^4$, $\Omega_0^+ = 0.2$

Figure 4.13 presents the C_p plots for $\alpha = 27^\circ$ and $\alpha = 30^\circ$. At these angles (well beyond the stall-onset angle of attack) the compressibility effects become more pronounced, however the same basic character in C_p curves is preserved, indicating essentially the same event history over the range of Mach numbers considered. The first appearance of any significant difference between the $M_\infty = 0.1$ and $M_\infty = 0.05$ solutions occurs at $\alpha = 30^\circ$ (Figure 4.13(b)).

Similar results to these $Re_c = 1.0 \times 10^4$ results are expected at $Re_c = 2.4 \times 10^4$ since minor variation in Re_c should have little to do with this compressibility issue. Thus for the conditions considered in this study, the effect of compressibility is not significant.

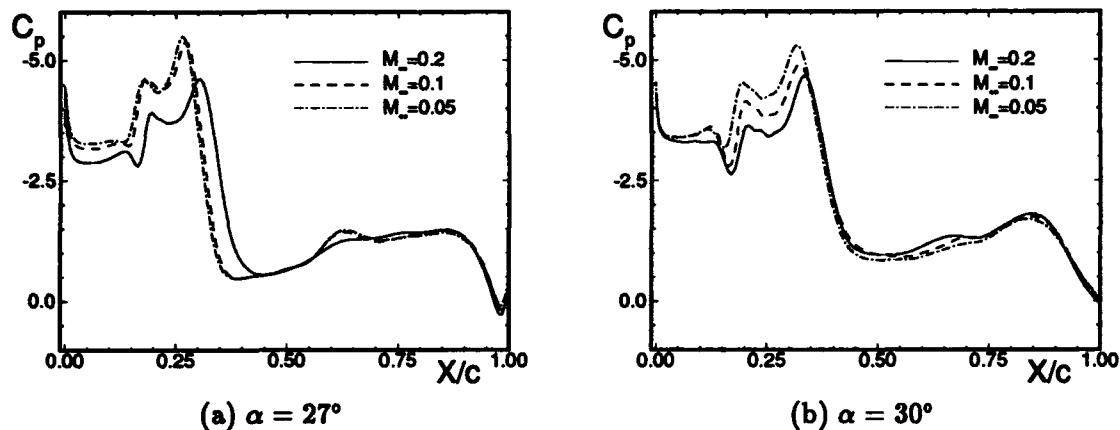


Figure 4.13 Effect of M_∞ on C_p ; 385x201, $Re_c = 1.0 \times 10^4$, $\Omega_0^+ = 0.2$

4.1.3.2 Compressibility assessment via the vorticity-transport equation.

As an alternate means of quantifying the role of compressibility, the vorticity variation was analyzed using the vorticity-transport equation. The vorticity-transport equation is derived by taking the curl of the momentum equation. For two-dimensional compressible flow about an airfoil (assuming constant viscosity and no body forces), the nondimensional vorticity-transport equation is as follows.

$$\omega_t = [-u\omega_x - v\omega_y] + [-\omega(u_x + v_y)] + \left[\frac{1}{\rho^2}(\rho_x P_y + \rho_y P_x) \right] + \left[\frac{1}{Re}(\omega_{xx} + \omega_{yy}) \right] \quad (4.2)$$

The left-hand-side term is the local time rate of change of vorticity (i.e., the z component of vorticity, since flow only in the x - y plane is considered) at a given location in the flow field. On the right-hand side, the first term represents the vorticity transported by convection. The second term is an expansion term. Note that if the flow is truly incompressible at a given point, this term is zero since $u_x + v_y = 0$ for incompressible flow. The third term is the baroclinic-torque term which represents the vorticity produced when the pressure and density gradients are not oriented in the same direction (since in 2-D, $\nabla \rho \times \nabla P = \rho_x P_y + \rho_y P_x$). The last term on the right-hand side represents the diffusion of vorticity.

To determine the relative importance of compressibility effects at $M_\infty = 0.2$, the expansion term is compared to the other terms in this equation. For convenience contour plots for each of the terms are presented in Figure 4.14(a) using contour levels that match

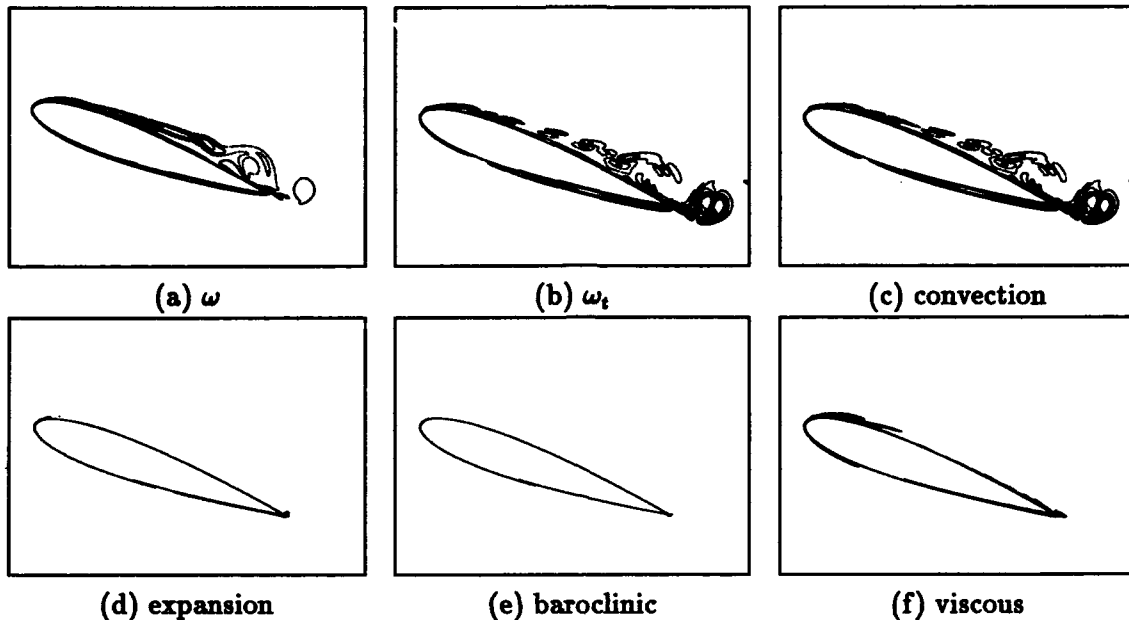


Figure 4.14 Isovorticity contours and contours of vorticity-transport equation terms; 361×201 , $\alpha = 20^\circ$, $Re_c = 2.4 \times 10^4$, $M_\infty = 0.2$, $\Omega_0^+ = 0.2$

previously used levels (e.g., Figure 4.4). The rest of the contour plots in Figure 4.14(b)–(f) use ten equally distributed contour levels between ± 1000 to provide a relative comparison of the terms of the vorticity-transport equation. Dynamic-stall onset occurs around $\alpha = 20^\circ$ as evidenced by the lifting shear layer near the leading edge (Figure 4.14(a)). Clearly, the process is dominated by convection (Figure 4.14(c)). The effect of viscous diffusion is also significant near the leading-edge surface (Figure 4.14(f)). A very slight amount of vorticity production occurs near the leading edge due to the expansion term (Figure 4.14(d)), and the baroclinic torque term (Figure 4.14(e)) produces almost no vorticity. Once the dynamic-stall vortex has formed (Figure 4.15(a)), the expansion term (Figure 4.15(d)) increases in magnitude, however as at the lower angle of attack, the effects of convection (Figure 4.15(c)) and diffusion (Figure 4.15(f)) are much more pronounced. Also as before, the baroclinic-torque term (Figure 4.15(e)) is insignificant.

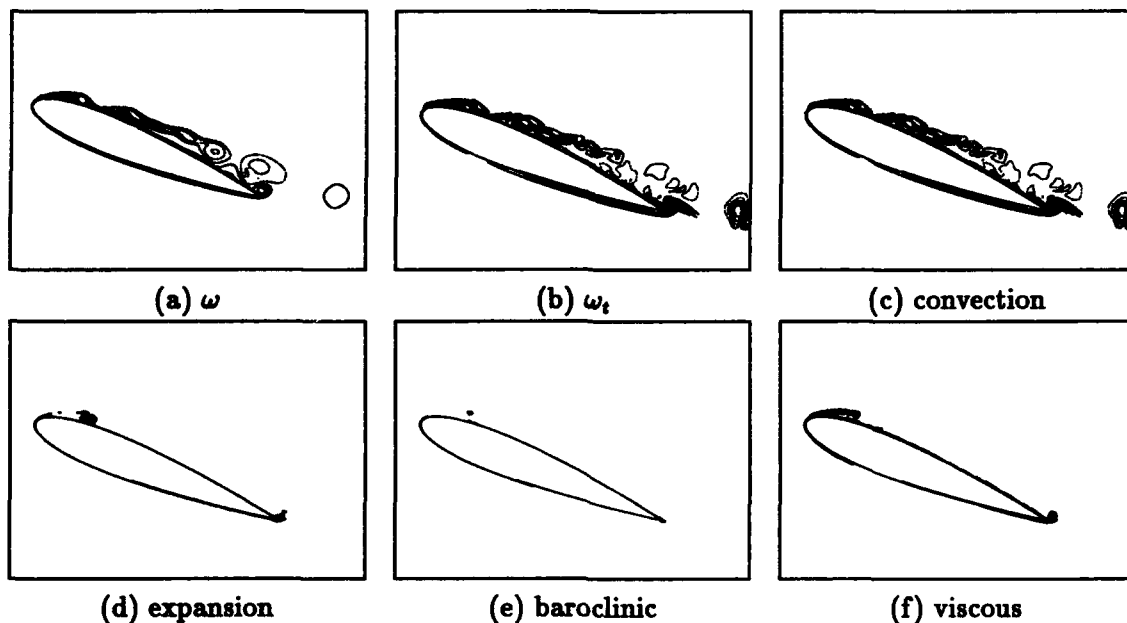


Figure 4.15 Isovorticity contours and contours of vorticity-transport equation terms; 361×201 , $\alpha = 22^\circ$, $Re_c = 2.4 \times 10^4$, $M_\infty = 0.2$, $\Omega_0^+ = 0.2$

Figure 4.16 presents profiles of $\nabla \cdot \mathbf{V}$ and the vorticity-transport-equation terms at $X = 0.10c$. All the vorticity-transport-equation terms are plotted using the same scales for five α 's.

Figure 4.16(a) indicates that $\nabla \cdot \mathbf{V}$ increases as α is increased and is small for the conditions shown. This is in agreement with previous conclusions.

A comparison of the various vorticity-transport-equation term profiles at this 10%-chord station (Figure 4.16(b)–(f)) supports the previous-made claim that dynamic-stall-vortex formation and development is convection dominated.

Summarizing, for the natural case at these conditions ($M_\infty = 0.2$, $Re_c = 2.4 \times 10^4$, $\Omega_0^+ = 0.2$), the compressibility effects are negligible when compared to the vorticity transported by convection (by far the greatest) and by diffusion. This finding is consistent with the result presented in Section 4.1.3.1 where M_∞ is lowered from 0.2 to 0.05.

4.1.4 Comparison with Experiment. As a means of assessing the accuracy of the natural solution, velocity-magnitude profiles along the surface were compared with $M_\infty <$

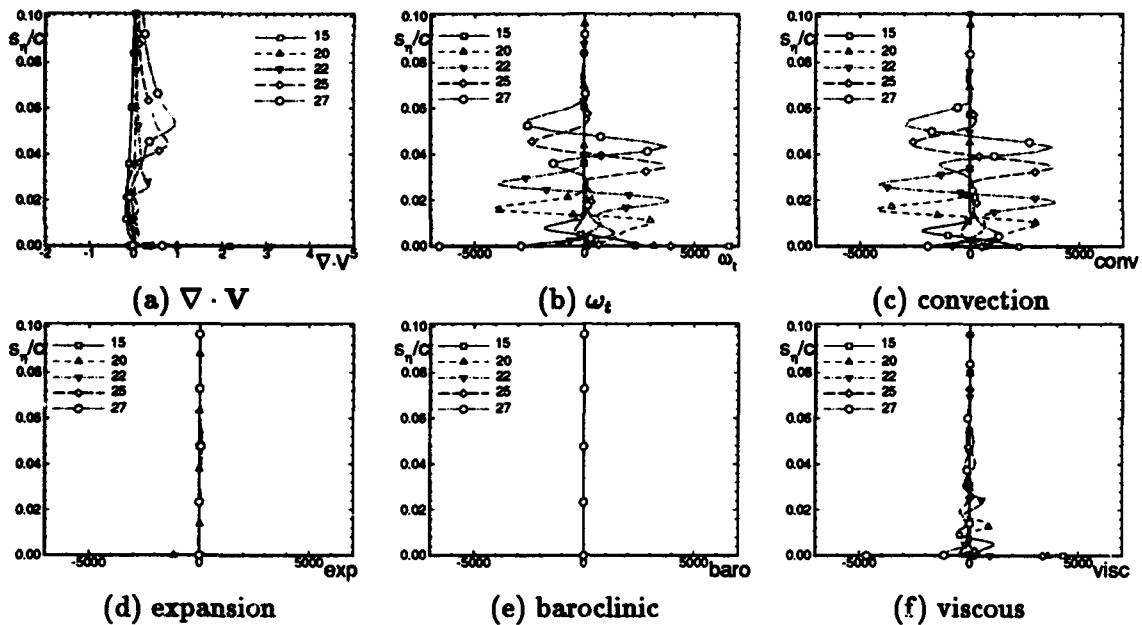


Figure 4.16 Profiles of $\nabla \cdot \mathbf{V}$ and vorticity-transport equation terms for natural case at $X = 0.1c$; 361×201 , $\alpha = 15^\circ, 20^\circ, 22^\circ, 25^\circ, 27^\circ$, $Re_c = 2.4 \times 10^4$, $M_\infty = 0.2$, $\Omega_0^+ = 0.2$

0.05 results obtained experimentally (Lovato and Troutt, 1992) at a pitch rate of $\Omega_0^+ = 0.05$ (Figure 4.17(a)). While the qualitative agreement is reasonable, some undershoot in velocity is present. One source of difference is that the grid used to generate the numerical results (385×201) was validated for $\Omega_0^+ = 0.2$ out to $\alpha = 33^\circ$ (in terms of C_p , after $\alpha = 25^\circ$ significant differences between the 385×201 and 505×201 grids become apparent), not $\Omega_0^+ = 0.05$ out to $\alpha = 20^\circ$. For this low pitch rate at $\alpha = 14^\circ$ (Figure 4.17(b)), the shear layer in the region $0.12c \leq X \leq 0.35c$ is already relatively far from the upper surface into an area of the mesh which may be too sparse for accurate resolution of the high-gradient flow. Therefore, after $\alpha = 14^\circ$ (Figure 4.17(c)), it is unlikely that the numerical solution will be very precise for this grid, pitch rate and flow condition.

4.2 Control via Tangential Blowing

As discussed in Section 2.3, the key to delaying dynamic stall onset is to inhibit fluid from pooling under the shear layer. The tangential-blowing approach introduces high-momentum fluid near the surface to delay the reverse-flowing-fluid pooling. This section

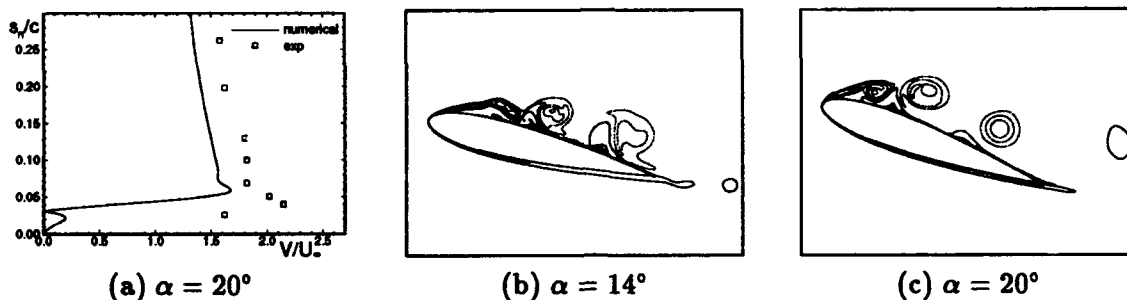


Figure 4.17 Comparison of computed velocity profile ($M_\infty = 0.2$) with experiment ($M_\infty < 0.05$) at $X = 0.1c$ (Lovato, 1992) and isovorticity contours for the computed solution (385x201); $Re_c = 2.4 \times 10^4$, $\Omega_0^+ = 0.05$ (Note: s_n is the coordinate direction normal to the wall).

presents several results for the tangential-blowing-control technique. Slot-location and slot-width effects are presented first followed by the effect of jet-velocity-magnitude variation. Next, results are shown for various blowing initiation angles of attack (α_b). Solution sensitivity to blowing angle (ϕ) and jet velocity profile is then demonstrated. Following that is a comparison between pulsed and constant blowing. Finally, compressibility effects for the constant-blowing case is presented.

Solution accuracy considerations with respect to numerical artifacts present in the tangential-blowing computations is addressed in Appendix C. The baseline grids (351x201, 361x201, 385x201) possess adequate global- and slot-grid resolution for tangential blowing study (Appendix C.1). A time step of $\Delta t^+ = 0.001$ is adequate for the tangential-blowing cases considered (Appendix C.2) as it is for the natural cases (Appendix B.2). When $v_j < 4U_\infty$, $\epsilon_4 = 0.01$ is satisfactory to maintain solution stability; however, for higher jet velocities, ϵ_4 requires doubling to maintain stability (Appendix C.3).

4.2.1 Slot-Location and Width Effects. One of the key issues which arises when attempting to control the flow over an airfoil with blowing is slot placement. Experimental (Karim and Acharya, 1993; Freymuth, et al., 1989; Carr and McCalister, 1983) and computational (Ghia, et al., 1992; Visbal, 1991) studies have demonstrated the utility of control devices (suction, moving wall, leading-edge slat) placed in the leading-edge area where the dynamic-stall vortex forms. Experimental studies (Lovato and Troutt,

1992) have also shown some benefit to pulsed blowing simultaneously through multiple slots located at $0.0c$, $0.2c$, and $0.4c$. Based on the previous dynamic-stall control work, slot locations at $0.0c$, $0.05c$, $0.2c$, and $0.4c$ are investigated. Once slot location is established, then a brief study is made of slot width effects. Unless otherwise stated, the following nominal conditions were used for the slot study: $M_\infty = 0.2$, $Re_c = 2.4 \times 10^4$, $\Omega_0^+ = 0.2$, $v_j = 2.83U_\infty$. A uniform jet velocity profile is used at a blowing angle (ϕ) that is 10° from the surface tangent (Figure 3.2). The time step used in the computations is $\Delta t^+ = 0.001$ and the damping coefficient used is $\epsilon_4 = 0.01$ (except for high- v_j cases where ϵ_4 is noted to be 0.02).

The 343×201 grid (Figure 4.1(a)) was first used to investigate blowing at $0.0c$, $0.2c$, and $0.4c$ slots. Along with the slot locations, the selected initial blowing velocity ($v_j = 2.83U_\infty$) and slot width ($0.0105c$) were based upon experimental work (Lovato, 1992; Lovato and Troutt, 1992). Figure 4.18 shows C_l for the natural case compared with

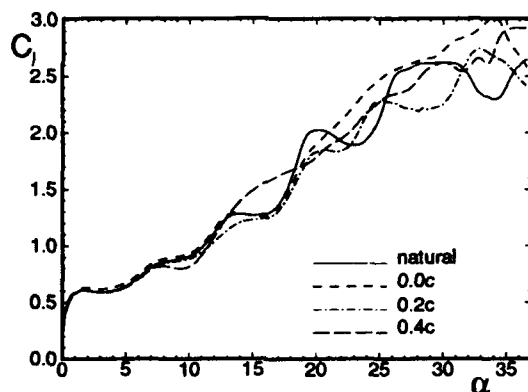


Figure 4.18 Effect of tangential blowing at $X = 0.0c$, $X = 0.2c$, $X = 0.4c$ slots on C_l ; 343×201 , $v_j = 2.83U_\infty$, $\phi = 10^\circ$, $Re_c = 2.4 \times 10^4$, $M_\infty = 0.2$, $\Omega_0^+ = 0.2$

tangential blowing at each of the three slots of the 343×201 grid. The relatively poor C_l results for the $0.2c$ slot, as compared to the other two slots, led to the dismissal of the $0.2c$ slot location from further consideration.

Based on the 343×201 -grid C_l results, a 385×201 grid (Figure 4.1(d)) was next constructed. This grid provided for slots at only $X = 0.0c$ and $0.4c$ and the possessed a more refined mesh in the area of dynamic-stall vortex formation. The isovorticity contours at

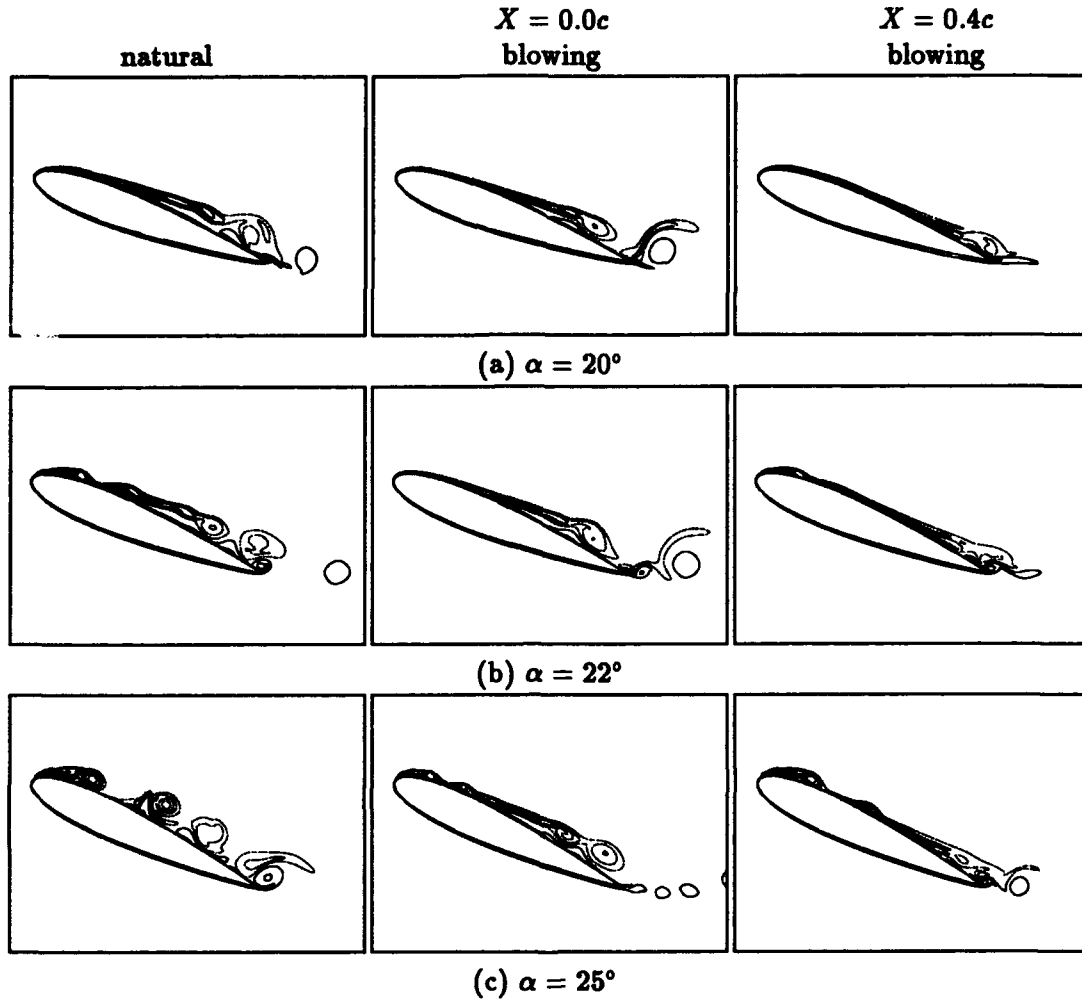


Figure 4.19 Effect of tangential blowing at $X = 0.0c$ and $0.4c$ slots on vorticity contours; 385×201 , $v_j = 2.83U_\infty$, $\phi = 10^\circ$, $Re_c = 2.4 \times 10^4$, $M_\infty = 0.2$, $\Omega_0^+ = 0.2$

$\alpha = 20^\circ$, 22° and 25° (Figure 4.19) demonstrate that for dynamic-stall suppression, blowing at $X = 0.0c$ is superior to blowing at $0.4c$. Blowing at $0.4c$ has little effect on the pooling that occurs due to the large adverse pressure gradient near the leading edge (Section 2.3).

An observed benefit of $0.4c$ blowing over $0.0c$ blowing is that much of the oscillation in C_l due to trailing-edge vortex-shedding (Section 4.1.2) is suppressed (Figure 4.18). This is easily seen in Figure 4.19(a) where blowing at $0.4c$ introduces relatively strong negative-vorticity (dashed contours) along the upper surface which counteracts the strong positive trailing-edge vortex.

The shear layers resulting from the two vorticity sources (i.e., the leading-edge stream-wise pressure gradient (Acharya and Metwally,1992) and the transpiration velocity from the 0.4c slot) can be observed in Figure 4.19(a) for the 0.4c-blowing case. The shear layer emanating from the leading-edge region terminates at $X \approx 0.85c$, slightly above the 0.4c-originating shear layer which persists past the airfoil trailing edge. This negative-vorticity shear layer resulting from blowing at the 0.4c slot reduces the trailing-edge vortex effect on airfoil integrated loads.

Using the 385x201 grid, the numerical solution for simultaneous blowing at the 0.0c and 0.4c slots was computed. Blowing simultaneously at the 0.0c and 0.4c slots reduces oscillations in the C_l - α curve (Figure 4.20) just as 0.4c-alone blowing does primarily due to

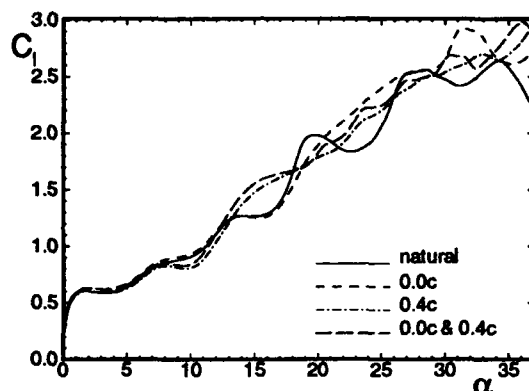


Figure 4.20 Effect of tangential blowing at $X = 0.0c$, $X = 0.4c$ slots (individually and simultaneously) on C_l ; 385x201, $v_j = 2.83U_\infty$, $\phi = 10^\circ$, $Re_c = 2.4 \times 10^4$, $M_\infty = 0.2$, $\Omega_0^+ = 0.2$

removal of the trailing-edge vortex effect (Figure 4.18). Simultaneous blowing also delays dynamic-stall vortex formation (Figure 4.21), just as 0.0c-alone blowing does. The reduction in trailing-edge vortex shedding effect by 0.4c-blowing is even more pronounced at lower pitch rates, as shown in Figure 4.22, since the trailing-edge vortex shedding produces a greater initial-condition effect for the natural case at lower pitch rates (Section 4.1.2). However, no significant additional benefit is obtained by the 0.4c blowing from the perspective of dynamic-stall-vortex-formation delay (Figure 4.21(b)). Thus, from a practical standpoint, simultaneous blowing at $X = 0.0c$ and 0.4c may not be warranted (especially in applications at higher Re_c where the trailing-edge vortex shedding is not a factor).

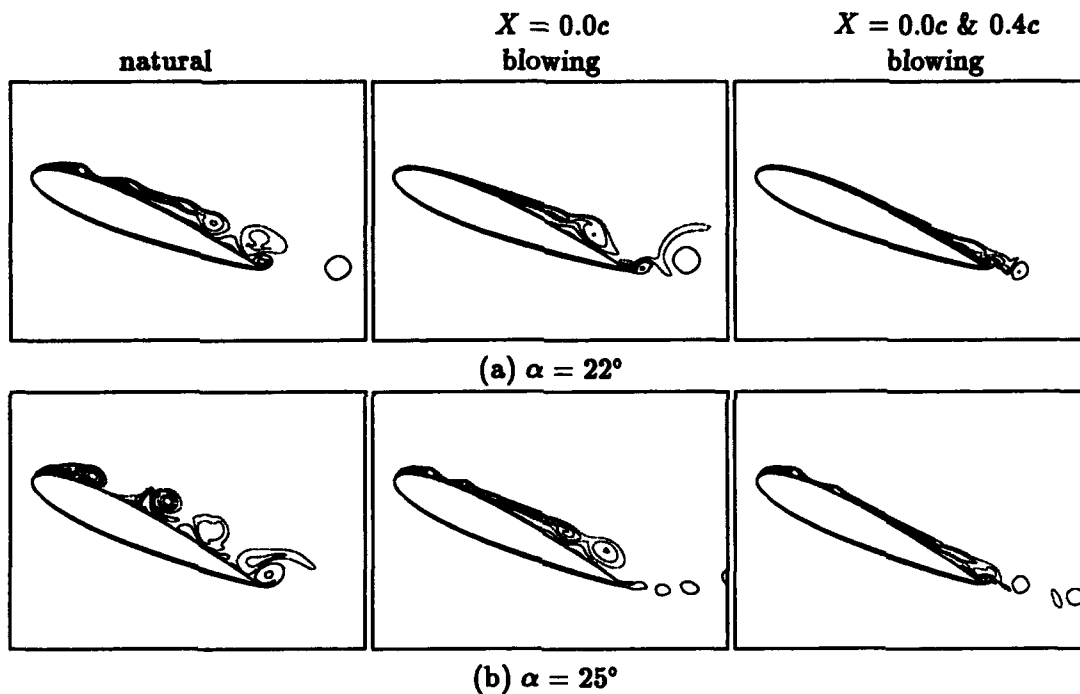


Figure 4.21 Effect of $X = 0.0c$ and $0.4c$ simultaneous tangential blowing on vorticity contours; 385×201 , $v_j = 2.83U_\infty$, $\phi = 10^\circ$, $Re_c = 2.4 \times 10^4$, $M_\infty = 0.2$, $\Omega_0^+ = 0.2$

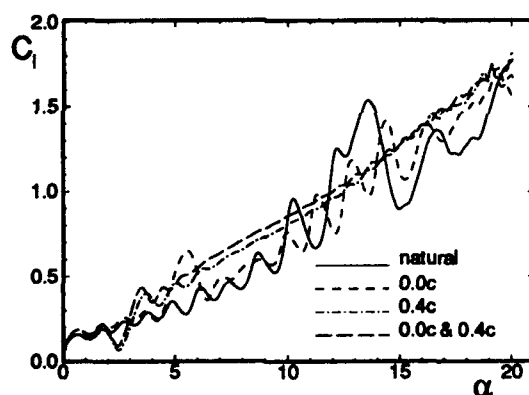


Figure 4.22 Effect of tangential blowing at $X = 0.0c$, $X = 0.4c$ slots (individually and simultaneously) on C_l for a low pitch rate ($\Omega_0^+ = 0.05$); 385×201 , $v_j = 2.83U_\infty$, $\phi = 10^\circ$, $C_\mu = 0.0292$, $Re_c = 2.4 \times 10^4$, $M_\infty = 0.2$

To this point in the analysis, the best slot position for control is the $X = 0.0c$ slot. A further refinement of slot location in the leading-edge region was motivated by the work of Karim and Acharya (1993) who examined dynamic-stall control using leading-edge suction. They varied their slot position from $X = 0.02c$ to $0.05c$ and found no significant qualitative differences in their control effectiveness. For suction control, they concluded that as long as the slot position is in a location that still removes the reverse-flowing fluid in order to prevent pooling under the shear layer near the leading edge, then the control technique is not dependent on slot position. To evaluate this finding for the case of tangential blowing and to compare blowing with suction control, two grids—351x201 and 361x201 (Figures 4.1(b) and (c) respectively)—were constructed (Section 4.3). These grids provide for slots at only $X = 0.0c$ and $0.05c$ and have differing slot widths at the $X = 0.05c$ slot.

The 351x201 grid, with a width of $0.0107c$ at the $X = 0.05c$ slot (compare with $0.0105c$ width for the $X = 0.0c$ slot for all grids), was used to investigate slot location effectiveness. The velocity at the $X = 0.0107c$ slot was adjusted slightly to $v_j = 2.78U_\infty$ to match mass flow with the $X = 0.0c$ slot ($v_j = 2.83U_\infty$). A comparison of the isovorticity contours between the $X = 0.0c$ and $0.05c$ slots (Figure 4.23) shows that the an extra 2° - 3° of dynamic-stall-vortex-formation delay is obtained by placement of the slot at $X = 0.05c$ instead of $0.0c$. The leading-edge blowing extends onset angle by $\sim 14\%$ while $0.05c$ -blowing extends it by $\sim 27\%$ for these conditions. This $X = 0.05c$ -chord location is more strategic than the $0.0c$ location because it more directly keeps the reverse-flowing fluid from pooling under the shear layer in the $X \approx 0.15c$ region (natural case, Figure 2.2(f)).

As greater control is applied, the region of pooled fluid moves toward the leading edge ($X \approx 0.09c$ region for $v_j = 2.83U_\infty$ at $X = 0.0c$ blowing; $X \approx 0.06c$ region for $v_j = 2.78U_\infty$ at $X = 0.05c$ blowing (Figure 4.23)). Thus it appears that the optimum location for the blowing slot is between the leading edge and the region of natural-case reverse-flowing-fluid pooling. Since the region of pooled reverse-flowing fluid moves up chord as control is applied, it makes sense to anticipate this movement and locate the slot closer to the leading edge rather than nearer to the natural-case location of this pooled fluid. The optimum choice of location, however, will depend not only upon parameters

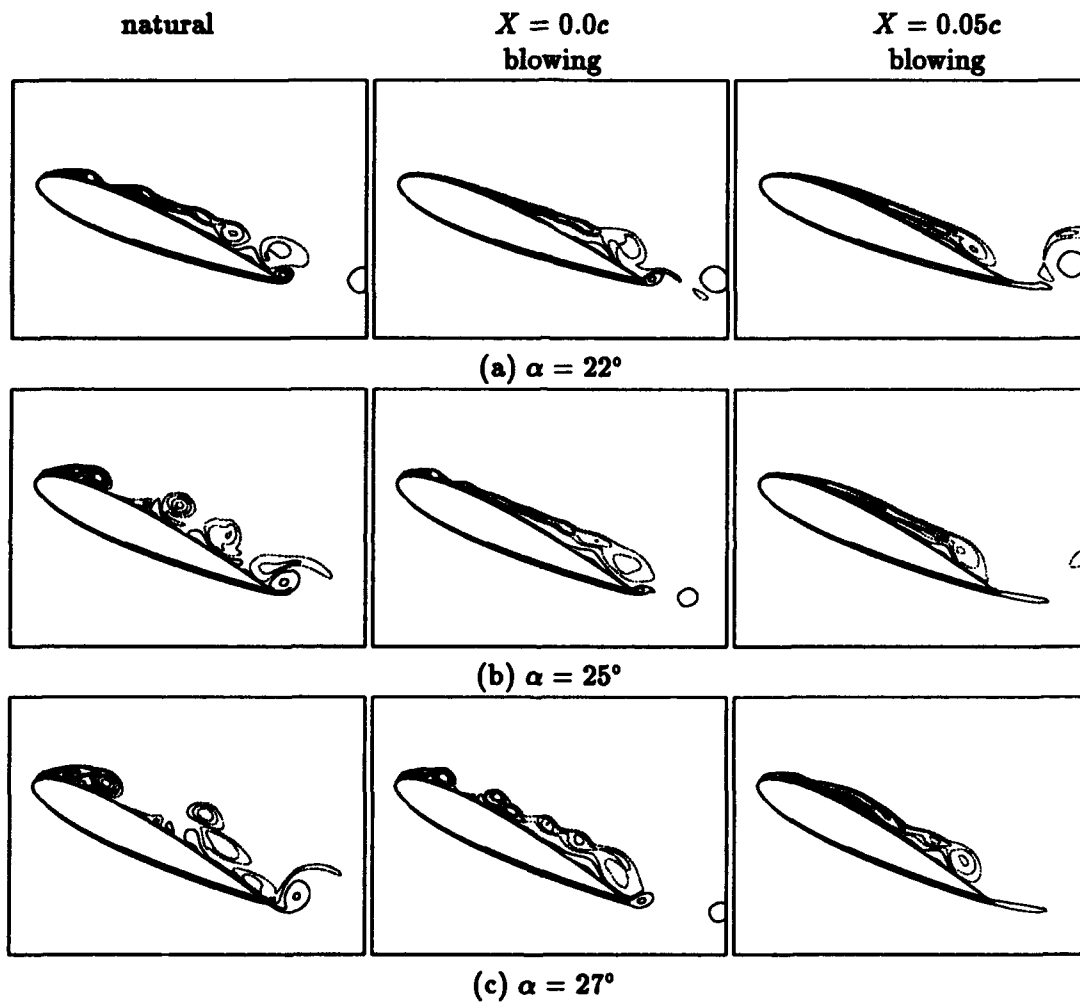


Figure 4.23 Effect of tangential blowing at $X = 0.0c$ and $0.05c$ slots on vorticity contours; 351×201 , $v_j = 2.8U_\infty$, $\phi = 10^\circ$, $Re_c = 2.4 \times 10^4$, $M_\infty = 0.2$, $\Omega_0^+ = 0.2$

that affect the location of pooled fluid (e.g., pitch rate, pitching center-of-rotation location, M_∞ , geometry) but also upon the amount of \dot{m} or C_μ that is available for use (which in practical applications means the amount of high-pressure air from some source such as the bleed air from a jet engine compressor).

Pressure coefficients for 0.0c and 0.05c blowing are shown in Figure 4.24 for $\alpha = 22^\circ$.

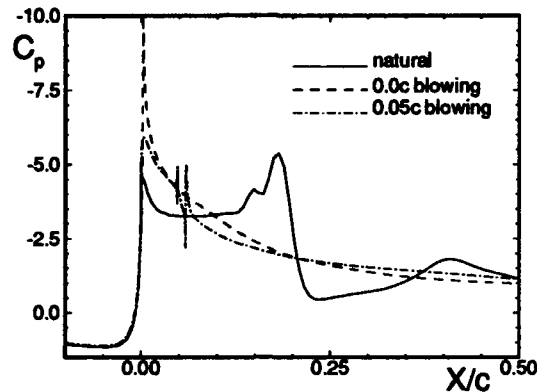


Figure 4.24 Effect of tangential blowing at $X = 0.0c$ and $0.05c$ slots on C_p for constant \dot{m} ; 351x201, $\alpha = 22^\circ$, $\phi = 10^\circ$, $Re_c = 2.4 \times 10^4$, $M_\infty = 0.2$, $\Omega_0^+ = 0.2$

The 0.0c blowing occurs in a very favorable pressure gradient region while the 0.05c blowing is located in a naturally adverse pressure gradient region for α 's near dynamic-stall-vortex formation. More investigation needs to be made to determine if the optimum slot location is just aft of the suction peak near the α at which leading-edge shear-layer lift off occurs ($\alpha \approx 20^\circ$ for the nominal conditions). Based upon examination of the dynamic-stall-vortex-formation region for the 0.05c-blowing case (Figure 4.25), it appears that the reverse-flowing fluid pools up chord of the 0.05c slot due to the extremely severe adverse pressure gradient at $\alpha = 27^\circ$. Static-stall control investigation (Williams, 1961:86) established that the optimum slot position lies in the first 1%-chord of medium- and moderately-thick airfoils, thus it is possible that further dynamic-stall-vortex-formation delay may be obtained by moving the slot still further up chord of the $X = 0.05c$ position.

Slot-width effects for tangential blowing were addressed using the 351x201 and 361x201 grids having $s_j = 0.0107c$ and $0.00717c$ at the 5%-chord slot respectively. To compare with

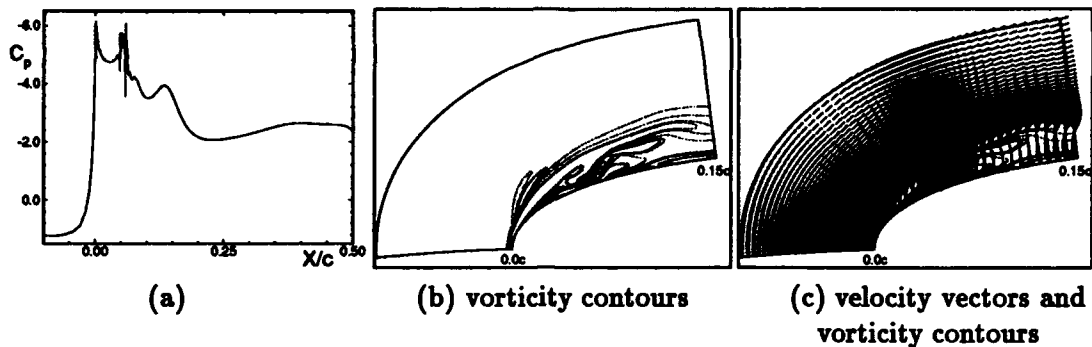


Figure 4.25 Effect of tangential blowing on C_p , vorticity contours, and velocity vectors at $\alpha = 27^\circ$; 351×201 , $v_j = 2.83U_\infty$, $\phi = 10^\circ$, $Re_c = 2.4 \times 10^4$, $M_\infty = 0.2$, $\Omega_0^+ = 0.2$

one another, constant C_μ ($= 0.0427$) and constant \dot{m} ($= 0.0052\rho_\infty U_\infty c$) cases¹ were computed. C_l curves (Figure 4.26) indicate that matching C_μ (assuming a constant ϕ for the

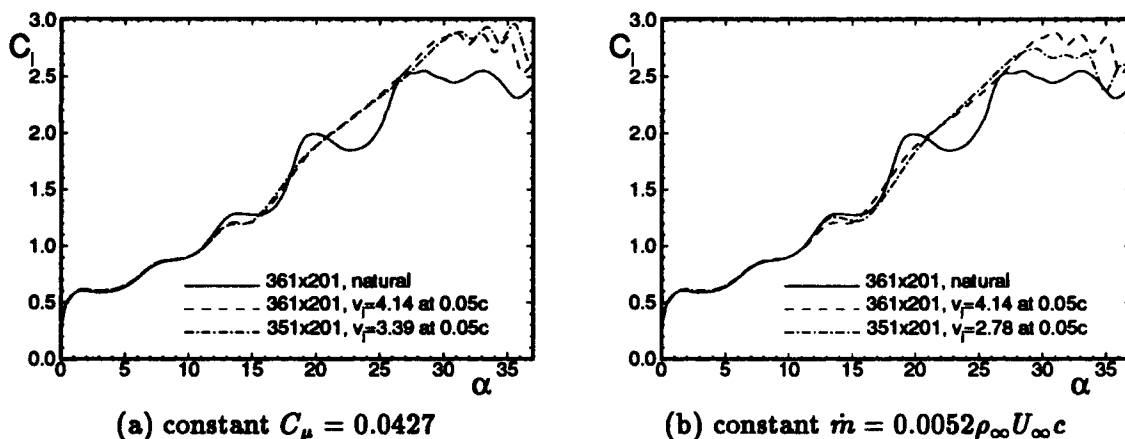


Figure 4.26 Effect of tangential blowing at $X = 0.05c$ slot on C_l for constant C_μ and constant \dot{m} ; $\phi = 10^\circ$, $Re_c = 2.4 \times 10^4$, $M_\infty = 0.2$, $\Omega_0^+ = 0.2$

entire pitch-up) provides nearly identical solutions for the different slot widths while for the same \dot{m} , the smaller slot exacts slightly better results. The isovorticity contours (Figure 4.27) confirm the conclusions drawn from the C_l plots, however differences between matching C_μ and \dot{m} appear minor. In this figure, the first column pictures are the baseline to which constant C_μ (second column) and constant \dot{m} (third column) for the larger

¹All C_μ and \dot{m} values given assume $\rho_j = \rho_\infty$.

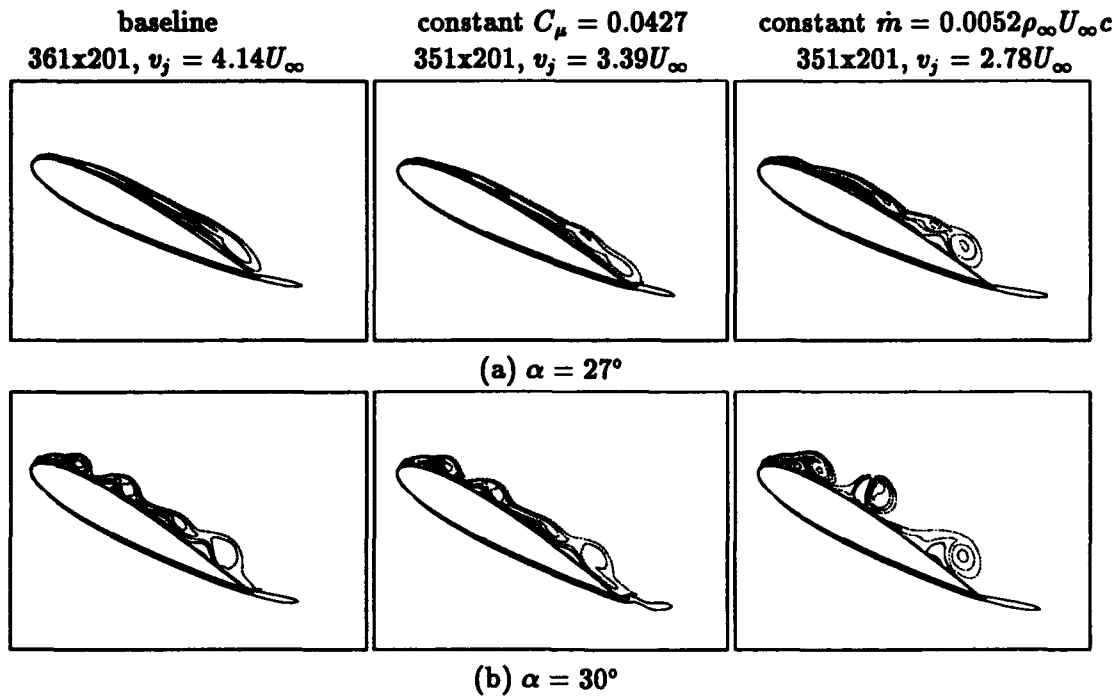


Figure 4.27 Effect of slot width on isovorticity contours; $\phi = 10^\circ$, $Re_c = 2.4 \times 10^4$, $M_\infty = 0.2$, $\Omega_0^+ = 0.2$

5%-chord slotted airfoil are compared. (Note that $\epsilon = 0.02$ for the high- v_j solutions, so $\epsilon = 0.01$ —the nominal value—is used only for the $v_j = 2.78$ solution on the 351x201 grid.)

The incompressible flow assumption (i.e., $\rho_j = \rho_\infty$) made in order to specify a constant v_j throughout the pitch-up maneuver is a poor assumption to make for large slot jet velocities (say, $v_j > 3U_\infty$). For $5^\circ \leq \alpha \leq 27^\circ$, the actual jet densities (averaged over all slot points at a given α) vary between 94% to 70% that of free-stream density (Figure 4.28(a)) for the three different cases being considered in this slot-width study. (Note that the subscripts “s” and “b” in the figure refer to the “small” and “big” slotted airfoils (i.e., 361x201 and 351x201 grids), respectively.) Figure 4.28(b) shows that the disparity between the “constant” C_μ cases and “constant” \dot{m} cases is reasonably benign since each case suffers, to some degree, from the breakdown of the incompressible assumption. Even though constant \dot{m} is not strictly enforced in these cases, it is clear that if \dot{m} is kept constant, then small-slot blowing will provide even better control than large-slot blowing for

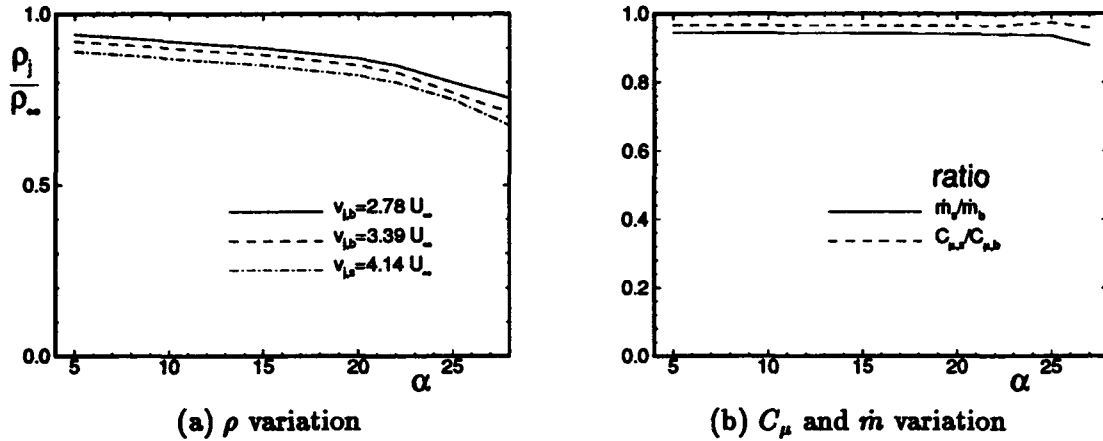


Figure 4.28 Breakdown of incompressible-flow jet assumption for blowing at $X = 0.05c$ slot; $Re_c = 2.4 \times 10^4$, $M_\infty = 0.2$, $\Omega_0^+ = 0.2$

these flow and pitch rate conditions (i.e., for the same \dot{m} a smaller slot achieves a higher C_μ).

Summarizing, the slot study in this section has shown that the best location for the slot appears to be between the leading edge of the airfoil and the natural-case location of the reverse-flow pooled fluid. In anticipation of up-chord movement of this pooled-fluid location with greater control application, a location closer to the leading edge (though not exactly at $X = 0.0c$) is probably best. The slot-width study has confirmed that for dynamic-stall control, just as in the static-control case (Williams, 1961:78), momentum blowing coefficient (C_μ) is the parameter that should be matched to get similar control performance from different sized slots at the same location (assuming ϕ is constant during entire pitch-up maneuver). Hence, in a practical application where a limited amount of high-pressure bleed air is available, a small slot is better (within the constraints of other factors such as the maximum pressure available) since for the same \dot{m} , a small slot exacts a higher C_μ than a larger slot.

4.2.2 Jet Velocity Effects. Tangential velocity was varied to study its effect on dynamic-stall-vortex-formation control at the $0.05c$ and $0.0c$ slots. The nominal flow and pitch-rate conditions used for this jet-velocity-variation study are $Re_c = 2.4 \times 10^4$, $M_\infty = 0.2$, $\Omega_0^+ = 0.2$. The nominal time step used is $\Delta t^+ = 0.001$ and the dissipation

coefficient used is $\epsilon_4 = 0.01$ (except for the $0.05c$ -blowing, $v_j = 4.17U_\infty$ case which used $\epsilon_4 = 0.02$). The blowing angle for all cases in this section is $\phi = 10^\circ$. Table 4.2 shows the six cases used in this study. The mass-flow rates and momentum-blowing coefficients listed in the table for these cases are calculated using incompressible-jet-flow assumptions (Section 4.2.1).

Table 4.2 Six Cases of Jet-Velocity-Variation Study

0.0c slot			0.05c slot		
$\frac{v_j}{U_\infty}$	$\frac{\dot{m}}{\rho_\infty U_\infty c}$	C_μ	$\frac{v_j}{U_\infty}$	$\frac{\dot{m}}{\rho_\infty U_\infty c}$	C_μ
1.415	0.00258	0.00365	1.39	0.00258	0.00359
2.83	0.00516	0.0146	2.78	0.00516	0.0144
4.25	0.00775	0.0329	4.17	0.00775	0.0323

For high jet velocities (say, $v_j > 2.5U_\infty$ at $X = 0.05c$), dynamic-stall-vortex formation is delayed as indicated by loads data (Figure 4.29) and isovorticity contours (Figure 4.30). The reason for this delay is that the high-momentum jet fluid adds stream-wise momentum

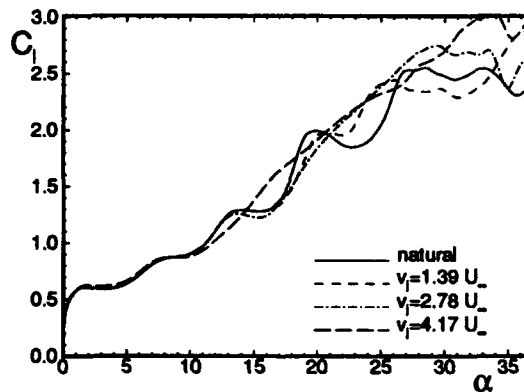


Figure 4.29 Effect of variation in tangential-blowing jet velocity at $0.05c$ slot on C_l ; 351×201 , $\phi = 10^\circ$, $Re_c = 2.4 \times 10^4$, $M_\infty = 0.2$, $\Omega_0^+ = 0.2$

to the flow near the surface which acts against the strong adverse pressure gradient that exists in the region near the slot. Recall for the natural case (Section 2.2), that as the airfoil pitches up and the pressure gradient in the $0.10c < X < 0.25c$ region becomes more adverse, fluid is drawn up-chord underneath the shear layer. This thin reverse-flowing fluid pools underneath the shear layer at $X \approx 0.15c$ (Figure 2.2(d)). Once the fluid accumulates

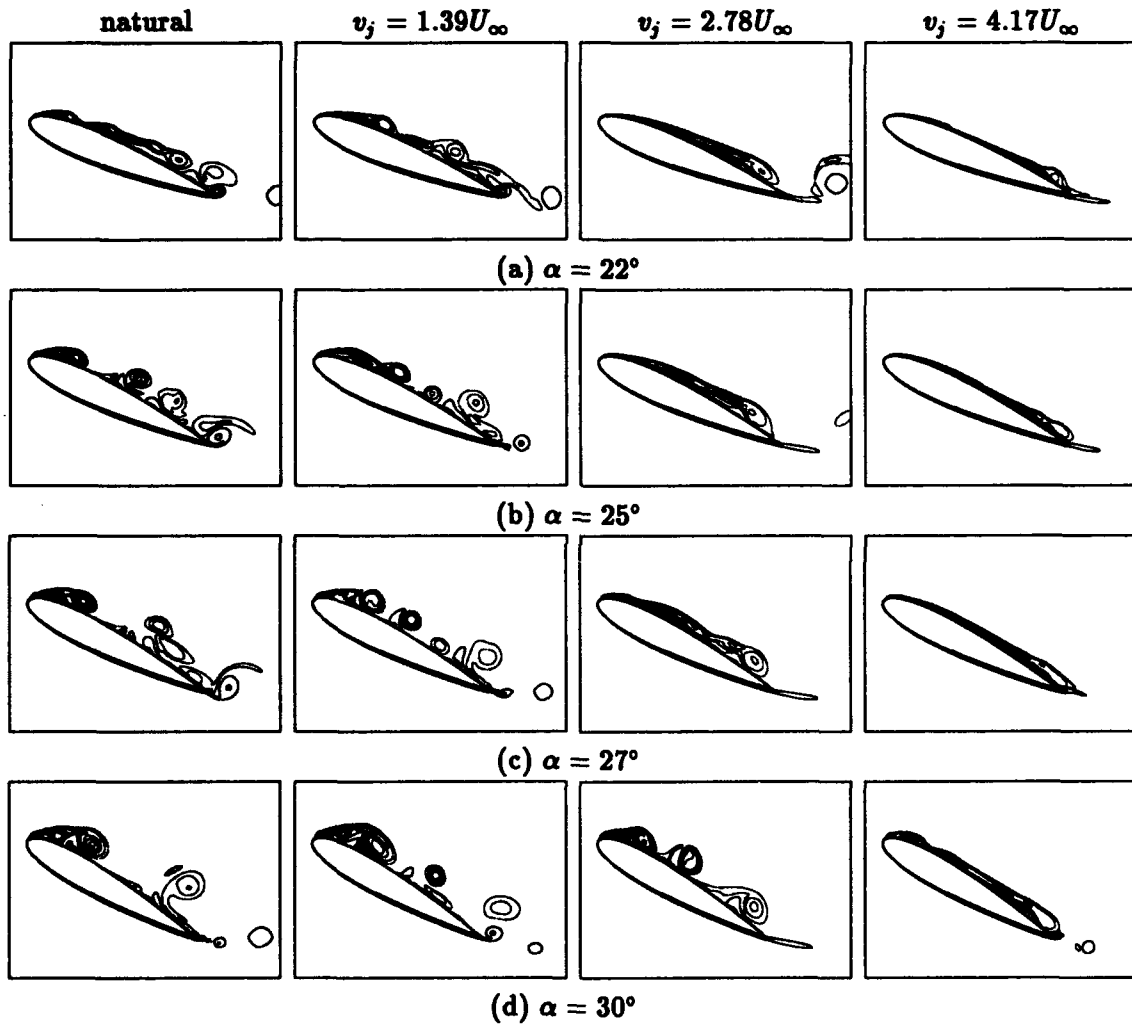


Figure 4.30 Effect of variation in tangential-blowing jet velocity at $0.05c$ slot on isovorticity contours; 351×201 , $\phi = 10^\circ$, $Re_c = 2.4 \times 10^4$, $M_\infty = 0.2$, $\Omega_0^+ = 0.2$

to a sufficient thickness, the shear layer kinks, and so begins the rapid, self-promoting process by which the dynamic-stall vortex forms (Section 2.2).

The isovorticity contours for the 0.05c-blowing, low- v_j case (Figure 4.30(a)) show that counterproductive effects occur when blowing at too low a velocity. Apparently, there are two flow features working together in this case. First, the jet is located in a region of a naturally occurring adverse pressure gradient at $\alpha \approx 20^\circ$ (Figure 2.2(d)). Second, with $v_j = 1.39U_\infty$, the momentum of the jet fluid is so low relative to the momentum of the fluid being introduced into for $\alpha \approx 20^\circ$ (natural $V < 2.1U_\infty$ for $\alpha = 22^\circ$ —Figure 4.31(b)), that the jet flow is actually causing a net decrease in the momentum of the fluid in its

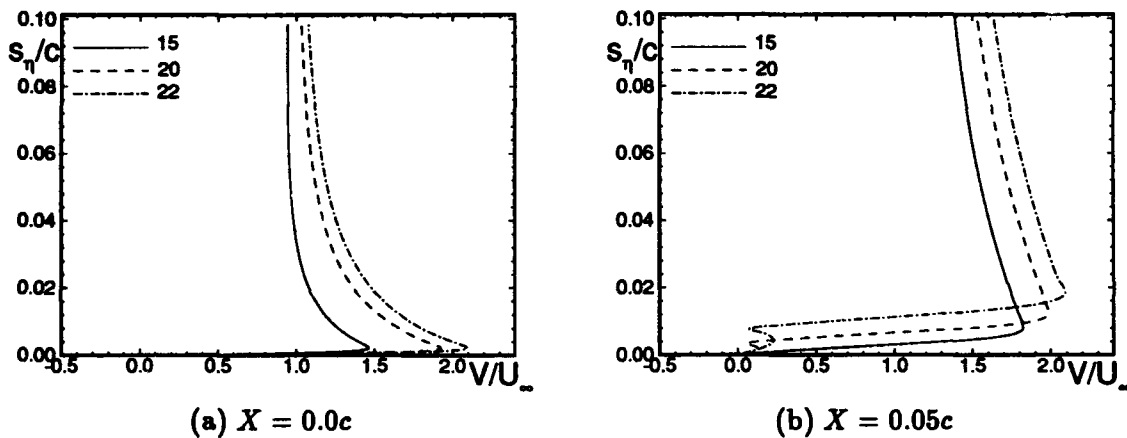


Figure 4.31 Velocity profile for natural case ($\alpha = 15^\circ, 20^\circ, 22^\circ$); 351×201 , $Re_c = 2.4 \times 10^4$, $M_\infty = 0.2$, $\Omega_0^+ = 0.2$

vicinity. Therefore, a less-severe adverse pressure gradient than in the natural case (such as that which exists around the quarter chord) is now capable of initiating the dynamic-stall-vortex-forming process (i.e., the reverse-flowing fluid pooling under the shear layer followed by the kinking of the shear layer). The result is that the fluid pools slightly sooner (i.e., at a slightly lower α) and further aft of the natural case ($X \approx 0.26c$ for the low- v_j case, compared to $X \approx 0.15c$ for the natural case).

For the conditions investigated in this study, the greater the jet velocity, the longer dynamic stall is delayed. However, it appears that with $v_j = 4.17U_\infty$ at the 0.05c slot (Figure 4.30(d)), the slight improvement in control that is gained over the $v_j = 2.78U_\infty$

case may not be worth the 50% increase in mass flow required to achieve this small gain. Hence, for the flow and pitch-rate conditions considered, it appears that $v_j \approx 4U_\infty$ is near the practical limit for 0.05c blowing, assuming there is enough \dot{m} available from the high-pressure source to blow even at this velocity. As previously mentioned (Section 4.2.1), this slot location still may not be optimum. Thus, the apparent useful maximum v_j may be higher for slots further up-chord.

For the 0.0c-blowing, high- v_j case as in the 0.05c-blowing case, dynamic-stall vortex formation is delayed longer at the highest blowing velocity (Figure 4.32). However, unlike

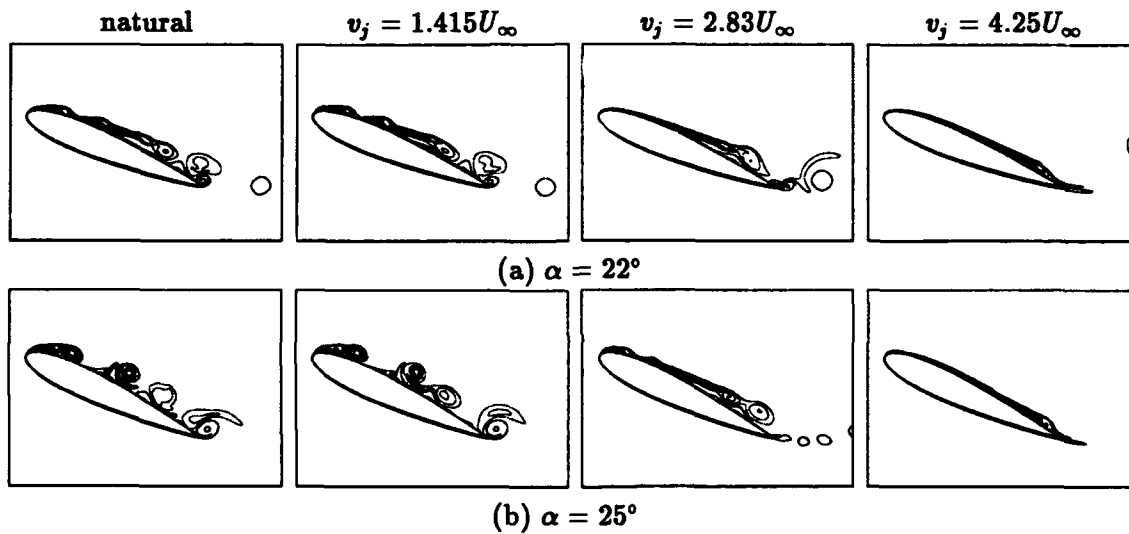


Figure 4.32 Effect of variation in tangential-blowing jet velocity at 0.0c slot on isovorticity contours; 385x201, $\phi = 10^\circ$, $Re_c = 2.4 \times 10^4$, $M_\infty = 0.2$, $\Omega_0^+ = 0.2$

the 0.05c-blowing case, 0.0c-slot blowing at the low velocity ($v_j = 1.415U_\infty$) does not cause the fluid to pool at a position aft of the natural-case pooling location, but rather slightly ahead of the natural-case location ($X \approx 0.13c$ for the 0.0c-blowing low- v_j case, compared to $X \approx 0.15c$ for the natural case). Apparently, since the natural-case pressure gradient at $X = 0.0c$ is extremely favorable (Figure 2.2(d)), then the low jet momentum at $X = 0.0c$ (relative to the natural case momentum (Figure 4.31(a)) for $\alpha = 20^\circ$) has little effect on the flow.

Higher blowing velocities were not investigated at the 0.0c slot, however, it seems likely that there is an optimum v_j for which dynamic-stall-vortex-formation control im-

provements are balanced with m and C_μ limitations as discussed at the end of Section 4.2.1. Also, at the $X = 0.0c$ slot the airfoil surface curvature is large. It is likely that when extremely high blowing velocities are used, the jet could cause a separation region at the leading edge thereby inducing prematurely, the formation of the dynamic-stall vortex. Obviously, optimum slot location (Section 4.2.1) and blowing velocity are closely linked. This upper limit issue on $0.0c$ -blowing jet velocity needs further investigation.

Blowing at either the $0.0c$ or $0.05c$ slot significantly strengthens and alters the shear layer as shown in Figure 4.33. As a representative example, this figure shows velocity

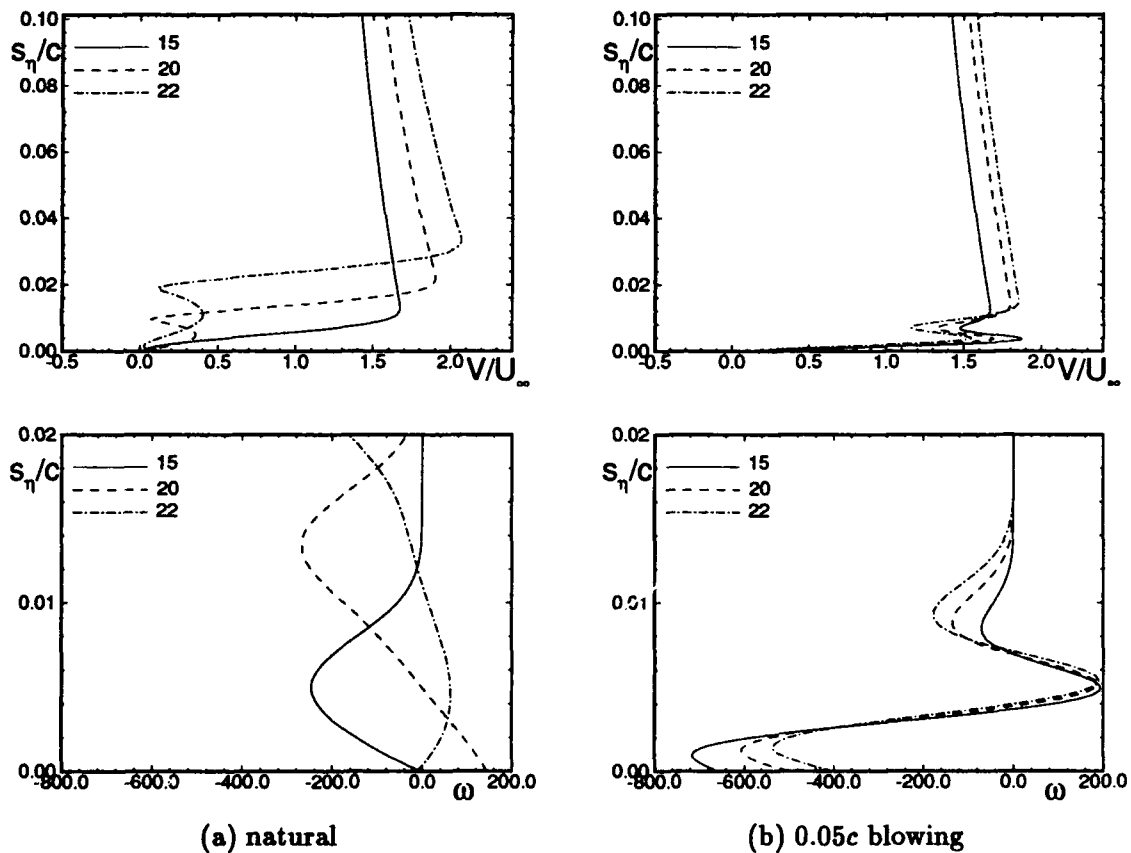


Figure 4.33 Velocity and vorticity profile for natural and $0.05c$ -blowing cases ($v_j = 2.78U_\infty$, $\phi = 10^\circ$) at $X = 0.1c$ ($\alpha = 15^\circ, 20^\circ, 22^\circ$); 351×201 , $Re_c = 2.4 \times 10^4$, $M_\infty = 0.2$, $\Omega_0^+ = 0.2$

magnitude profiles with the associated vorticity profiles over three angles of attack at the

$X = 0.1c$ station. Near the wall, where $v_x \approx 0$, the vorticity in the x - y plane² is simply $\omega \approx -u_x$ (which is also proportional to wall shear stress). Obviously, with the introduction of blowing, greater negative vorticity is generated at the wall aft of the slot since the jet significantly increases the wall velocity gradient, thereby producing a stronger shear layer. As the jet velocity is increased, the near-wall velocity gradient increases, producing additional negative vorticity. This stronger shear layer (in terms of levels of vorticity and velocity) stays closer to the surface than the natural shear layer (Figure 4.30(a)) thereby inhibiting fluid from flowing up chord (compared to the natural case). The high-velocity jet also causes additional profile inflections (and thus a change of sign of vorticity for each inflection) which introduce positive vorticity into the shear layer ($0.003 < s_\eta/c < 0.008$ region for α 's shown at this station) as observed in Figure 4.33(b).

The jet-velocity-variation study presented in this section indicates that in general (to a practical upper limit), the higher the jet velocity, the greater the duration of dynamic-stall-vortex-formation delay.

4.2.3 Effect of Delaying α_b . As a means of refining the control of dynamic-stall-vortex formation by blowing, a study was conducted to determine the latest angle of attack at which control must begin. For the NACA 0012 airfoil pitching at $\Omega_0^+ = 0.15$ ($Re_c = 3.0 \times 10^4$) in a free stream with velocity $40 \frac{m}{s}$ ($M_\infty \approx 0.12$), Karim and Acharya (1993) found that shear-layer lift up (which occurs just prior to dynamic-stall-vortex formation) occurs at $\alpha \approx 18^\circ$. They reported that for suction control, as long as $\alpha_b < 20^\circ$, then the dynamic-stall vortex is successfully suppressed.

For the NACA 0015 airfoil at nominal conditions ($M_\infty = 0.2$, $Re_c = 2.4 \times 10^4$, $\Omega_0^+ = 0.2$), $\alpha \approx 20^\circ$ (Figure 2.1(a)) is the angle at which shear-layer lift up occurs. (Note that this is also the angle at which a constant-pressure plateau is present (Figure 2.2(d))—an observation that has significant control-strategy implications and will be discussed shortly.) Numerical solutions were obtained for the nominal conditions using a jet velocity of $v_j = 4.14U_\infty$ at the $0.05c$ slot ($s_j = 0.00717c$). The time step and dissipation coefficient for

²Here, the x - y coordinate system is assumed to lie on the airfoil surface, and not at the airfoil pivot point as defined in Figure 3.1.

the blowing cases in this α_b study are $\Delta t^+ = 0.001$ and $\epsilon_4 = 0.02$, respectively. For these conditions, the dynamic-stall vortex is similarly suppressed for $\alpha_b = 0^\circ, 5^\circ, 10^\circ, 15^\circ, 20^\circ$ (Figure 4.34). However, when blowing begins at $\alpha_b = 22^\circ$ (Figure 4.34(f)), then dynamic-

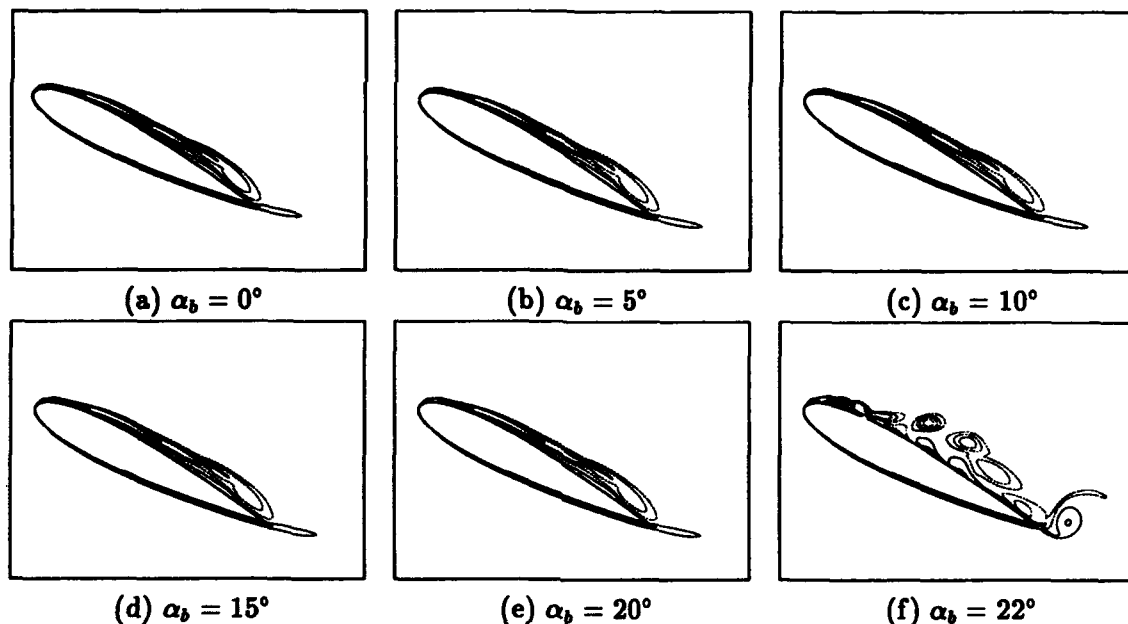


Figure 4.34 Effect of tangential-blowing α_b on vorticity contours ($\alpha = 27.0^\circ$); 361×201 , $v_j = 4.14U_\infty$ at $0.05c$, $\phi = 10^\circ$, $Re_c = 2.4 \times 10^4$, $M_\infty = 0.2$, $\Omega_0^+ = 0.2$

stall-vortex formation is not delayed as it is for the lower α_b cases.

Natural-case isovorticity contours are shown in Figure 4.35 for comparative purposes.

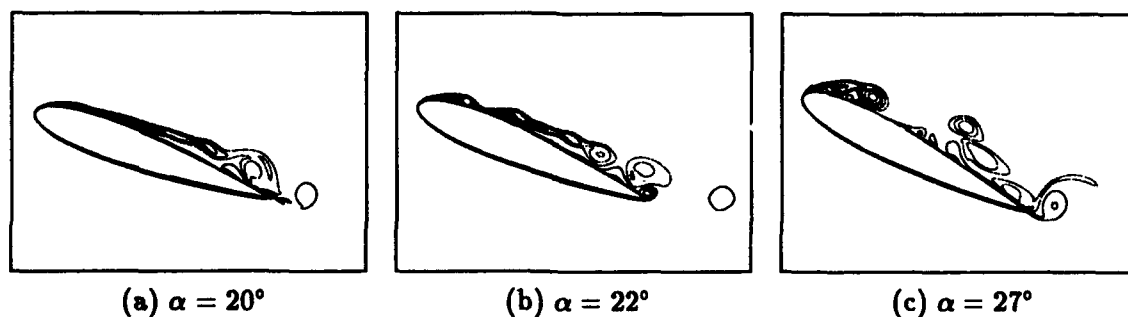


Figure 4.35 Isovorticity contours for natural case; 361×201 , $Re_c = 2.4 \times 10^4$, $M_\infty = 0.2$, $\Omega_0^+ = 0.2$

The natural-case shear-layer lift up is evident at $\alpha = 20^\circ$ (Figure 4.35(a)). At $\alpha = 22^\circ$

(Figure 4.35(b)), a dynamic-stall vortex is just forming—this is too late to apply effective control, although there is some small benefit to doing so (compare Figure 4.34(f) with Figure 4.35(c)).

One potential control strategy suggested by Metwally (1990) when using suction control, involves monitoring two pressures in the region where a constant pressure plateau would form. When the two pressures are within a certain difference band during a pitch-up maneuver that would produce a dynamic-stall vortex, then this condition would be read as a pressure plateau and suction control would be applied to delay the dynamic-stall vortex. The numerical results presented in this section demonstrate that this same strategy is applicable to tangential blowing.

The fact that dynamic-stall-vortex formation is nearly identical for all $\alpha_b \leq 20^\circ$ emphasizes the dominant role that the pooled fluid under the shear layer plays (Section 2.2) in the dynamic-stall phenomenon. The critical time to blow is just after shear-layer lift up, just before the fluid naturally pools beneath the shear layer. These results also highlight the speed at which the reverse-flowing fluid pools as there is only 2° difference in α_b between a successful and unsuccessful control scenario for the current simulation conditions.

4.2.4 Jet Orientation Angle Effect. The choice of velocity boundary conditions at the airfoil surface (U_{slot}) for the numerical simulations in this research (Section 3.3) result in the choice of a blowing angle ϕ . This angle is measured from the slot surface tangent, which is defined by the first and last point of the slot (Figure 3.2). For the majority of blowing cases contained in this research, the nominal blowing angle is 10° . This value was used as a best estimate of an experimental blowing angle (Lovato and Troutt, 1992) until the actual blowing angle was later experimentally determined ($\phi = 12.2^\circ$ at the 0.0c slot for all α 's in the pitch-up maneuver (Lovato, 1994)). With the uncertainty of the proper blowing angle to use for a realistic numerical simulation, three series of computations were accomplished to investigate the sensitivity of the solution to blowing angle for 0.0c-slot blowing at the nominal flow and pitch-rate conditions ($Re_c = 2.4 \times 10^4$, $M_\infty = 0.2$, $\Omega_0^+ = 0.2$). Blowing angles half and double the nominal angle ($\phi = 5^\circ$ and 20°) were used in the study. The first series maintained the same slot jet velocity ($v_j = 2.83U_\infty$), the second

series maintained the same mass flow rate ($\dot{m} = 0.00516\rho_\infty U_\infty c$) through the slot, and the third series maintained the same slot-momentum-blowing coefficient ($C_\mu = 0.0292$).

Matching \dot{m} or C_μ at different blowing angles leads to different slot velocities. If incompressible flow is assumed (i.e., $\rho_j = \rho_\infty$), Equation 3.7 for momentum blowing coefficient reduces to the following.

$$C_\mu = 2 \frac{s_j}{c} \left(\frac{v_j}{U_\infty} \right)^2 \sin \phi \quad (4.3)$$

Incompressible flow is assumed for obtaining v_j when matching values of \dot{m} and C_μ . After making the runs with the value of v_j under the incompressible assumption, the validity of this assumption can be examined as shown in Section 4.2.1 (Figure 4.28). The density variation along the slot for the low- and high-velocity cases (i.e., $v_j = 2.016U_\infty$ and $v_j = 3.995U_\infty$) of the constant C_μ series show that the incompressible assumption is reasonable for the low-velocity case (average $\rho_j \approx 0.98\rho_\infty$ and $0.91\rho_\infty$ at $\alpha = 5^\circ$ and 25° respectively), but not such a good assumption for the high-velocity case (average $\rho_j \approx 0.92\rho_\infty$ and $0.82\rho_\infty$ at $\alpha = 5^\circ$ and 25° respectively). To better fix C_μ or \dot{m} constant for a pitch-up maneuver, the code should be modified to use the newest density solved for at the slot (i.e., lag density one time level) in order to constantly update the jet velocity at each grid point every time step. However, even with the more crude approach of assuming incompressible flow for the entire pitch-up maneuver, the calculations are sufficient for gaining insight into the effect of blowing angle.

For all three series of computations, a significant amount of solution sensitivity was observed with variation in ϕ . Figure 4.36 presents isovorticity contours for the constant- C_μ series at $\alpha = 25^\circ$. The three cases in this series indicate that lower blowing angles delay dynamic-stall-vortex formation. This is because the high-momentum fluid is introduced closer to the surface, thereby more effectively suppressing the forward propagation of reverse-flowing fluid. This delays the pooling of fluid under the shear layer which causes shear-layer lift off from the surface (Section 2.3), thus delaying the onset of dynamic stall. Figures 4.37 and 4.38 show the effect seen in C_l and C_m (about the quarter chord), respectively, for each of the three series. Even though varying ϕ produces significant differences in

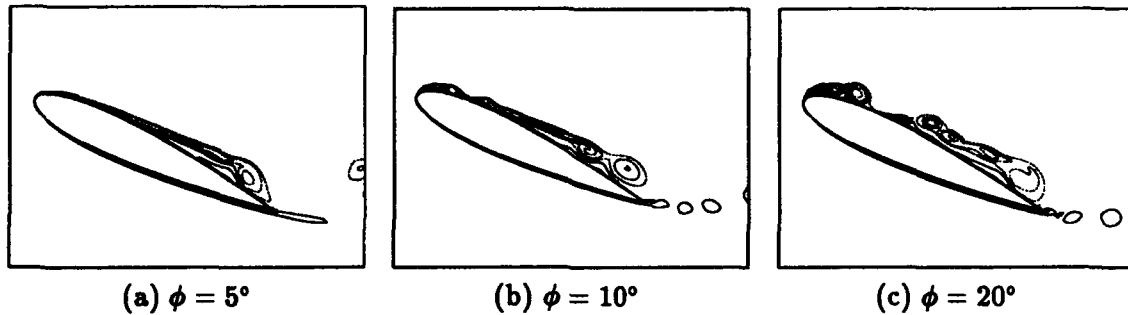


Figure 4.36 Effect of blowing-angle variation (using constant $C_\mu = 0.0292$) on iso-vorticity contours at $\alpha = 25^\circ$; 385x201, $X = 0.0c$ slot, $Re_c = 2.4 \times 10^4$, $M_\infty = 0.2$, $\Omega_0^+ = 0.2$

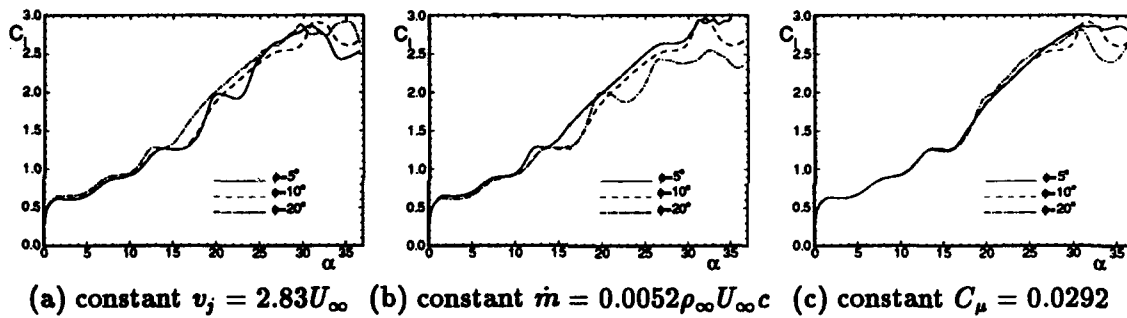


Figure 4.37 Effect of blowing-angle variation on C_l ; 385x201, $X = 0.0c$ slot, $Re_c = 2.4 \times 10^4$, $M_\infty = 0.2$, $\Omega_0^+ = 0.2$

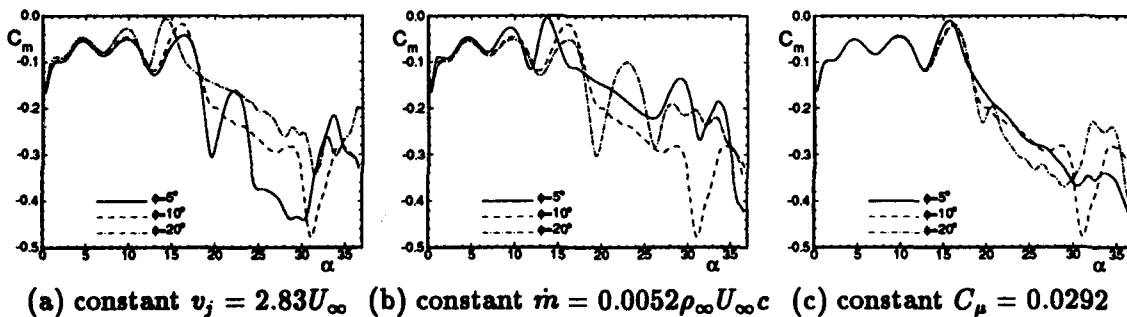


Figure 4.38 Effect of blowing-angle variation on C_m about the quarter chord; 385x201, $X = 0.0c$ slot, $Re_c = 2.4 \times 10^4$, $M_\infty = 0.2$, $\Omega_0^+ = 0.2$

flow structure over the leeward surface (Figure 4.36), the large difference is not as apparent in C_l (Figure 4.37(c)) as in isovorticity contours due to cancellation that occurs during the integration process used to calculate C_l . However, compared to C_l , the difference in the solutions is more pronounced for C_m (Figure 4.38(c)) beyond $\alpha = 19^\circ$. The oscillations in C_m are indicative of vortex formation, convection, and interaction with the surface which occurs during the dynamic-stall process (Figure 2.1). The lower the blowing angle, the less oscillatory C_m is since the smaller blowing angle results in a stronger shear layer much as increased blowing velocity at a given ϕ does (Section 4.2.2).

One way to address solution sensitivity to blowing angle is to catalog the angle of attack at which a visible dynamic-stall vortex forms for each case. For example, Figure 4.39 compares the isovorticity contours for the natural case at $\alpha = 22^\circ$ with the constant- C_μ

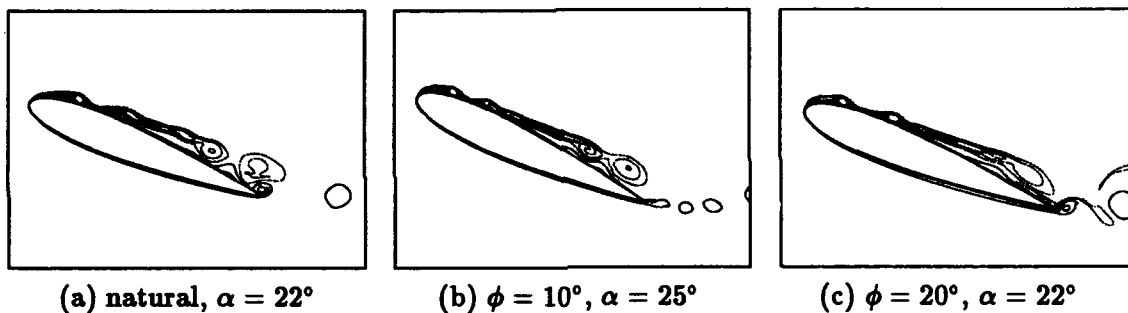


Figure 4.39 Dynamic-stall-vortex formation comparison for natural and two blowing angle cases (using constant $C_\mu = 0.0292$); 385x201, blowing at $X = 0.0c$ slot, $Re_c = 2.4 \times 10^4$, $M_\infty = 0.2$, $\Omega_0^+ = 0.2$

cases of $\phi = 10^\circ$ and $\phi = 20^\circ$ at $\alpha = 25^\circ$ and 22° respectively. Dynamic-stall vortex development is approximately the same for all three cases. Using the natural case angle of attack as a point of reference, blowing angles of $\phi = 10^\circ$ and $\phi = 20^\circ$ delay dynamic-stall onset by 3° and 0° , respectively. The delay in dynamic-stall-vortex formation (DSVF) for all three series of cases (constant v_j , \dot{m} , C_μ) is shown in Table 4.3. It should be noted that the DSVF delay values lack some precision since they were estimated from isovorticity contours at $\alpha = 20^\circ, 22^\circ, 25^\circ, 27^\circ, 30^\circ, 33^\circ$. Also, as previously mentioned, incompressible flow at the slot exit is assumed when declaring the cases to be at constant \dot{m} or constant C_μ . Nonetheless, some useful observations can be made from these results (with the additional

Table 4.3 Solution Sensitivity to Blowing-angle (ϕ) Variation

constant	ϕ	$\frac{v_j}{U_\infty}$	$\frac{\dot{m}}{\rho_\infty U_\infty c}$	C_μ	DSVF delay
v_j	5°	2.83	0.00259	0.0146	2°
	10°	2.83	0.00516	0.0292	3°
	20°	2.83	0.0102	0.0575	0°
\dot{m}	5°	5.64	0.00516	0.0582	9°
	10°	2.83	0.00516	0.0292	3°
	20°	1.44	0.00517	0.0149	-1°
C_μ	5°	3.995	0.00366	0.0292	5°
	10°	2.83	0.00516	0.0292	3°
	20°	2.016	0.00724	0.0292	0°

caveat that this study was done for blowing at the 0.0c slot with nominal flow and pitch-rate conditions of $M_\infty = 0.2$, $Re_c = 2.4 \times 10^4$, $\Omega_0^+ = 0.2$).

At a blowing angle of 20°, tangential blowing control is not effective from the perspective of delaying dynamic-stall vortex formation. In fact, it is counterproductive for $v_j = 1.44U_\infty$. Also, in general, it appears that the lower the blowing angle, the greater the delay of dynamic-stall-vortex formation. This means that if flush slots are being used to achieve “tangential” blowing, then the slot cavity through the surface of the wing should be constructed in such a way to obtain a low blowing angle.

If experiments show that the blowing angle is not controllable, then a comment is in order regarding the slot location with respect to blowing angle. As previously mentioned at the beginning of this section, when blowing at the 0.0c slot (which is in a highly favorable pressure gradient region) a blowing angle of $\phi = 12.2^\circ$ was observed for the entire pitch-up (Lovato, 1994). However, there may be variation in ϕ for a slot which occurs in a region with a large adverse pressure gradient (e.g., 0.05c). As discussed previously (Section 3.3), experimentally the slot-plenum pressure is set, which in turn produces a slot velocity. Computationally, instead of setting a plenum pressure, the jet velocity at the slot is specified under the assumption that v_j and ϕ remain constant for the entire pitch-up. Thus, experimental investigation needs to be made into this issue to gain confidence in the constant- ϕ numerical results for blowing in a region with an adverse pressure gradient.

4.2.5 Jet Profile Effect. The effect of the jet profile on the numerical solution was investigated. In addition to the nominal uniform-jet-velocity profile used in the previous studies, a jet profile after Yeh et al., (1989) was employed for the profile investigation. The formulation for this profile is given below.

$$v_j(\bar{s}) = V_{max}[1 - (2 - \bar{s})^2]^\beta$$

where \bar{s} is the normalized slot length and ranges from $0.0 \leq \bar{s} \leq 1.0$. Two values of the profile-altering parameter β were considered— $\beta = 0.1$ for turbulent profile simulation and $\beta = 0.5$ for an elliptical profile. Note that V_{max} was chosen for each β such that the jet mass flow was the same as that which was used in the uniform-jet portion of the study (i.e., the average $v_j = 2.83U_\infty$ for all three cases). Again, as in Section 4.2.4, incompressible flow is assumed for purposes of v_j specification. Relative to the solution differences found from other parameter variations (e.g., blowing angle of Section 4.2.4), the variation in blowing profile generates a small difference that is evident in C_l (Figure 4.40) for these

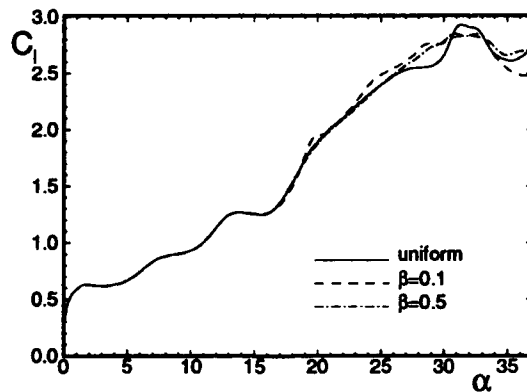


Figure 4.40 Effect of a variation in slot velocity profile on C_l ; 385x201, average $v_j = 2.83U_\infty$ at $X = 0.0c$, $\phi = 10^\circ$, $Re_c = 2.4 \times 10^4$, $M_\infty = 0.2$, $\Omega_0^+ = 0.2$

conditions ($M_\infty = 0.2$, $Re_c = 2.4 \times 10^4$, blow at $X = 0.0c$ with average $v_j = 2.83U_\infty$, $\Omega_0^+ = 0.2$). Isovorticity contours (Figure 4.41) for $\alpha = 25^\circ$ shows the close agreement as well. Even out to $\alpha = 33^\circ$ (Figure 4.42), the three blowing profiles give close agreement in the dynamic-stall-vortex region.

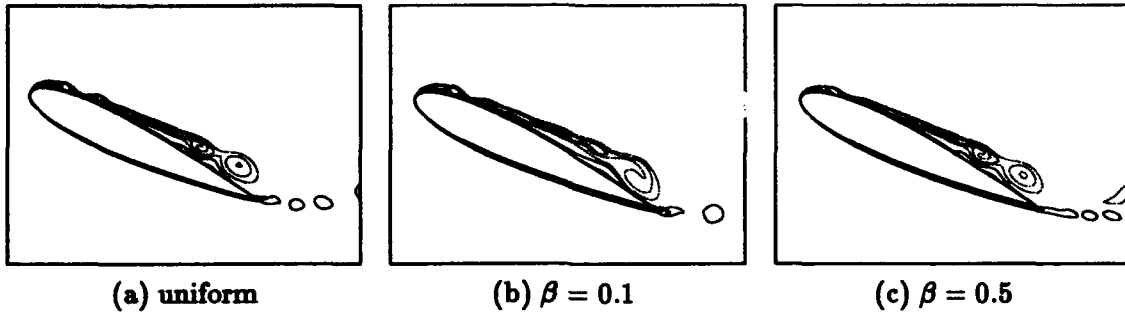


Figure 4.41 Effect of variation in slot velocity profile on isovorticity contours at $\alpha = 25^\circ$; 385x201, average $v_j = 2.83U_\infty$ at $X = 0.0c$, $\phi = 10^\circ$, $Re_c = 2.4 \times 10^4$, $M_\infty = 0.2$, $\Omega_0^+ = 0.2$

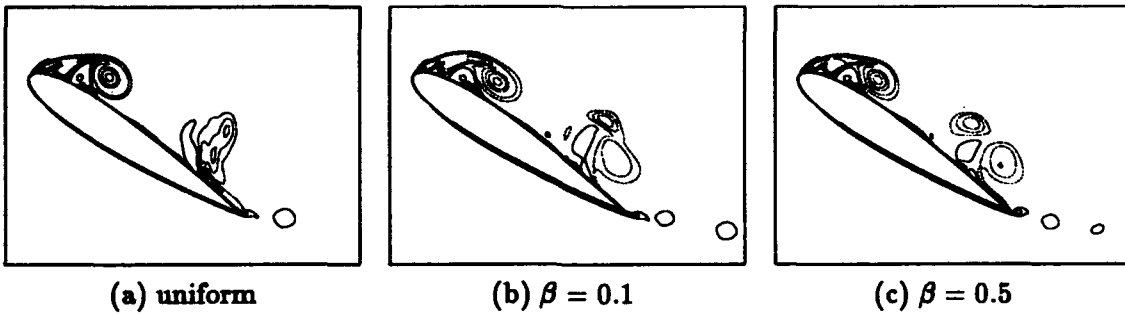


Figure 4.42 Effect of variation in slot velocity profile on isovorticity contours at $\alpha = 33^\circ$; 385x201, average $v_j = 2.83U_\infty$ at $X = 0.0c$, $\phi = 10^\circ$, $Re_c = 2.4 \times 10^4$, $M_\infty = 0.2$, $\Omega_0^+ = 0.2$

Based on this brief velocity-profile study at the $X = 0.0c$ slot, the simple uniform velocity profile is deemed acceptable for investigation of the suppression of dynamic-stall onset using tangential blowing.

4.2.6 Effect of Pulsed Blowing. Lovato and Troutt (1992) experimentally investigated the use of impulsively-applied pulsed blowing to delay the onset of dynamic stall and to control its development to higher angles of attack. Tangential blowing at $v_j = 2.83U_\infty$ per slot (with three slots blowing simultaneously) was applied to an airfoil pitching at $\Omega_0^+ = 0.05$ at frequencies experimentally determined by Lovato (1992) from a study of static stall (20, 10, and 5 Hz corresponding to nondimensional frequencies of 1.00, 0.50, 0.25). Pulse duration in their experiment was 0.01 seconds. As previously mentioned (Section 4.2.1), the three slots of the NACA 0015 airfoil used in the experiment were each $0.0105c$ wide and located at $X = 0.0c$, $0.2c$, and $0.4c$. Flow visualization data indicates that pulsed blowing diminishes the size of the separation region *after* the dynamic-stall vortex forms.

For the computations, blowing at only the $0.0c$ slot was first applied at the beginning of the pitch-up process for a pulse duration of $\Delta t^+ = 0.2$ (for $\Omega_0^+ = 0.2$ and $t_0^+ = 0.5$, blowing for the first pulse stops at $\alpha = 1.24^\circ$). For the conditions of the current study, the nondimensional fundamental frequency ($f^+ = fc/U_\infty$) is $f^+ = 1.00$. Pulsed blowing was also conducted at sub-harmonic frequencies of $f^+ = 0.50$ and 0.25 . The nominal conditions for all cases were $M_\infty = 0.2$, $Re_c = 2.4 \times 10^4$, $v_j = 2.83U_\infty$, $\phi = 10^\circ$, $\Omega_0^+ = 0.2$. Figure 4.43 shows the blowing history for the $f^+ = 1.00$ case in terms of t^+ and α . The first subharmonic ($f^+ = 0.50$) blowing history has just the first and third pulses of the $f^+ = 1.00$ case, and the second subharmonic ($f^+ = 0.25$) has only the first pulse of the $f^+ = 1.00$ case.

No significant variation in the flow structure from the natural flow (particularly true for the $f^+ = 0.25$ case) was observed over this frequency range. In particular, for the conditions of the current simulation, a frequency of $f^+ = 0.25$ amounts to blowing only once at the beginning of the pitch-up cycle. No observable change in the onset and post-onset flow structure or aerodynamic loading was observed (Figure 4.44), suggesting that pulsed

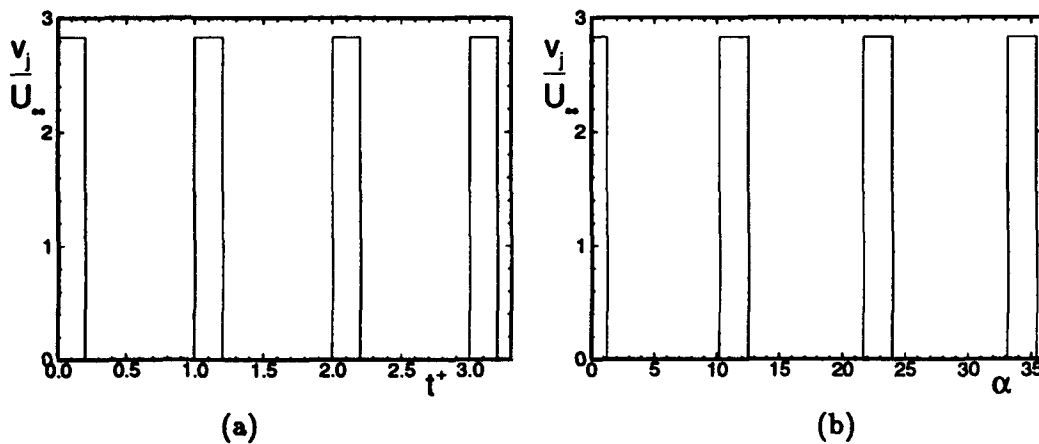


Figure 4.43 Pulse history for the $f^+ = 1.00$ case; $\Omega_0^+ = 0.2$

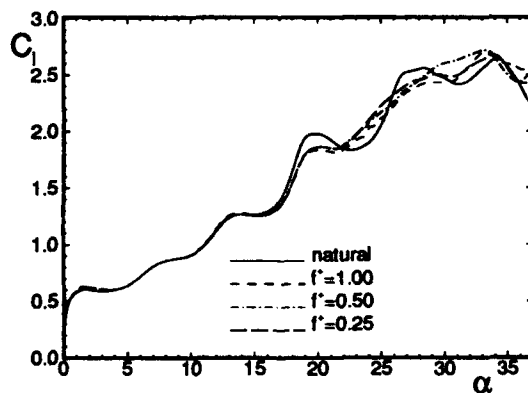


Figure 4.44 C_l Comparison of frequency variation for of pulsed tangential blowing at $X = 0.0c$; 385×201 , $v_j = 2.83U_\infty$ or $v_j = 0$, $\phi = 10^\circ$, $Re_c = 2.4 \times 10^4$, $M_\infty = 0.2$, $\Omega_0^+ = 0.2$

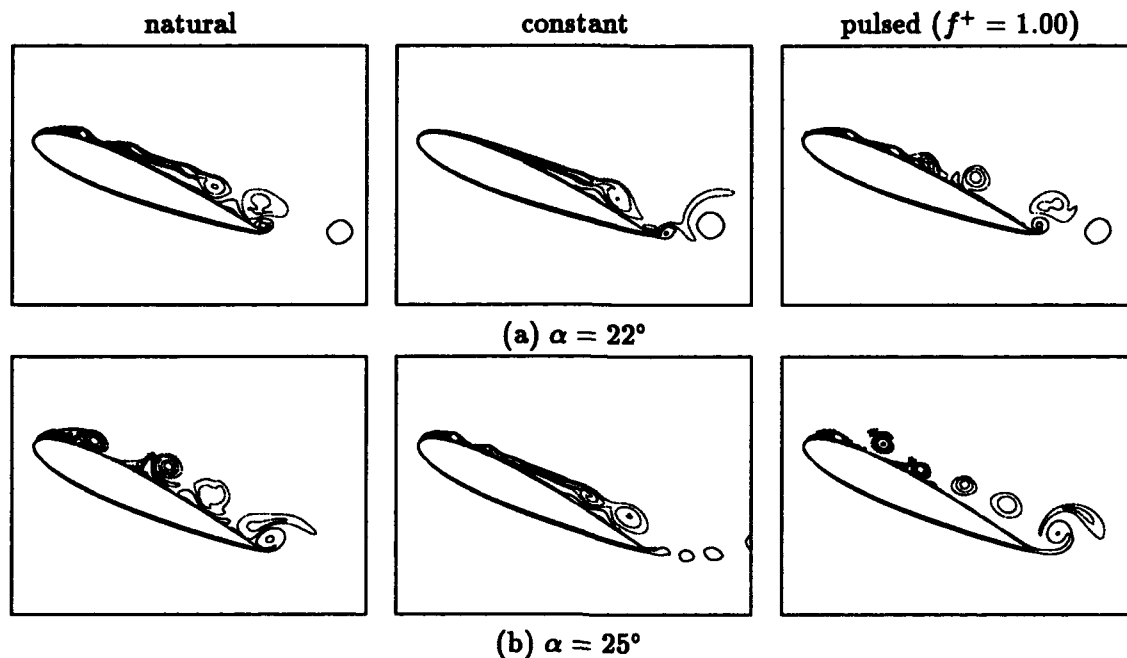


Figure 4.45 Effect of pulsed tangential blowing on isovorticity contours; 385×201 , $v_j = 2.83U_\infty$ or $v_j = 0$, $\phi = 10^\circ$, $Re_c = 2.4 \times 10^4$, $M_\infty = 0.2$, $\Omega_0^+ = 0.2$

blowing applied far in advance (e.g., for blowing when $0 \leq \alpha \leq 1.24^\circ$) of the dynamic-stall-onset angle is ineffective. This observation makes sense in light of Section 4.2.3 results which indicate that the most critical time for blowing is just before the time that reverse-flow-fluid pooling will naturally begin.

The difference in flow structure near the natural-dynamic-stall-onset α induced by constant and pulsed blowing ($f^+ = 1.00$) at the leading edge is presented in the form of vorticity contours in Figure 4.45. Blowing introduces an additional inflection point into the boundary layer profiles along the leading edge resulting in a less stable shear layer. Further, pulsing of the blowing introduces an additional time scale into the flow which may lead to the formation of modes in the shear layer less stable than those present under constant blowing conditions. In fact, for the case considered, the temporal and spatial development of the induced shear layer is far less stable than even the natural-case shear layer as evidenced by the premature break-up of the aft shear layer (Figure 4.45).

In addition to changes at low α , the flow-field structure following the development of the dynamic-stall vortex is dramatically altered by pulsed blowing. Evident in Figure 4.45(b) is the presence of additional discrete shear-layer vortices of decreased wavelength; these vortices convect downstream at roughly the same rate as the shear layer vortex. This flow modification does alter the airfoil loading (Figure 4.44), suggesting that there may be some measure of benefit to be gained by introducing vorticity of the the correct amplitude and phase such that the post-onset development of the shear layer is constructively altered, however post-onset control of dynamic stall is beyond the scope of this work.

A comparison of lift coefficients indicates that for the conditions considered, constant blowing yields the greatest improvement (Figure 4.46) as well as being far easier to implement as part of a control strategy.

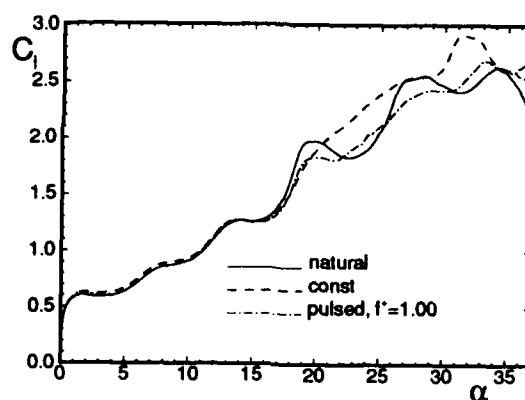


Figure 4.46 Effect of constant and pulsed tangential blowing at $X = 0.0c$ on C_l ; 385x201, $v_j = 2.83U_\infty$ or $v_j = 0$, $\phi = 10^\circ$, $Re_c = 2.4 \times 10^4$, $M_\infty = 0.2$, $\Omega_0^+ = 0.2$

Based on previous work (Karim and Acharya, 1993; Visbal, 1991) and the constant-tangential-blowing investigations contained in this document, it is obvious that pulsed blowing does not directly address the problem of reverse-flow fluid pooling under the shear layer (Section 2.2) which is key to dynamic-stall vortex formation.

4.2.7 Compressibility Assessment. As in the natural case, compressibility effects are examined in the same two ways—by comparing solutions at a lower M_∞ to the $M_\infty = 0.2$ solution, and by an examination the relative magnitude of terms in the vorticity-

transport equation. The issue of compressibility will first be addressed by obtaining a numerical solution at a lower Mach number.

4.2.7.1 Computations at $M_\infty < 0.2$. The natural-case results (Section 4.1.3) indicate that compressibility effects are negligible for the flow conditions ($M_\infty = 0.2$, $Re_c = 2.4 \times 10^4$) and pitch rate ($\Omega_0^+ = 0.2$) studied. The 385x201 grid was used to examine the 0.0c-blowing case with $v_j = 2.83U_\infty$ (blowing angle at 10° off the tangent, constant profile) at $M_\infty = 0.1$ and $Re_c = 1.0 \times 10^4$. C_l for $M_\infty = 0.2$ is quite similar to C_l for $M_\infty = 0.1$ (Figure 4.47(a)). C_p values are nearly identical up to $\alpha = 20^\circ$, with the first

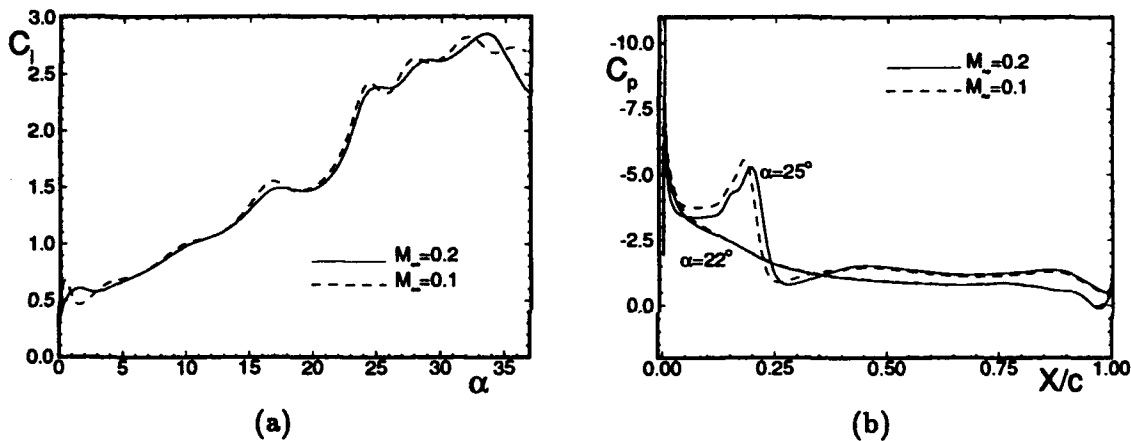


Figure 4.47 Effect of M_∞ on C_l and C_p for 0.0c-blowing case; 385x201, $v_j = 2.83U_\infty$, $\phi = 10^\circ$, $Re_c = 1.0 \times 10^4$, $\Omega_0^+ = 0.2$

significant difference appearing at $\alpha = 22^\circ$ (Figure 4.47(b)) when the dynamic-stall vortex begins to form. Again, as before with the natural case, the compressibility becomes more prominent after the dynamic-stall vortex grows (Figure 4.48). This one comparison in conjunction with the extensive natural-case results (Section 4.1.3.1) indicates that for study of suppression of dynamic-stall vortex formation, $M_\infty = 0.2$ results are essentially incompressible.

4.2.7.2 Compressibility assessment via the vorticity-transport equation.

Contours of the vorticity-transport-equation terms are shown for the 361x201 grid in Figure 4.49. The conditions used to generate the solution are as follows: $Re_c = 2.4 \times 10^4$, $M_\infty = 0.2$, $\Omega_0^+ = 0.2$, $v_j = 4.14U_\infty$ at a blowing angle of 10° off the tangent at the 0.05c

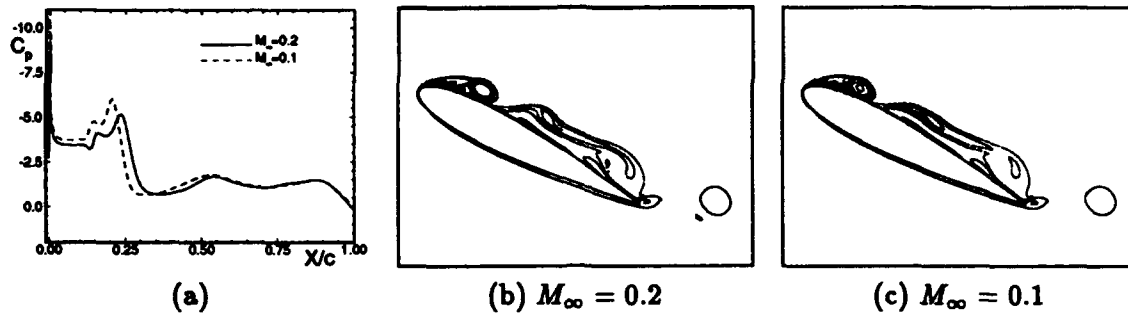


Figure 4.48 Effect of M_∞ on C_p and isovorticity contours for 0.0c-blowing case at $\alpha = 27^\circ$; 385×201 , $v_j = 2.83U_\infty$, $\phi = 10^\circ$, $Re_c = 1.0 \times 10^4$, $\Omega_0^+ = 0.2$

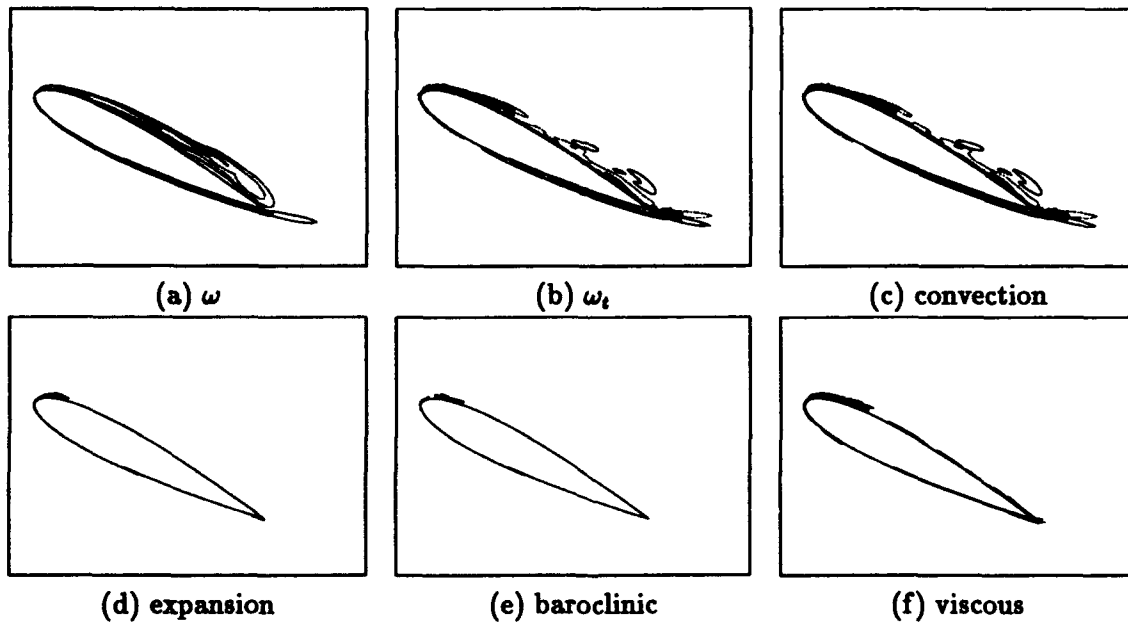


Figure 4.49 Isovorticity contours and contours of vorticity-transport equation terms for 0.05c-blowing case; 361×201 , $v_j = 4.14U_\infty$, $\alpha = 27^\circ$, $\phi = 10^\circ$, $Re_c = 2.4 \times 10^4$, $M_\infty = 0.2$, $\Omega_0^+ = 0.2$

slot. The contour levels shown are the same as those used for the natural case (Figure 4.14). As in the natural case, all terms are small compared to the convection term. Though the expansion term is still small for this very-high blowing velocity case ($v_j = 4.14U_\infty$ for $M_\infty = 0.2$ flow produces a local Mach number at the slot that is roughly 0.8), it is noticeably larger near the slot ($X = 0.05c$) than it was for the natural case prior to dynamic-stall vortex formation (Figure 4.14(d)). This indicates that in the vicinity of the jet the flow is not incompressible (Section 4.2.1) since this term is nonzero only if $\nabla \cdot \mathbf{V} \neq 0$ (Equation 4.2). Also, the vorticity in the shear layer is much greater for this blowing case, and this will have an effect of magnifying what small, nonzero $\nabla \cdot \mathbf{V}$ is present.

Just prior to dynamic-stall-vortex formation the expansion, viscous-diffusion, and baroclinic-torque terms become more significant (Figure 4.50) than they were at the lower α (Figure 4.49)—the same trend as for the natural case (Figures 4.14 and 4.15). In fact, the

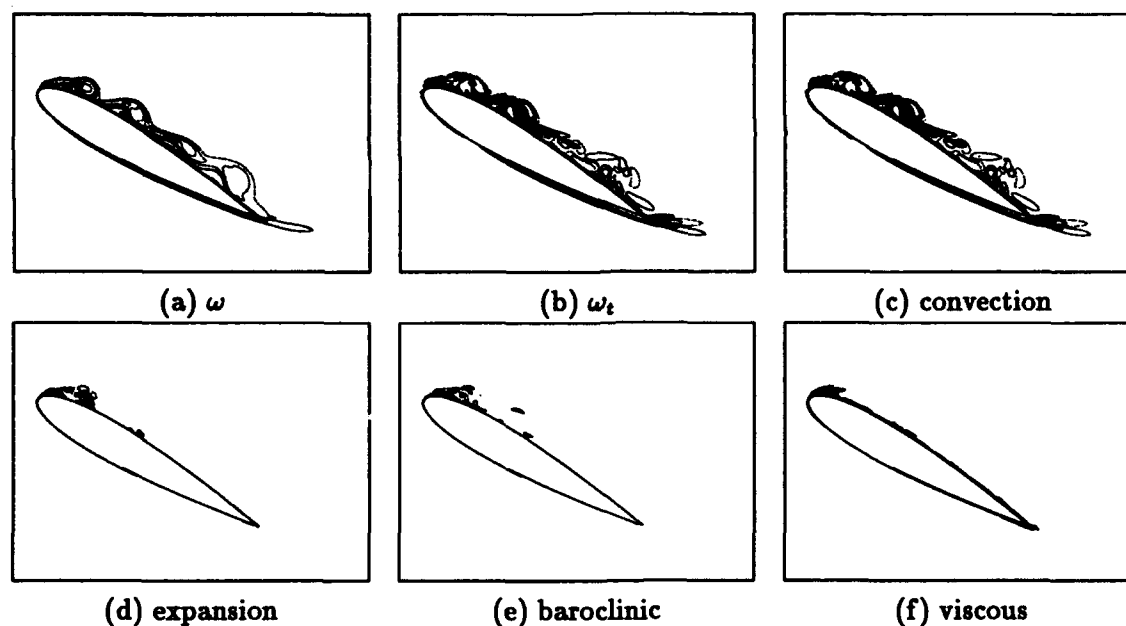


Figure 4.50 Isovorticity contours and contours of vorticity-transport equation terms for 0.05c-blowing case; 361×201 , $v_j = 4.14U_\infty$, $\alpha = 30^\circ$, $\phi = 10^\circ$, $Re_c = 2.4 \times 10^4$, $M_\infty = 0.2$, $\Omega_0^+ = 0.2$

baroclinic-torque term is now significant when compared with the expansion and viscous diffusion terms whereas with the natural case, this was not so. This is due to the larger value of ∇P for the blowing case (Equation 4.2).

Figure 4.51 presents profiles of $\nabla \cdot \mathbf{V}$ and the vorticity-transport-equation terms at $X = 0.10c$. All the vorticity-transport-equation terms are plotted using the same scales for five α' 's.

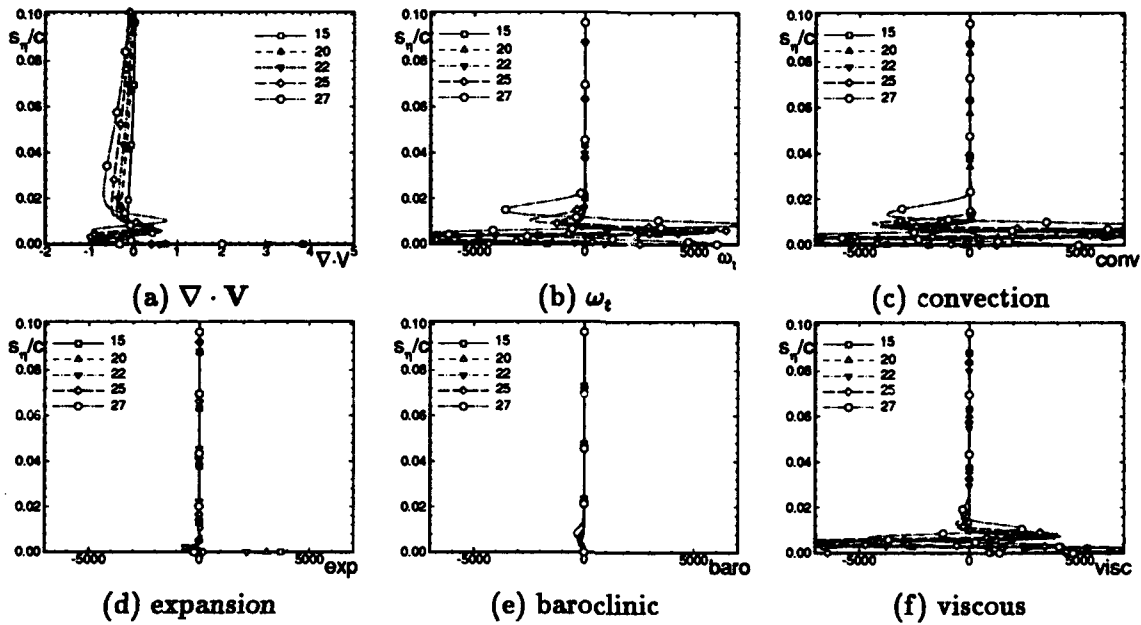


Figure 4.51 Profiles of $\nabla \cdot \mathbf{V}$ and vorticity-transport equation terms for blowing case; 361×201 , $v_j = 4.14U_\infty$, $\alpha = 15^\circ, 20^\circ, 22^\circ, 25^\circ, 27^\circ$, $Re_c = 2.4 \times 10^4$, $M_\infty = 0.2$, $\Omega_0^+ = 0.2$

Comparison of $\nabla \cdot \mathbf{V}$ for the natural (Figure 4.16(a)) and blowing (Figure 4.51(a)) cases indicates that compressibility effects are now present near the surface due to the high-velocity jet. Comparison of the expansion term (Figure 4.51(d)) to the other terms of the vorticity-transport equation demonstrate that compressibility contributes little to the vorticity budget (just as with the natural case).

Very near the surface, in contrast to the natural case (Figure 4.16(f)), the viscous diffusion term is now significant compared to the other terms. However, beyond $0.012c$ above the airfoil at this 10% chord station, this term is insignificant. The baroclinic torque term is not significant at this station, though closer to the slot, it will become more significant due to the large pressure gradients in the vicinity of the high-velocity flow emanating from the slot.

The profiles and contour plots of the vorticity-transport-equation terms have demonstrated the lack of significant compressibility in the solution, a result in agreement with Section 4.2.7.1 results.

4.3 Control via Suction

Motivated by experimental work (Karim and Acharya, 1993) which showed the benefits of active suction control of dynamic stall for a NACA 0012 airfoil, a numerical study was undertaken in order to compare suction control directly to tangential blowing. As previously stated, Karim and Acharya demonstrated that the key to dynamic-stall-vortex-formation suppression is to remove fluid from underneath the leading-edge-originating shear layer at the same rate as the reverse-flowing-fluid-pooling accumulation rate (Section 2.3). Numerical studies were conducted prior to the experimental work of Karim and Acharya, investigating dynamic-stall control via constant suction (Visbal, 1991) and modulated suction (Ghia, et al., 1992), though they did not compare directly with tangential blowing as is done in this section

This section presents results for dynamic-stall control using a suction slot near the leading edge ($X = 0.05c$). First, the effect of suction initiation angle (α_b) is examined. Following that, results from investigation into the effect that varying suction velocity has on suction control are shown. The effect of slot width is presented next, and last, a direct comparison is made between control via suction and blowing. The nominal flow and pitch-rate conditions used throughout this suction study are $M_\infty = 0.2$, $Re_c = 2.4 \times 10^4$, and $\Omega_0^+ = 0.2$.

The 351x201 and 361x201 grids were found to possess satisfactory spatial resolution (Appendix E) for the suction-control study. Based on the tangential-blowing time-step and dissipation-coefficient studies (Appendices C.2 and C.3), the time step and dissipation coefficient chosen for all the suction-case computations are $\Delta t^+ = 0.001$ and $\epsilon_4 = 0.01$.

4.3.1 Effect of Delaying α_b . As is the case for tangential-blowing (Section 4.2.3), effective control is accomplished as long as suction is applied before shear-layer lift-off. For

the natural-case nominal conditions ($M_\infty = 0.2$, $Re_c = 2.4 \times 10^4$, $\Omega_0^+ = 0.2$), this lift off occurs at $\alpha \approx 20^\circ$ (Figure 2.1(a)).

Numerical solutions were obtained for the nominal conditions using a suction velocity of $v_s = 0.697U_\infty$ at the $0.05c$ slot ($s_j = 0.00717c$). As was the case for tangential blowing, the dynamic-stall vortex was similarly suppressed for α_b 's ranging to 20° (Figure 4.52) and not as successfully suppressed when suction begins at $\alpha_b = 22^\circ$. Note that the shear layer

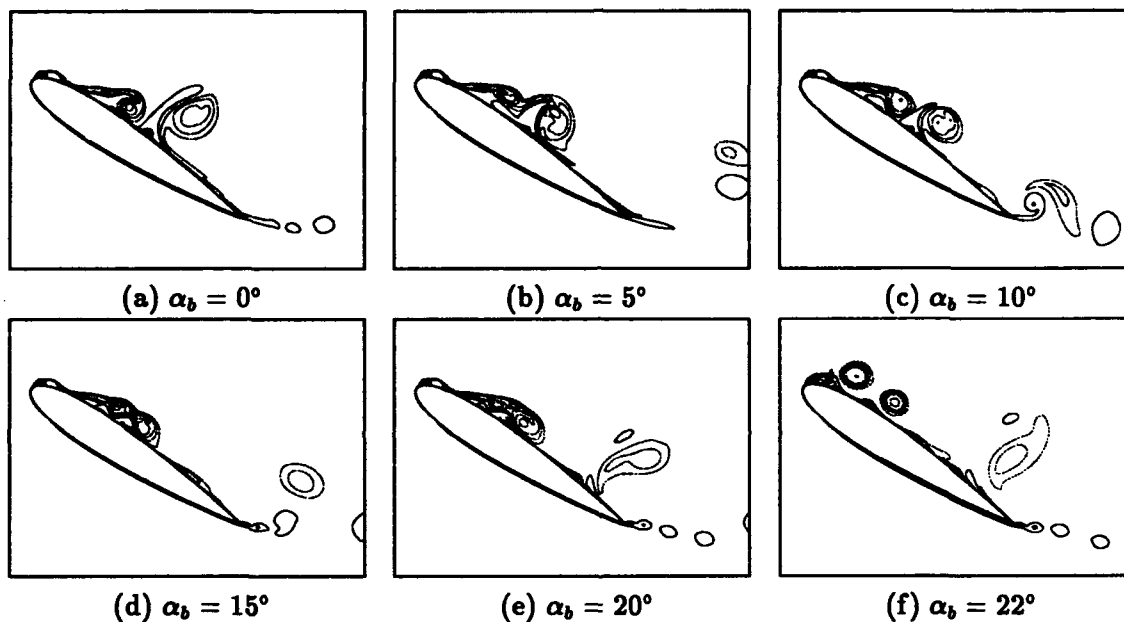


Figure 4.52 Effect of suction α_b on vorticity contours ($\alpha = 33.0^\circ$); 361×201 , $v_s = 0.697U_\infty$, $Re_c = 2.4 \times 10^4$, $M_\infty = 0.2$, $\Omega_0^+ = 0.2$

aft of the leading-edge region is quite different for each suction- α_b case while this is not the case for tangential blowing (Figure 4.34). Blowing produces a strong shear layer which gives a consistent solution along the aft portion of the airfoil. Figure 4.53 illustrates this difference in C_l at the higher α 's.

4.3.2 Suction Velocity Effects. Suction velocity was varied to study its effect on dynamic-stall-vortex-formation control at the $0.05c$ slot. The suction velocity ($v_s = 0.697U_\infty$) used for the slot-grid study (Section E) and the α_b study (Section 4.3.1) is halved and doubled to investigate the effect of suction-velocity variation on the solution.

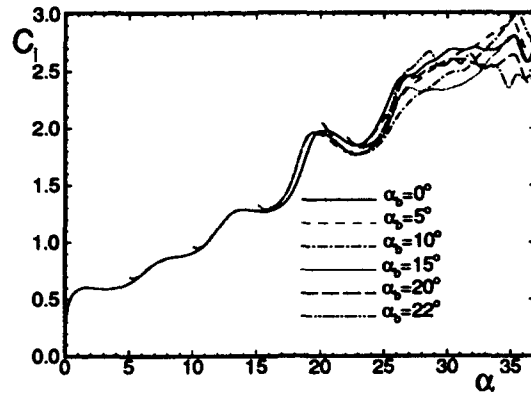


Figure 4.53 Effect of suction at $0.05c$ slot on C_l ; 361×201 , $v_s = 0.697U_\infty$, $Re_c = 2.4 \times 10^4$, $M_\infty = 0.2$, $\Omega_0^+ = 0.2$

Mass-flow rate through the slot for tangential blowing is given by Equation 3.5. For suction, the jet subscripts (j) are exchanged for suction subscripts (s) and the angle at which the fluid enters the slot is considered to be $\phi = 90^\circ$ giving the following mass-flow equation for suction.

$$\dot{m}_s = \rho_s s v_s$$

Assuming $\rho_s = \rho_\infty$ (Section 4.2.1), the mass-flow rates through the $0.00717c$ -wide slot for $v_s/U_\infty = 0.3845, 0.697, 1.394$ are $\dot{m}/(\rho_\infty U_\infty c) = 0.0025, 0.0050, 0.0100$ respectively.

As expected, postponement of the dynamic-stall-vortex formation increases with increased suction rates (Figure 4.54). The α -delay from the three velocities ranges from about 5° to about 16° (compare $\alpha = 22^\circ$ -natural case in Figure 4.30(a) with $v_s = 0.3485U_\infty$ case at $\alpha = 27^\circ$ (Figure 4.54) and with $v_s = 1.394U_\infty$ at $\alpha = 38^\circ$ in (Figure 4.54(d)).

The effect on loading is presented in Figure 4.55. Note that each case begins at $\alpha_b = 5^\circ$ with a discontinuity due to the impulsive start of the suction. Based on the α_b study (Section 4.3.1), this should have no significant effect on the dynamic-stall-vortex formation.

4.3.3 Slot Width Effects. Karim and Acharya (1993) show that as long as the reverse-flowing fluid at the surface is not allowed to pool under the shear layer near the leading edge (Section 2.2), then dynamic-stall-vortex formation will be delayed. They

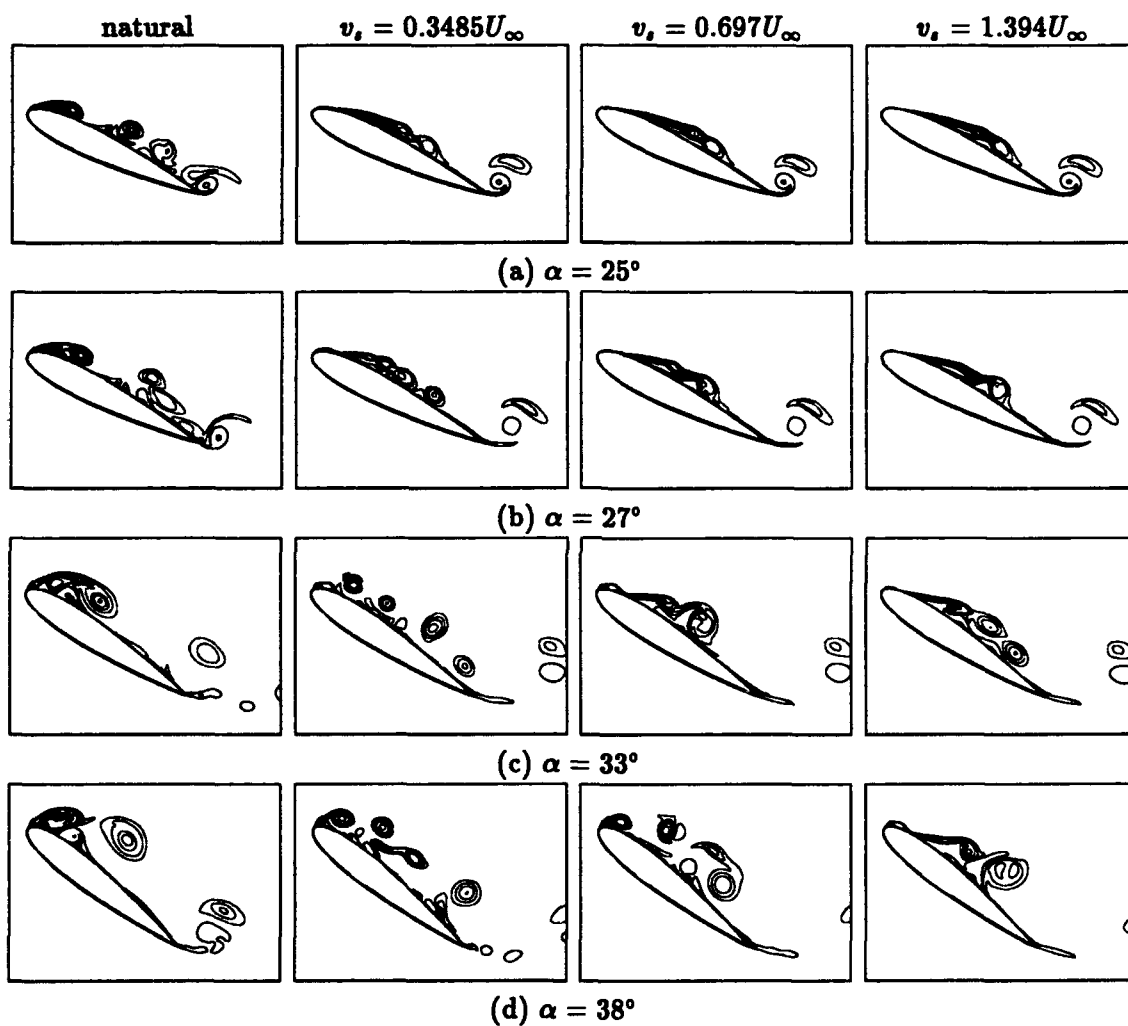


Figure 4.54 Effect of variation in suction velocity at $0.05c$ slot on isovorticity contours; 361×201 , $\alpha_b = 5^\circ$, $Re_c = 2.4 \times 10^4$, $M_\infty = 0.2$, $\Omega_0^+ = 0.2$

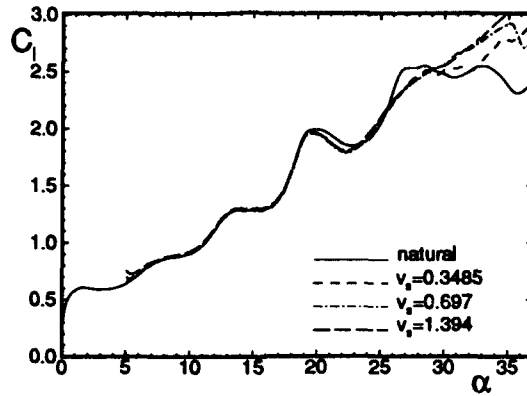


Figure 4.55 Effect of variation in suction velocity at 0.05c slot on C_l ; 361x201, $\alpha_b = 5^\circ$, $Re_c = 2.4 \times 10^4$, $M_\infty = 0.2$, $\Omega_0^+ = 0.2$

varied slot position from $X = 0.02c$ to $0.05c$ and slot width by a factor of four, and neither variation had significant effect on the resulting flow field. They concluded that these results indicate that the suction volume rate is the important parameter, and not suction velocity.

Computations were accomplished to verify this conclusion regarding the effect of slot width. The 361x201 and 351x201 grids ($s_s = 0.00717c$ and $0.0107c$, respectively), each having a slot at $X = 0.05c$, were used in the study. Suction mass flow ($\dot{m} = 0.0052\rho_\infty U_\infty c$) was matched for the two grids assuming $\rho_s = \rho_\infty$. C_l (Figure 4.56) and isovorticity contours

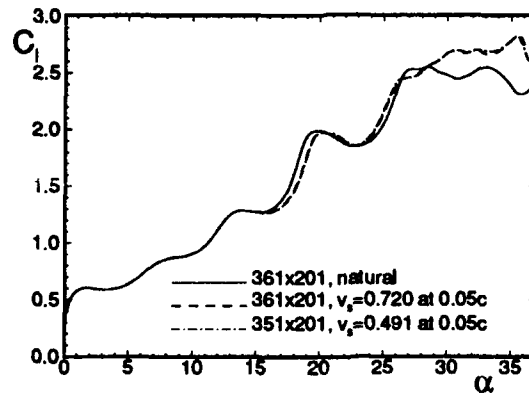


Figure 4.56 Effect of slot-width variation at 0.05c slot on C_l ; $Re_c = 2.4 \times 10^4$, $M_\infty = 0.2$, $\Omega_0^+ = 0.2$

(Figure 4.57) demonstrate nearly identical results for the two different slot widths and thereby confirm the findings of Karim and Acharya.

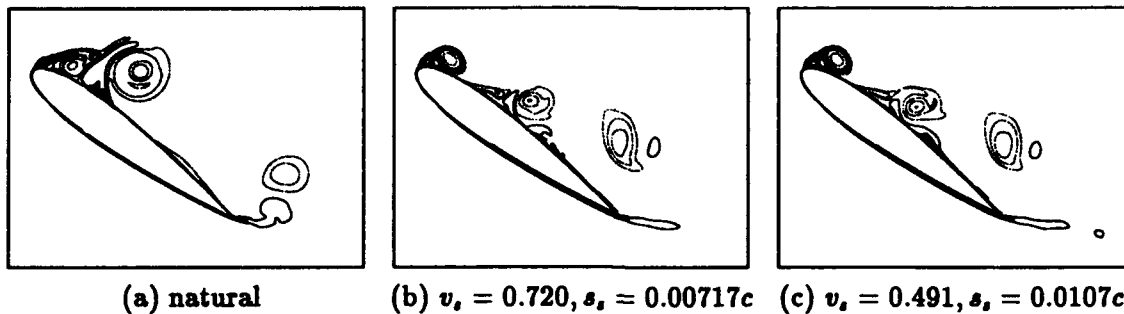


Figure 4.57 Effect of slot-width variation on isovorticity contours ($\alpha = 36.0^\circ$); 361x201 (a, b) and 351x201 (c), $Re_c = 2.4 \times 10^4$, $M_\infty = 0.2$, $\Omega_0^+ = 0.2$

Static-stall control experiments on a 10%-thick wing (Williams, 1961:91) indicated that the optimum slot location is before the 2%-chord position. More investigation needs to be made to see if this static-stall result holds true for the dynamic-stall case.

4.3.4 Suction versus Tangential Blowing. Final implementation of a control technique (e.g., suction, tangential blowing, moving wall (Freymuth, et al., (1989)) into a real-life application will have the usual system-engineering compromises associated with it. The advantages and disadvantages of each approach need to be weighed against each other using the best available data. The purpose of this section is simply to show a direct comparison between suction control and tangential-blowing control. The nominal flow and pitch-rate conditions are used for the comparison ($M_\infty = 0.2$, $Re_c = 2.4 \times 10^4$, $\Omega_0^+ = 0.2$). The time step used is $\Delta t = 0.001$ and the dissipation coefficient is $\epsilon_4 = 0.01$ for the natural and suction cases, and $\epsilon_4 = 0.02$ for the tangential-blowing case. The specified velocities at the $X = 0.05c$, $0.00717c$ -width slot are $v_j = 4.14U_\infty$ and $v_s = 0.720U_\infty$ for blowing and suction, respectively. These velocities result in the same specified slot mass flow ($\dot{m} = 0.0052\rho_\infty U_\infty c$) for blowing and suction, assuming $\rho_j = \rho_s = \rho_\infty$.

Figure 4.58 presents the isovorticity contours of approximately the same dynamic-stall-onset condition (to the nearest degree of α). It is arguable whether or not “dynamic-stall vortex” is still an appropriate term to apply to the vortical formations which occur after leading-edge-shear-layer lift off for the suction-control cases. For example, at $\alpha = 33^\circ$ for the suction case, there is a significant vortex at $X \approx 0.4c$ (Figure 4.58(c)) that may

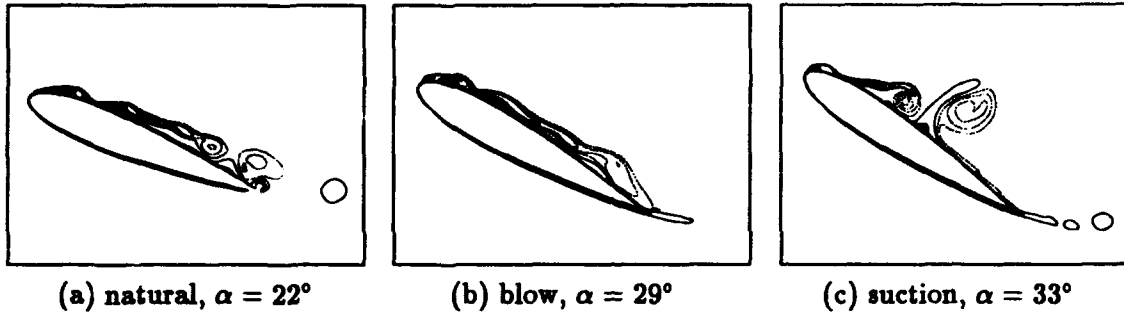


Figure 4.58 Isovorticity contour comparison for natural case, tangential-blowing control, and suction control at $0.05c$ slot; 361×201 , $\dot{m} = 0.0052\rho_\infty U_\infty c$ for blowing and suction, $Re_c = 2.4 \times 10^4$, $M_\infty = 0.2$, $\Omega_0^+ = 0.2$

be akin to a dynamic-stall vortex. However, for describing α -shifts due to control, if the leading-edge vortical flow which forms shortly after shear-layer lift-off near the leading edge is used as a common reference point for stall onset, then for these conditions, tangential blowing delays dynamic-stall-vortex formation by $\sim 7^\circ$ while suction delays it by $\sim 11^\circ$. These offset angles translate into an increase in the dynamic-stall-onset angle by approximately 30% and 50% for blowing and suction control.

The shear layer aft of the dynamic-stall-vortex region is stronger for blowing than for suction and hence remains near the surface up to $\alpha = 30^\circ$ for blowing (Figure 4.59). This behavior has a dramatic effect on the aerodynamic loading. From a comparison of isovorticity contours (Figure 4.59), C_l and C_m plots (Figure 4.60), it is evident that the stronger shear layer over the middle-to-aft section of the airfoil upper surface for blowing results in a reduced trailing-edge-vortex-shedding effect much as the $0.4c$ -blowing did (Section 4.2.1). This stronger shear-layer also translates into slightly greater $C_{l_{max}}$ for the blowing case.

More investigation into high- C_μ tangential-blowing cases (employing the same \dot{m} by using smaller slot widths) is required since the blowing cases are directly dependent on C_μ (Section 4.2.2) and the suction cases are directly dependent on \dot{m} (Section 4.3.2). In addition to investigating higher C_μ cases, there are at least two other questions requiring further study. First, the suction-control experiments (Karim and Acharya, 1993) showed that as Reynolds number increases (or pitch rate decreases at the same Re_c),

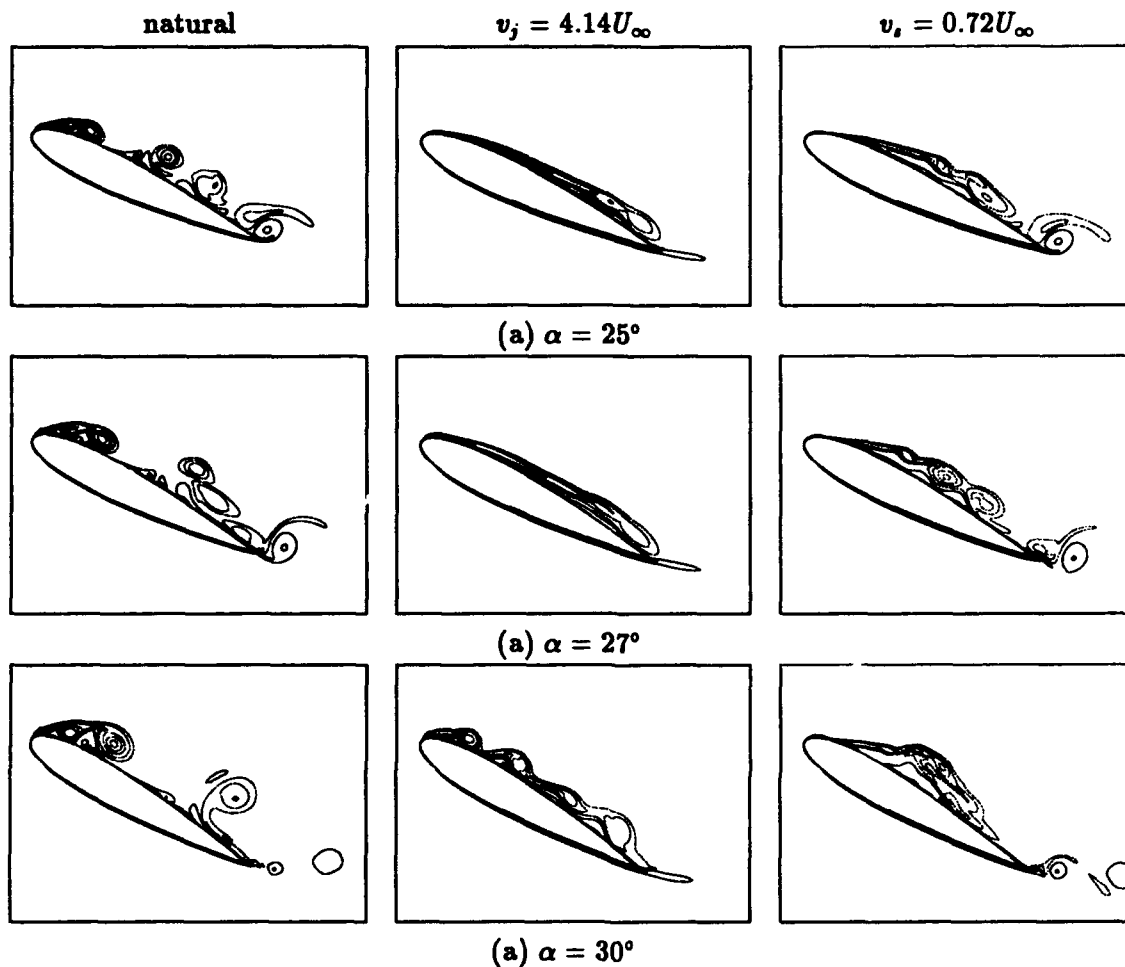


Figure 4.59 Isovorticity contour comparison for natural case, tangential-blowing control, and suction control at $0.05c$ slot over three α 's; 361×201 , $\dot{m} = 0.0052\rho_\infty U_\infty c$ for blowing and suction, $Re_c = 2.4 \times 10^4$, $M_\infty = 0.2$, $\Omega_0^+ = 0.2$

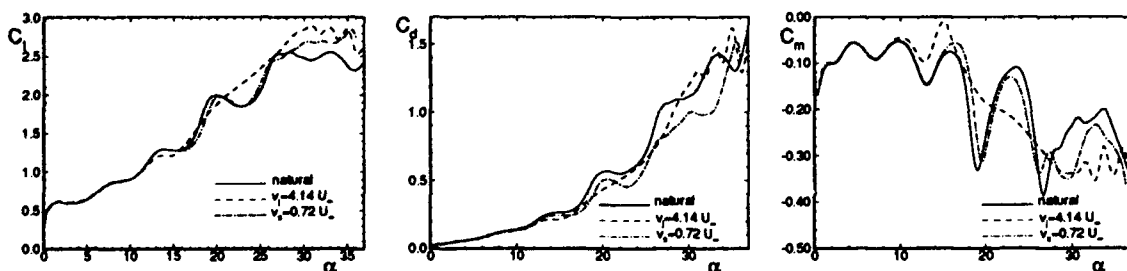


Figure 4.60 C_l , C_d , and C_m (about $X = 0.25c$) comparisons for natural case, tangential-blowing control, and suction control at $0.05c$ slot; 361×201 , $\dot{m} = 0.0052\rho_\infty U_\infty c$ for blowing and suction, $Re_c = 2.4 \times 10^4$, $M_\infty = 0.2$, $\Omega_0^+ = 0.2$

suction control becomes less effective due to the thicker reverse-flow region. Tangential-blowing control for dynamic stall at higher Reynolds numbers needs to be investigated as the tangential-blowing technique may not suffer as much from this reverse-flow region thickness problem.

Second, a certain amount of control over the blowing angle (ϕ) may be possible. For the flow and pitch-rate conditions studied here, as ϕ increased, dynamic-stall control effectiveness decreased (Section 4.2.3). However, for thicker reverse-flow regions that exist at higher Reynolds numbers, there may possibly be some benefit to slightly increasing the blowing angle in order to beneficially affect the thicker reverse-flowing region.

This direct comparison of tangential-blowing and suction control suggests that tangential-blowing control at high- C_{μ} values may be as effective at flight Reynolds numbers as suction. Also, real-life control implementation issues are likely to favor blowing control over suction control (Poisson-Quinton and Lepage, 1961:35-36). Suction control requires the use of large ducts inside wings which take up precious volume often used for fuel. However, blowing control requires very little inner-wing volume as small-diameter high-pressure lines are plumbed to a blowing plenum just under the slot surface. Additionally, the added weight and space required on board for a low-pressure source for suction control compared to using jet-engine compressor bleed air for blowing control makes blowing more attractive as well.

V. Conclusions

The use of tangential blowing to delay the appearance and development of the dynamic stall vortex generated on a NACA 0015 airfoil experiencing constant-rate pitch-up was investigated numerically. The 2-D compressible Navier-Stokes equations were solved using a well-validated, implicit, finite-difference code (Visbal, 1986a) which uses the Beam-Warming algorithm. The computations were made for low-Reynolds number, low-Mach number flow. For the conditions examined, several conclusions are drawn. These conclusions, along with suggested future research opportunities, are enumerated below.

1. Blowing in a nearly tangential sense through a surface slot near the leading edge of an airfoil has numerically been demonstrated to be an effective technique to suppress dynamic stall. As non-dimensional pitch rate (Ω_0^+) is decreased, tangential-blowing control becomes even more effective. By increasing momentum of the flow near the surface, tangential-blowing control delays dynamic-stall-vortex formation as long as the blowing keeps reverse-flowing fluid from pooling under the shear layer near the leading edge.
2. The blowing initiation angle of attack (α_b) has no significant bearing on dynamic-stall-vortex formation so long as α_b is less than the angle at which shear layer lift off occurs ($\alpha \approx 20^\circ$ for the nominal conditions used in this research). Blowing after this angle is ineffective at suppressing dynamic-stall vortex formation (though the dynamic-stall-vortex structure is significantly modified). A pressure plateau which occurs near the leading edge around the lift-off α may be an exploitable characteristic of the dynamic-stall phenomenon that will permit blowing to be delayed until lift-off just begins to occur. Further investigation into this matter is warranted.
3. Blowing in the leading-edge region up-chord of the location where fluid will naturally pool (around $0.18c$ for the nominal conditions) just prior to dynamic-stall-vortex formation gives the greatest delay in dynamic-stall-vortex formation. Tangential blowing through a $0.05c$ slot of the NACA 0015 airfoil delays dynamic-stall-vortex formation to a higher α than blowing at a $0.0c$ slot. Further investigation is needed

to determine if blowing between these locations will produce even greater delays in the angle at which the dynamic-stall vortex forms.

4. For a given blowing angle (ϕ), increasing the jet momentum results in a delay in dynamic-stall vortex formation.
5. A slot-width study established that for a given blowing angle, tangential-blowing-control effectiveness for dynamic-stall is directly related to the blowing momentum coefficient (C_μ), as is the case with static-stall control using nearly tangential blowing (Lachmann, 1961).
6. A direct comparison between tangential-blowing and suction control for the same mass flow rate per unit span (\dot{m}) and slot width (and thus, the same C_μ) showed that suction-control delays dynamic-stall-vortex formation to a higher α (50% α -delay for suction, 30% for blowing). However, since tangential-blowing-control effectiveness depends directly on C_μ (for a given ϕ , increasing C_μ delays dynamic-stall-vortex formation) and not \dot{m} as suction control does (Karim and Acharya, 1993), further investigation of blowing at higher C_μ 's for a fixed \dot{m} (smaller slot widths) is required.
7. Significant sensitivity to jet orientation angle was observed. For the same C_μ , a smaller jet-blowing angle (ϕ) delays dynamic-stall-vortex formation over the range of ϕ 's considered. The slot blowing velocity is a controlled parameter for the computations whereas slot plenum pressure is specified in experiments. Experiments on jet-blowing-angle behavior during pitch-up for a slot located in a region possessing a naturally adverse pressure gradient (say, at $X = 0.05c$) are needed to assess the constant- ϕ assumption made in the computations. Furthermore, experiments are required to discover if ϕ can be sufficiently controlled to take advantage of lower- ϕ -blowing benefits for laminar boundary layers, and potential greater- ϕ -blowing benefits for turbulent boundary layers.
8. Pulsed blowing was applied at a $0.0c$ slot for experimentally-determined frequencies deemed most effective for controlling the static-stall separation region (Lovato, 1992). This technique is less effective than simply constant-blowing control. Pulsed blowing does not significantly delay dynamic-stall onset because it does not affect

the pool of reverse-flowing fluid; however, pulsing does alter the structure of the shear layer once the dynamic-stall vortex forms. Compared to constant blowing, pulsed blowing produces additional vortices on the leeward side of the airfoil aft of the leading-edge region. The possible benefits of using this technique to control the flow over the airfoil after the dynamic-stall vortex is formed is beyond the scope of this work and was not investigated.

9. Aerodynamic-loads dependence on the initial condition (taken from the time-periodic solution for $\alpha = 0^\circ$) was demonstrated as the timing of events is dictated to some degree by the initial state of the trailing edge flow. A similar dependence was observed when the airfoil-exponential-acceleration time constant (t_0^+) was varied. Both phenomena stem from the unsteady trailing-edge vortex shedding which affects a large aft portion of the airfoil. At higher non-dimensional pitch rates (e.g., $\Omega_0 = 0.6$), the behavior vanishes due to dominant motion-history effects (as explained by Koochesfahani and Smiljanovski (1993)). It is therefore appropriate to document the initial condition (e.g., give the point in the time-periodic C_l curve at which pitch-up begins) and acceleration profile used to achieve the constant non-dimensional pitch rate for low Reynolds number simulations of dynamic stall, particularly for low pitch rates where this effect is more pronounced. However, initial condition and t_0^+ variation (as long as dynamic-stall onset occurs after $t^+ = t_0^+$) do not affect dynamic-stall-vortex formation.
10. A term-by-term examination of the vorticity transport equation showed that the transport of vorticity is overwhelmingly dominated by convection. The baroclinic-torque and expansion terms are small, suggesting that for the Mach number and pitch rate examined ($M_\infty = 0.2$ and $\Omega_0^+ = 0.2$, respectively), the flow is essentially incompressible.
11. Computations at $M_\infty = 0.1, 0.05$ and 0.2 were qualitatively similar, suggesting that, for the conditions considered, simulations at $M_\infty = 0.2$ are suitable for direct comparison with low-speed experimental data. However, slight compressibility effects begin to appear (in the form of a lower dynamic-stall-vortex suction peak and a change in events timing) as the dynamic-stall-vortex begins to form. These computations also

demonstrated the feasibility of solving the incompressible-flow dynamic-stall problem using a compressible code rather than using the pseudocompressible technique (which would require approximately 10× the computer time to solve the same problem).

Appendix A. Grid Constants and Flux Jacobians

This appendix contains grid and reference-dependent constants a , b , and c used in flux terms of Equation 3.1 and flux Jacobian terms for compressible, laminar flow (Visbal, 1986a).

A.1 Grid Constants

$$b_1 = \frac{4}{3}\xi_x^2 + \xi_y^2 \quad b_2 = \frac{1}{3}\xi_x\xi_y \quad b_3 = \xi_x^2 + \frac{4}{3}\xi_y^2 \quad b_4 = \frac{c_p}{Pr}(\xi_x^2 + \xi_y^2)$$

$$c_1 = \frac{4}{3}\xi_x\eta_x + \xi_y\eta_y \quad c_2 = -\frac{2}{3}\xi_x\eta_y + \xi_y\eta_x \quad c_3 = \xi_x\eta_y - \frac{2}{3}\xi_y\eta_x$$

$$c_4 = \xi_x\eta_x + \frac{4}{3}\xi_y\eta_y \quad c_5 = \frac{c_p}{Pr}(\xi_x\eta_x + \xi_y\eta_y)$$

$$d_1 = \frac{4}{3}\eta_x^2 + \eta_y^2 \quad d_2 = \frac{1}{3}\eta_x\eta_y \quad d_3 = \eta_x^2 + \frac{4}{3}\eta_y^2 \quad d_4 = \frac{c_p}{Pr}(\eta_x^2 + \eta_y^2)$$

A.2 Flux Jacobians

$$A = \begin{pmatrix} 0 & \xi_x & \xi_y & 0 \\ \xi_x\phi - u\bar{U} & \bar{U} - (\gamma - 2)\xi_x u & -(\gamma - 1)\xi_x v + \xi_y u & (\gamma - 1)\xi_x \\ \xi_y\phi - v\bar{U} & \xi_x v - (\gamma - 1)\xi_y u & \bar{U} - (\gamma - 2)\xi_y v & (\gamma - 1)\xi_y \\ (2\phi - \gamma e)\bar{U} & (\gamma e - \phi)\xi_x - (\gamma - 1)u\bar{U} & (\gamma e - \phi)\xi_y - (\gamma - 1)v\bar{U} & \gamma\bar{U} \end{pmatrix}$$

$$B = \begin{pmatrix} 0 & \eta_x & \eta_y & 0 \\ \eta_x\phi - u\bar{V} & \bar{V} - (\gamma - 2)\eta_x u & -(\gamma - 1)\eta_x v + \eta_y u & (\gamma - 1)\eta_x \\ \eta_y\phi - v\bar{V} & \eta_x v - (\gamma - 1)\eta_y u & \bar{V} - (\gamma - 2)\eta_y v & (\gamma - 1)\eta_y \\ (2\phi - \gamma e)\bar{V} & (\gamma e - \phi)\eta_x - (\gamma - 1)u\bar{V} & (\gamma e - \phi)\eta_y - (\gamma - 1)v\bar{V} & \gamma\bar{V} \end{pmatrix}$$

$$\phi = \frac{1}{2}(\gamma - 1)(u^2 + v^2) \quad \bar{U} = \xi_x + \xi_x u + \xi_y v \quad \bar{V} = \eta_x + \eta_x u + \eta_y v$$

$$R = \frac{\mu}{\rho} \begin{pmatrix} 0 & 0 & 0 & 0 \\ -(b_1 u + b_2 v) & b_1 & b_2 & 0 \\ -(b_2 u + b_3 v) & b_2 & b_3 & 0 \\ \Psi & (b_1 - b_4 \Gamma)u + b_2 v & b_2 u + (b_3 - b_4 \Gamma)v & b_4 \Gamma \end{pmatrix}$$

$$S = \frac{\mu}{\rho} \begin{pmatrix} 0 & 0 & 0 & 0 \\ -(d_1 u + d_2 v) & d_1 & d_2 & 0 \\ -(d_2 u + d_3 v) & d_2 & d_3 & 0 \\ \Psi & (d_1 - d_4 \Gamma)u + d_2 v & d_2 u + (d_3 - d_4 \Gamma)v & d_4 \Gamma \end{pmatrix}$$

$$\Psi \equiv -(b_1 u^2 + 2b_2 uv + b_3 v^2) + b_4 \Gamma(u^2 + v^2 - e), \quad \Gamma \equiv \gamma(\gamma - 1)$$

Appendix B. Natural Numerical Artifacts Effects

As with any numerical analysis, great care must be taken to ensure the accuracy of the computed results. Application of numerical schemes to the discretized form of the governing equations introduces numerical effects that need to be properly identified in order that they not mask the real physics of the problem. Previous work (Rizzetta and Visbal, 1992; Visbal, 1991; Visbal and Shang, 1989; Visbal, 1986b) is relied on for the selection of implicit boundary conditions and far-field boundary position for the work contained in this publication, thereby alleviating the need for studies of these issues. Along with addressing the usual concerns regarding temporal and spatial discretization errors via time-step and grid studies, the sensitivity of the computed solutions to the amount of numerical damping is also addressed. The sensitivity of the computed solution to the aforementioned numerical artifacts is first evaluated for a single flow and pitch-rate condition given by $M_\infty = 0.2$, $Re_c = 2.4 \times 10^4$, and $\Omega_0^+ = 0.2$. For a given flow and pitch-rate condition, the first step in this rigorous sensitivity study is to start with the most important parameter to be varied (spatial discretization) while fixing the two less sensitive variables at nominal values. Once the solution is deemed accurate enough for the chosen grid, the next step is to vary the temporal discretization while fixing the least sensitive parameter (dissipation coefficient) until the solution is independent of the temporal increment. Using this time increment and grid, the final step is the determination of the value of the dissipation coefficient for which the computed solution no longer varies. Thus, the order of presentation (spatial discretization, temporal discretization, numerical damping) in the following three sections coincides with the sensitivity-study-strategy order employed.

B.1 Grid Study

Six of the O-grids listed in Table 4.1 and used in the grid study for this research are shown in Figure 4.1. High grid density is observable at $X = 0.4c$ (Figure 4.1 (a), (d) – (f)), $X = 0.2c$ (Figure 4.1 (a)), $X = 0.05c$ (Figure 4.1 (b), (c)), and $X = 0.0c$ (all meshes). Stream-wise-direction clustering of points is applied in slotted regions for control cases (Sections 4.2 and 4.3). The 385x201 grid (Figure 4.1 (d)) has minimum ξ - and η -spacings

of $0.000082c$ (at the rounded trailing edge) and $0.00005c$ (at the surface), respectively. For nominal flow conditions ($M_\infty = 0.2$, $Re_c = 2.4 \times 10^4$), between 60 – 70 grid points are in the boundary layer at $X = 0.5c$ for $\alpha = 0^\circ$. Nominal choices of time step and explicit damping coefficient for this grid study are $\Delta t^+ = 0.001$ and $\epsilon_4 = 0.01$. First, consideration is given to the ξ -spacing around the airfoil (ξ - and η -spacing refinements could not be accomplished simultaneously due to resource constraints).

A comparison of C_l - α curves, as well as drag polars, indicates that there is good agreement between three solutions (343x201, 361x201, 505x201 grids) to an angle of attack of 27° (Figure B.1). The isovorticity contours for these three grids exhibit qualitatively

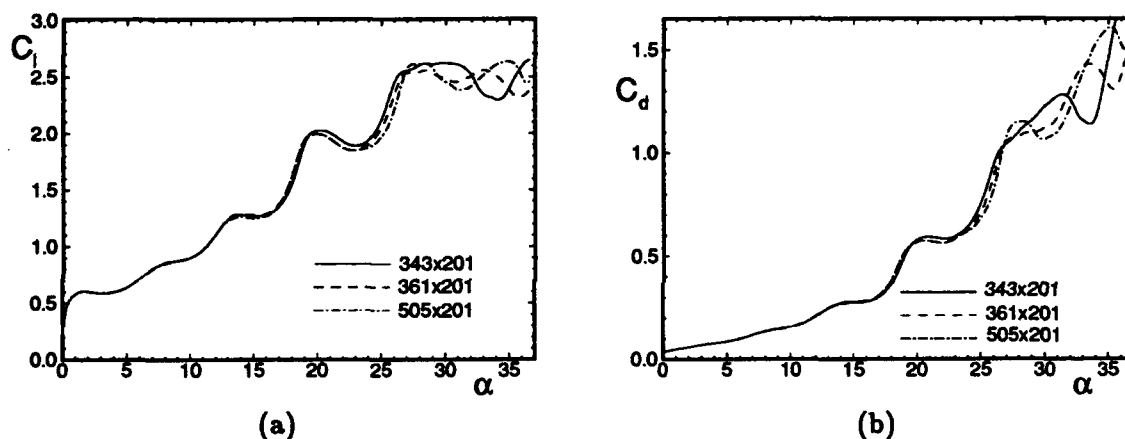


Figure B.1 Effect of mesh refinement on C_l and C_d ; $Re_c = 2.4 \times 10^4$, $M_\infty = 0.2$, $\Omega_0^+ = 0.2$

good agreement to $\alpha \approx 25^\circ$ (Figure B.2(a)), after which the 343x201 grid is too sparse to fully capture the physics in the region of the dynamic stall vortex which has begun to lift away from the airfoil surface to a more sparsely defined region of the grid (Figure B.2(b)). The first significant difference that appears in the pressure coefficient plots (Figure B.3) occurs at $\alpha = 20^\circ$. At this angle of attack, the steep adverse pressure gradient at $X \approx 0.2c$, where the dynamic stall vortex begins to form, is not captured as well by the sparser 343x201 grid. At $\alpha = 22^\circ$, the suction peak associated with the dynamic stall vortex ($X \approx 0.2c$) is highest and sharpest for the most refined grid (Figure B.3(b)), though the 361x201 grid comes considerably closer to the 505x201-grid result than does the 343x201 grid. The solutions for the three more refined grids (361x201, 385x201, 505x201) are

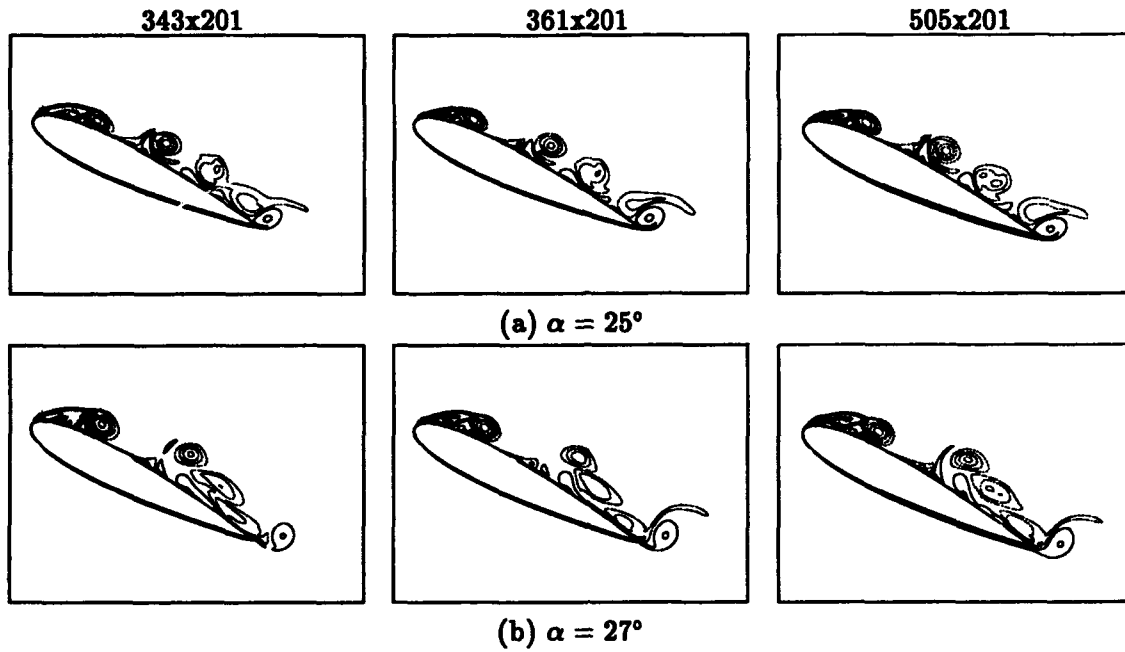


Figure B.2 Effect of mesh refinement on vorticity contours; $Re_c = 2.4 \times 10^4$, $M_\infty = 0.2$, $\Omega_0^+ = 0.2$

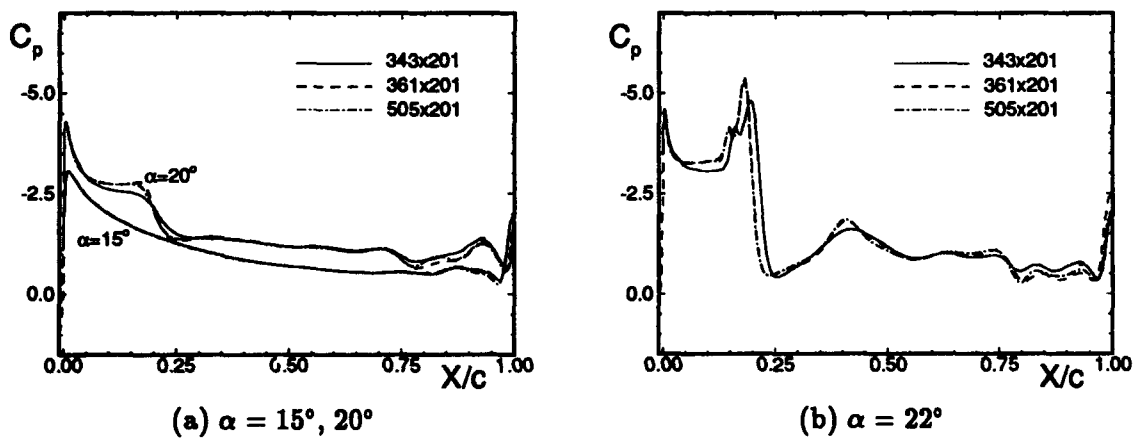


Figure B.3 Effect of mesh refinement on C_p ; $Re_c = 2.4 \times 10^4$, $M_\infty = 0.2$, $\Omega_0^+ = 0.2$

essentially the same to $\alpha = 27^\circ$ as evidenced by the C_l , C_d (Figure B.4) and C_p plots (Figure B.5). Observe that differences between simulations is most evident in C_p while field vorticity and integrated quantities (C_l and C_d) information tend to be less sensitive measures of solution accuracy.

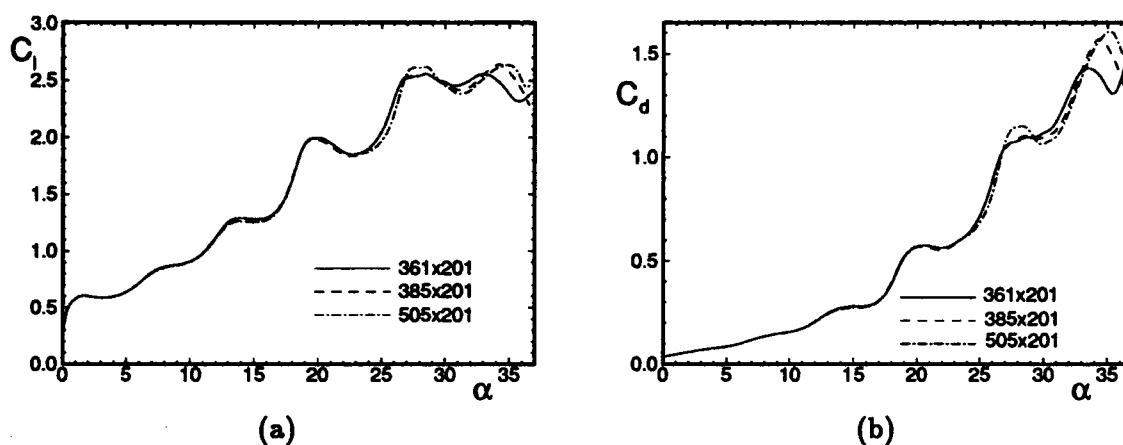


Figure B.4 Comparison of C_l and C_d for 361x201, 385x201, and 505x201 grids; $Re_c = 2.4 \times 10^4$, $M_\infty = 0.2$, $\Omega_0^+ = 0.2$

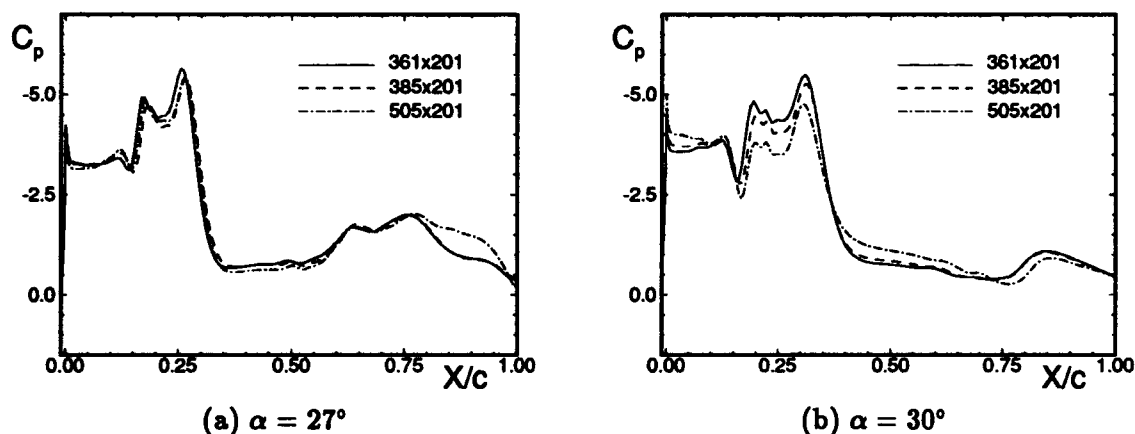


Figure B.5 Comparison of C_p for 361x201, 385x201, and 505x201 grids; $Re_c = 2.4 \times 10^4$, $M_\infty = 0.2$, $\Omega_0^+ = 0.2$

The 351x201 and 361x201 grids differ only near the 0.05c slot. They each use 21 points to define the slot region, but the 361x201 grid slot width is 0.00717c while the 351x201 grid has a slot width of 0.0107c. The additional 10 ξ -direction points are present

about the $0.05c$ slot for the 361×201 grid to maintain proper metric smoothness in the slot region. These two grids give essentially identical solutions (Figure B.6).

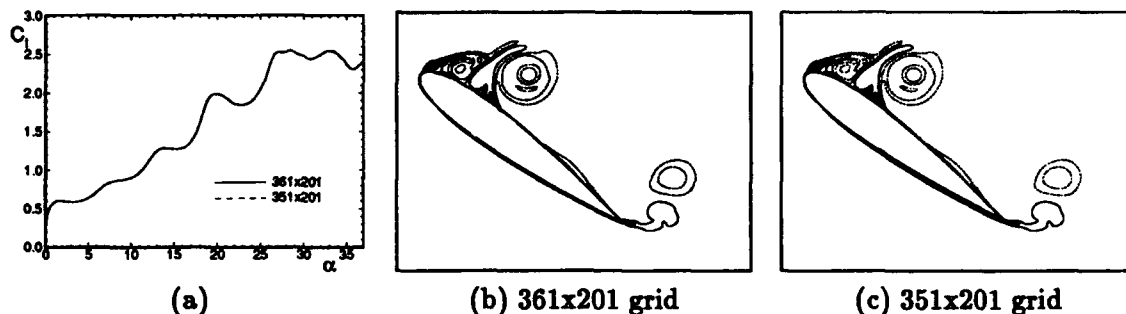


Figure B.6 Effect of slot width variation on C_l and vorticity contours ($\alpha = 36^\circ$); $Re_c = 2.4 \times 10^4$, $M_\infty = 0.2$, $\Omega_0^+ = 0.2$

To ensure that 201 grid points normal to the airfoil is adequate, solutions were also generated for 385×151 and 385×301 meshes and compared with those obtained for the 385×201 mesh. The normal-grid-point distribution (η -direction) is shown in Figure B.7 along with C_l versus α for these three grids. C_l is in excellent agreement for all three grids

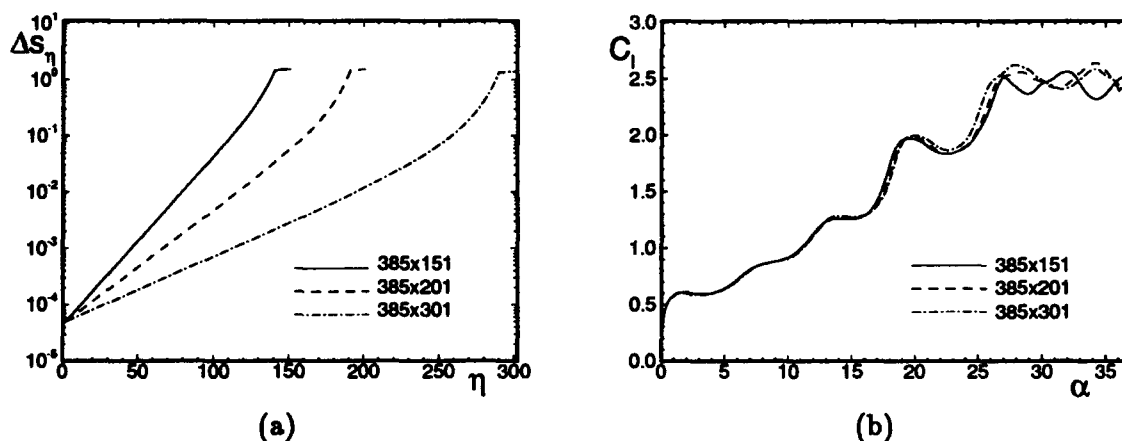


Figure B.7 Grid refinement in the normal direction and its effect on C_l ; $Re_c = 2.4 \times 10^4$, $M_\infty = 0.2$, $\Omega_0^+ = 0.2$

to an angle of attack of 25° and to an angle of attack of 36° for the 201- and 301-normal-spaced grids, demonstrating that 201 grid points offers adequate spatial resolution in the η -direction. As the region of α in the stall-onset range was of principal concern (for the flow conditions considered, this occurs around $20^\circ - 22^\circ$ (Figure 2.2) for the natural case at

$\Omega_0^+ = 0.2$), the 385x201 and 361x201 grids were used for the majority of the natural-case analysis.

B.2 Temporal Discretization Study

The sensitivity of the computed solutions to temporal increment was investigated on the 385x201 and 505x201 meshes. As previously mentioned, the nominal time step used for the grid study of Section B.1 was 0.001. Based on C_l plots, 385x201-grid solutions were determined to be relatively insensitive to time step to $\alpha = 33^\circ$ so long as the time step remained at or below 0.001 (Figure B.8). Isovorticity contours are quite similar far

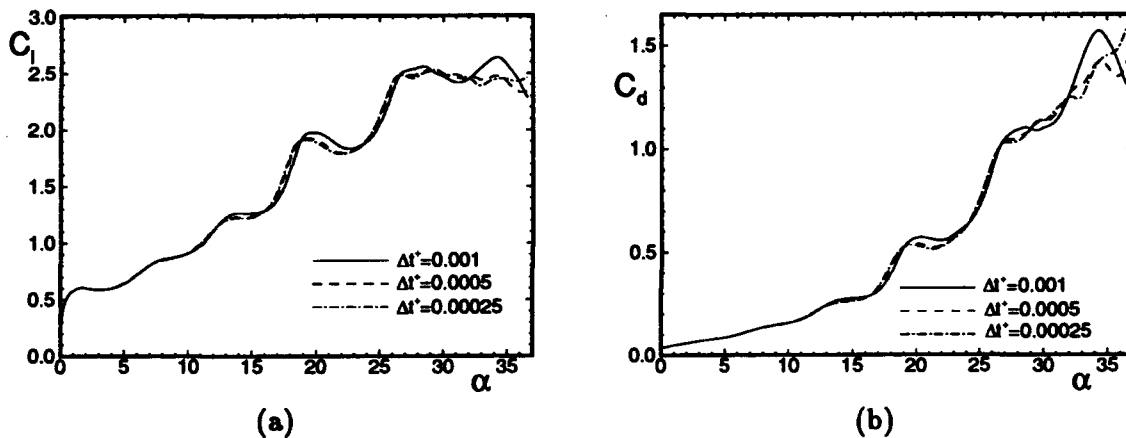


Figure B.8 Effect of time step on C_l and C_d ; 385x201, $Re_c = 2.4 \times 10^4$, $M_\infty = 0.2$, $\Omega_0^+ = 0.2$

past stall onset up to $\alpha = 27^\circ$ (Figure B.9) for all time steps, after which the temporal inaccuracies begin to grow. C_p plots also show close agreement to $\alpha = 27^\circ$ (Figure B.10).

Since finer meshes typically dictate smaller temporal increments, the effect of time step for the 505x201 grid was also examined to ensure that sufficiently accurate results were used in the grid study (Section B.1) for determining solution independence to spatial discretization errors. For $\Delta t^+ = 0.001$ and 0.0005, C_l and C_d show good agreement to $\alpha = 25^\circ$ (Figure B.11), an angle of attack at which the dynamic-stall vortex is well formed (Figure B.12(a)). Note that the C_p plot and isovorticity contours show acceptable agreement for these two time steps even out to $\alpha = 30^\circ$ (Figure B.12(b)), however a

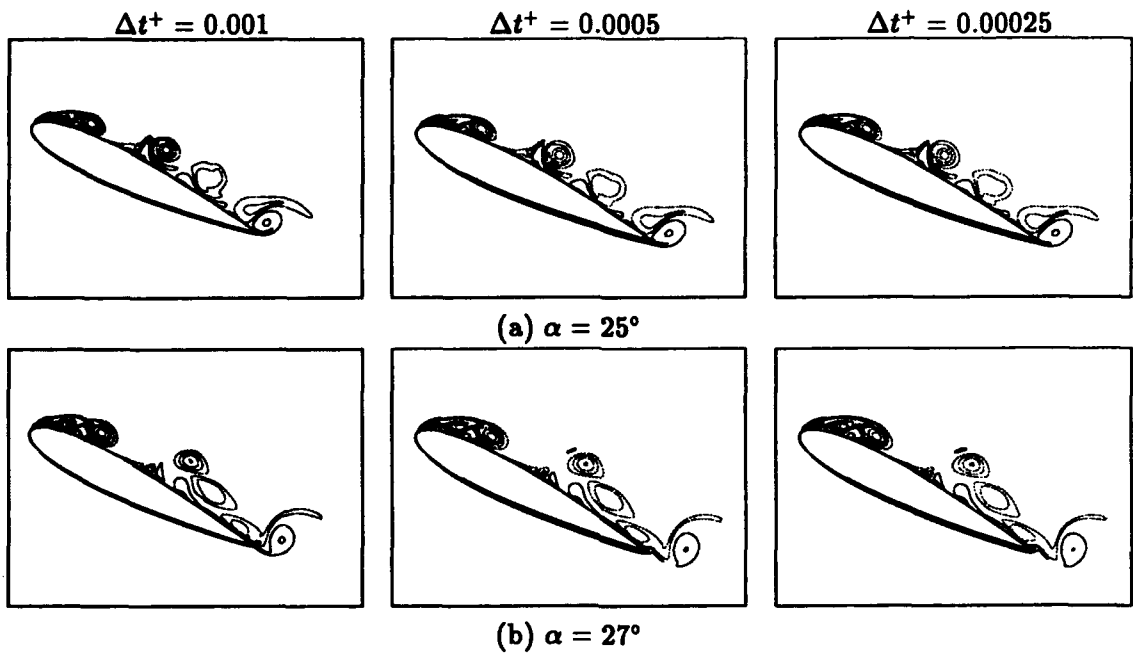


Figure B.9 Effect of time step on vorticity contours; 385x201, $Re_c = 2.4 \times 10^4$, $M_\infty = 0.2$, $\Omega_0^+ = 0.2$

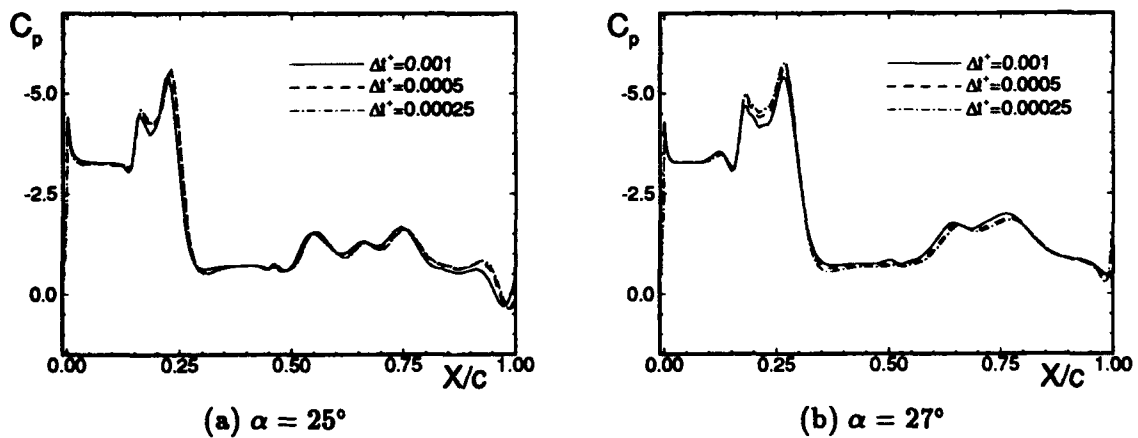


Figure B.10 Effect of time step on C_p ; 385x201, $Re_c = 2.4 \times 10^4$, $M_\infty = 0.2$, $\Omega_0^+ = 0.2$

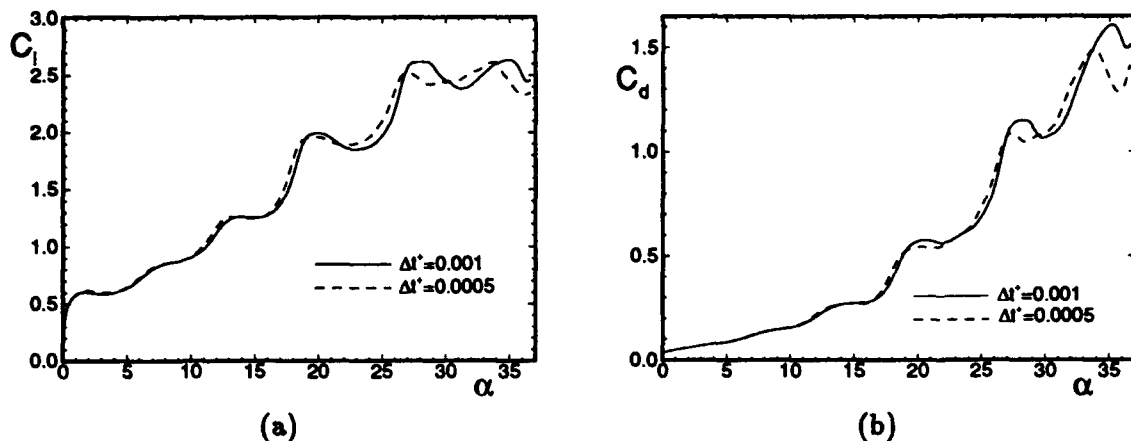


Figure B.11 Effect of time step on C_l and C_d ; 505x201, $Re_c = 2.4 \times 10^4$, $M_\infty = 0.2$, $\Omega_0^+ = 0.2$

large disagreement is evident at $\alpha = 33^\circ$ (Figure B.12(c)). Based on this time-step study, $\Delta t^+ = 0.001$ is a small enough time step for the 505x201 grid when studying dynamic-stall onset for these pitch-rate and flow conditions.

B.3 Dissipation Coefficient Study

Numerical smoothing is necessary for the Beam-Warming algorithm to control oscillations which arise from the discretization of governing equations with central differences (central differences are not dissipative (Pullium, 1986)). Thus, fourth-order terms (which are dissipative in nature) are added to the scheme in order to damp out the short wavelengths and to keep the scheme spatially second-order accurate. The effect of a variation in the amount of this numerical smoothing was examined for two grids used for the majority of the control study (385x201 and 361x201). As previously indicated, the nominal explicit damping coefficient used for the grid study (Section B.1) and time-step study (Section B.2) was $\epsilon_4 = 0.01$. Figures B.13 and B.14 show the minor effect on C_l of halving and doubling ϵ_4 for the 385x201 and 361x201 grids, respectively. As seen in these figures, all three values for the smoothing factors were found to produce essentially the same result well beyond the angle of attack at which the dynamic-stall vortex is formed. Thus the nominal value of $\epsilon_4 = 0.01$ was selected for most of the study (the notable exception being the need to increase ϵ_4 when high blowing rates are used, which is addressed in Section C.3).

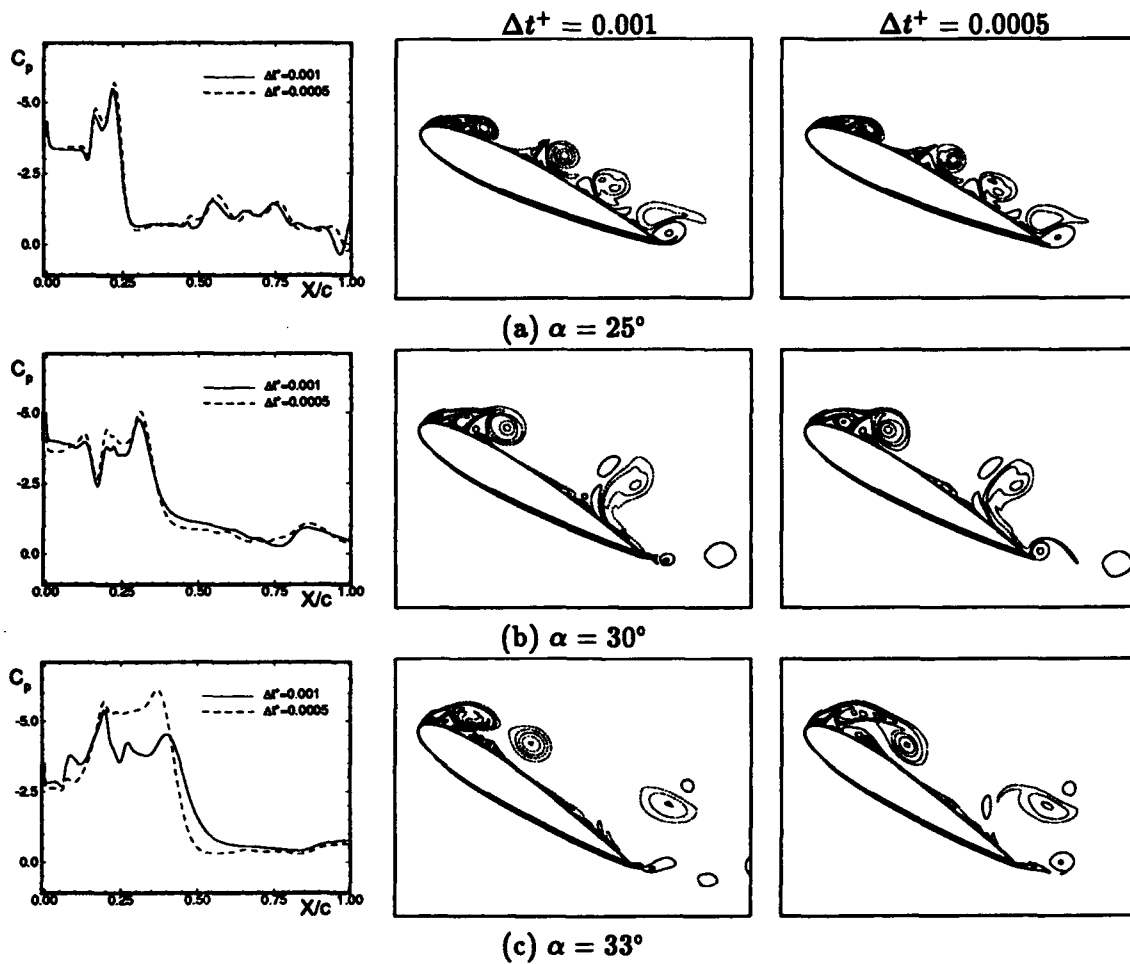


Figure B.12 Effect of time step on C_p and vorticity contours; 505×201 , $Re_c = 2.4 \times 10^4$, $M_\infty = 0.2$, $\Omega_0^+ = 0.2$

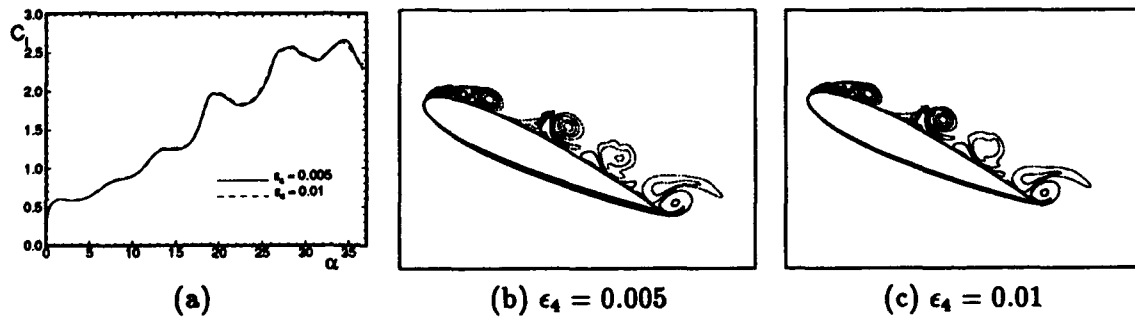


Figure B.13 Effect of halving dissipation coefficient on C_i and isovorticity contours; 385×201 , $\alpha = 25^\circ$, $Re_c = 2.4 \times 10^4$, $M_\infty = 0.2$, $\Omega_0^+ = 0.2$

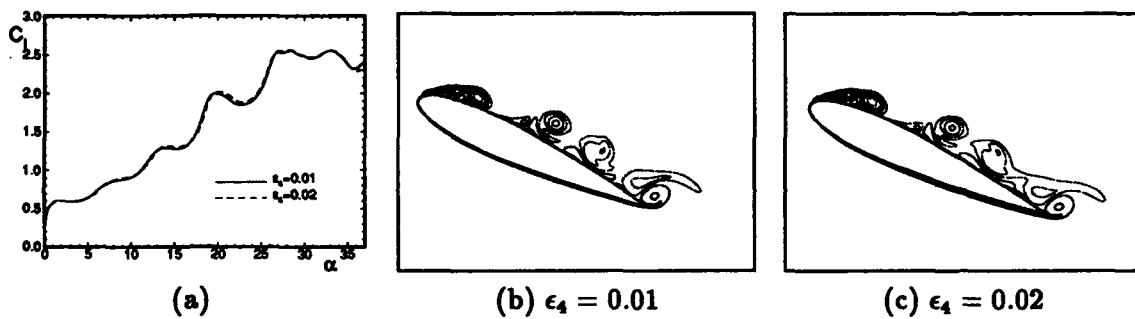


Figure B.14 Effect of doubling dissipation coefficient on C_f and isovorticity contours; 361×201 , $\alpha = 25^\circ$, $Re_c = 2.4 \times 10^4$, $M_\infty = 0.2$, $\Omega_0^+ = 0.2$

Appendix C. Tangential Blowing Numerical Artifacts Effects

The study conducted for the natural case (Section B) to insure that the dynamic-stall physics are not masked by the numerical inaccuracies introduced by the discretization of the governing equations lays a strong foundation for this section. The introduction of tangential blowing necessitates that additional investigations be conducted to insure that the spatial and temporal discretizations along with the dissipation coefficient selected for the natural case are still valid.

C.1 Global and Slot Grid Study

Two grid issues are addressed in this section: 1) the effect that tangential blowing has on solution accuracy and 2) the effect that tangential blowing in conjunction with slot grid refinement has on solution accuracy. The $0.0c$ slot has a width of $0.0105c$ as does the $0.4c$ slot, while the $0.05c$ slot has widths of $0.0107c$ and $0.00717c$. Unless otherwise noted, for the blowing part of the grid study presented in this section, the blowing angle and jet velocity were fixed at nominal values of $\phi = 10^\circ$ and $v_j = 2.83U_\infty$, respectively, and the slot velocity profile was a uniform, constant profile.

Solutions for four grids (Figure 4.1(a), (c), (d), (f)) were computed employing tangential blowing at the airfoil leading edge. The lift- and pressure-coefficient plots along with the isovorticity-contour plots shown in Figures C.1 and C.2 demonstrate that well beyond stall onset, all four grids are in close agreement. As in the natural case (Section B.1), the 351×201 grid shows nearly identical agreement with the 361×201 grid for blowing at $0.0c$ (Figure C.3). Three of the grids (Figure 4.1(a), (d), (f)) which possess clustered grid points at the $0.4c$ -slot location also demonstrate excellent solution agreement beyond stall onset (Figures C.4 and C.5). These results indicate that the grids shown to be accurate in the natural case (Section B.1) are also accurate for the same pitch-rate and flow conditions when the no-slip boundary condition at the airfoil surface is modified at the slot locations to simulate nearly-tangential blowing.

Though the results shown in Figures C.1– C.5 demonstrate the global-grid accuracy for the nominal blowing case, they do not necessarily prove that the grid is locally accurate

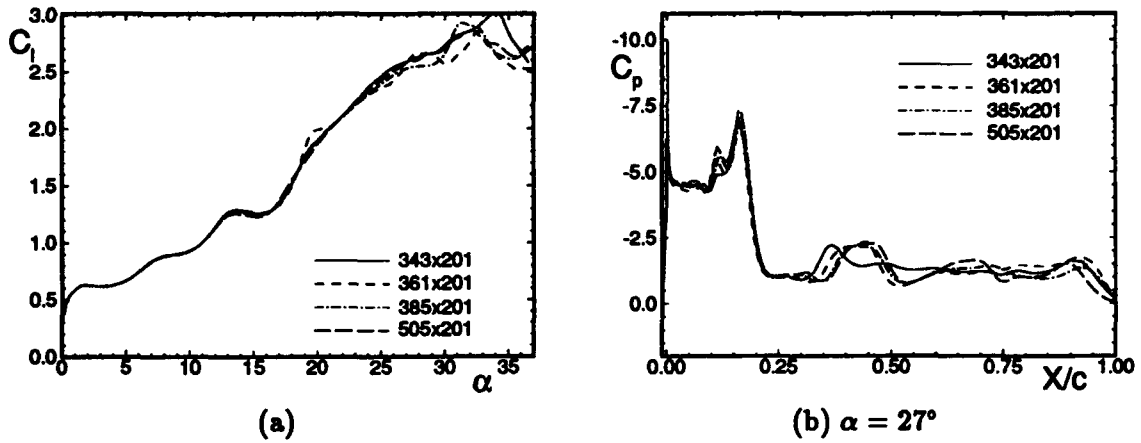


Figure C.1 Effect of tangential blowing at $0.0c$ slot on C_l and C_p ; $v_j = 2.83U_\infty$, $\phi = 10^\circ$, $Re_c = 2.4 \times 10^4$, $M_\infty = 0.2$, $\Omega_0^+ = 0.2$

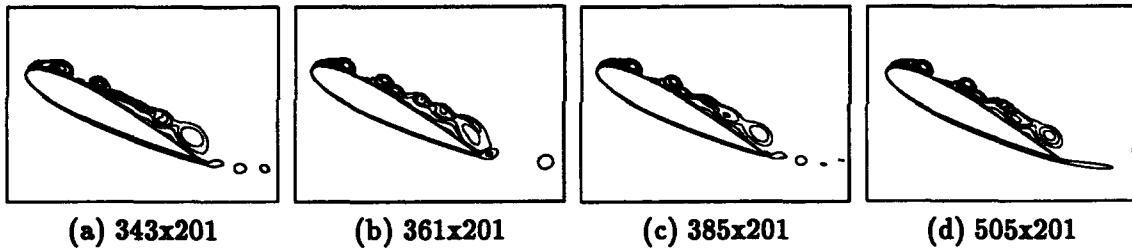


Figure C.2 Effect of tangential blowing at $0.0c$ on isovorticity contours; $v_j = 2.83U_\infty$, $\phi = 10^\circ$, $\alpha = 27^\circ$, $Re_c = 2.4 \times 10^4$, $M_\infty = 0.2$, $\Omega_0^+ = 0.2$

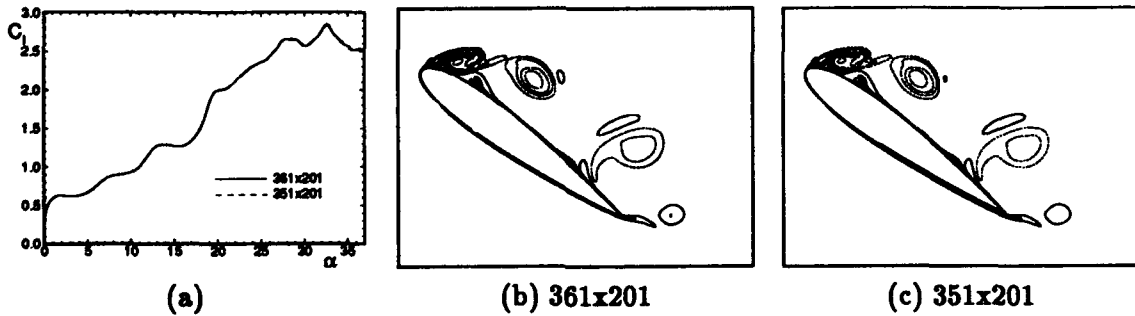


Figure C.3 Effect of tangential blowing at $0.0c$ on C_l and isovorticity contours ($\alpha = 36^\circ$); $v_j = 2.83U_\infty$, $\phi = 10^\circ$, $Re_c = 2.4 \times 10^4$, $M_\infty = 0.2$, $\Omega_0^+ = 0.2$

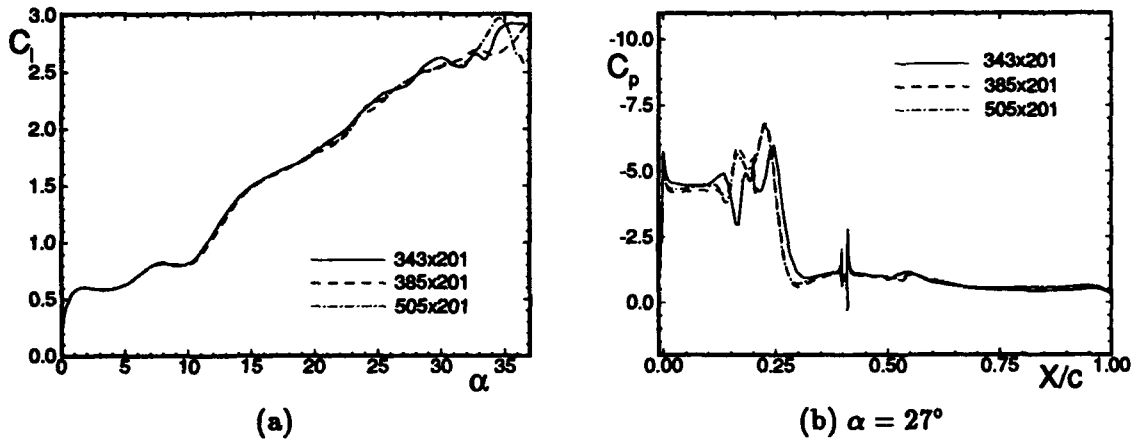


Figure C.4 Effect of tangential blowing at 0.4c slot on C_l and C_p ; $v_j = 2.83U_\infty$, $\phi = 10^\circ$, $Re_c = 2.4 \times 10^4$, $M_\infty = 0.2$, $\Omega_0^+ = 0.2$

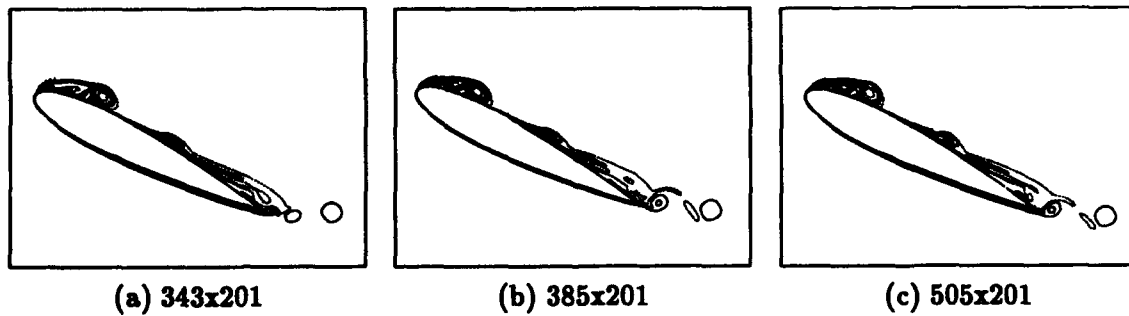


Figure C.5 Effect of tangential blowing at 0.4c on isovorticity contours; $v_j = 2.83U_\infty$, $\phi = 10^\circ$, $\alpha = 27^\circ$, $Re_c = 2.4 \times 10^4$, $M_\infty = 0.2$, $\Omega_0^+ = 0.2$

in the vicinity of the jet slot. To address this issue, the mesh spacing in the slot region was halved for the 0.0c and 0.4c slots of the 385x201 grid, producing two other grids (Table C.1). The mesh spacing in the 0.05c slot region was halved for the 361x201 grid

Table C.1 0.0c- and 0.4c-Slot Grid Study

Grid	Number of Points	
	0.0c Slot	0.4c Slot
385x201	25	21
405x201	25	41
419x201	49	21

as well, producing one additional grid (Table C.2). Note that as the slot spacing is halved at each of the respective slots, the mesh very near the slot is also affected. Additional grid points are required adjacent to the slot-refinement in order to keep the near-slot grid spacing as refined as the baseline grids (385x201 and 361x201) while at the same time give smooth metric variation in the ξ -direction. Thus, the slot-refined grids are essentially the same as the baseline grids, except for the region in the vicinity of the slot.

Table C.2 0.05c-Slot Grid Study

Grid	Number of Points
	0.05c Slot
361x201	21
391x201	41

Tangential-blowing solutions were obtained using the same conditions employed for the 385x201 grid at the 0.0c slot (Figure C.1) and the 0.4c slot (Figure C.4). The natural case was first computed before the blowing case for these grids to insure the solution was invariant with respect to slot-grid refinement. The 0.0c-slot-refined grid (Figure C.6(a)) and 0.4c-slot-refined grid (Figure C.8(a)) show almost no deviation from the baseline 385x201-grid natural-case solution. For tangential blowing, both of these slot-refined grids produce nearly identical results (to $\alpha = 33^\circ$) as the baseline 385x201 grid produces (Figures C.6(b), C.7, C.8(b), C.9). Therefore, computations proceeded on the 385x201 grid.

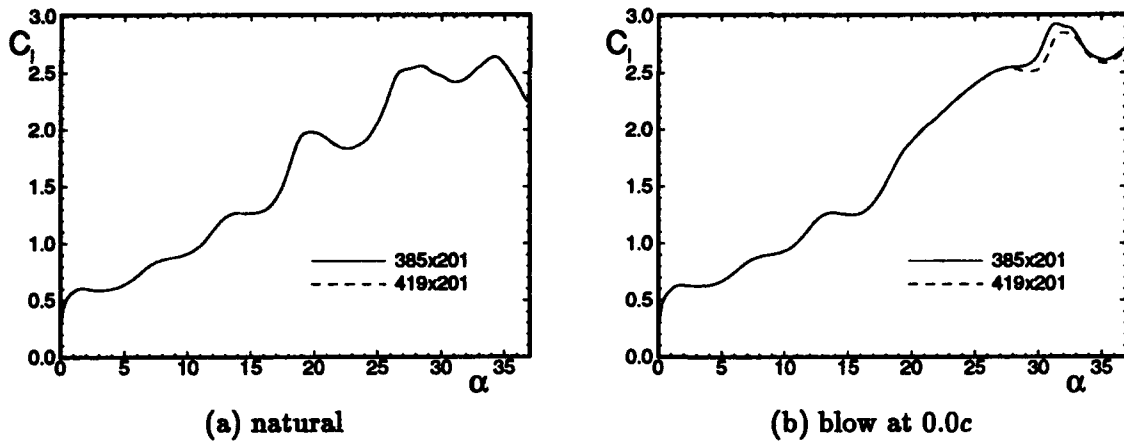


Figure C.6 Effect of 0.0c-slot grid resolution on C_l for natural and blowing cases; $v_j = 2.83U_\infty$, $\phi = 10^\circ$, $Re_c = 2.4 \times 10^4$, $M_\infty = 0.2$, $\Omega_0^+ = 0.2$

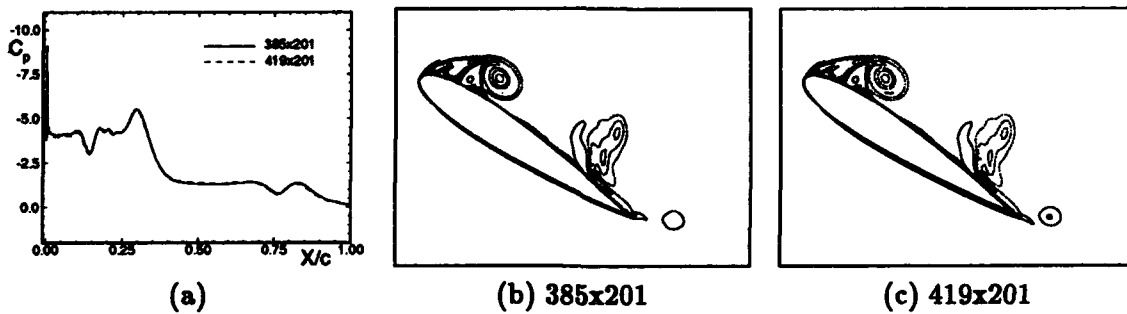


Figure C.7 Effect of 0.0c-slot grid resolution on C_p and isovorticity contours for blowing case; $v_j = 2.83U_\infty$, $\phi = 10^\circ$, $\alpha = 33^\circ$, $Re_c = 2.4 \times 10^4$, $M_\infty = 0.2$, $\Omega_0^+ = 0.2$

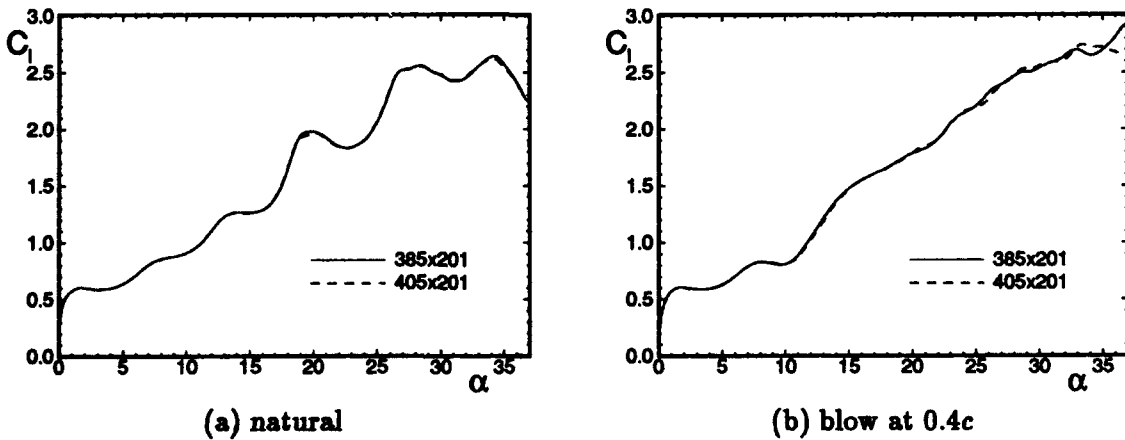


Figure C.8 Effect of 0.4c-slot grid resolution on C_l for natural and blowing cases; $v_j = 2.83U_\infty$, $\phi = 10^\circ$, $Re_c = 2.4 \times 10^4$, $M_\infty = 0.2$, $\Omega_0^+ = 0.2$

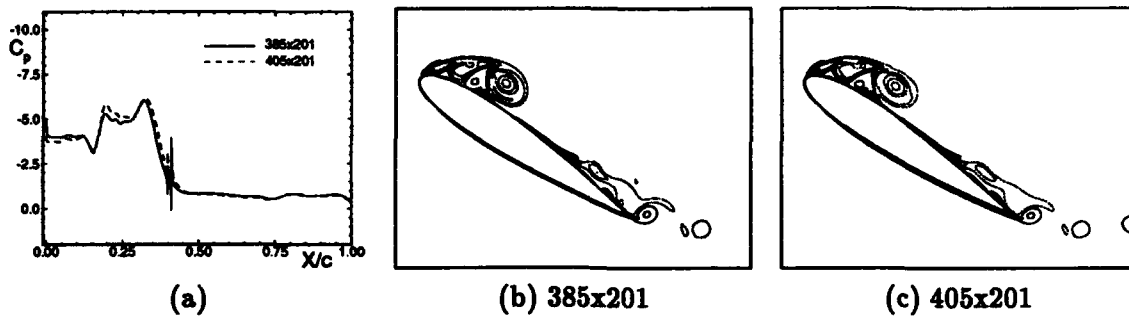


Figure C.9 Effect of $0.4c$ -slot grid resolution on C_p and isovorticity contours for blowing case; $v_j = 2.83U_\infty$, $\phi = 10^\circ$, $\alpha = 33^\circ$, $Re_c = 2.4 \times 10^4$, $M_\infty = 0.2$, $\Omega_0^+ = 0.2$

The other baseline grid (361x201) has a smaller slot width ($0.00717c$) at $0.05c$ than the 385x201 grid ($0.0105c$) has for the $0.0c$ and $0.4c$ slots. Therefore, a higher jet velocity ($v_j = 4.14U_\infty$) is employed in order to maintain the same mass flow (mass-flow issues appear in Section 4.2.1). As with the 385x201 grid and its accompanying slot-refined grids, the slot-refined version of the 361x201 grid gives the same C_l results for the baseline case and matches the blowing-case C_l values to $\alpha = 30^\circ$ (Figure C.10). However, at this

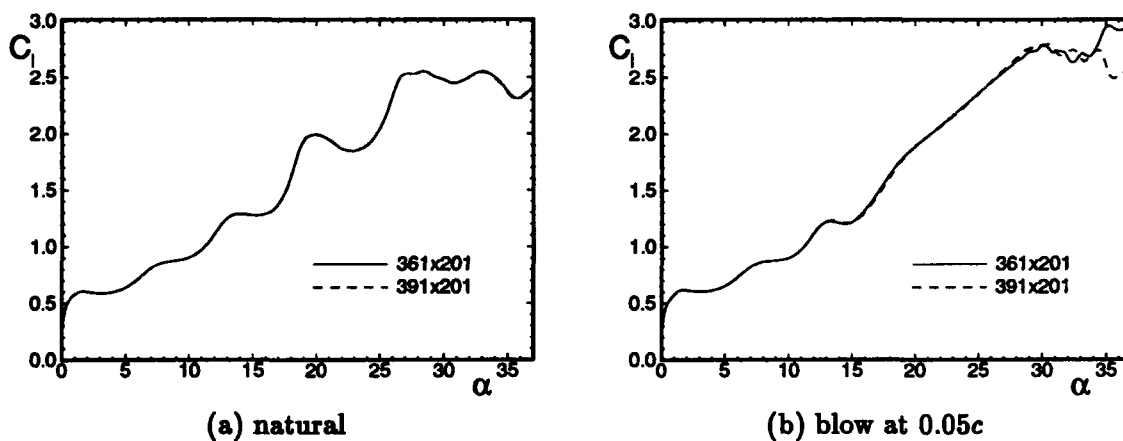


Figure C.10 Effect of $0.05c$ -slot grid resolution on C_l for natural and blowing cases ($v_j = 4.14U_\infty$); $\phi = 10^\circ$, $Re_c = 2.4 \times 10^4$, $M_\infty = 0.2$, $\Omega_0^+ = 0.2$

high blowing velocity, solution degradation is evident when comparing the baseline grid to the slot-refined grid at $\alpha = 30^\circ$ (Figure C.11). Though the difference around the dynamic-stall vortex is quite discernible at this angle of attack, the error in the 361x201 grid is not severe enough to warrant the extra expense of the additional grid points, especially since

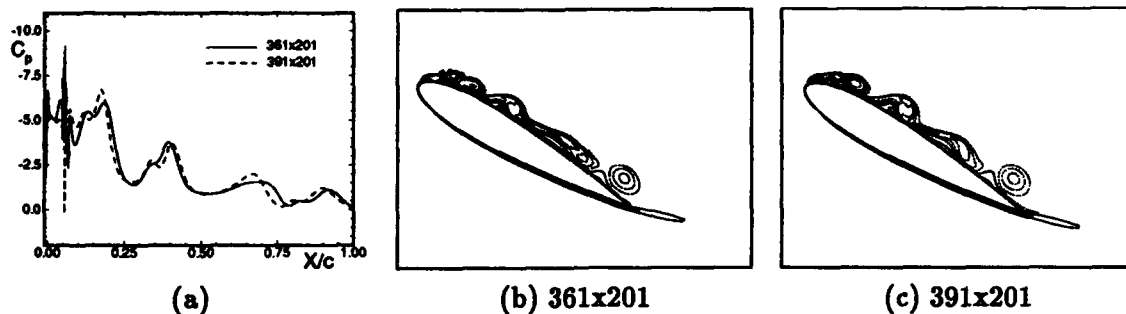


Figure C.11 Effect of 0.05c-slot grid resolution on C_p and isovorticity contours for blowing case ($v_j = 4.14U_\infty$); $\phi = 10^\circ$, $\alpha = 30^\circ$, $Re_c = 2.4 \times 10^4$, $M_\infty = 0.2$, $\Omega_0^+ = 0.2$

the errors are insignificant just prior to dynamic-stall-vortex formation. Also, this problem which exists at these high blowing velocities may be addressed by increasing the numerical damping as will be noted in a following section (Section C.3). Based on these comparisons, this 361x201 grid was deemed adequate to properly spatially resolve the local physics of the flow associated with nearly tangential blowing. The close similarity between the 361x201 and 351x201 grids, in conjunction with the nearly identical agreement between these grids for 0.0c blowing (Figure C.3), indicates this 361x201 slot-grid refinement study is valid for the 351x201 grid as well.

This global- and slot-grid study has verified that the baseline grids (351x201, 361x201, 385x201), determined adequate for the natural case, are also spatially adequate for the tangential blowing case. Temporal discretization and dissipation coefficient issues are next addressed in the following two sections.

C.2 Temporal Discretization Study

A brief check was made to verify that a time step of $\Delta t^+ = 0.001$ is still adequate upon application of the tangential blowing case (Section B.2). Figure C.12 compares the nominal time step with a time step half the value for the 385x201 grid (blowing parameters set to same nominal values as in the slot-grid study of Section C.1). The comparison shows that $\Delta t^+ = 0.001$ is indeed a low-enough time step for accurate study of dynamic-stall onset when tangential blowing is applied (using the nominal conditions).

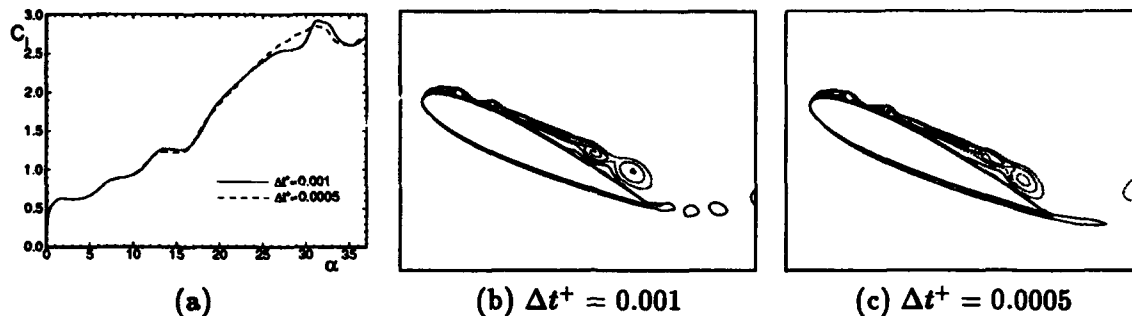


Figure C.12 Effect of time step on C_l and isovorticity contours ($\alpha = 25^\circ$) for 0.0c-slot blowing case; 385x201, $v_j = 2.83U_\infty$, $\phi = 10^\circ$, $Re_c = 2.4 \times 10^4$, $M_\infty = 0.2$, $\Omega_0^+ = 0.2$

C.3 Dissipation Coefficient Study

For the natural case (Section B.3), the nominal explicit damping coefficient of $\epsilon_4 = 0.01$ produces acceptable results. Doubling and halving this value causes almost no discernible solution difference. When tangential blowing is introduced, the solution becomes more sensitive to the same range of dissipation coefficient values, especially after the dynamic-stall vortex is formed.

Halving the nominal dissipation coefficient for 0.0c-blowing (blowing parameters set to same nominal values as in the slot-grid study of Section C.1) with the 385x201 grid shows essentially no difference in C_l until $\alpha = 25^\circ$ (Figure C.13(a)). However, the isovorticity

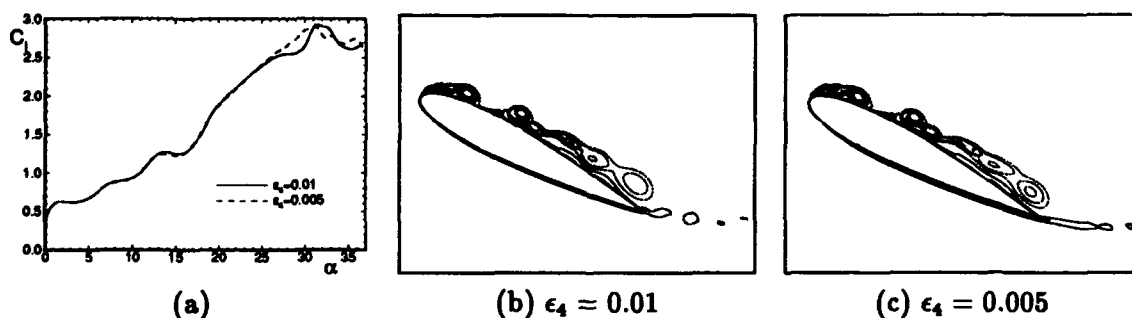


Figure C.13 Effect of dissipation coefficient on C_l and isovorticity contours ($\alpha = 27^\circ$) for 0.0c-slot blowing case; 385x201, $v_j = 2.83U_\infty$, $\phi = 10^\circ$, $Re_c = 2.4 \times 10^4$, $M_\infty = 0.2$, $\Omega_0^+ = 0.2$

contours for $\alpha = 27^\circ$ (Figure C.13(b)-(c)) show little difference well past dynamic-stall

vortex formation. The 0.4c-blowing case (Figure C.14) shows good agreement in C_l to $\alpha = 32^\circ$ and the isovorticity contours compare very well far past dynamic-stall vortex formation.

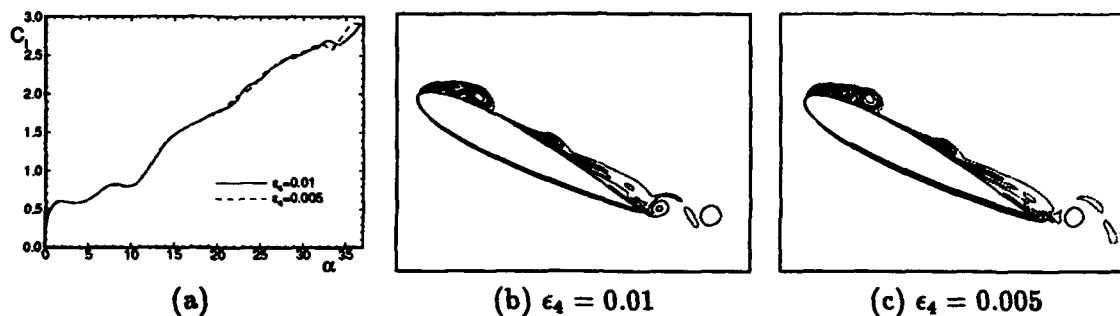


Figure C.14 Effect of dissipation coefficient on C_l and isovorticity contours ($\alpha = 27^\circ$) for 0.4c-slot blowing case; 385×201 , $v_j = 2.83U_\infty$, $\phi = 10^\circ$, $Re_c = 2.4 \times 10^4$, $M_\infty = 0.2$, $\Omega_0^+ = 0.2$

The nominal dissipation coefficient was doubled for the 0.05c-blowing case using the 361×201 grid. Recall (Section C.1) that for this 361×201 grid the jet velocity is increased in order to compare results for the same mass flow ($v_j = 4.14U_\infty$ for the 0.05c slot, while $v_j = 2.83U_\infty$ for the 0.0c and 0.4c slots). At this higher jet velocity, numerical instabilities begin to appear when using the nominal dissipation coefficient ($\epsilon_4 = 0.01$) shortly after dynamic-stall vortex formation (Figure C.15(b)). Since artificial dissipation

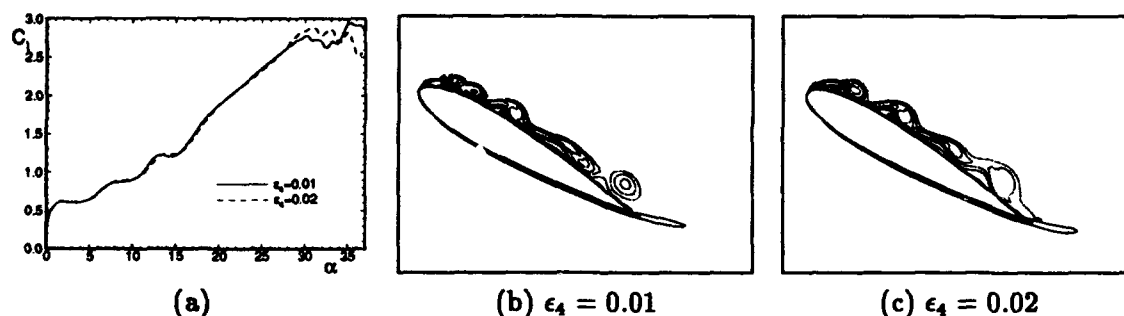


Figure C.15 Effect of dissipation coefficient on C_l and isovorticity contours ($\alpha = 30^\circ$) for 0.05c-slot blowing case; 361×201 , $v_j = 4.14U_\infty$, $\phi = 10^\circ$, $Re_c = 2.4 \times 10^4$, $M_\infty = 0.2$, $\Omega_0^+ = 0.2$

tends to smooth out high gradients in the flow (be they physically real or numerically

generated), doubling the nominal coefficient suppresses the numerical instabilities which cause the high numerically-generated gradients that occur at $\alpha = 30^\circ$ in the dynamic-stall-vortex region (Figure C.15(c)). Attempting to run the code at $\epsilon_4 = 0.01$ and $v_j = 4.245U_\infty$ at the $0.05c$ slot produced such high numerical instabilities that the solution diverged following dynamic-stall vortex formation. Even with high numerical instabilities present in the $\epsilon_4 = 0.01$ solution, differences in C_l are minor far past the onset of dynamic stall (Figure C.15(a)).

Based on this dissipation coefficient study for tangential blowing, the nominal value ($\epsilon_4 = 0.01$) found acceptable for the natural case is adequate also for blowing cases when $v_j < 4U_\infty$.

Appendix D. $M_\infty < 0.2$ Grid and Time-Step Study

The effect of time-step variation on C_l for the 385x201 grid (Figure D.1(a)) is insignificant when going from $\Delta t^+ = 0.0005$ to $\Delta t^+ = 0.00025$, however, $\Delta t^+ = 0.001$

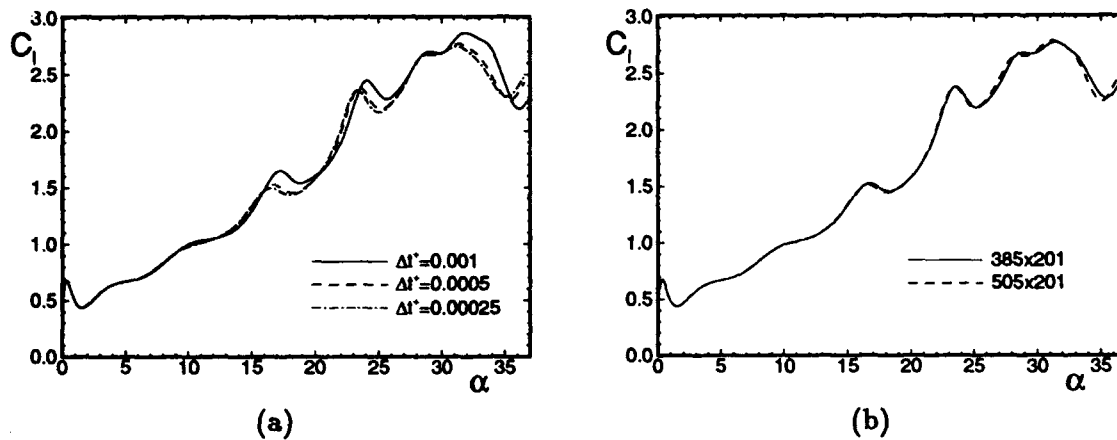


Figure D.1 Effect of time step on C_l (385x201) and effect of grid resolution on C_l (385x201 and 505x201— $\Delta t^+ = 0.0005$); $Re_c = 1.0 \times 10^4$, $M_\infty = 0.1$, $\Omega_0^+ = 0.2$

was deemed too large a time step below $M_\infty = 0.2$. It was determined that, for the pitch-rate and flow conditions considered, a time step of $\Delta t^+ = 0.0005$ is satisfactory for the 385x201 grid. Based on C_l , the 385x201 grid is considered spatially adequate when compared to the 505x201 grid for the same time step of $\Delta t^+ = 0.0005$ (Figure D.1(b)). The C_p plots and isovorticity contours support this conclusion as Figure D.2 presents the excellent agreement between the two different grids to $\alpha = 30^\circ$ and even very good agreement to $\alpha = 36^\circ$.

The 385x201 and 505x201 grids were also used to compute results at $M_\infty = 0.05$ ($Re_c = 1.0 \times 10^4$ and $\Omega_0^+ = 0.2$ as before). The two grids give nearly identical results (using $\Delta t^+ = 0.00025$) demonstrating that the 385x201 grid possesses sufficient spatial resolution (Figure D.3). A time-step study was conducted for the 385x201 grid at the afore mentioned conditions to address temporal discretization errors (Figure D.4 and D.5).

The $\Delta t^+ = 0.0005$ time step (which amounts to 174 time steps per degree α for constant Ω_0^+) appears inadequate when compared against the $\Delta t^+ = 0.00025$ time step for higher angles of attack (Figure D.4(a)), though C_p (Figure D.4(b)) and the isovorticity contours

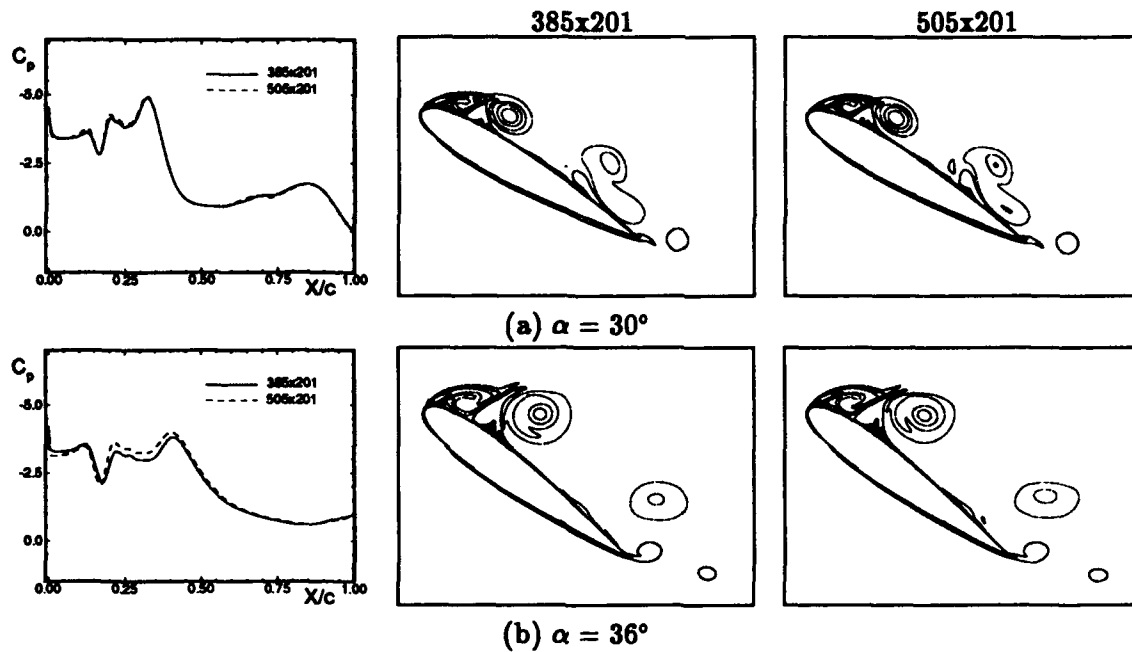


Figure D.2 Effect of spatial resolution on C_p and isovorticity contours; $Re_c = 1.0 \times 10^4$, $M_\infty = 0.1$, $\Omega_0^+ = 0.2$, $\Delta t^+ = 0.0005$

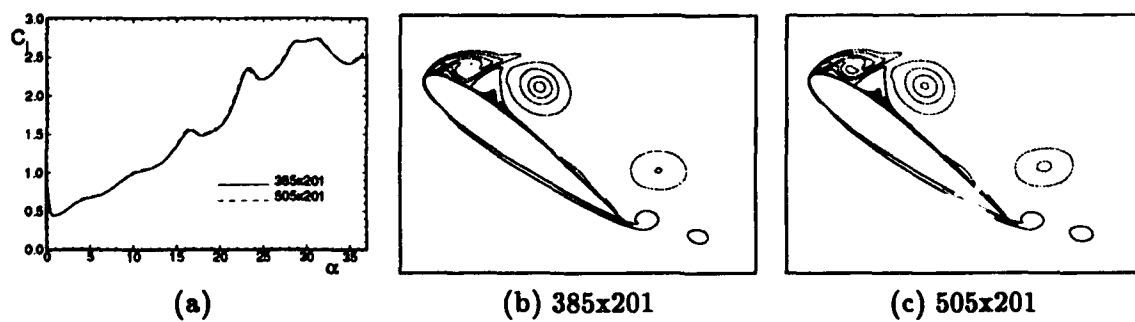


Figure D.3 Effect of spatial resolution on C_l and isovorticity contours ($\alpha = 36^\circ$); $Re_c = 1.0 \times 10^4$, $M_\infty = 0.05$, $\Omega_0^+ = 0.2$, $\Delta t^+ = 0.00025$

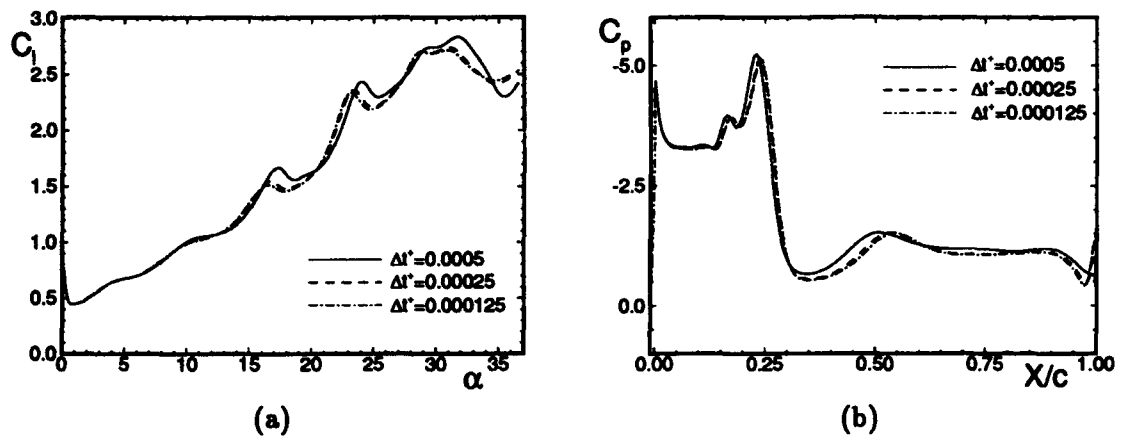


Figure D.4 Effect of time step on C_l and C_p ($\alpha = 25^\circ$); 385x201, $Re_c = 1.0 \times 10^4$, $M_\infty = 0.05$, $\Omega_0^+ = 0.2$

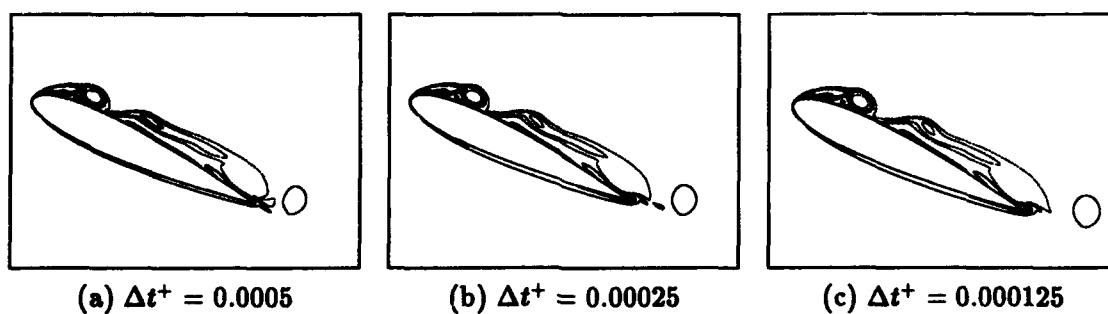


Figure D.5 Effect of time step on isovorticity contours ($\alpha = 25^\circ$); 385x201, $Re_c = 1.0 \times 10^4$, $M_\infty = 0.05$, $\Omega_0^+ = 0.2$

(Figure D.5) look quite similar beyond the stall-onset angle. Solution convergence with respect to time step is reached for $\Delta t^+ = 0.00025$ at $M_\infty = 0.05$.

Appendix E. Suction Slot Grid Study

With solid numerical-artifacts groundwork laid for the natural (Section B) and tangential-blowing (Section C) cases, the only numerical-artifact issue investigated for suction control is slot spatial-resolution. Thus, the previous natural and tangential-blowing global grid studies, time-step studies, and dissipation coefficient studies are deemed valid for this suction-control study.

The 361x201 grid (Figure 4.1(c)) was created for suction-control investigation. Another grid (391x201) was created with half the slot-mesh cell size in the 0.05c-slot region as the 361x201 grid, to verify that the 361x201 grid contains adequate slot spatial resolution to properly capture the physics in the slot region when suction is applied. Good agreement between these two grids has already been shown for tangential-blowing (Figure C.11). For suction, solutions for these grids show even better agreement well past dynamic-stall-vortex formation (Figure E.1). Therefore, based on this comparison in conjunction with

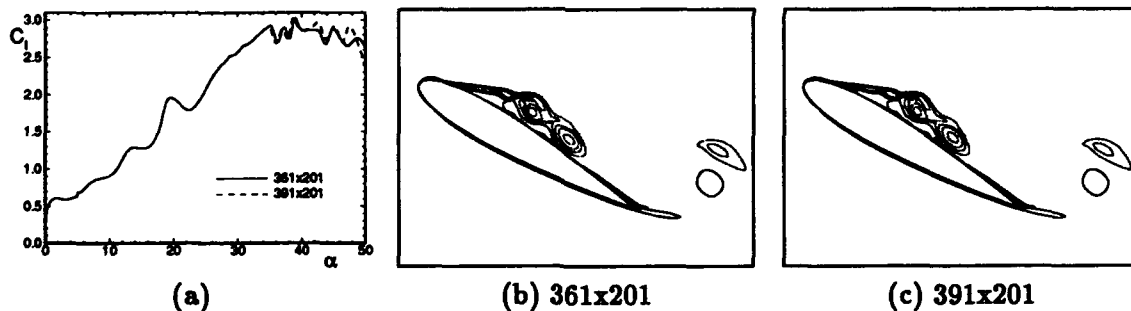


Figure E.1 Effect of 0.05c-slot grid resolution on C_p and isovorticity contours ($\alpha = 42^\circ$) for suction case; $v_s = 0.697U_\infty$, $Re_c = 2.4 \times 10^4$, $M_\infty = 0.2$, $\Omega_0^+ = 0.2$

grid-studies already presented for this grid (Sections B.1 and C.1) the 361x201 grid is deemed to contain adequate spatial resolution to produce grid-independent solutions for dynamic-stall-onset study for suction control.

Since the 351x201 grid (which is very similar to the 361x201 grid) showed such good agreement with the 361x201 0.0c-blowing results (Figure C.3), then this 351x201 grid is also deemed to contain adequate spatial resolution to properly resolve the flow about the NACA 0015 airfoil when suction-control is applied to the 0.05c slot.

Appendix F. Incompressible Flow Code

In this section, the incompressible, laminar-flow, Navier-Stokes equations in two dimensions, the pseudocompressible modification to those equations, and a numerical scheme used to solve the equations with their associated boundary conditions will be presented. It is assumed that the fluid is Newtonian and that Stokes' Law applies.

F.1 Incompressible Flow Governing Equations

The governing equations for two-dimensional, incompressible, laminar flow can be readily written in strong conservative form from the the compressible flow equations (Equation 3.1). With density constant and assuming viscosity constant, then the continuity and momentum equations become decoupled from the energy equation. Dividing through by the density results in a system of equations very similar to the system for compressible flow. In general curvilinear coordinates, the equations are the following. (Note that the flux vector symbols used in the compressible flow case are again used.)

$$\frac{\partial U}{\partial \hat{t}} + \frac{\partial E}{\partial \xi} + \frac{\partial F}{\partial \eta} = \frac{\partial V}{\partial \xi} + \frac{\partial W}{\partial \eta} \quad (\text{F.1})$$

$$U = \bar{J} \begin{pmatrix} 0 \\ u \\ v \end{pmatrix} \quad E = \bar{J} \begin{pmatrix} \bar{U} \\ u\bar{U} + \xi_x p \\ v\bar{U} + \xi_y p \end{pmatrix} \quad F = \bar{J} \begin{pmatrix} \bar{V} \\ u\bar{V} + \eta_x p \\ v\bar{V} + \eta_y p \end{pmatrix}$$

$$V = \bar{J} \nu \begin{pmatrix} 0 \\ b_1 u_\xi + b_2 v_\xi + c_1 u_\eta + c_2 v_\eta \\ b_2 u_\xi + b_3 v_\xi + c_3 u_\eta + c_4 v_\eta \end{pmatrix} \quad W = \bar{J} \nu \begin{pmatrix} 0 \\ c_1 u_\xi + c_3 v_\xi + d_1 u_\eta + d_2 v_\eta \\ c_2 u_\xi + c_4 v_\xi + d_2 u_\eta + d_3 v_\eta \end{pmatrix}.$$

The expressions p and ν result from dividing through by density.

$$p = P/\rho \quad \nu = \mu/\rho$$

The terms b , c , and d are the same as before for the compressible equations (Appendix Section A.1). For this incompressible development, only a non-moving grid is considered,

thus the metric transformations are

$$\xi = \xi(x, y) \quad \eta = \eta(x, y) \quad \hat{t} = t.$$

This gives the same contravariant velocity components (\bar{U} and \bar{V}) and metric relationships as for the compressible case in Section 3.1, except here $\xi_t = \eta_t = 0$.

In Cartesian coordinates the system in Equation F.1 may be written in the following manner (Anderson, et al., 1984:490).

$$\frac{\partial u}{\partial x} + \frac{\partial v}{\partial y} = 0 \quad (\text{F.2})$$

$$\frac{\partial u}{\partial t} + \frac{\partial(u^2 + p)}{\partial x} + \frac{\partial(uv)}{\partial y} = \frac{\partial[\nu(\frac{4}{3}u_x - \frac{2}{3}v_y)]}{\partial x} + \frac{\partial[\nu(u_y + v_x)]}{\partial y} \quad (\text{F.3})$$

$$\frac{\partial v}{\partial t} + \frac{\partial(uv)}{\partial x} + \frac{\partial(v^2 + p)}{\partial y} = \frac{\partial[\nu(u_y + v_x)]}{\partial x} + \frac{\partial[\nu(\frac{4}{3}v_y - \frac{2}{3}u_x)]}{\partial y} \quad (\text{F.4})$$

System F.1 serves as the basis for the system discretization in general curvilinear coordinates used for the cylinder simulation (Section F.4). Equations F.2 - F.4 are used to develop the modified governing equations using pseudocompressibility (Section F.2.1).

F.2 Beam-Warming Scheme for Incompressible Flow

The incompressible Navier-Stokes equations can be solved using the Beam-Warming algorithm when the *pseudocompressibility* (also commonly referred to as *artificial compressibility*) technique is used. Before applying the Beam-Warming algorithm to the incompressible equations, the pseudocompressibility modification is made to the governing equations.

F.2.1 Pseudocompressible Modification to Governing Equations. The difficulty with the incompressible Navier-Stokes equations from a computational perspective is that we now have a hyperbolic-elliptic mixed set of partial differential equations for which standard time-integration techniques are not readily applicable as they are for the hyperbolic-parabolic mixed set that characterize the compressible Navier-Stokes equations (Ander-

son, et al., 1984:479). To circumvent this problem, the continuity equation (expressed in Cartesian coordinates) is modified from Equation F.2 to

$$\frac{\partial p}{\partial \tau} + \beta \left(\frac{\partial u}{\partial x} + \frac{\partial v}{\partial y} \right) = 0, \quad (\text{F.5})$$

where τ is a manufactured variable referred to in the literature as *pseudotime*. It has no physical meaning. It is simply a trick to turn our system of partial differential equations back into a hyperbolic-parabolic mixed system for which many techniques for flow solution already exist. β is a term that is set to a large number such that when the modified continuity equation is satisfied in a pseudotime "steady state" sense; then the actual continuity equation is satisfied to a degree deemed appropriate for a given problem. This modification causes all three unknown flow variables (u , v , and p) to appear explicitly in each of the three equations that comprise the system of governing equations for incompressible, laminar flow. The system of equations expressed in Cartesian coordinates is now the modified continuity equation given in Equation F.5 along with the two momentum equations given by Equations F.3 and F.4. It is to this system that the Beam-Warming algorithm is applied.

F.2.2 Steady-State Incompressible Flow. Solving the modified system (Equations F.3, F.4, and F.5), for a steady-state solution is essentially the same as solving the compressible Navier-Stokes equations. The main difference is that the incompressible Navier-Stokes equations are advanced in pseudotime (τ) instead of computational time (\hat{t} - which for our transformation, is actually the same as physical time, t). The step-by-step process of arriving at the Beam-Warming algorithm for the steady-state solution to the incompressible, laminar flow equations is outlined in this section.

After switching the time differentiation to pseudotime for the two momentum equations (Equations F.3 and F.4), the system of equations can be expressed in vector form for a general curvilinear coordinate system as follows.

$$\frac{\partial U}{\partial \tau} + \frac{\partial E}{\partial \xi} + \frac{\partial F}{\partial \eta} = \frac{\partial V}{\partial \xi} + \frac{\partial W}{\partial \eta} \quad (\text{F.6})$$

The flux vectors are now the following.

$$U = \bar{J} \begin{pmatrix} p \\ u \\ v \end{pmatrix} \quad E = \bar{J} \begin{pmatrix} \beta \bar{U} \\ u \bar{U} + \xi_x p \\ v \bar{U} + \xi_y p \end{pmatrix} \quad F = \bar{J} \begin{pmatrix} \beta \bar{V} \\ u \bar{V} + \eta_x p \\ v \bar{V} + \eta_y p \end{pmatrix}$$

$$V = \bar{J} \nu \begin{pmatrix} 0 \\ b_1 u_\xi + b_2 v_\xi + c_1 u_\eta + c_2 v_\eta \\ b_2 u_\xi + b_3 v_\xi + c_3 u_\eta + c_4 v_\eta \end{pmatrix} \quad W = \bar{J} \nu \begin{pmatrix} 0 \\ c_1 u_\xi + c_3 v_\xi + d_1 u_\eta + d_2 v_\eta \\ c_2 u_\xi + c_4 v_\xi + d_2 u_\eta + d_3 v_\eta \end{pmatrix}$$

Equation F.6 is identical to F.1 except U is now differentiated with respect to pseudo-time instead of computational time and the modified continuity equation has replaced the physical continuity equation.

Discretizing Equation F.6 in pseudotime using Euler implicit time differencing gives the following.

$$U^{k+1} - U^k = \Delta\tau(-\partial_\xi E - \partial_\eta F + \partial_\xi V + \partial_\eta W)^{k+1} \quad (\text{F.7})$$

The terms on the right hand side of this equation are at the $k + 1$ pseudotime level. For the Beam-Warming approach, these terms are linearized with respect to pseudotime. For example, the first term is linearized as follows.

$$E^{k+1} = E^k + \left(\frac{\partial E}{\partial U} \right)^k \Delta^k U + O[(\Delta\tau)^2]$$

where $\Delta^k U$ is defined as

$$\Delta^k U \equiv U^{k+1} - U^k.$$

F is linearized in a similar way as E . This linearization produces flux Jacobians A and B .

$$A = \frac{\partial E}{\partial U} \quad B = \frac{\partial F}{\partial U}$$

where the terms of the incompressible flow flux Jacobians are as follows. Note that for steady-state calculations, $\tilde{\beta} = \beta$. For time-dependent calculations, $\tilde{\beta} = \frac{\Delta\tau}{\Delta t} \beta$.

$$A = \begin{pmatrix} 0 & \bar{\beta}\xi_x & \bar{\beta}\xi_y \\ \xi_x & \bar{U} + u\xi_x & u\xi_y \\ \xi_y & v\xi_x & \bar{U} + v\xi_y \end{pmatrix}$$

$$B = \begin{pmatrix} 0 & \bar{\beta}\eta_x & \bar{\beta}\eta_y \\ \eta_x & \bar{V} + u\eta_x & u\eta_y \\ \eta_y & v\eta_x & \bar{V} + v\eta_y \end{pmatrix}$$

The viscous flux vectors contain terms that can destroy the tridiagonal nature of the system when factorizing it into distinct sweeps in the ξ direction and η direction. This problem can be avoided by regrouping the viscous flux terms into two expressions involving only ξ -derivative and η -derivative expressions respectively, as was done for the compressible case. The approximate factorization employed for the compressible case accounts for the effect of the V_1 and W_2 viscous flux vectors at each time step through the flux Jacobians R and S (Equations 3.8 and 3.9). The effect of the viscous flux vectors containing cross derivative terms ($\partial_\xi V_2^{n+1}$ and $\partial_\eta W_1^{n+1}$) are ignored at a given time step; this has no impact on the formal first-order time accuracy of the scheme (Beam and Warming, 1978). Here for the incompressible case, the same procedure is used.

$$V = V_1 + V_2 \quad W = W_1 + W_2$$

where

$$V_1 = \bar{J}\nu \begin{pmatrix} 0 \\ b_1 u_\xi + b_2 v_\xi \\ b_2 u_\xi + b_3 v_\xi \end{pmatrix} \quad V_2 = \bar{J}\nu \begin{pmatrix} 0 \\ c_1 u_\eta + c_2 v_\eta \\ c_3 u_\eta + c_4 v_\eta \end{pmatrix}$$

$$W_1 = \bar{J}\nu \begin{pmatrix} 0 \\ c_1 u_\xi + c_3 v_\xi \\ c_2 u_\xi + c_4 v_\xi \end{pmatrix} \quad W_2 = \bar{J}\nu \begin{pmatrix} 0 \\ d_1 u_\eta + d_2 v_\eta \\ d_2 u_\eta + d_3 v_\eta \end{pmatrix}$$

Linearizing $V_1(U_\xi)$ and $W_2(U_\eta)$ with respect to pseudotime gives the following.

$$V_1^{k+1} = V_1^k + \left(\frac{\partial V_1}{\partial U_\xi} \right)^k \Delta^k U_\xi + O[(\Delta\tau)^2] = V_1^k + R^k \Delta^k U_\xi + O[(\Delta\tau)^2]$$

$$W_2^{k+1} = W_2^k + \left(\frac{\partial W_2}{\partial U_\eta} \right)^k \Delta^k U_\eta + O[(\Delta\tau)^2] = W_2^k + S^k \Delta^k U_\eta + O[(\Delta\tau)^2]$$

where $R^k = \left(\frac{\partial V_1}{\partial U_\xi} \right)^k$ and $S^k = \left(\frac{\partial W_2}{\partial U_\eta} \right)^k$ are the V_1 and W_2 viscous term flux Jacobians, respectively. With U_ξ and U_η given by

$$U_\xi = \bar{J} \begin{pmatrix} p_\xi \\ u_\xi \\ v_\xi \end{pmatrix} \quad U_\eta = \bar{J} \begin{pmatrix} p_\eta \\ u_\eta \\ v_\eta \end{pmatrix},$$

then the viscous flux Jacobians R and S are given by the following.

$$R = \frac{\partial(0, b_1 u_\xi + b_2 v_\xi, b_2 u_\xi + b_3 v_\xi)}{\partial(p_\xi, u_\xi, v_\xi)} = \nu \begin{pmatrix} 0 & 0 & 0 \\ 0 & b_1 & b_2 \\ 0 & b_2 & b_3 \end{pmatrix} \quad (\text{F.8})$$

$$S = \frac{\partial(0, d_1 u_\eta + d_2 v_\eta, d_2 u_\eta + d_3 v_\eta)}{\partial(p_\eta, u_\eta, v_\eta)} = \nu \begin{pmatrix} 0 & 0 & 0 \\ 0 & d_1 & d_2 \\ 0 & d_2 & d_3 \end{pmatrix} \quad (\text{F.9})$$

Thus, V_1^{k+1} and W_2^{k+1} are now expressed as follows.

$$V_1^{k+1} \simeq V_1^k + \frac{\partial}{\partial \xi} (R \Delta^k U)$$

$$W_2^{k+1} \simeq W_2^k + \frac{\partial}{\partial \eta} (S \Delta^k U)$$

Substituting in the linearized values, Equation F.7 now becomes the following.

$$\begin{aligned} \Delta^k U &= \Delta\tau(-\partial_\xi E - \partial_\eta F + \partial_\xi V + \partial_\eta W)^k + \\ &\quad \Delta\tau(-\partial_\xi A^k - \partial_\eta B^k + \partial_{\xi\xi} R + \partial_{\eta\eta} S) \Delta^k U + O(\Delta\tau) \end{aligned} \quad (\text{F.10})$$

Equation F.10 is rewritten in approximate factored form as follows.

$$[I + \Delta\tau(\partial_\xi A^k - \partial_{\xi\xi} R)] [I + \Delta\tau(\partial_\eta B^k - \partial_{\eta\eta} S)] \Delta^k U = \mathfrak{R}^k \quad (\text{F.11})$$

where

$$\mathfrak{R}^k = \Delta\tau(-\partial_\xi E - \partial_\eta F + \partial_\xi V + \partial_\eta W)^k$$

Equation F.12 is solved using a three-step process.

$$(\text{step 1: } \xi \text{ sweep}) \quad [I + \Delta\tau(\partial_\xi A^k - \partial_{\xi\xi} R)] D = \mathfrak{R}^k$$

$$(\text{step 2: } \eta \text{ sweep}) \quad [I + \Delta\tau(\partial_\eta B^k - \partial_{\eta\eta} S)] \Delta^k U = D$$

$$(\text{step 3: update}) \quad U^{k+1} = U^k + \Delta^k U$$

F.2.3 Local Time Step. Pullium (1984) indicates that for steady-state solution to the Navier-Stokes equations, a local time step may be used to accelerate convergence two to three times. He recommends using a local time step of the form

$$\Delta t_0 \left(\frac{1}{1 + \sqrt{J}} \right)$$

where Δt_0 is chosen to be $O(1)$. For the pseudocompressible technique Δt_0 of 0.1 was found superior to other values for the case of flow about a cylinder using an 85×41 grid and a β value of 400.

F.2.4 Artificial Viscosity. The Beam-Warming algorithm usually requires the addition of dissipative terms to damp out short wavelengths inherent in the scheme (Beam and Warming, 1978). Fourth-order explicit damping and second-order implicit damping is added to control numerical instabilities. The fourth-order damping added to the right-hand side of Equation F.11 is

$$-\epsilon_e \Delta\tau \bar{J} (\delta_{\xi\xi\xi\xi} + \delta_{\eta\eta\eta\eta}) JU.$$

The ξ -sweep and η -sweep second-order implicit damping operators added to the left-hand side of Equation F.11 are as follows.

$$-\epsilon_i \Delta \tau \bar{J} \delta_{\xi\xi} J I \qquad - \epsilon_i \Delta \tau \bar{J} \delta_{\eta\eta} J I.$$

The damping coefficients are of $O(1)$ and $\epsilon_i \geq 2\epsilon_c$.

The scheme, using difference operator notation and including damping terms, becomes the following.

$$\left[I + \Delta \tau (\delta_\xi A^k - \delta_{\xi\xi} R - \epsilon_i \bar{J} \delta_{\xi\xi} J) \right] \left[I + \Delta \tau (\delta_\eta B^k - \delta_{\eta\eta} S - \epsilon_i \bar{J} \delta_{\eta\eta} J) \right] \Delta^k U = \mathfrak{R}^k \quad (\text{F.12})$$

where

$$\mathfrak{R}^k = \Delta \tau (-\delta_\xi E - \delta_\eta F + \delta_\xi V + \delta_\eta W - \epsilon_c \bar{J} (\delta_{\xi\xi\xi\xi} + \delta_{\eta\eta\eta\eta}) J U)^k.$$

F.2.5 Outflow Boundary Conditions. The boundary conditions used for the outer boundary are:

$$\text{except wake: } u = u_\infty \quad v = v_\infty \quad p = p_\infty = p_{ref}$$

$$\text{wake region: } u_x = 0 \quad v_x = 0 \quad p = p_\infty = p_{ref}$$

In general curvilinear coordinates, the extrapolated boundary conditions become the following.

$$u_x = 0 = u_\xi \xi_x + u_\eta \eta_x$$

The extrapolated conditions in the wake region are represented using second-order finite difference representations for the derivatives. This leads to a tridiagonal system of equations to solve for outer boundary points contained in the wake region.

$$\frac{u_{i+1,j} - u_{i-1,j}}{2} \xi_{x,i,j} + \frac{3u_{i,j} - 4u_{i,j-1} + u_{i,j-2}}{2} \eta_{x,i,j} = 0$$

$$-u_{i-1,j} + 3u_{i,j} \left(\frac{\eta_x}{\xi_x} \right)_{i,j} + u_{i+1,j} = (4u_{i,j-1} - u_{i,j-2}) \left(\frac{\eta_x}{\xi_x} \right)_{i,j}$$

F.2.6 Time-Accurate Incompressible Flow. The procedure to obtain a time-accurate solution to the incompressible Navier-Stokes equations using pseudocompressibility is presented by Rogers and Kwak (1990). Once the basic equations are obtained, they use an upwind scheme based on flux-vector splitting to compute the flow. In this section, the basic equations for incompressible, laminar flow are developed and the Beam-Warming scheme is applied to the resulting equations.

From Equation F.6, the two momentum equations expressed in general curvilinear coordinates are as follows.

$$\frac{\partial \hat{u}}{\partial \hat{t}} = -\frac{\partial \hat{e}}{\partial \xi} - \frac{\partial \hat{f}}{\partial \eta} + \frac{\partial \hat{v}}{\partial \xi} + \frac{\partial \hat{w}}{\partial \eta} = \hat{r} \quad (\text{F.13})$$

The flux vectors are now the following.

$$\hat{u} = \bar{J} \begin{pmatrix} u \\ v \end{pmatrix} \quad \hat{e} = \bar{J} \begin{pmatrix} u\bar{U} + \xi_x p \\ v\bar{U} + \xi_y p \end{pmatrix} \quad \hat{f} = \bar{J} \begin{pmatrix} u\bar{V} + \eta_x p \\ v\bar{V} + \eta_y p \end{pmatrix}$$

$$\hat{v} = \bar{J}_\nu \begin{pmatrix} b_1 u_\xi + b_2 v_\xi + c_1 u_\eta + c_2 v_\eta \\ b_2 u_\xi + b_3 v_\xi + c_3 u_\eta + c_4 v_\eta \end{pmatrix} \quad \hat{w} = \bar{J}_\nu \begin{pmatrix} c_1 u_\xi + c_3 v_\xi + d_1 u_\eta + d_2 v_\eta \\ c_2 u_\xi + c_4 v_\xi + d_2 u_\eta + d_3 v_\eta \end{pmatrix}$$

The modified continuity equation in general curvilinear coordinates is the following.

$$\frac{\partial(\bar{J}p)}{\partial \tau} = -\beta \left[\frac{\partial(\bar{J}\bar{U})}{\partial \xi} + \frac{\partial(\bar{J}\bar{V})}{\partial \eta} \right] \quad (\text{F.14})$$

Letting n represent the computational time (\hat{t}) level and k represent the pseudo-time (τ) level, then the modified continuity equation becomes the following after Euler pseudotime differencing at the $n + 1$ computational time level.

$$\bar{J}(p^{n+1,k+1} - p^{n+1,k}) = -\Delta\tau\beta[\partial_\xi(\bar{J}\bar{U})^{n+1,k+1} + \partial_\eta(\bar{J}\bar{V})^{n+1,k+1}] \quad (\text{F.15})$$

The momentum equations are next Euler computational-time differenced at the $k + 1$ pseudotime level to give

$$\hat{u}^{n+1,k+1} - \hat{u}^n = \Delta \hat{t} \hat{r}^{n+1,k+1} \quad (\text{F.16})$$

Note that $\hat{u}^{n,k+1} = \hat{u}^{n,k} = \hat{u}^n$. Subtracting $\hat{u}^{n+1,k}$ from both sides of Equation F.16 and rearranging terms gives the following.

$$\hat{u}^{n+1,k+1} - \hat{u}^{n+1,k} = \Delta \hat{t} \hat{r}^{n+1,k+1} - (\hat{u}^{n+1,k} - \hat{u}^n) \quad (\text{F.17})$$

Equations F.15 and F.17 can now be expressed in the following vector notation using delta form.

$$\Delta^k U^{n+1} = \Delta \hat{t} [-\partial_\xi E - \partial_\eta F + \partial_\xi V + \partial_\eta W]^{n+1,k+1} - \Delta^n \check{U}^k \quad (\text{F.18})$$

$$U = \bar{J} \begin{pmatrix} p \\ u \\ v \end{pmatrix} \quad E = \bar{J} \begin{pmatrix} \frac{\Delta \tau}{\Delta t} \beta \bar{U} \\ u \bar{U} + \xi_x p \\ v \bar{U} + \xi_y p \end{pmatrix} \quad F = \bar{J} \begin{pmatrix} \frac{\Delta \tau}{\Delta t} \beta \bar{V} \\ u \bar{V} + \eta_x p \\ v \bar{V} + \eta_y p \end{pmatrix} \quad \check{U} = \bar{J} \begin{pmatrix} 0 \\ u \\ v \end{pmatrix}$$

$$V = \bar{J} \nu \begin{pmatrix} 0 \\ b_1 u_\xi + b_2 v_\xi + c_1 u_\eta + c_2 v_\eta \\ b_2 u_\xi + b_3 v_\xi + c_3 u_\eta + c_4 v_\eta \end{pmatrix} \quad W = \bar{J} \nu \begin{pmatrix} 0 \\ c_1 u_\xi + c_3 v_\xi + d_1 u_\eta + d_2 v_\eta \\ c_2 u_\xi + c_4 v_\xi + d_2 u_\eta + d_3 v_\eta \end{pmatrix}$$

The flux terms on the right-hand side of Equation F.18 are linearized in pseudotime. For example, the first term on the right-hand side is linearized as follows.

$$E^{n+1,k+1} = E^{n+1,k} + \left(\frac{\partial E}{\partial U} \right)^{n+1,k} \Delta^k U^{n+1} = E^{n+1,k} + A \Delta^k U^{n+1}$$

The same linearization is done for F . Since we will be iterating in pseudotime until pseudotime "steady-state" is reached, the viscous terms are lagged in pseudotime and then neglected as in the steady-state case (Section F.2.2). The resulting time-dependent

form of the Beam-Warming algorithm for incompressible flow using pseudocompressibility is the following.

$$[I + \Delta\hat{t}(\partial_\xi A - \partial_{\xi\xi} R)][I + \Delta\hat{t}(\partial_\eta B - \partial_{\eta\eta} S)]\Delta^k U^{n+1} = \mathfrak{R}^{n+1,k} \quad (\text{F.19})$$

where

$$\mathfrak{R}^{n+1,k} = \Delta\hat{t}(-\partial_\xi E - \partial_\eta F + \partial_\xi V + \partial_\eta W)^{n+1,k} - \Delta^n \check{U}^k$$

Flux Jacobians A and B are found in Appendix Section F.2.2. The usual Beam-Warming three-step process is used for solving Equation F.19.

$$\begin{aligned} (\text{step 1: } \xi \text{ sweep}) \quad & [I + \Delta\hat{t}(\partial_\xi A - \partial_{\xi\xi} R)]D = \mathfrak{R}^{n+1,k} \\ (\text{step 2: } \eta \text{ sweep}) \quad & [I + \Delta\hat{t}(\partial_\eta B - \partial_{\eta\eta} S)]\Delta^k U^{n+1} = D \\ (\text{step 3: update}) \quad & U^{n+1,k+1} = U^{n+1,k} + \Delta^k U^{n+1} \end{aligned}$$

When this process converges to the desired level of accuracy (i.e., steady state in pseudotime), then the result is one computational time step taken, as expressed by Equation F.20.

$$0 \approx \mathfrak{R}^{n+1} = \Delta\hat{t}(-\partial_\xi E - \partial_\eta F + \partial_\xi V + \partial_\eta W)^{n+1} - \Delta^n \check{U} \quad (\text{F.20})$$

The number of pseudotime sub-iterations required to successfully advance one computational time step will be addressed in Section F.3.3.

Note that Euler computational-time differencing was used for this development giving $O[\Delta\hat{t}]$ results. If $O[(\Delta\hat{t})^2]$ is desired, this can be easily accomplished by modifying the last term of Equation F.20. In place of $\Delta^n \check{U}$ a three-point difference $(\frac{3}{2}\check{U}^{n+1} - 2\check{U}^n + \frac{1}{2}\check{U}^{n-1})$ may be substituted.

F.3 Incompressible Flow in Driven Cavity

The driven cavity problem will be used to present incompressible flow results for the pseudocompressible technique developed in Section F.2. The boundary and initial conditions will first be presented for this problem followed by steady-state and time-accurate results. For these calculations, the $\partial_{\xi\xi} R$ and $\partial_{\eta\eta} S$ terms (Equations F.8 and F.9) are ne-

glected, which impacts only the convergence of the scheme, and not the accuracy since the right-hand-side of the equation is being driven to zero.

F.3.1 Boundary and Initial Conditions. On all four walls of the square cavity (length of wall $L = 1$), no-slip boundary conditions are used along with specification of a zero normal pressure gradient. For the three non-moving walls, the boundary conditions in equation form are the following.

$$u = 0 \quad v = 0 \quad \frac{\partial p}{\partial n} = 0$$

The lid moves at velocity $u = u_{ref} = 1$.

Initially, everywhere within the interior u , v , and p are specified as

$$u = 0 \quad v = 0 \quad p = p_{ref} = 1.$$

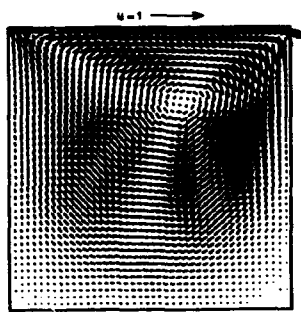
F.3.2 Steady-State Results. The steady-state formulation of the Beam-Warming scheme was used for a 129x129 grid. Convergence criteria required that $\nabla \cdot \mathbf{V} \leq tol$, and $\frac{\mathcal{R}}{\Delta\tau} \leq tol$ (\mathcal{R} of Equation F.12). For this case, $tol = 10^{-9}$.

Figure F.1 shows velocity vectors and streamlines for steady-state flow in the cavity.

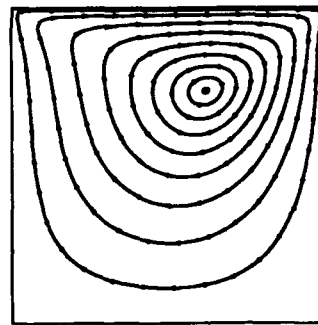
Figure F.2 shows the u and v velocities along a constant y and x station through the middle of the cavity. These match published results for the same flow conditions using the vorticity-stream function approach (Ghia, et al., 1982).

The excellent agreement with published results validates the steady-state pseudo-compressible technique for this driven cavity problem.

F.3.3 Time-Accurate Results. The time-dependent formulation of the Beam-Warming scheme was used for a 41x41 grid. Convergence criteria required that $\nabla \cdot \mathbf{V} \leq tol$, and $\mathcal{R}^{n+1} \leq tol$ (\mathcal{R}^{n+1} of Equation F.20). For this case, $tol = 10^{-5}$.

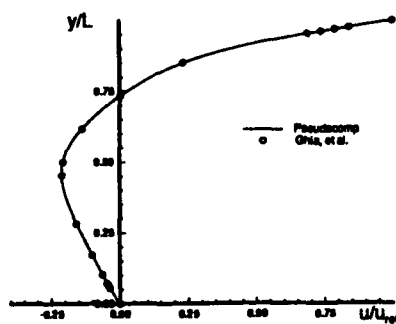


(a)

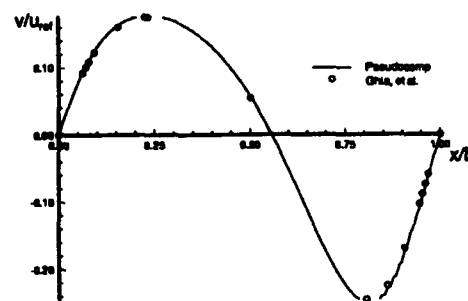


(b)

Figure F.1 Steady-state solution for driven cavity; 129x129 grid ($Re_L = 100, \Delta\tau^+ = 0.005, \beta = 10^3$)



(a)



(b)

Figure F.2 u and v velocities along $y/L = 0.5$ and $x/L = 0.5$ stations, respectively (middle of cavity, $Re_L = 100$)

Figure F.3 presents velocity vector plots and streamlines at various times for the time-dependent calculation of incompressible, viscous flow inside the cavity. These compare very well with the results of Soh and Goodrich (1988).

Figure F.4 shows the drag force (D) acting on the lid as a function of time. The drag force was computed using the following equation.

$$D = \int_0^1 \left(\frac{\partial u}{\partial y} \right)_{y=1} dx \quad (\text{F.21})$$

where

$$\left(\frac{\partial u}{\partial y} \right)_{y=1} \cong \frac{3u_{i,J} - 4u_{i,J-1} + u_{i,J-2}}{2\Delta y}. \quad (\text{F.22})$$

These drag results match Soh and Goodrich's published results. The good agreement with published results validates the time-dependent pseudocompressible technique for this driven cavity problem.

As the time-accurate pseudocompressible code advances in time, fewer pseudotime sub-iterations are required to converge to the desired tolerance. This is shown in Figure F.5. It was observed that the divergence-free flow criteria (i.e., $\nabla \cdot \mathbf{V} \leq \text{tol}$) was more stringent than the residual criteria (i.e., $\mathfrak{R}^{n+1} \leq \text{tol}$). A closer look at the selection of convergence criteria is needed to determine to what degree divergence-free flow needs to be enforced to obtain a good result. It is also quite likely that this criteria will problem and configuration dependent.

F.4 Incompressible Flow About a Cylinder

Incompressible flow at $Re_D = 20$ about a cylinder was also computed using the pseudocompressible technique on an 155x151 grid (Figure F.6(a)). The five-grid-point overlap necessary for periodic boundary conditions is evident in the streamline plot (Figure F.6(b)). At this Reynolds number, there exists a steady-state solution. The solution matches that of Fornberg's (1980) very well (Figure F.6(c)). The solution used tol values for $\nabla \cdot \mathbf{V}$ and \mathfrak{R} of 10^{-5} and 10^{-4} , respectively.

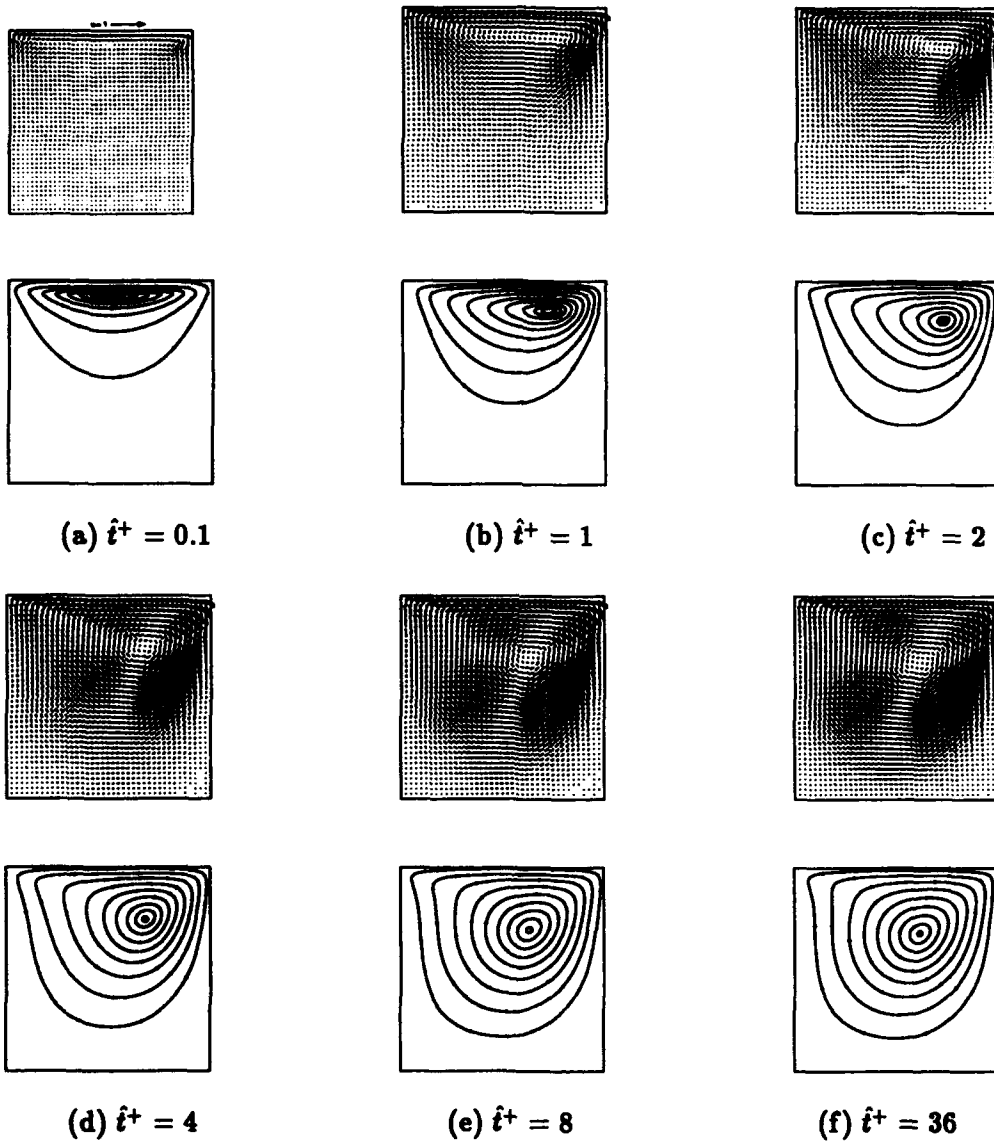


Figure F.3 Velocity vectors and streamlines for time-dependent driven cavity; $Re_L = 200$, $\Delta t^+ = 0.01$, $\Delta \tau^+ = 0.01$, $\beta = 400$

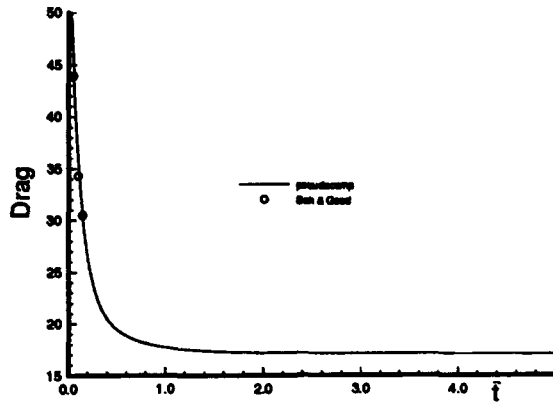


Figure F.4 Drag on lid at various times ($Re_L = 200$, $\Delta t^+ = 0.01$, $\Delta \tau^+ = 0.01$, $\beta = 400$)

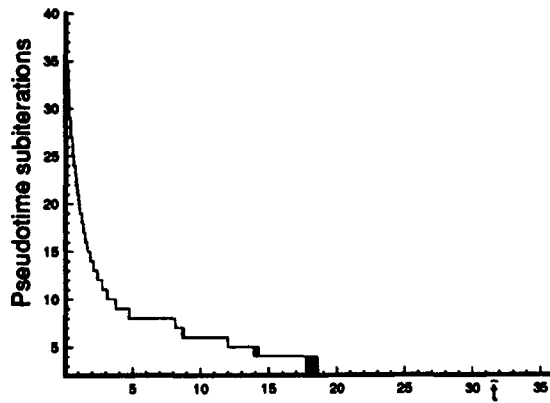


Figure F.5 Pseudotime sub-iterations needed at various time steps ($Re_L = 200$, $\Delta t^+ = 0.01$, $\Delta \tau^+ = 0.01$, $\beta = 400$)

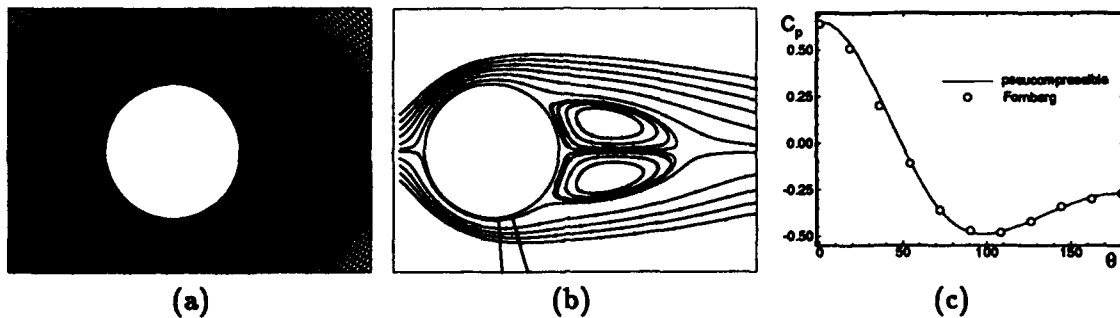


Figure F.6 Grid (155x151), streamlines and C_p for cylinder in incompressible flow; $Re_D = 20$, $t_0 = 0.1$, $\beta = 400$, $\epsilon_4 = 1.0$, $\epsilon_2 = 2.0$

F.5 Difficulties with Pseudocompressibility Technique for Dynamic-Stall Problem

Difficulties were encountered when the pseudocompressible technique described by Equation F.19 was used to solve a time-dependent problem such as flow over a cylinder at higher Re_D or an airfoil at $Re_c = 1.0 \times 10^4$. The technique that was successful for the time-dependent driven cavity problem was monotonically convergent for these problems, however, it was extremely slow (i.e., tens of thousands pseudotime sub-iterations for one computational time iteration).

Investigation into the problem led to the conclusion that the formulation represented by Equation F.19 is slow because only the modified continuity equation (i.e., variable p of U) is explicitly advanced in pseudotime, and the momentum equations (i.e., variables u and v of U) are only implicitly advanced in pseudotime. Note that the steady-state formulation of this technique advances all equations explicitly in pseudotime. Therefore, this formulation of the time-dependent pseudocompressible technique makes for a very slow algorithm.

Other formulations were attempted (Merkle and Athavale, 1987) using approximate factorization schemes that advanced all three equations in pseudotime at much computational time level, but to no avail.

All of these approximate factorization schemes for the time-dependent case suffered from large approximate-factorization errors due to the introduction of the β term into the equations (Steger and Kutler, 1977). This makes the system of equations quite stiff.

The upwinding technique of Rogers and Kwak (1990) (the current state-of-the-art implementation of the pseudocompressible technique) achieves a nearly diagonally dominant system of equations which speeds up convergence considerably. Even with this upwinding technique, it is estimated (based on their cylinder results for $Re_D = 200$) that it will take at least $10\times$ the computer time to compute a pseudocompressible solution to the Navier-Stokes equations compared to a compressible solution for a 385×201 grid (assumes $\nabla \cdot \mathbf{V} < 10^{-2}$ is maintained for the pseudocompressible solution). A $10\times$ increase in computer time translates into approximately 85 CRAY-YMP hours for one dynamic-stall solution (~ 70 hours for the initial condition and ~ 15 hours for the pitch-up). This was considered much too expensive to pursue the pseudocompressible technique any further. Therefore, based upon this resource estimate, the pseudocompressible approach was abandoned in favor of computing the low- M_∞ solutions using the compressible code based on Volpe's (1993) findings (Section 4.1.3).

Bibliography

- Acharya, M., Metwally, M. H. "Unsteady Pressure Field and Vorticity Production over a Pitching Airfoil," *AIAA Journal*, vol. 30, no. 2: 403-411 (Feb 1992).
- Addington, G. A., Schreck, S. J., Luttgies, M. W. "Static and Dynamic Flow Field Development about a Porous Suction Surface Wing," *AIAA Paper 92-2628* (1992).
- Ahmed, S. "Control of Unsteady Separated Flow Associated with the Dynamic Pitching of Airfoils," *NASA-CR-189758, N92-15966* (1992).
- Albertson, J. A., Troutt, T. R., Siuru, W. D., Walker, J. M. "Dynamic Stall Vortex Development and the Surface Pressure Field of a Pitching Airfoil," *AIAA Paper 87-1333* (1987).
- Anderson, D., Tannehill, J., Pletcher, R. *Computational Fluid Mechanics and Heat Transfer*. New York: Hemisphere Publishing Corporation, 1984.
- Beam, R. M., Warming, R. F. "An Implicit Factored Scheme for the Compressible Navier-Stokes Equations," *AIAA Journal*, vol. 16, no. 4 (April 1978).
- Bertin, J. J., Smith, M. L. *Aerodynamics for Engineers*. Englewood Cliffs, New Jersey: Prentice-Hall, Inc., 1979.
- Carr, L. W. "Aerodynamics of Airfoils and High Aspect Ratio Wings Operating at High Angle of Attack in Unsteady Flow," *AIAA Short Course on Unsteady Aerodynamics*, (Aug 1989).
- Carr, L. W. "Dynamic Stall Progress in Analysis and Prediction," *AIAA Paper 85-1769 CP* (1985).
- Carr, L. W., McAlister, K. W. "The Effect of a Leading-Edge Slat on the Dynamic Stall of an Oscillating Airfoil," *AIAA Paper 83-2533* (1983).
- Carr, L. W., McCroskey, W. J. "A Review of Recent Advances in Computational and Experimental Analysis of Dynamic Stall," *UTAM Symposium for Aerodynamics of High Angle of Attack*, Tokyo Japan (Sep 1992).
- Chan, W. M., Steger, J. L. "A Generalized Scheme for Three-Dimensional Hyperbolic Grid Generation," *AIAA Paper 91-1588* (1991)
- Chorin, A. J. "A Numerical Method for Solving Incompressible Viscous Flow Problems," *Journal of Computational Physics*, vol. 2, pp. 12-26 (1967).
- Dindar, M., Kaynak, U. "Effect of Turbulence Modeling on Dynamic Stall of a NACA0012 Airfoil," *AIAA Paper 92-0027* (1992).
- Fant, D. B. "White Paper on the AFOSR Supermaneuverability Workshop at Lehigh University April 9 and 10, 1992," AFOSR (1992).
- Fornberg, B. "A Numerical Study of Steady Viscous Flow Past a Circular Cylinder," *Journal of Fluid Mechanics*, vol. 98: 819-850 (1980).
- Freytmuth, P., Jackson, S., Bank, W. "Toward Dynamic Separation without Dynamic Stall," *Experiments in Fluids*, vol. 7, pp. 187-196 (1989).

- Fung, K. Y., Carr, L. W. "Effects of Compressibility on Dynamic Stall," *AIAA Journal*, vol. 29, no. 2, pp. 306-308 (1991).
- Gendrich, C. P., Koochesfahani, M. M., Visbal, M. R. "Initial Acceleration Effects on the Flow Field Development around Rapidly Pitching Airfoils," *AIAA Paper 93-0438* (1993).
- Ghia, K. N., Yang, J., Osswald, G. A., Ghia, U. "Study of Role of Unsteady Separation in Formation of Dynamic Stall Vortex," *AIAA Paper 92-0196* (Jan 1992).
- Ghia, U., Ghia, K. N., Shin, C. T. "High-Re Solutions for Incompressible Flow Using the Navier-Stokes Equations and a Multigrid Method," *Journal of Computational Physics*, vol. 48, pp. 387-411 (1982).
- Ham, N. D. "Aerodynamic Loading on a Two-Dimensional Airfoil during Dynamic Stall," *AIAA Journal*, vol. 6, no. 10, pp. 1927-1934 (October 1968).
- Ham, N. D., Garelick, M. S. "Dynamic Stall Considerations in Helicopter Rotors," *Journal of the American Helicopter Society*, vol. 13, no. 2, pp. 49-55 (April 1969).
- Ham, N. D., Young, M. I. "Torsional Oscillation of Helicopter Blades Due to Stall," *Journal of Aircraft*, vol. 3, no. 3, pp. 218-224 (1966).
- Harper, P. W., Flannigan, R. E. "The Effect of Change of Angle of Attack on the Maximum Lift of a Small Model," *NACA TN-2061* (1950).
- Harris, F. D., Pruyn, R. R. "Blade Stall—Half Fact, Half Fiction," *Journal of the American Helicopter Society*, vol. 13, no. 2, pp. 27-48 (April 1968).
- Helin, H. E., Walker, J. M. "Interrelated Effects of Pitch Rate and Pivot Point on Airfoil Dynamic Stall," *AIAA Paper 85-0130* (1985).
- Jumper, E. J., Schreck, S. J., Dimmich, R. L. "Lift-Curve Characteristic for an Airfoil Pitching at Constant Rate," *Journal of Aircraft*, vol. 24:680-687 (1987).
- Karim, M. A., Acharya, M. "Control of the Dynamic-Stall Vortex over a Pitching Airfoil by Leading-Edge Suction," *AIAA Paper 93-3267* (1993).
- Koochesfahani, M. M., Smiljanovski, V. "Initial Acceleration Effects on Flow Evolution Around Airfoils Pitching to High Angles of Attack," *em AIAA Journal*, vol. 31, no. 8: 1529 - 1531 (1993).
- Kramer, von M. "Die Zunahme des Maximalauftriebes von Tragflügeln bei plotzlicher Anstellwinkelvergrößerung (Böeneffekt)," *Zeitschrift für Flugtechnik und Motorluftschiffahrt*, vol. 7, pp. 185-189 (April 14, 1932).
- Lachmann, D. (ed.) *Boundary Layer Control*, Pergamon Press, Ltd., 1961.
- Lang, J. D., Francis, M. S. "Unsteady Aerodynamics and Dynamic Aircraft Maneuverability," *AGARD CP-386* (November 1985).
- Lighthill, M. J. *Boundary Layer Theory in Laminar Boundary Layers*, Ed. L. Rosenhead, Oxford University Press (1963).
- Lovato, J. A. Personal correspondence. May 1994.
- Lovato, J. A. "Active Control of the Separation Region on a Two-Dimensional Airfoil," *FJSRL-TR-92-0001* (1992).

- Lovato, J. A., Troutt, T. R. "Active Control of Vortex Structures in a Separating Flow over an Airfoil," *AIAA Paper 92-2728-CP*: 963-970 (1992).
- Luttges, M. W., Robinson, M. C., Kennedy, D. A., "Control of Unsteady Separated Flow Structures on Airfoils," *AIAA Paper 85-0531* (1985).
- McCloud, J. L. III, Hall, L. P., Erady, J. A. "Full-Scale Wind-Tunnel Tests of Blowing Boundary-Layer Control Applied to a Helicopter Rotor," *NASA TN D-335* (September 1960).
- Mehta, U. B. "Dynamic Stall of an Oscillating Airfoil," *AGARD Conference Proceedings CP-227, Symposium on Unsteady Aerodynamics, Paper 23*, (1977).
- Merkle, C. L., Athavale, M. "Time-Accurate Unsteady Incompressible Flow Algorithms Based on Artificial Compressibility," *AIAA Paper 87-1137*, (1987).
- Metwally, M. H. *Investigation and Control of the Unsteady Flow Field over a Pitching Airfoil*, PhD dissertation. Illinois Institute of Technology, Chicago IL, 1990 (ON9301990).
- Oshima, H., Ramaprian, B. R. "Measurements of the Velocity and Vorticity Fields Around a Pitching Airfoil," *AIAA Paper 92-2626-CP* (1992).
- Poisson-Quinton, P., Lepage, L. "French Research on Control of Boundary Layer and Circulation," in *Boundary Layer Control*, (Lachmann, D., ed.), Pergamon Press, Ltd., 1961.
- Pullium, T. H. "Artificial Dissipation Models for the Euler Equations," *AIAA Journal*, vol. 24, no. 12: 1931 - 1940 (1986).
- Pullium, T. H. "Euler and Thin Layer Navier Stokes Codes: ARC2D, ARC3D," *UTSI Computational Fluid Dynamics User's Workshop*, (March 1984).
- Rizzetta, D. P., Visbal, M. R. "Comparative Study of Two Numerical Models for Airfoil Static and Dynamic Stall," *AIAA Paper 92-4649* (1992).
- Rogers, S. E., Kwak, D. "Upwind Differencing Scheme for the Time-Accurate Incompressible Navier-Stokes Equations," *AIAA Journal*, vol. 28, no. 2 (February 1990).
- Schlichting, H. *Boundary Layer Theory*. New York: McGraw-Hill, 1960.
- Sears, W. R., Telionis, D. P. "Boundary-Layer Separation in Unsteady Flow," *SIAM Journal of Applied Math*, vol. 28, no. 1: 215 - 235 (Jan 1975).
- Shih, C., Lourenco, L., Krothapalli, A. "Structure of an Unsteady Separated Flow Near and Airfoil's Leading and Trailing Edges — A Particle Image Velocimetry Study," *AFOSR Workshop on Supermaneuverability: Physics of Unsteady Separated Flows at High Angle-of-Attack*, Lehigh University (Apr 1992).
- Shrewsbury, G. D., Sankar, L. N. "Dynamic Stall of Circulation Control Airfoils," *AIAA Paper 90-0573* (1990).
- Silverstein, A., Katzoff, S., Hootman, J. A. "Comparative Flight and Full-Scale Wind-Tunnel Measurements of the Maximum Lift of an Airplane," *NACA Report 618* (1938).

- Soh, W. Y., Goodrich, J. W. "Unsteady Solution of Incompressible Navier-Stokes Equations," *Journal of Computational Physics*, vol. 79, pp. 113-134 (1988).
- Steger, J. L. "Implicit Finite-Difference Simulation of Flow about Arbitrary Two-Dimensional Geometries," *AIAA Journal*, vol. 16, no. 7: 679 - 686 (Jul 1978).
- Steger, J. L., Kutler, P. "Implicit Finite-Difference Procedures for Computation of Vortex Wakes," *AIAA Journal*, vol. 15, no. 4, 581 - 590 (Apr 1977).
- Towne, M. C., Buter, T. A. "Numerical Simulation of Dynamic Stall Suppression by Tangential Blowing," *AIAA Paper 94-0184* (Jan 1994).
- Visbal, M. R. "On the Formation and Control of the Dynamic Stall Vortex on a Pitching Airfoil," 29th Aerospace Sciences Meeting, *AIAA Paper 91-0006* (January 1991).
- Visbal, M. R. "On Some Physical Aspects of Airfoil Dynamic Stall," *ASME International Symposium on Nonsteady Fluid Dynamics*, June 4-7, 1990, ASME Proceedings, pp. 127-147 (1990a).
- Visbal, M. R. "Dynamic Stall of a Constant-Rate Pitching Airfoil," *Journal of Aircraft*, vol. 27, no. 5: 400-407 (May 1990b).
- Visbal, M. R. "Calculation of Viscous Transonic Flows About a Supercritical Airfoil," *AFWAL-TR-86-3013* (1986a).
- Visbal, M. R. "Evaluation of an Implicit Navier-Stokes Solver for Some Unsteady Separated Flows," *AIAA Paper 86-1053* (1986b).
- Visbal, M. R., Shang, J. S. "Investigation of the Flow Structure Around a Rapidly Pitching Airfoil," *AIAA Journal*, vol. 27, no. 8: 1044-1051 (August 1989).
- Visbal, M. R., Shang, J. S. "Numerical Investigation of the Flow Structure Around a Rapidly Pitching Airfoil," *AIAA Paper 87-1424* (June 1987).
- Volpe, G. "Performance of Compressible Flow Codes at Low Mach Numbers," *AIAA Journal*, vol. 31, no. 1: 49 - 56 (Jan 1993).
- Walker, J., Helin, H., Chou, D. "Unsteady Surface Pressure Measurements on a Pitching Airfoil," *AIAA Paper 85-0532* (1985a).
- Walker, J., Helin, H., Strickland, J. H. "An Experimental Investigation of an Airfoil Undergoing Large Amplitude Pitching Motions," *AIAA Paper 85-0039* (1985b).
- Williams, J. "A Brief History of British Research on Boundary Layer Control for High Lift," in *Boundary Layer Control*, (Lachmann, D., ed.), Pergamon Press, Ltd., 1961.
- Yeh, D. T., Tavella, D. A., Roberts, L., Fujii, K. "Numerical Study of the Effect of Tangential Leading Edge Blowing on Delta Wing Vortical Flow," *AIAA Paper 89-0341* (1989).

Vita

Matthew Carroll Towne was born in Burlington, Vermont on May 15, 1958, the son of Carroll E. Towne and Nina H. Towne. He attended elementary, junior high, and senior high school in Milton, Vermont. In 1981, he received a Bachelor of Science degree in Mechanical Engineering from the University of Vermont, and received a commission as an officer in the United States Air Force. He entered active duty in the Air Force at NASA Ames Research Center at Moffett Field, California in June 1981. From there, in June 1983 he was reassigned to Arnold Engineering Development Center in Tullahoma, Tennessee. He was then assigned to the Air Force Institute of Technology (AFIT) Civilian Institution Program, located at the University of Tennessee Space Institute in Tullahoma, Tennessee where he received a Masters of Science degree in Aeronautical Engineering. In May 1989 he was assigned to the United States Air Force Academy as an instructor in the Aeronautics Department. After two years of teaching, the Department of Aeronautics sponsored his Ph.D. studies at AFIT (in residence) which began in July 1991. After graduating from AFIT as a Doctor of Philosophy, Major Towne will return to the Air Force Academy as an Assistant Professor.

Major Towne married the former Miss Donna R. West of Manchester, Tennessee in May 1988. They have a son, Isaac, who was born in May 1991.

Permanent address: Route 6, Box 6773
Keele Road
Manchester, Tennessee 37355

REPORT DOCUMENTATION PAGE

Form Approved
OMB No. 0704-0188

Public reporting burden for this collection of information is estimated to average 1 hour per response, including the time for reviewing instructions, searching existing data sources, gathering and maintaining the data needed, and completing and reviewing the collection of information. Send comments regarding this burden estimate or any other aspect of this collection of information, including suggestions for reducing this burden, to Washington Headquarters Services, Directorate for Information Operations and Reports, 1215 Jefferson Davis Highway, Suite 1204, Arlington, VA 22202-4302, and to the Office of Management and Budget, Paperwork Reduction Project (0704-0188), Washington, DC 20503

1. AGENCY USE ONLY (Leave blank)	2. REPORT DATE July 1994	3. REPORT TYPE AND DATES COVERED Dissertation Jul 91 - Jul 94
----------------------------------	-----------------------------	--

4. TITLE AND SUBTITLE NUMERICAL SIMULATION OF DYNAMIC-STALL SUPPRESSION BY TANGENTIAL BLOWING	5. FUNDING NUMBERS
--	--------------------

6. AUTHOR(S) Matthew C. Towne, Maj, USAF	
---	--

7. PERFORMING ORGANIZATION NAME(S) AND ADDRESS(ES) Air Force Institute of Technology, WPAFB OH 45433-6583	8. PERFORMING ORGANIZATION REPORT NUMBER AFIT/DS/AA/94-4
--	---

9. SPONSORING / MONITORING AGENCY NAME(S) AND ADDRESS(ES) Flight Dynamics Directorate Wright Laboratory (WL/FIMC) Air Force Materiel Command Wright-Patterson AFB OH 45433-7913	10. SPONSORING / MONITORING AGENCY REPORT NUMBER
---	--

11. SUPPLEMENTARY NOTES

12a. DISTRIBUTION / AVAILABILITY STATEMENT Distribution Unlimited	12b. DISTRIBUTION CODE
--	------------------------

13. ABSTRACT (Maximum 200 words)

The use of tangential blowing to suppress the dynamic stall of a pitching airfoil is investigated numerically. The laminar two-dimensional, compressible Navier-Stokes equations are solved time-accurately using a Beam-Warming algorithm. A slot is located at four different positions along the surface of a NACA 0015 airfoil and air is injected in a nearly tangential sense along the upper surface. Suction control is also employed at one of these slot locations to directly compare with tangential-blowing control. Solution sensitivity to grid refinement, time-step size, numerical smoothing, and initial conditions is investigated at a Reynolds number of 2.4×10^4 . Initial-condition and initial-airfoil-acceleration effects are analyzed for various pitch rates. Compressibility of $M_\infty = 0.2$ solutions is investigated. Numerical simulation uncertainties of jet-orientation angle and jet velocity profile are investigated. Studies are conducted to establish the effects of slot position, slot width, blowing-initiation angle, blowing velocity, pulsed blowing, and blowing at different pitch rates.

14. SUBJECT TERMS Computational Fluid Dynamics, Dynamic Stall, Control, Tangential Blowing, Navier-Stokes Equations, Compressible Flow, Laminar Flow	15. NUMBER OF PAGES 164
	16. PRICE CODE

17. SECURITY CLASSIFICATION OF REPORT UNCLASSIFIED	18. SECURITY CLASSIFICATION OF THIS PAGE UNCLASSIFIED	19. SECURITY CLASSIFICATION OF ABSTRACT UNCLASSIFIED	20. LIMITATION OF ABSTRACT UL
---	--	---	----------------------------------